sid.inpe.br/mtc-m21d/2021/11.20.17.51-TDI

THE FINITE ELEMENT METHOD APPLIED TO GRAVITY FIELDS

Natasha Camargo de Araujo

Doctorate Thesis of the Graduate Course in Space Engineering and Technology/Space Mechanics and Control Division, guided by Dr. Evandro Marconi Rocco, approved in November 30, 2021.

URL of the original document:
<http://urlib.net/8JMKD3MGP3W34T/45R6A42>

INPE
São José dos Campos
2021

PUBLISHED BY:

Instituto Nacional de Pesquisas Espaciais - INPE
Coordenação de Ensino, Pesquisa e Extensão (COEPE)
Divisão de Biblioteca (DIBIB)
CEP 12.227-010
São José dos Campos - SP - Brasil
Tel.:(012) 3208-6923/7348
E-mail: pubtc@inpe.br

sid.inpe.br/mtc-m21d/2021/11.20.17.51-TDI

THE FINITE ELEMENT METHOD APPLIED TO GRAVITY FIELDS

Natasha Camargo de Araujo

Doctorate Thesis of the Graduate Course in Space Engineering and Technology/Space Mechanics and Control Division, guided by Dr. Evandro Marconi Rocco, approved in November 30, 2021.

URL of the original document:
<http://urlib.net/8JMKD3MGP3W34T/45R6A42>

INPE
São José dos Campos
2021

Cataloging in Publication Data

Araujo, Natasha Camargo de.

Ar15f The finite element method applied to gravity fields / Natasha Camargo de Araujo. – São José dos Campos : INPE, 2021.

xxviii + 146 p. ; (sid.inpe.br/mtc-m21d/2021/11.20.17.51-TDI)

Thesis (Doctorate in Space Engineering and Technology/Space Mechanics and Control Division) – Instituto Nacional de Pesquisas Espaciais, São José dos Campos, 2021.

Guiding : Dr. Evandro Marconi Rocco.

1. Finite element method. 2. Asteroids. 3. Gravity field. 4. Small bodies. 5. Mass concentration. I.Title.

CDU 531.216:523.44

MINISTÉRIO DA CIÊNCIA, TECNOLOGIA E INOVAÇÕES

INSTITUTO NACIONAL DE PESQUISAS ESPACIAIS
Serviço de Pós-Graduação - SEPGR

DEFESA FINAL DE TESE DE NATASHA CAMARGO DE ARAUJO
BANCA Nº283/2021, REG 132799/2017.

No dia 30 de novembro de 2021, as 09h00min, por teleconferência, o(a) aluno(a) mencionado(a) acima defendeu seu trabalho final (apresentação oral seguida de arguição) perante uma Banca Examinadora, cujos membros estão listados abaixo. O(A) aluno(a) foi APROVADO(A) pela Banca Examinadora, por unanimidade, em cumprimento ao requisito exigido para obtenção do Título de Doutor em Engenharia e Tecnologia Espaciais/Mecânica Espacial e Controle. O trabalho precisa da incorporação das correções sugeridas pela Banca e revisão final pelo(s) orientador (es).

Título: "THE FINITE ELEMENT METHOD APPLIED TO GRAVITY FIELDS"

Membros da Banca:

Dr. Marcelo Lopes de Oliveira e Souza– Presidente – INPE.
Dr. Evandro Marconi Rocco Orientador – INPE.
Dr. Rodolpho Vilhena de Moraes – Membro Interno – INPE.
Dra. Liana Dias Gonçalves - Membro Interno – INPE.
Dra. Walkiria Schulz – Membro Externo - Universidad Nacional de Córdoba – UNC.
Dr. Aguinaldo Cardozo da Costa Filho – Membro Externo - Instituto Federal de Educação, Ciência e Tecnologia de São Paulo - IFSP

Documento assinado eletronicamente por **Evandro Marconi Rocco**, **Tecnologista**, em 18/12/2021, às 10:35 (horário oficial de Brasília), com fundamento no § 3º do art. 4º do Decreto nº 10.543, de 13 de novembro de 2020.

Documento assinado eletronicamente por **Liana Dias Gonçalves (E)**, **Usuário Externo**, em 20/12/2021, às 08:52 (horário oficial de Brasília), com fundamento no § 3º do art. 4º do Decreto nº 10.543, de 13 de novembro de 2020.

Documento assinado eletronicamente por **Walkiria schulz (E)**, **Usuário Externo**, em 20/12/2021, às 10:19 (horário oficial de Brasília), com fundamento no § 3º do art. 4º do Decreto nº 10.543, de 13 de novembro de 2020.

Documento assinado eletronicamente por **AGUINALDO CARDOZO DA COSTA FILHO (E)**, **Usuário Externo**, em 20/12/2021, às 11:42 (horário oficial de Brasília), com fundamento no § 3º do art. 4º do Decreto nº 10.543, de 13 de novembro de 2020.

Documento assinado eletronicamente por **Rodolpho Vilhena de Moraes (E)**, **Usuário Externo**, em 20/12/2021, às 14:41 (horário oficial de Brasília), com fundamento no § 3º do art. 4º do Decreto nº 10.543, de 13 de novembro de 2020.

Documento assinado eletronicamente por **marcelo lopes de oliveira e souza (E)**, **Usuário Externo**, em 20/12/2021, às 17:23 (horário oficial de Brasília), com fundamento no § 3º do art. 4º do Decreto nº 10.543, de 13 de novembro de 2020.

A autenticidade deste documento pode ser conferida no site http://sei.mctic.gov.br/verifica.html, informando o código verificador **8503468** e o código CRC **C896F20F**.

Referência: Processo nº 01340.007967/2021-67 SEI nº 8503468

“As above, so below.”

Hermes Trismegistus

In *Emerald Tablet*

To Apollo

ACKNOWLEDGEMENTS

I would like to express my gratitude to Professor Evandro Rocco for introducing me to this world full of orbits and spacecrafts, for all the help and support given in this work (even when I was freaking out), and for the friendship built through all these years. I also want to thank Professor Daniel Scheeres for hosting me at the CSML at the University of Colorado Boulder and for showing me the ways to find an incredible scientist inside of me.

I also want to thank Walkiria Schulz from the University of Córdoba for all the precious help and for being a powerful female inspiration. My sincere thanks to all students of the CSML for caring and showing me the importance of sharing. I am also grateful for Professor Marcelo Mota for the help at some points of this work. I'd also like to thanks CAPES.

I am profoundly grateful to my parents Rita and Renato for making me who I am and sharing these awesome genes with me. I want to thank my grandma, Helena, one of the sweetest human beings on Earth I have met so far. A special thank you to my dear friends Elis, Will and Gabriel for being with me in good and bad moments, even when I didn't have the energy to keep going, even when they were miles away from me.

The warmest thanks to Apollo for showing me that the purest love exists on this planet. Secret thanks to Anthony Rastelli, even now that he is not part of my life anymore, he was an important and special part of this process, you can go now. And finally fresh air was brought to me again and I can say that I am profoundly grateful to Diego Guerra and all the support he gave me at the very end of this road. I thank all the Gods for bringing you to my life, I love you to the moon and back.

ABSTRACT

The main goal of this research is to validate the hypothesis of computing with high degree of precision the gravity field of a small body, we do so revisiting the finite elements method and using mass concentration definitions. To achieve this goal, the results obtained with this model are compared with the polyhedron method, the spherical harmonics, and another model known as Method of the Potential Expansion in Series associated to the discretization of the asteroid in tetrahedrons (MEPS) to check if it is possible to apply this technique to gravity fields. The greatest innovation of this method is not to use the Finite Element Method (FEM) to compute the gravity field, but to revisit it and model the body in a much more sophisticated and intricate way, considering a refined tetrahedral mesh to model the interior of the body. We call this approach the Revisited Finite Elements Method (FEMR). To justify the use of this approach, two applications are delivered, showing that the model obtained is not only an innovation in terms of accuracy of results, but it also has its applications. The first application is to evaluate the effect of the asteroid's gravity field on the trajectory of a spacecraft using the FEMR. The second application consists of mapping internal heterogeneities within an asteroid, something that can be done with mastery when using this methodology thanks to its sophisticated and original way to refine the body. Regarding the model validation, three asteroids were selected: 2063 Bacchus, 25143 Itokawa, and 101955 Bennu.

Keywords: Finite Element Method. Asteroids. Gravity Field. Small Bodies. Mass Concentration.

O MÉTODO DOS ELEMENTOS FINITOS APLICADO A CAMPOS GRAVITACIONAIS

RESUMO

O objetivo principal deste trabalho é validar a hipótese de computar com alto grau de precisão o campo gravitacional ao redor de pequenos corpos, usando um método de elementos finitos refinado e alocação de concentrações de massa nos centroides dos elementos. Para atingir este objetivo, os resultados obtidos com esse modelo são comparados com o método poliédrico, o método dos harmônicos esféricos e um modelo híbrido conhecido como método da expansão do potencial em série associado a decomposição do asteroide em elementos tetraédricos. Estes resultados são a chave para validar o novo modelo, e checar se é possível aplicar esta técnica a campos gravitacionais. A maior inovação desse método não é usar o Método dos Elementos Finitos (FEM) para calcular o campo gravitacional, mas revisitá-lo e modelar o corpo de uma forma muito mais sofisticada e intrincada, considerando uma malha tetraédrica refinada para modelar o interior do corpo. Esta abordagem será denominada Método dos Elementos Finitos Revisitado (FEMR). Para justificar o uso desta abordagem, duas aplicações são apresentadas, mostrando que o modelo obtido não é apenas uma inovação em termos de precisão de resultados, mas também é útil. A primeira aplicação é obter o campo gravitacional do asteroide e avaliar sua influência na trajetória de um veículo espacial. A segunda consiste em mapear a heterogeneidade interna do asteroide, algo que pode ser feito com maestria quando esta metodologia (FEMR) é utilizada, graças à maneira original de discretizar o corpo. Três asteroides foram selecionados para a validação do modelo, sendo eles 2063 Bacchus, 25143 Itokawa, e 101955 Bennu.

Palavras-chave: Método dos Elementos Finitos. Asteroides. Campo Gravitacional. Pequenos Corpos. Concentrações de Massa.

LIST OF FIGURES

Page

LIST OF TABLES

Page

LIST OF INITIALS AND ABREVIATIONS

FEM	Finite Element Method
FEMR	Finite Element Method Revisited
MEPS	Method of the Expansion of The Potential in Series
NASA	National Aeronautics and Space Administration
NEA	Near Earth Asteroid
STRS	Spacecraft Trajectory Simulator

LIST OF SYMBOLS

a	Semi-major axis
Fg	Gravitational attraction between two bodies
G	Universal gravitational constant
$M1, M2$	Masses
r	Distance between bodies of mass M_1 and M_2
∇	Gradient
$\ddot{r}$	Second derivative of r
U	Potential
δ	Latitude
λ	Longitude
μ	Gravitational parameter of the body
r_0	Reference radius
P_{nm}	Associated Legendre function
n	Association Legendre function degree
m	Association Legendre function order
C_{nm}, S_{nm}	Gravity field harmonic coefficient
δ_m^0	Kronecker delta
$\bar{C}_{nm}, \bar{S}_{nm}$	Normalized gravity field harmonic coefficient
ρ	Density
$\boldsymbol{r}_e$	Vector from any point of the edge to the polyhedron centroid
$\boldsymbol{r}_f$	Vector from any point of the face to the polyhedron centroid
F_f, E_e	Dyad
L_e	Dimensionless parameter that sums the connections of the polyhedron's edges
V	Volume
i	Inclination
e	Eccentricity
M	Mean Anomaly

TABLE OF CONTENTS

Page

1 INTRODUCTION

Asteroids seem to be just random rocks floating through space, but they are more than what our eyes can see. Many scientists are interested in these bodies, but why? Maybe the main reason is that they can carry with them some clues and even some answers regarding the early stages of our Solar System. It is also important to know as much as we can about them as we may need to deflect a hazardous object one day so it would not collide with Earth. There's also another item that is of interest to scientists and the industry: mining. However, we leave this item for the future right now.

There are numerous small bodies in orbit around the Sun, they can be made of rock or metallic compounds, and can also be binary systems that consist of two bodies rotating through their common center of mass (MARGOT et al., 2002), they can even have moons (GLEISSLER et al., 1996a). Due to their larger number, there are some ways of dividing them. We present some here for the reader to get more familiarized with these objects. Respecting their observable optical properties, and even their composition, asteroids can be divided into various types (BOWELL et al., 1978; CHAPMAN et al., 1975).

- C-type: Dark carbonaceous objects.
- S -type: Stony bodies.
- M-type: Metallic type.
- U-type U: Unclassifiable objects that are out of the mentioned classification.

There is also a class of stony bodies called chondritic meteorites, in which some examples are the H-chondrites and L-chondrites (CHAPMAN, 1996). Small bodies can also be characterized by their parent body, the asteroid that for some reason, like a collision, broke into smaller pieces (KEIL et al., 1994)

Asteroids can also be grouped according to their orbits. And they can be at the asteroid belt, between the orbits of Mars and Jupiter (GRADIE, TEDESCO, 1982). When sharing an orbit with a planet they are called Trojans, being the most famous the Jupiter Trojans (MARZARI; WEIDENSCHILLING, 2002). There is also the Near-Earth Asteroids (NEA), which are objects close to Earth that can be potentially hazardous, and for that deserve special attention (BOTTKE et al., 2000).

There are groups of asteroids that are agglomerates of rocks united by gravity attraction called "rubble pile", and they have diameters between 200 m and 10 km (WALSH, 2018). A good example of a rubble pile is Itokawa. From images captured by Hayabusa showing the existence of boulders and some other elements, scientists brought up the hypothesis of the cigar-shaped asteroid being a product of a collisional breakup that was rebuilt as a rubble pile (FUJIWARA et al., 2006). Rubble piles are of special interest in this work because of a specific application of the model that we are going to present.

Concerning possible origins of asteroids, collisional disruption is not the only way scientists think asteroids originated. Some studies were done to investigate the formation of asteroids by tidal disruption: simulations showed as results bodies similar to the ones in the NEA population (WALSH et al., 2008). Rotational breakup is also a good candidate when thinking about asteroid formation. This kind of breakup can be the result of the Yarkovsky and the YORP effects (VOKROUHLICKÝ et al., 2015; WALSH et al., 2008).

1.1 Motivation and research background

Making a brief analysis of the past, present, and future space missions, it is possible to note a growing attention to asteroids and comets with the most different scientific interests, which is the greatest motivation for this work. Some examples of missions with small bodies as a target can be checked below:

- Aiming to characterize the S-type asteroid 433 EROS the mission NEAR was designed, the mission helped researchers to understand more about small bodies (VERVEKA et al., 2000).

- Talking about small bodies, we can also mention comets, the Rosetta mission to the comet 67P/ChuryumovGerasimenko explored the evolution of the comet (GLASSMEIER et al., 2007).

- Hayabusa that visited asteroid 25143 Itokawa had as the main objective collecting a sample of the body (FUJIWARA et al, 2006)

- Hayabusa 2 also aimed to collect a sample of the target body, but this time of the asteroid (162173) Ryugu (WATANABE et al., 2017).

- MMX to be launched in 2024 to the Martian moons, Phobos and Deimos, seeking to collect a Phobos sample (USUI et al., 2018).

- Janus is going to investigate in-depth binary asteroids (SCHEERES et al., 2020).

- Lucy will explore Jupiter Trojans (STANBRIDGE et al., 2017).

- OSIRIS-Rex a mission to investigate and collect a sample of the asteroid 101955 Bennu (LAURETTA, 2015).

A key concept concerning the design of the trajectory of a spacecraft is the evaluation of the gravity field, and when it comes to small irregular bodies, such as asteroids, this can be a challenging task (FURFARO et al., 2021). Thinking of all these facts and after researching the existing previous models to compute asteroids gravity fields, the idea of this work was born, that is to revisit the idea of modelling the gravity field of small bodies using the finite element method and a mass concentration approach.

But why a finite element model? Mainly because it makes it possible to reach a high degree of refinement within the body that other models were not able to attain. The FEM is revisited in this work so we can bring light to a different way of refining the geometry of a small body in a more sophisticated way than it is usually done when using finite elements for this purpose. Also, the new approach opens up novel and different possibilities of studies that are of the scientific community

interest. Since new methodologies can only be accepted when they are validated and trustworthy, this is one of the main goals of this work.

We begin the study by giving the references that helped to build up this work and presenting all the important concepts to understand it. The following chapters document a brief introduction of the gravity field and the theory of the potential that began with Newton and Laplace (MACMILLAN, 1958). We present some methods to evaluate the gravity field in addition to the approaches presented. We exhibit the approaches used to build and validate the model and also some useful devices such as the Spacecraft Trajectory Simulator (STRS) (ROCCO, 2008a; ROCCO, 2008b), a software that simulates orbital trajectories. The finite element model was adapted and implemented in the STRS for the asteroids that will be mentioned ahead. We do this not only as validation but also to explore the gravity field when the other models fail to do so regarding trajectories simulations. After presenting some previous models, we introduce the finite element model itself. We present the tools derived from the FEM as well as all the equations and theories used to hone the method so it could be ready to evaluate the gravitational potential.

After we display all the references and the model itself, we conduct a careful validation. We do this validation for three selected asteroids, Bacchus, Itokawa, and Bennu, using three different methods for this task. We choose these approaches to guarantee that we can perform the validation checking of the model in many ways. We also do this to show that the model has a general nature and can be used broadly, not only for one specific item of interest or one specific body. With all this done, it is possible to achieve the answer to the main question of this research, that is: finite element definitions can be used to obtain the gravity field of a small body?

After the validation of the model, we present an extension of the study that consists of some trajectory studies, obtained with the FEM, that we present as an important application. The FEM discretization is also used to explore the case of a non-constant density body. We utilize the FEM to map the heterogeneity of asteroid Bennu and compare these results with the ones previously obtained with

the constant density model to check what happens with the gravity field and its coefficients. We also realize both analyses to show that the main goal of the thesis is to create a model that is not only original and general but above all things useful.

1.2 Research goals and contributions

The main hypothesis is to verify the possibility of evaluating the gravity field of an asteroid using finite element definitions to discretize the body in a more refined way than usually used in works found in the literature, and then, apply theories derived from the Mass Concentration Method to obtain the gravitational field.

For this procedure, we model the body using tetrahedrons generating a tetrahedral mesh. This is a step that already generates an important contribution because the method not only discretizes the asteroid's surface, but it also models the inside of the asteroid with high precision leaving no gaps between elements.

The main goal of this work is to validate the model to prove that it works, so it can deliver all the contributions it brings with it. We compare three different methods with the FEM: the polyhedron method, the spherical harmonics approach and Method of the expansion of the Potential in Series. We also select three different asteroids in a way to guarantee that the method works.

After the validation that concludes the first and most important goal. Following; there are two other minor goals. The first of these minor goals is to use the Spacecraft Trajectory Simulator (STRS) to simulate some orbital trajectories. To reach this objective we implemented the FEM approach in the STRS so it can compute the gravity potential using the FEM method.

The second minor objective is to use the FEM method regarding gravity fields to allocate volumes with different densities within the body. With this done we can then estimate the gravity field and check the differences between this approach and the one that considers a constant density. This is another important contribution of our approach as we can only do this because of the way a small body is discretized with the FEM.

Upon reaching all these objectives, it becomes possible to provide a new ready-to-use model, capable of being applied in the modeling of the asteroid's gravitational field, both for high and short distances, including distances within the sphere that circumscribes the asteroid and even on its surface. Furthermore, depending on the number of elements used in the model, it is possible to obtain the same precision of the models found in the literature, or even surpass the precision of those models, as will be demonstrated throughout the work.

Thus, this work represents an advance, not only concerning the gravitational model but also for new, original, and relevant applications that this sophisticated form of discretization of the interior of the asteroid makes possible.

2 THEORETICAL FRAMEWORK AND REFERENCES

When we think about the design of orbital trajectories, we have to consider many aspects. Disturbances are of particular interest because they can degenerate the orbit bringing disastrous impacts to the mission. Perturbations can have a non-gravitational origin, such as the Yarkovsky effect that consists of a force produced by the absorption and re-radiation of the thermal energy. This same force can produce the YORP effect, a torque capable of altering the spin of the body (BOTTKE et al., 2006). Another example of a non-gravitational origin disturbance is the one due to albedo, which is the part of the solar energy reflected from the surface of a body. Examples of the effect of this disturbance on the trajectories of space vehicles around the Earth and the moon can be found in Rocco (2010) and Gonçalves et al. (2015) respectively.

Disturbances can also have a gravitational nature; they can exist due to a third or more bodies. An example is Jupiter and its many moons (ARAUJO, 2017; ARAUJO, ROCCO, 2017; ARAUJO; ROCCO, 2019) or the case of a spacecraft aiming to approach the Martian moons (GONÇALVES, 2018). It is also important to study the impact that the target body's gravitational field can have on a mission, with an analysis of the variation and intensity of the body's gravitational field.

On July 5th, 1687 Isaac Newton's *The Principia* was first published. In this book, Newton has stated the law of gravitational attraction, which states that two particles are attracted by each other with a force equal to the multiplication of their masses, and inversely proportional to the square of their distance. But of course, the study hasn't stopped with Newton, and in 1782 Laplace's equation was created, a largely used tool for the study of the theory of the potential, being the functions that satisfy Laplace's equation, the so-called harmonic functions. George Green in, 1828, has also brought some contributions to the study of the potential such as Gauss, in 1841 (MACMILLAN, 1958).

Since then, many techniques were built and developed to estimate and understand gravitational fields, especially talking about small bodies, as their shape is far from a sphere. Every different approach has its pros and cons. Maybe one can be more accurate but with a high computational price or presents more

complex mathematics but, thinking computationally, it is faster than the others. All methods that are capable of computing the gravity field accurately are useful and can fit specific requirements that some other approaches cannot.

The gravity field of simple polyhedrons was explored by many authors in different ways (NAGGY, 1966; WALDVOGEL, 1997). The potential of bodies with irregular mass distribution was studied using geometric shapes (KELLOG, 1929).

The most classical way to model the gravitational potential of a body is the Spherical Harmonics Method. The Spherical Harmonics coefficients were analytically obtained for a homogeneous body, describing its shape with expressions up to fifth order (BALMINO, 1994). An issue with this approach is that it diverges inside the circumscribing sphere, however this problem can be handled using ellipsoid harmonics (DECHAMBRE; SCHEERES, 2002).

The Exterior gravitational potential of polyhedrons with constant density was obtained analytically, and asteroids were modeled using constant density polyhedrons (WERNER; SCHEERES, 1996).

The polyhedron is of special interest as it can be used to model the gravity field regarding great proximity with the target body (SCHEERES, 1998; SCHEERES, 2012; SCHEERES et al., 2000). A method inspired by the polyhedron that obtained accurate results for the spherical harmonics was also explored thinking of the landing problem (ZHENJIANG et al., 2012).

Another largely used approach is the mascon due to its simplicity and fast implementation. The geopotential was studied using this approach (KOCH; MORRISON, 1970). The volume of an asteroid was filled with point masses, the mascons, in a uniform grid in a way that the summation of these masses was the total mass of the asteroid (GEISSLER et al., 1996b). The mascons were used such as a comparison of the gravitation representation of the asteroid Castalia 4769 with other methods (WERNER, SCHEERES, 1996).

There are also hybrid methods to try to build more realistic and accurate approaches using more than one approach or technique. For example, the Polyhedron model was merged with a mass concentration approach. In this case, the triangular faces are connected with the centroid of the polyhedron creating

tetrahedrons. Later these tetrahedrons are divided into truncated tetrahedrons to refine the polyhedron. After this division mass concentrations, equivalent to the mass of each tetrahedron, are allocated at the centroids of the tetrahedrons and the gravitational potential is computed (GONÇALVES et al., 2017; ROCCO, 2019; ROCCO; GONÇALVES, 2017; VENDITTI, 2013). This method is called the Method of Mass Concentrations with Finite Elements Discretization.

Another method to model the gravitational field of a body with irregular mass distribution was developed by Mota (2017). Applying the potential expansion in series, associated with the decomposition of the body in tetrahedrons linked with the centroid of the polyhedron shape model, the Method of the Expansion of the Potential in Series (MEPS) was created. This method produced coherent results, confirming its validity by comparing the coefficients of spherical harmonics in the cases of asteroids (25143) Itokawa (SCHEERES et al., 2004), (433) Eros (MILLER et al., 2002), (101955) Bennu (CHANUT et al., 2017) and (1580) Betulia (MAGRI et al., 2007; MOTA; ROCCO, 2019). In addition to these cases in which the method was applied, the Method of the Potential Expansion in Series was also applied in determining and analyzing the stability of the equilibrium points referring to the asteroid (21) Lutetia (MOTA; ROCCO, 2019). The results obtained were ratified by comparison with the results of Chanut et al. (2017).

Finite Element definitions were also used to compute gravity fields. The geopotential was studied by (JUNKINS, 1976) using a FEM approximation, and a Finite Element software was created for his analysis opening up possibilities for this kind of application. The two-body problem was explored with the FEM, using the method for a binary asteroid system analysis (YU et al., 2019). Failure modes of the asteroid (25143) Itokawa was investigated using the Finite Element technique (HIRABAYASHI; SCHEERES, 2015), the theme was brought up again considering rotational failure (HIRABAYASHI; SCHEERES, 2019). Finite Element definitions were also used to model the gravity fields using simple geometric shapes such as spheres and cubes (PARK et al., 2010).

Even knowing that the FEM approach was already explored in this field, we chose to revisit it because for the applications desired on this research the body has to

present a high level of discretization not only on the surface, but also within the interiors of the target body, this being the biggest difference and contribution of this new approach.

After this overview to give a taste of the many ways that the gravity field can be characterized, we focus on the methods that we use in this work and present all the essential tools regarding them.

2.1 Gravitational attraction

Starting with Newton, consider an inertial frame of reference, that is, a frame with no translation nor rotational acceleration relative to the fixed stars. According to Newton's law of gravity, the gravitational attraction between two bodies of mass M_1 and M_2 is given by Equation 2.1 (CURTIS, 2019).

$$F_g = \frac{G(M_1 M_2)}{r^2} \tag{2.1}$$

where r is the distance between the bodies of mass M_1 and, and G is the universal gravitational constant equals to $6.67x10^{-11}\ m^3 kg^{-1} s^{-2}$.

The potential energy U is given by Equation 2.2 (CURTIS, 2019). And can be obtained from the force using the gradient ∇ as Equation 2.3 (CURTIS, 2019).

$$U = -\frac{G(M_1 M_2)}{r} \tag{2.2}$$

$$\boldsymbol{F} = -\nabla \boldsymbol{U} \tag{2.3}$$

where ∇ is given by Equation 2.4.

$$\nabla = \frac{\partial}{\partial_x}\hat{\imath} + \frac{\partial}{\partial_y}\hat{\jmath} + \frac{\partial}{\partial_z}\hat{k} \tag{2.4}$$

Considering a symmetric spherical body, with symmetric mass distribution, the potential is given by Equation 2.2. However, when it comes to the real world, this is usually not true, even the Earth is not a perfectly spherical body. And for small bodies, this is not realistic, as they usually are very asymmetrical. With this in mind, let us consider a system of *p* particles, each one with a mass M_i with a

rectangular coordinate system ξ_i, η_i, ζ_i, attracted by another body of mass M_o with coordinates x, y, z. The attraction force of the set M_i on M_o is given by Equation 2.5 (WERNER; SCHEERES, 1996).

$$F = \frac{GM_oM_i}{(r_i)^2} \tag{2.4}$$

Where:

$$r_i = \sqrt{(\xi_i - x)^2 + (\eta_i - y)^2 + (\zeta_i - z)^2} \tag{2.5}$$

The director cosines can be found with Equation 2.6 (MACMILLAN, 1958).

$$\begin{cases} (\xi_i - x)/(r_i) \\ (\eta_i - y)/(r_i) \\ (\zeta_i - z)/(r_i) \end{cases} \tag{2.6}$$

So, for *p* particles, M_i the components X, Y and Z of the attractive force are given by Equation 2.7 (MACMILLAN, 1958).

$$\begin{cases} X = G(Mo)\sum_{i=1}^{p} \dfrac{\xi_i - x}{(r_i)^3} \\ Y = G(Mo)\sum_{i=1}^{p} \dfrac{\eta_i - y}{(r_i)^3} \\ Z = G(Mo)\sum_{i=1}^{p} \dfrac{\zeta_i - z}{(r_i)^3} \end{cases} \tag{2.7}$$

Considering the set of particles M_i as a continuous body the sum turns into an integral as Equation 2.8 (MACMILLAN, 1958).

$$\begin{cases} X = G(Mo)\int \dfrac{\xi_i - x}{(r_i)^3} dM \\ Y = G(Mo)\int \dfrac{\eta_i - y}{(r_i)^3} dM \\ Z = G(Mo)\int \dfrac{\zeta_i - z}{(r_i)^3} dM \end{cases} \tag{2.8}$$

Where:

$$dM = \sigma d\xi d\eta d\zeta$$

2.2 The two-body problem

As is known from Newtonian mechanics, the only way to alter the motion of a body is by applying a force upon it. Given a body with mass M Newton's second law is given by Equation 2.9 (CURTIS, 2019).

$$F = Ma \tag{2.9}$$

where a is the absolute acceleration, measured on an inertial frame. Considering two bodies with mass M_1 and M_2, again, from Equation 2.1, the force on M_2 by M_1 is given by Equation 2.10 (CURTIS, 2019).

$$F_{21} = -\frac{M_1 M_2}{r_i^2} \tag{2.10}$$

Applying Equation 2.10 to the body M_2 is possible to write Equation 2.11 (CURTIS, 2019).

$$\frac{M_1 M_2}{r_i^2} = M_2 \ddot{r}_2 \tag{2.11}$$

Where $\ddot{r}_2$ is the second derivative of r_2.From Newton's third law, that states that for every action there is always an opposed equal reaction (BATE, 2020) we can state Equation 2.12.

$$\boldsymbol{F_{12} = -F_{21}} \tag{2.12}$$

Manipulating the previous equations, it is possible to obtain equation 2.13 that rules the motion of M_2 relative to M_1.

$$\ddot{r} = -\frac{\mu}{r_2} \tag{2.13}$$

Where:

$$\mu = G(M_1 + M_2)$$

2.3 Spherical harmonics

The exterior gravity field, or spherical harmonic gravity field, is one of the most traditional ways to obtain the gravity field and is used in many applications. For

this approach, some coefficients are computed as integrals over the volume of the body (MACMILLAN, 1958). Equation 2.14 (KAULA, 2013) gives the potential

$$U(r,\delta,\gamma) = \frac{\mu}{r}\sum_{n=0}^{\infty}\sum_{m=0}^{n}\left(\frac{r_o}{r}\right)^n P_{nm}(\sin\delta)[C_{nm}\cos(m\lambda) + S_{nm}\sin(m\lambda)] \qquad (2.14)$$

where $\mu = GM$ is the gravitational parameter of the body, r_o is the reference radius, r is the position, δ is the latitude and λ is the longitude, P_{nm} is the associated Legendre function of degree n and order m, C_{nm} and S_{nm} are the gravity field harmonic coefficients given by Equation 2.15 and Equation 2.16.

$$C_{nm} = \frac{2-\delta_m^0}{M}\frac{(1-m)!}{(n+m)!}\int_B\left(\frac{r}{r_o}\right)^n P_{nm}\sin\delta\cos(m\lambda)\sigma dV \qquad (2.15)$$

$$S_{nm} = \frac{2-\delta_m^0}{M}\frac{(1-m)!}{(n+m)!}\int_B\left(\frac{r}{r_o}\right)^n P_{nm}\sin\delta\sin(m\lambda)\sigma dV \qquad (2.16)$$

Where:

$$\sigma dV = \sigma(r,\delta,\lambda)r^2 cos\delta dr d\delta d\lambda$$

Where δ_m^0 is the Kronecker delta.

The gravity coefficients we present in this work are the ones known as normalized coefficients. The normalized coefficients were chosen because for coefficients of higher order and degree their numeric value starts to drop, getting to a point that this generates a numeric error. The coefficient used for the normalization rectifies these errors. The normalized coefficients are given by Equation 2.17 (MONTEBRUCK et al., 2002).

$$\begin{Bmatrix}\bar{C}_{nm}\\ \bar{S}_{nm}\end{Bmatrix} = \sqrt{\frac{(n+m)!}{(2-\delta_{0m})(2n+1)(n-m)!}}\begin{Bmatrix}C_{nm}\\ S_{nm}\end{Bmatrix} \qquad (2.17)$$

A great advantage of this methodology is that the gravity field coefficients can be estimated based on the tracking of a particle moving through the gravity field. This is the foundation for the measurement of a planet's or asteroid's gravity field and provides data on the mass distribution (CHELSEY et al., 2020; LAURETTA et al., 2019). However, since the gravity coefficients are defined as integrals over

the mass distribution, measurement of these coefficients only provides an overall constraint on internal mass distribution and does not provide a unique insight into how the internal mass is distributed. A downside is that the potential does not converge inside the Brillouin sphere, also known as circumscribing sphere, that is a sphere that circumscribes the body. This issue can be softened with the use of ellipsoid harmonics as small bodies usually don't have a shape close to a sphere but to elongated non spherical shapes (ROMAIN; BARRIOT, 2001).

2.4 The polyhedron

The polyhedron method uses as a basis a polyhedron with triangular faces to perform a series of calculations to obtain the gravity field. This method requires an algorithm as it has numerous mathematical expressions. The potential is obtained from Equation 2.18 to 2.22 (WERNER; SCHEERES, 1996).

$$U_p = \frac{1}{2} G\rho \left[\sum_{e \in edges} \mathrm{br}_e \cdot \boldsymbol{E_e} \cdot \boldsymbol{r_e} L_e - \sum_{f \in faces} \mathrm{br}_f \cdot \boldsymbol{F_f} \cdot \boldsymbol{r_f} \omega_f \right] \tag{2.18}$$

$$\boldsymbol{E_e} = \hat{\boldsymbol{n}}_{\boldsymbol{f}} \hat{\boldsymbol{n}}_{\boldsymbol{e}}^{\boldsymbol{f}} + \hat{\boldsymbol{n}}_{\boldsymbol{f}'} \hat{\boldsymbol{n}}_{\boldsymbol{e}}^{\boldsymbol{f}'} \tag{2.19}$$

$$L_e = ln \frac{r_1^e + r_2^e + e_e}{r_1^e + r_2^e - e_e} \tag{2.20}$$

$$\boldsymbol{F_f} = \hat{\boldsymbol{n}}_{\boldsymbol{f}} \hat{\boldsymbol{n}}_{\boldsymbol{f}} \tag{2.21}$$

$$\omega_f = \frac{\boldsymbol{r}_{e1} \cdot \boldsymbol{r}_{e2} \times \boldsymbol{r}_{e3}}{r_{e1} r_{e2} r_{e3} + r_{e1}(\boldsymbol{r}_{e2} \cdot \boldsymbol{r}_{e3}) + r_{e2}(\boldsymbol{r}_{e3} \cdot \boldsymbol{r}_{e1}) + r_{e3}(\boldsymbol{r}_{e1} \cdot \boldsymbol{r}_{e2})} \tag{2.22}$$

Where ρ is the asteroid's density, r_e the distance from any point of the edge e_d to r, and r_f the distance from any point of the face to r. $\boldsymbol{F_f}$, $\hat{\boldsymbol{n}}_{\boldsymbol{f}}$ and $\boldsymbol{E_e}$ both represent a dyad that has magnitude and two associated directions. L_e is a dimensionless parameter that sums the connections of the polyhedron's edges. r_1 and r_2 are distances from the centroid of the body to the points of an edge.

When we think about applications that aim at a close proximity to the body, missions that aim to collect a sample of the target and need an accurate result of the gravity field over the face, we can use the polyhedron for these applications. The strongest advantage of this method is that the gravitational potential, and its

gradients, are known exactly near the surface. It also provides a direct mapping between a body's shape and its gravity field. A drawback is that the potential is only known for a constant density assumption, and thus the computation does not capture the internal mass distribution. Not to say that this method depends on the number of facets, with more facets it is possible to reach a more precise model, however the computing cost is even higher.

2.5 The mass concentration method with finite elements discretization

Another approach to compute the gravity field is the Mass Concentration Method with Finite Elements Discretization (MCMFED) (ROCCO, 2019; ROCCO; VENDITTI, 2013; MOTA, 2019). This is the method used as basis in this work that aims to improve the model with a state-of-the-art FEM mesh.

The basic idea of this approach is to discretize the body by dividing the asteroid's volume into smaller elements, the so-called finite elements. After the division, the position of each centroid of the elements and their respective masses are determined. Then, the mass of each element is concentrated and allocated at the element's centroid. The basic idea of the mass concentration approximation is to divide the asteroid's volume into smaller pieces. With the division done, the mass is distributed through the body in such a way that each one of the pieces would have a certain mass. The summation of all these masses would result in the asteroid's total mass.

We use Figure 2.1 to simplify the understanding of the equations to be presented from Equation 2.23 to Equation 2.39. Where r refers to the position vector that is the distance from the spacecraft to the asteroid's centroid. $\boldsymbol{r}_i$ is the position vector that gives the distance from the spacecraft and a mass concentration centroid $\boldsymbol{m}_i$. $\boldsymbol{R}_i$ is the distance from the mass concentration centroid and the asteroid`s centroid. $\boldsymbol{f}_{gi}$ describes the gravitational force due to a mass concentration element i.

Figure 2.1 - Position vectors.

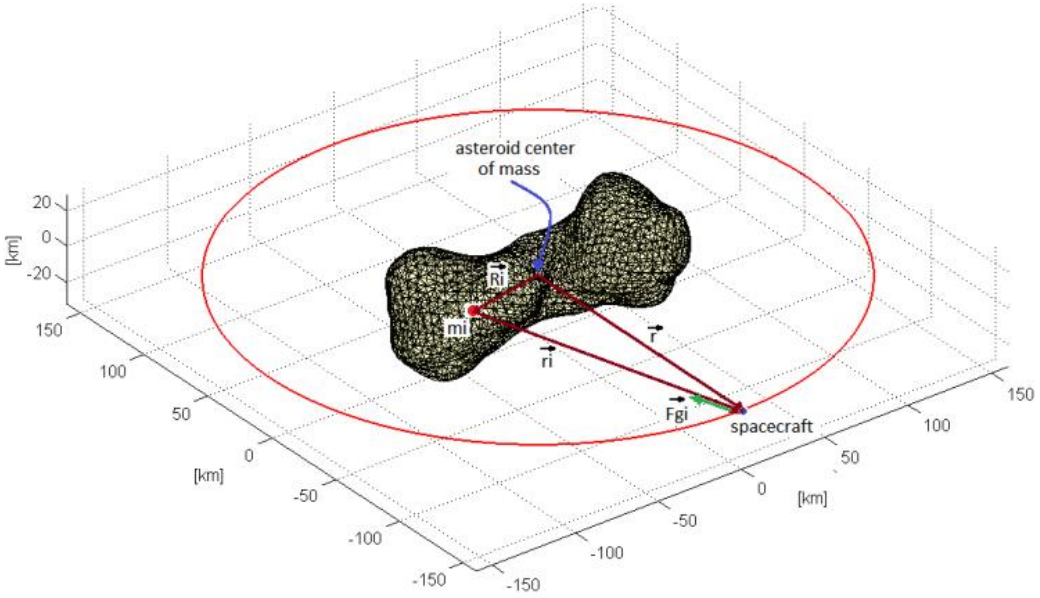

Source: Rocco (2019).

As previously mentioned, the asteroid is divided into many tetrahedrons. In each tetrahedron's barycenter an equivalent concentration of mass is allocated. Given the scenario, the mass of a solid with volume V and density function $\rho(x, y, z)$. The tetrahedron's centroid coordinates are given from Equation 2.23 to Equation 2.39 (ROCCO, 2019).

We obtain position vectors from Equation 2.42 to Equation 2.47. Equation 2.48 to Equation 2.54 give all the gravitational forces. $F_{gi_x}\hat{\imath}$, $F_{gi_y}\hat{\jmath}$ and $F_{gi_z}\hat{k}$ are the force components produced by each one of the concentrations of mass. $F_{gT_x}\hat{\imath}$, $F_{gT_y}\hat{\jmath}$ and $F_{gT_z}\hat{k}$ are total gravitational force components produced by the asteroid (ROCCO, 2019).

$\boldsymbol{F}_C$ is the vector representing the central field gravitational force, that the force considering a central field in which the entire asteroid`s mass would be allocated on the centroid. $\boldsymbol{F}_{gT}$ is the vector representing the actual gravitational force generated by the asteroid (ROCCO, 2019). And $\boldsymbol{F}_p$ represents the disturbance force due to the asteroid`s gravity field.

$$m = \iiint \rho(x,y,z)dV \tag{2.23}$$

$$\bar{x} = \frac{\iiint x\,\rho(x,y,z)dV}{m} \tag{2.24}$$

$$\bar{y} = \frac{\iiint y\,\rho(x,y,z)dV}{m} \tag{2.25}$$

$$\bar{z} = \frac{\iiint z\,\rho(x,y,z)dV}{m} \tag{2.26}$$

$$\boldsymbol{R}_l + \boldsymbol{r}_l = \boldsymbol{r} \tag{2.27}$$

$$\boldsymbol{R}_l = R_{ix}\hat{\imath} + R_{iy}\hat{\jmath} + R_{iz}\hat{k} \tag{2.28}$$

$$\boldsymbol{r_l} = r_{ix}\hat{\imath} + r_{iy}\hat{\jmath} + r_{iz}\hat{k} \tag{2.29}$$

$$\boldsymbol{r} = r_x\hat{\imath} + r_y\hat{\jmath} + r_z\hat{k} \tag{2.30}$$

$$\boldsymbol{r_l} = (r_x - R_{ix})\hat{\imath} + \left(r_y - R_{iy}\right)\hat{\jmath} + (r_z - R_{iz})\hat{k} \tag{2.31}$$

$$r_i = \sqrt{(r_x - R_{ix})^2 + \left(r_y - R_{iy}\right)^2 + (r_z - R_{iz})^2} \tag{2.32}$$

$$F_{gi_x}\hat{\imath} = -\frac{Gm_i m_{sp}}{{r_i}^2}\,\frac{(r_x - R_{ix})}{r_i}\hat{\imath} \tag{2.33}$$

$$F_{gi_y}\hat{\jmath} = -\frac{Gm_i m_{sp}}{{r_i}^2}\,\frac{\left(r_y - R_{iy}\right)}{r_i}\hat{\jmath} \tag{2.34}$$

$$F_{gi_z}\hat{k} = -\frac{Gm_i m_{sp}}{{r_i}^2}\,\frac{(r_z - R_{iz})}{r_i}\hat{k} \tag{2.35}$$

$$F_{gT_x}\hat{\imath} = \sum_{i=1}^{N} F_{gi_x}\,\hat{\imath} \tag{2.36}$$

$$F_{gT_y}\hat{\jmath} = \sum_{i=1}^{N} F_{gi_y}\,\hat{\jmath} \tag{2.37}$$

$$F_{gT_z}\hat{k} = \sum_{i=1}^{N} F_{gi_z}\,\hat{k} \tag{2.38}$$

$$\boldsymbol{F}_p = \boldsymbol{F}_{gT} - \boldsymbol{F}_C \tag{2.39}$$

This basic theory makes this mass concentration approach suitable to merge with the FEM, revisiting it to reach a much more accurate and practical model, without the issue of having a deficient discretization.

One of the greatest advantages of MCMFED approach is its simplicity. With this approach the possibility of using more simple equations is open, which is a relevant contribution for trajectory simulations regarding faster outputs. However, in this approach there is a limitation regarding the precision, which hangs on the body discretization. Depending on the number of elements used to discretize the body, the results may be inaccurate for some applications. Nevertheless, revisiting the FEM we can eliminate this limitation, being this a significant contribution of this work.

2.6 Method of the expansion of the potential in series

One more method of interest in this study is the Method of the Expansion of the Potential in Series (MEPS), that associates the discretization of the asteroid in tetrahedrons with the expansion of the potential in series. The MEPS is an approach created using the method of the expansion in series of the potential, associated with the decomposition of the asteroid into tetrahedral elements. In this method the solid is modelled using a polyhedron, that is, a result of the union of many tetrahedrons, linking the vertex of the triangular basis on the surface to the centroid of the asteroid.

The main objective of the methodology is to express the potential function in an analytical way, providing an advantageous algebraic manipulation, allowing to determine the acceleration vector and other orbital elements that are fundamental in the simulation of trajectories around asteroids. Therefore, following the procedure established by Mota (2017), the potential is given by Equation 2.40.

$$U = \sum_{k=1}^{n} U^{(k)} = G\frac{M}{V}\sum_{1}^{n}\sum_{i=0}^{m}\iiint_{Q} P_i(u)\frac{\beta^i r^i}{r^{2i+1}}dV + \epsilon \qquad (2.40)$$

where U is the potential corresponding to degree n G is the gravitational constant, M is the asteroid mass, V is the asteroid volume, Q is a generic tetrahedral element, r is the modulus of the particle position vector, β is the modulus of the

position vector of the mass element inside the asteroid, $P_i(u)$ are the Legendre's polynomials, and ϵ is the truncation error. With the gravitational potential model and choosing $N(N+2)$ distinct points in the gravitational field of the asteroid, in the form $A_i(\mathrm{r}_i, \delta_i, \lambda_i)$ with $i = 1,2,\dots,N(N+2)$.

With the gravity potential model obtention and choosing $N\ (N\ +\ 2)$ distinct points in the asteroid gravity field, in the form $A_i(\rho_i, \delta_i, \lambda_i)$ with $I\ = 1, 2, \dots, N\ (N\ +\ 2)$. According with (Zhenjiang, 2012) is possible to define a set of $N\ (N\ +\ 2)$ linear equations. The spherical harmonics are computed solving the linear equations, given by Equation (2.41).

$$\sum_{n=1}^{N}\sum_{m=0}^{n}\left(\frac{a}{\rho_1}\right)^n P_{nm}(\sin\delta_1)\left[C_{nm}\cos(m\lambda_1)+S_{nm}\sin(m\lambda_1)\right]=\frac{\rho_1}{\mu}U(A_1)-1$$

$$\sum_{n=1}^{N}\sum_{m=0}^{n}\left(\frac{a}{\rho_1}\right)^n P_{nm}(\sin\delta_1)\left[C_{nm}\cos(m\lambda_1)+S_{nm}\sin(m\lambda_1)\right]=\frac{\rho_1}{\mu}U(A_1)-1 \qquad (2.41)$$

$$\vdots$$

$$\sum_{n=1}^{N}\sum_{m=0}^{n}\left(\frac{a}{\rho_K}\right)^n P_{nm}(\sin\delta_k)\left[C_{nm}\cos(mK)+S_{nm}\sin(m\lambda_k)\right]=\frac{\rho_k}{\mu}U(A_k)-1$$

Where $k\ =\ N\ (N\ +\ 2)$. The Equation (2.24) can be rewritten in the linear form $Ax\ =\ b$, which the solution consists of the spherical harmonics (MOTA, 2019).

Concluding the presentation of the Method of the Expansion of the Potential in Series, it is worth noting that the method applied in the asteroid (21) Lutetia (MOTA; Rocco, 2019) presented excellent results, not only for calculating the potential, but also in determining the equilibrium points around the asteroid, as well as in the analysis of the stability of these points.

2.7 Revisiting the finite element method: gravity fields application

The FEM is a common tool used in many areas of engineering such as electricity, fluid dynamics, structural analysis etc. It has been used in various ways with different purposes. The term Finite Elements was first used by Clough (1960). The basic idea of the method is to divide a complex volume into simple geometric shapes such as hexahedrons and tetrahedrons, these are called Finite Elements

(CHANDRUPATLA et al., 2002). With the divided body, some matrices are used to compute the most diverse properties such as tension and temperature variation over the entire body.

The FEM carries with it a set of complex theories, equations, and algorithms. As the objective of this work is not to create FEM software from scratch, as there are many tools to do so and even free software, here we simply give a brief introduction about the concepts from the method that was used in this work.

2.7.1 FEM mesh

One of the most important FEM concepts we use in this work are the meshes. The mesh we use in this work is not bi-dimensional but is necessary to talk about it first to bring a consistent analysis. In this case, we divide the geometry into triangles, Figure 2.2. The vertices of the triangles are called nodes, and the triangles themselves are the elements. The 3D case is similar, we divide the body in tetrahedrons, Figure 2.3, or hexahedrons, Figure 2.4, for example.

There are many ways to characterize a mesh. In general terms it can be divided between structured and unstructured. The structured mesh has constant connectivity and usually consists of hexahedrons, and it is better for obtaining data such as internal tension. Unstructured meshes have irregular connectivity; usually, they consist of tetrahedra and is better for applications regarding irregular shapes. Some algorithms used for unstructured meshes are presented by Owen (1998), such as Delaunay triangulation.

There are also the option of hybrid meshes (BERN; PLASSMANN, 1997), which can present both geometries. There are more sophisticated ways to classify a mesh. An example is to classify the meshes based on the order of creation of the elements (HO-LE, 1988). Which mesh is better? It depends on each case as they are unique, and all types of mesh have their advantages and weak points (WANG; RAUCH, 2004).

Figure 2.2 - Triangular 2D mesh.

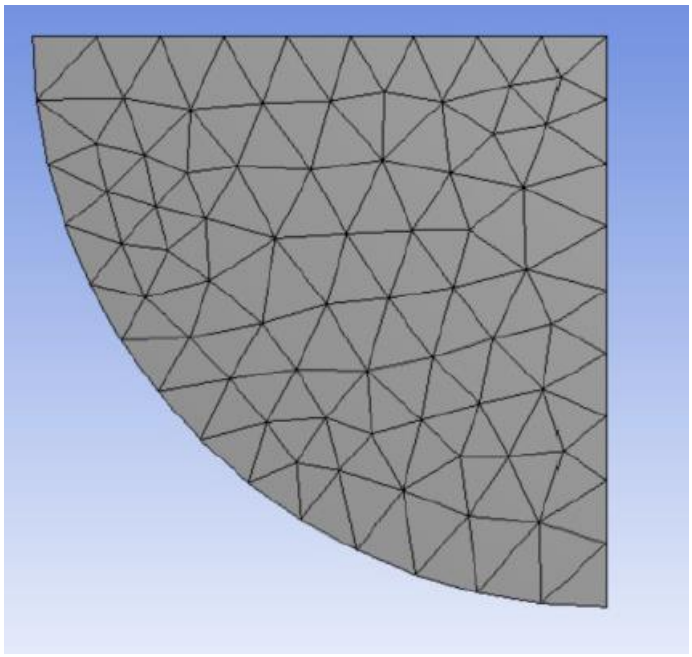

Source: Author.

Figure 2.3 - Tetrahedral 3D mesh.

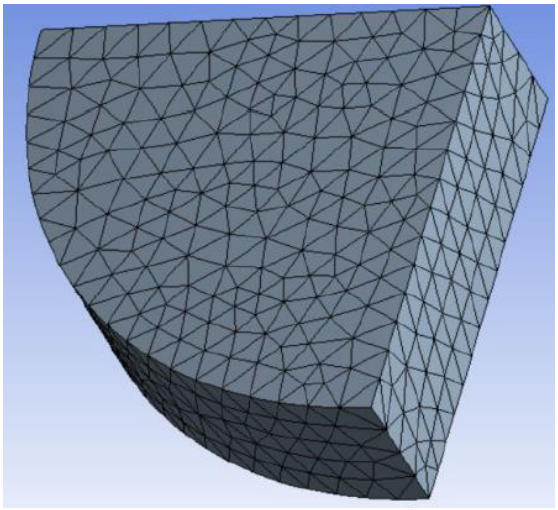

Source: Author.

Figure 2.4 - Hexahedral 3D mesh.

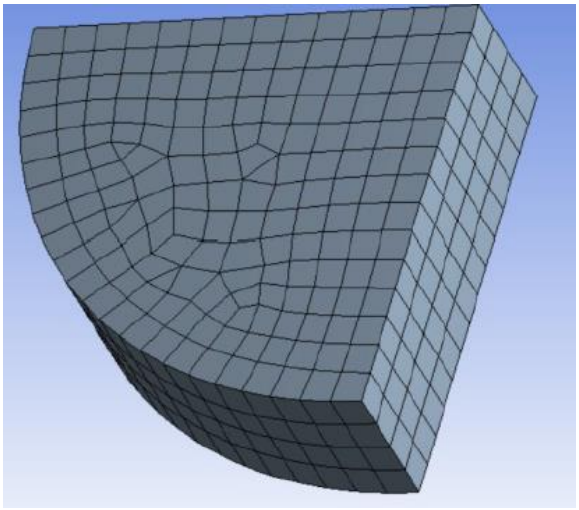

Source: Author.

As asteroids are irregular bodies, to fit them better in this work we use tetrahedral meshes. From a shape model, that is of a polyhedron made of triangular facets, the mesh is created over the surface, Figure 2.5, with a software such as TetGen a free software that generated a 4-nodes mesh, and the ANSYS student version that generates a 10-nodes mesh. The mesh is not only created on the surface,

but also in the interior of the body, Figure 2.6, and this is one of the greatest differences of the technique, because it has a highly refined discretization within the body, and it doesn't compromise the geometry of the surface as the surface is refined such as a blanket over the surface of the asteroid.

Figure 2.5 - FEM mesh over the surface.

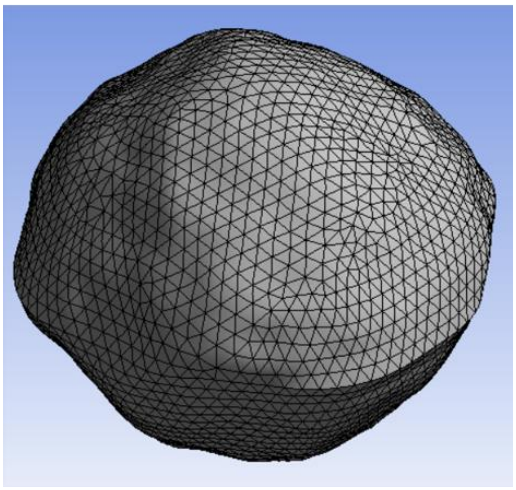

Source: Author.

Figure 2.6 - Asteroid's FEM mesh cross section.

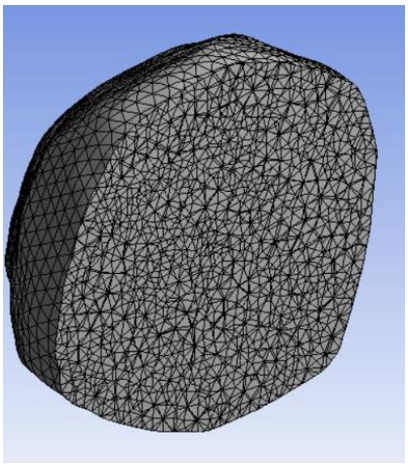

Source: Author.

With the mesh built some data is extracted from it like the volume of each one of the tetrahedrons that compose the mesh, and its centroids and nodes coordinates. Then, with that information on hands, mass concentration definitions are applied to the model creating the methodology we present in this work that from now on we will call the Finite Element Method Revisited (FEMR). Regarding the methodology, first, the contribution of each element for the body's potential is obtained using Equation 2.42, with the results of the potentials of all the elements, they are combined into a summation, giving, as a result, the total potential of the body given by Equation 2.43.

$$U_e = \frac{G\rho_e V_e}{r} \tag{2.42}$$

Where:

$$r = \sqrt{\left(x - x_g\right)^2 + \left(y - y_g\right)^2 + \left(z - z_g\right)^2}$$

$$U_T = \sum_e U_e \tag{2.43}$$

Where G is the gravitational parameter, ρ_e is the density of an element, V_e is the volume of an element x, y and z are coordinates of the field point, and x_g, y_g and z_g are coordinates of each element centroid. The subscript e refers to the number of elements.

Although these equations may look simple, they bring with them a lot of power with the finite element approach. With both together it is possible to obtain accurate results, as it will be shown in the next sessions, and with basic equations it is also possible to gain agility when thinking of the computing cost of the trajectory's simulation, with an easy-to-implement light model.

2.7.2 The FEMR regarding gravity coefficients

Finite Element definitions can also be applied to the theory of the Spherical Harmonics to obtain the gravity coefficients. To do so, essentially the integral turns into a summation, Equation 2.15 and Equation 2.16 can be rewritten as Equation 2.44 and Equation 2.45.

$$C_{lm} = \frac{2 - \delta_m^0}{M} \frac{(l-m)!}{(l+m)!} \sum_e \left(\frac{r}{r_o}\right)^l P_{lm} \sin\delta_e \cos(m\lambda_e)\, \Delta\sigma V_e \tag{2.44}$$

$$S_{lm} = \frac{2 - \delta_m^0}{M} \frac{(l-m)!}{(l+m)!} \sum_e \left(\frac{r}{r_o}\right)^l P_{lm} \sin\delta_e \sin(m\lambda_e)\, \Delta\sigma V_e \tag{2.45}$$

Where the subscript e denotes each element and δ_e is the element density.

This is a useful representation because it delivers a simple way to obtain the coefficients, as there are no integrals anymore. The solution to obtain more accurate results is also simple, since increasing the number of elements is an easy and quick task for today's software and computers.

2.7.3 Procedure for the FEMR validation

After the creation of a new model, it is important to perform validation, otherwise it is not possible to know if the new approach works or even if it is accurate. After obtaining some data and making some comparisons the steps for the validation were careful as follows:

a) For the first validation the FEMR model was implemented in the STRS to obtain results of the deviation of the spacecraft's velocity when submitted to the gravity field of asteroids. This analysis presents two results, the one obtained with the FEMR and with the MEPS, both results are compared to check and validate the FEMR. It is also important to notice that the method of the expansion of the potential in series was compared and validated comparing its results with well-known ones presented in the literature (MOTA, 2017). The combination of the FEMR and the STRS will also be used to analyze orbital trajectories;

b) The second validation was done comparing the FEMR results with the results obtained with the polyhedron method (WERNER; SCHEERES, 1996). To do so the potential and acceleration over the surface of the asteroid were computed. Then the results for the FEMR are presented along with the deviation between the polyhedron and the FEMR, so it was possible to verify if the results of the FEMR were coherent;

c) The last validation computes the gravity coefficients using the FEMR approach and then compares the outcome with the classical spherical harmonics procedure and the MEPS. The Root Mean Square (RMS) of the three models are compared to make a third validation.

2.8 Spacecraft trajectory simulator

An important tool used to validate the FEMR and present a relevant application, as mentioned, is the Spacecraft Trajectory Simulator (STRS) (ROCCO, 2008a; ROCCO, 2008b; ROCCO, 2013) which uses a Drag-Free approach, that

represents the state of the art in space vehicle trajectory control. This simulation environment was developed in a suitable architecture for the simulation of the trajectory of a space vehicle controlled by a closed-loop control system, considering the modeling of the actuators and sensors, with the nonlinearities inherent to this equipment, besides considering the orbital disturbance models applied to the vehicle along its trajectory. Therefore, the STRS can simulate the control, in a closed loop, of the three degrees of liberty about the translation of the vehicle.

One of the goals of this work is to adjust and implement the FEMR in the STRS in order to evaluate the effect of perturbation generated by the potential of the asteroid on the spacecraft trajectory.

To study the evolution of a space vehicle's orbit, it is necessary to propagate the spacecraft's orbit over time, under the effect of perturbations generated by the asteroid's gravitational field. For this, the dynamics model must provide the rates of change of the orbital elements that define the orbit. The classical equations used to describe the dynamics of a space vehicle exposed to perturbations, known as the Lagrange planetary equations, Equation 2.46 to Equation 2.54, (CHOBOTOV, 2020). These equations consider the classical orbital elements, the semi-major axis (a), eccentricity (e), inclination (i), right ascension of ascending node (Ω), argument of periapsis (ω), and mean anomaly (M).

$$\frac{da}{dt} = \frac{2\mathrm{e}\sin\theta}{nx} F_r + \frac{2ax}{nr} F_s \tag{2.46}$$

$$\frac{de}{dt} = \frac{x\sin\theta}{na} F_r + \frac{x}{na^2 e}\left(\frac{a^2x^2}{r} - r\right) F_s \tag{2.47}$$

$$\frac{di}{dt} = \frac{x\cos u}{na^2 x} F_w \tag{2.48}$$

$$\frac{d\Omega}{dt} = \frac{x \sin u}{na^2 x \sin i} F_w \tag{2.49}$$

$$\frac{d\omega}{dt} = -\frac{x \cos \theta}{na} F_r + \frac{p}{eh}\left[\sin \theta \left(1 + \frac{1}{1 + e \cos \theta}\right)\right] F_s - \frac{r \cot i \sin u}{na^2 x} F_w \tag{2.50}$$

$$\frac{dM}{dt} = n - \frac{1}{na}\left(\frac{2r}{a} - \frac{x^2}{\mathrm{e}} \cos \theta\right) F_r - \frac{x^2}{na}\left(1 + \frac{r}{ax^2}\right) \sin \theta \, F_s \tag{2.51}$$

Where F_r, F_S and F_w are perturbing accelerations along the position vector r, θ is the true anomaly, n the mean motion, u the argument of latitude, and x, p and h are given by Equation 2.35 to Equation 2.37.

$$x = \sqrt{1 - e^2} \tag{2.52}$$

$$p = a(1 - e^2) \tag{2.53}$$

$$h = \sqrt{\mu p} \tag{2.54}$$

However, the solution of the planetary equations might be exhaustive and time consuming and, depending on the disturbances considered, it might be even more challenging to obtain these results.

Considering these facts, the STRS offers a different approach, simple but more accurate, to achieve the same goal and provide the rates of change of the orbital elements, in the same way as the Lagrange planetary equations. However, STRS makes use of the state propagation, position and velocity, for each simulation step, considering the accelerations generated by the disturbances.

To perform the orbital propagation, the cartesian coordinates, added to the perturbing velocity increments, are converted to orbital elements. Then, the Kepler equation is used to propagate the orbital elements one step further, which allows the calculation of the orbital elements variation rates. These new propagate elements are converted to cartesian coordinates and the process starts over to the next step.

For an adequate size simulation step, this approach is quite efficient to be used in space vehicle simulations, possibly more suitable than the Lagrange planetary

equations, as it can consider very accurate perturbation models and provides the vehicle state at each fixed step of the simulation, which is mandatory if a trajectory control in closed loop is applied.

The basic STRS architecture can be checked in Figure 2.7 and Figure 2.8, this architecture has already been widely presented and used in Agostinho (2019), Gomes and Rocco (2012), Gonçalves (2013; 2018), Gonçalves, Rocco and Moraes (2014; 2017), Mota (2017), Santos (2015) and Silva (2017).

The modelling of the disturbances consists of obtaining its force and inserting them into the dynamics of the vehicle at each step of the simulation. Considering the velocity increments and the disturbances of the environment, the state of the spacecraft can be altered, therefore, the same happens with the Keplerian elements of the orbit (ROCCO, 2019).

To start with, we use the spacecraft's initial state as the input at the beginning of the process (A). The initial Keplerian elements are inserted in the subsystem (A) and converted to cartesian coordinates of position and velocity. Then this data is sent to the guidance subsystem (B) and also to the subsystems (C) and (D). Both subsystems (C) and (D) are related to orbital dynamics, (C) refers to the reference state and considers the signal coming from the guidance subsystem, while subsystem (D) refers to the current state and considers the effect of disturbances. The current state is measured and estimated by subsystem (G).

The orbital perturbations, which are obtained as functions of the current state, are determined by the subsystem (H) and inserted in the subsystem (D) of the current dynamics.

Then, with the signals generated by the subsystems (C) and (G), the error signal is determined to be inserted in the control subsystem (E), which in turn, sends the control signal to the subsystem (F) of the actuators. Finally, subsystem (F) produces an actuation signal that is inserted into the subsystem (D), closing the control loop.

Figure 2.7 - STRS Architecture.

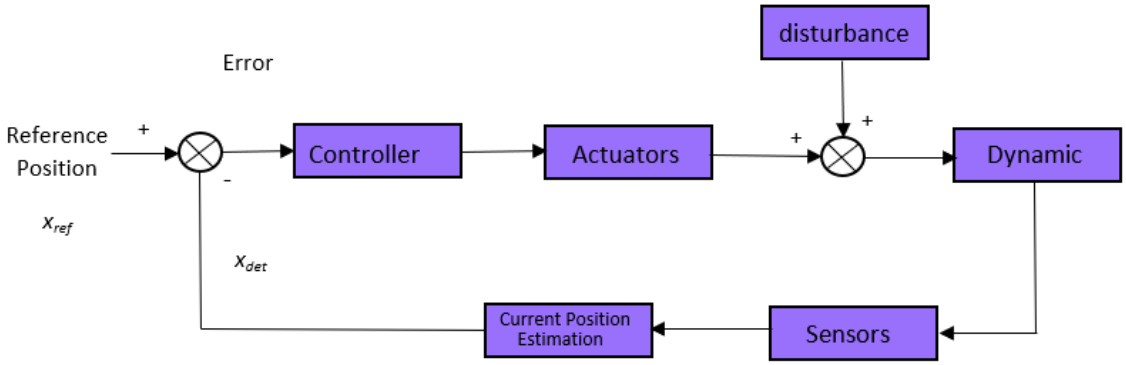

Source: Adapted from Rocco (2012).

Figure 2.8 - Detailed STRS architecture.

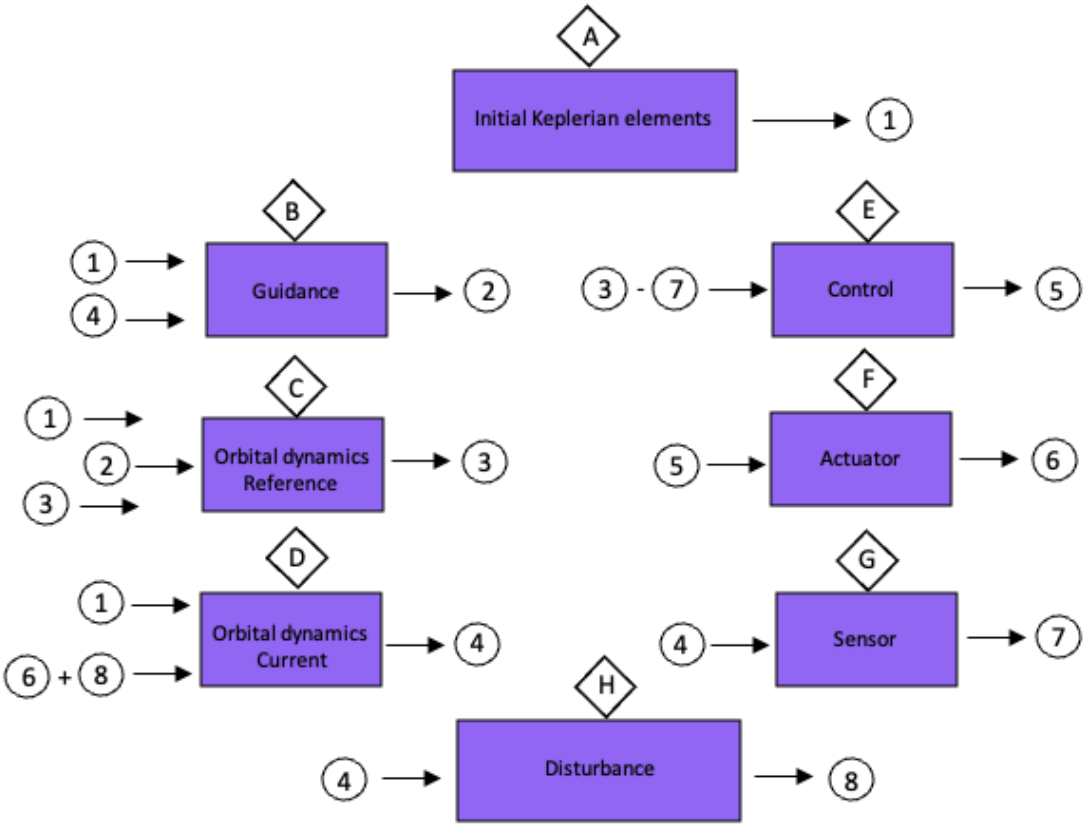

Source: Adapted from Mota (2017).

To complement, Figure 2.9 illustrates the orbital dynamics configuration regarding the asteroid's discretization. Summarizing, we start obtaining the spacecraft position. From the asteroid discretization we compute the gravitational force generated by each polyhedron to obtain the total gravitational force. Then, the gravitational force considering the central field is calculated to be compared with the disturbance force to finally get the spacecraft position having s a result the disturbance force due to the asteroid's gravity field as mentioned on Section 2.5. After obtaining the disturbance force it is inserted into the vehicle dynamics to get the current position and the cycle starts again.

Figure 2.9 – Dynamics considering the asteroid's discretization.

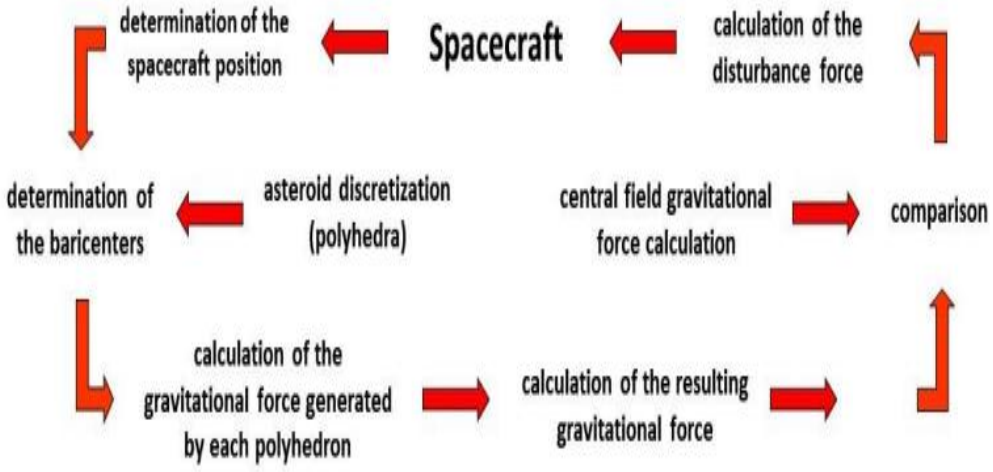

Source: Rocco (2019).

3 ASTEROID 2063 BACCHUS

Now, we begin to present the results obtained in this work, we start performing the validations comparing the methods already mentioned. The first small body we select for this work is the asteroid 2063 Bacchus. Bacchus is an NEA that had its closer encounter with Earth in March 1996. From data collected from radar observations. Bacchus would belong to the H-chondrite group, and the shape of the asteroid consists of two connected lobes, Bacchus has dimensions of 1.11 × 0.53 × 0.50 km, density of 2.1 g/cm^3 and volume equals to 0.135 km^3 (BENNER, 1999). Figure 3.1 shows a 3D representation of Bacchus.

Figure 3.1 - 3D Representation of the asteroid 2063 Bacchus.

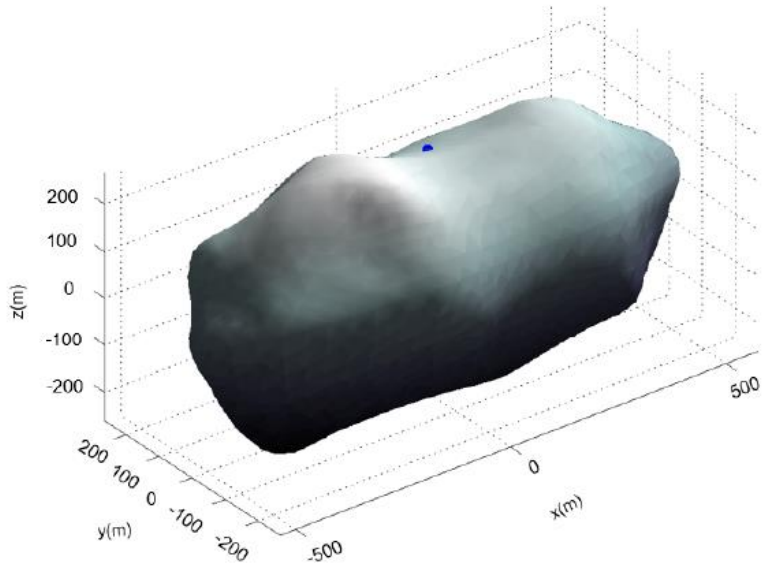

Source: Author.

For Bacchus, the shape model we use in the studies was obtained from radar data and it is available on the NASA Planetary Data System. The model has 2048 vertices and 4092 facets, Figure 3.3, Bacchus density is set to 2.1 g/cm^3 in this model, and we build the Finite Element model with 3,593 elements, Figure 3.2 and Figure 3.3 present the FEMR mesh and its cross section showing the internal refinement.

Figure 3.2 - Bacchus 3593 elements Mesh.

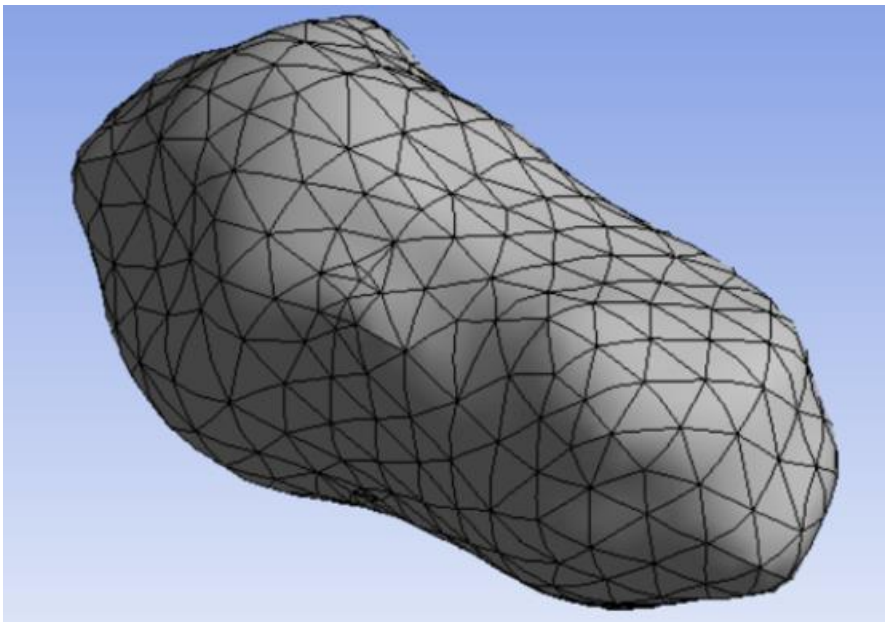

Source: Author.

Figure 3.3 - Bacchus 3593 elements Mesh Cross Section.

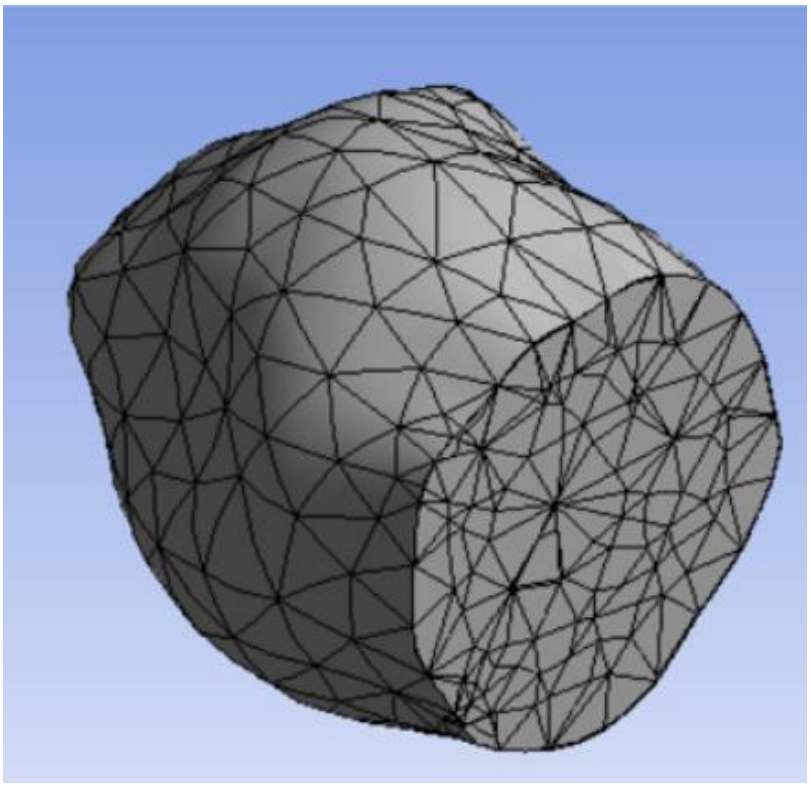

Source: Author.

3.1 Bacchus STRS comparison and validation

We perform the first validation using the STRS, the goal of this study is to obtain the disturbance generated by the potential of the asteroid. We adapt Bacchus's finite element model and implement it in the STRS to perform a simulation considering a spacecraft in orbit around Bacchus.

After obtaining the solid FEMR model we compute the centroid to verify if the procedure has not corrupted the data setting the centroid to a position that would make no sense. We perform the computation of the centroid and inertia tensor to check their values, especially for the centroid. The calculation of the centroid and the inertia tensor must be done as presented by Equation 3.1 to Equation 3.10 (BEATTY, 2006).

$$x_c = \sum_e \frac{x_e V_e}{V_T} \tag{3.1}$$

$$y_c = \sum_e \frac{y_e V_e}{V_T} \tag{3.2}$$

$$z_c = \sum_e \frac{z_e V_e}{V_T} y_c = \sum_e \frac{y_e V_e}{V_T} \tag{3.3}$$

$$I_{xx} = \sum_e (y_e^2 + z_e^2)\sigma V_e \tag{3.4}$$

$$I_{yy} = \sum_e (x_e^2 + z_e^2)\sigma V_e \tag{3.5}$$

$$I_{zz} = \sum_e (x_e^2 + y_e^2)\sigma V_e \tag{3.6}$$

$$I_{xy} = I_{yx} = \sum_e x_e y_e \, \sigma V_e \tag{3.7}$$

$$I_{xz} = I_{zx} = \sum_e x_e z_e \, \sigma V_e \tag{3.8}$$

$$I_{yz} = I_{zy} = \sum_e y_e z_e \, \sigma V_e \tag{3.9}$$

$$I = \begin{pmatrix} I_{xx} & -I_{xy} & -I_{xz} \\ -I_{yx} & I_{yy} & -I_{yz} \\ -I_{zx} & -I_{zy} & I_{zz} \end{pmatrix} \tag{3.10}$$

Where x_e, y_e, z_e, are the coordinates of an element, σ is the density of the body. I_{xx}, I_{yy} and I_{zz} are the moments of inertia and I_{xy}, I_{xz} and I_{yz} are the products of inertia, and I is the Inertia tensor. For Bacchus the results for the centroid and Inertia tensor are given below.

$$x_c = 0.4180\ m$$

$$y_c = -0.0066\ m$$

$$z_c = 0.0775\ m$$

$$I = 1.0x10^{16} \begin{pmatrix} 0.6639 & -0.0011 & -0.0003 \\ 0.0011 & 2.1476 & 0.0001 \\ -0.0003 & 0.0001 & 2.1680 \end{pmatrix} gm^2$$

The centroid results are coherent, and we can proceed to the validation.

Regarding the validation, the results compare the spacecraft's velocity deviation using the FEMR and the Method of the Expansion of the Potential in Series. Since the goal of this analysis is to present a comparison to validate the FEMR model. We show the orbital parameters of the spacecraft in Table 3.1 and the simulation was executed to complete one orbit around Bacchus.

Table 3.1 - Orbital elements (STRS Validation) – Bacchus.

Semi-major axis(m)	900
Eccentricity	0
Inclination (degrees)	0
Right ascension of the ascending node (degrees)	0
Argument of periapsis (degrees)	0
Mean anomaly (degrees)	0

Source: Author.

In Figure 3.4 we present a comparison between models showing the evolution through time of the spacecraft’s absolute velocity increment for the FEMR in pink

and for the series expansion in blue. This figure shows us that the models have close results as both lines overlap which is a first step regarding the FEMR validation. Figure 3.5 shows the difference of the velocity increment between both models (FEMR and MEPS) over time for x, y, and z axes. As we can see from the plot, the difference between both methods has a magnitude of 10^{-5}.

From the results presented we see that the FEMR results are accurate and coherent. These simulations also show that the FEMR has an application regarding spacecraft trajectories.

Figure 3.4 - Spacecraft absolute velocity Increment comparison – Bacchus.

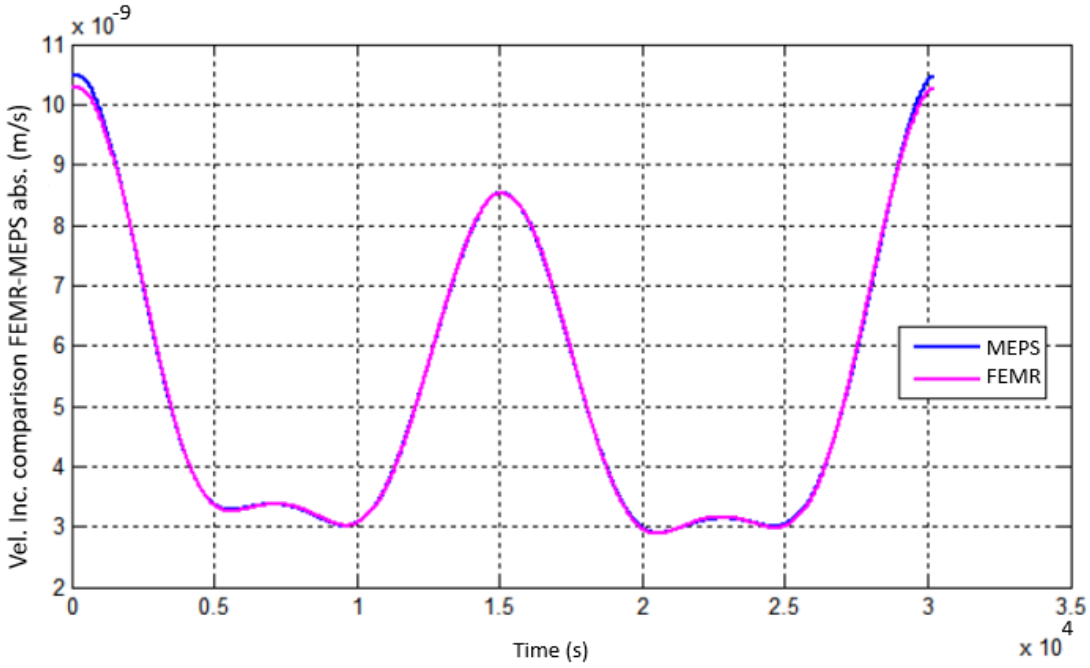

Source: Author.

Figure 3.5 - Spacecraft velocity Increment difference between FEMR and MEPS – Bacchus.

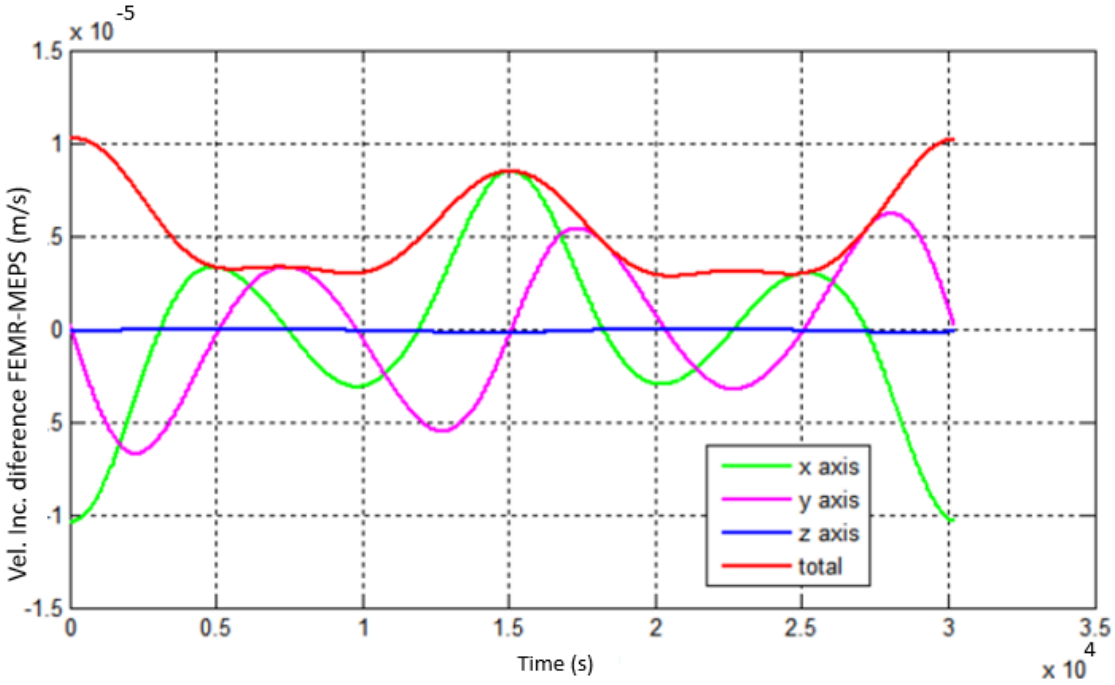

Source: Author.

3.2 Bacchus validation with the polyhedron method

The second study regarding the Finite Element approach validation is done comparing the FEMR model and the Polyhedron. The potential over the surface for Bacchus using the FEMR is shown in Figure 3.6, and the gravity acceleration in Figure 3.7 in order to check the distribution and magnitude.

Figure 3.6 - Bacchus Potential over the surface.

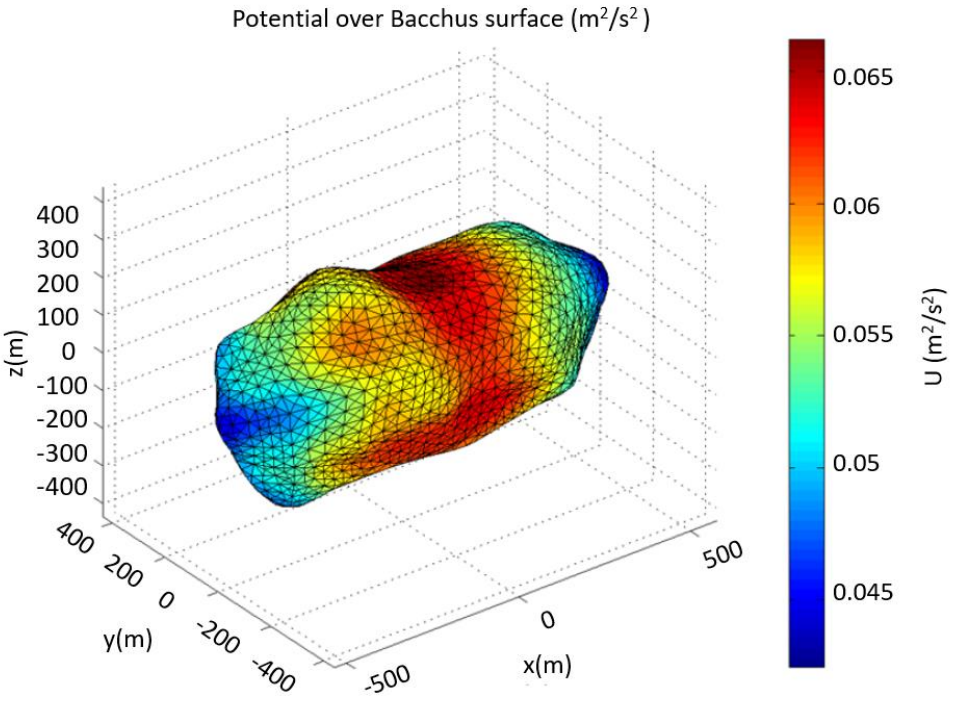

Source: Author.

Figure 3.7 - Bacchus Acceleration over the surface.

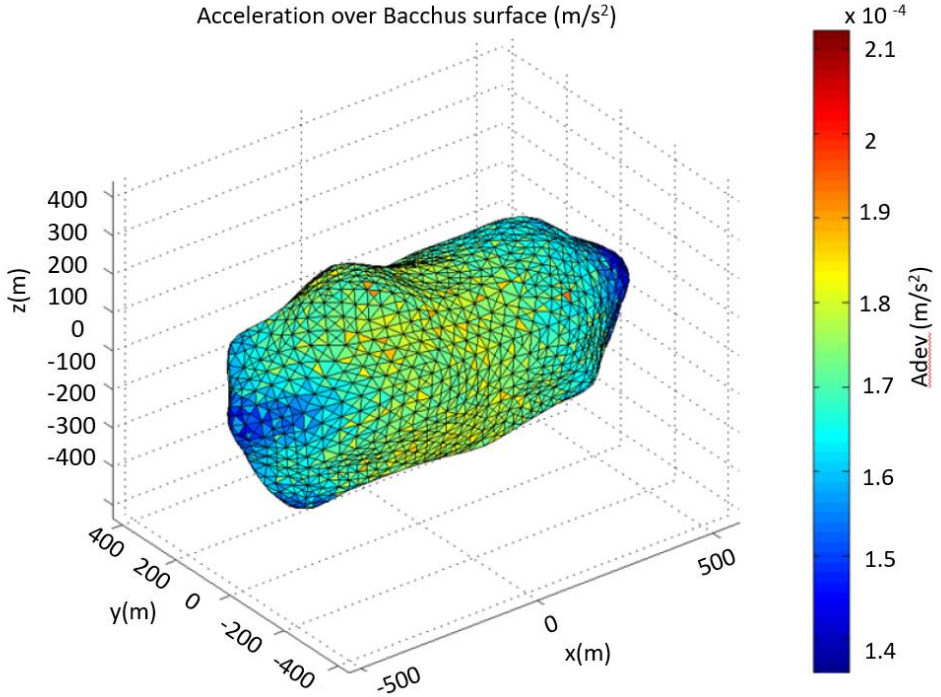

Source: Author.

From Figure 3.8 to Figure 3.13 is possible to see the potential and gravity acceleration respectively with more detail through different views of the object.

Figure 3.8 - Bacchus Potential over the surface-XY view.

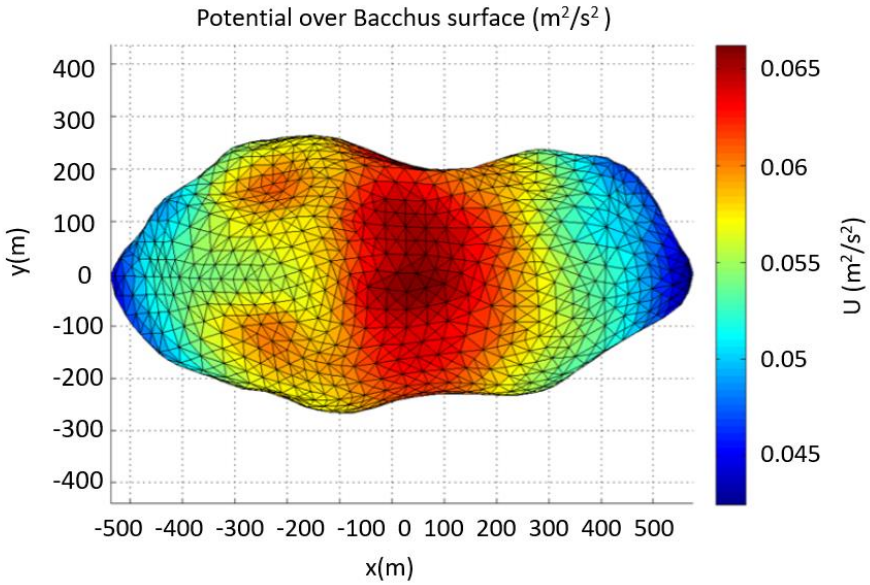

Source: Author.

Figure 3.9 - Bacchus Potential over the surface-XZ view.

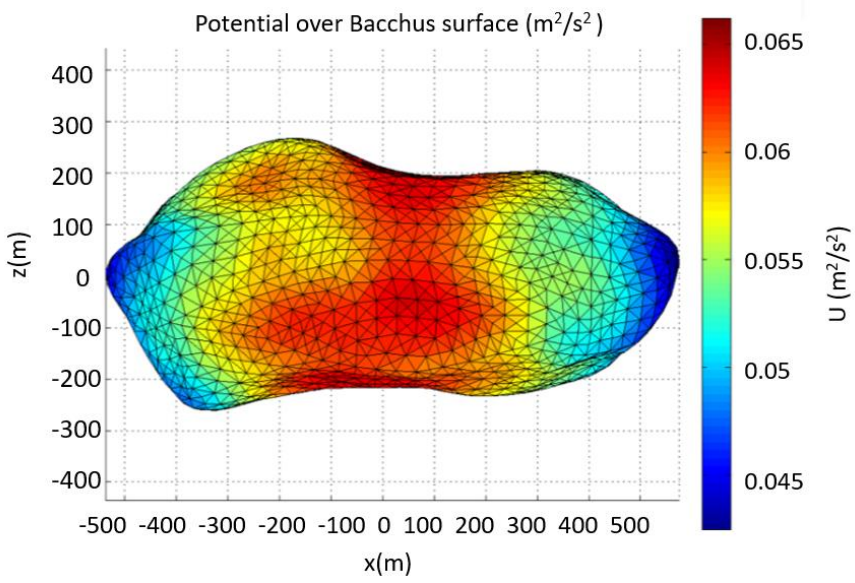

Source: Author.

Figure 3.10 - Bacchus Potential over the surface-YZ view.

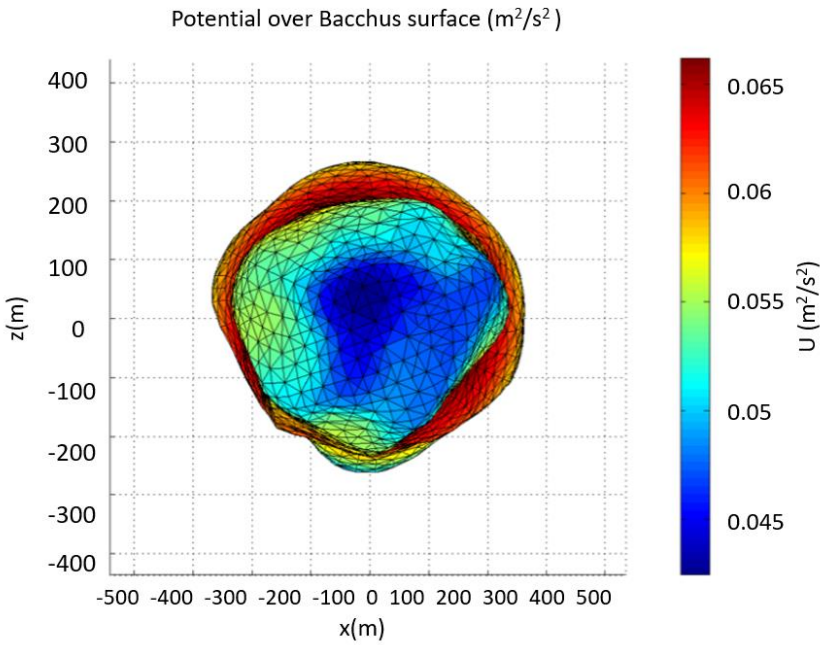

Source: Author.

Figure 3.11 - Bacchus acceleration over the surface-XY view.

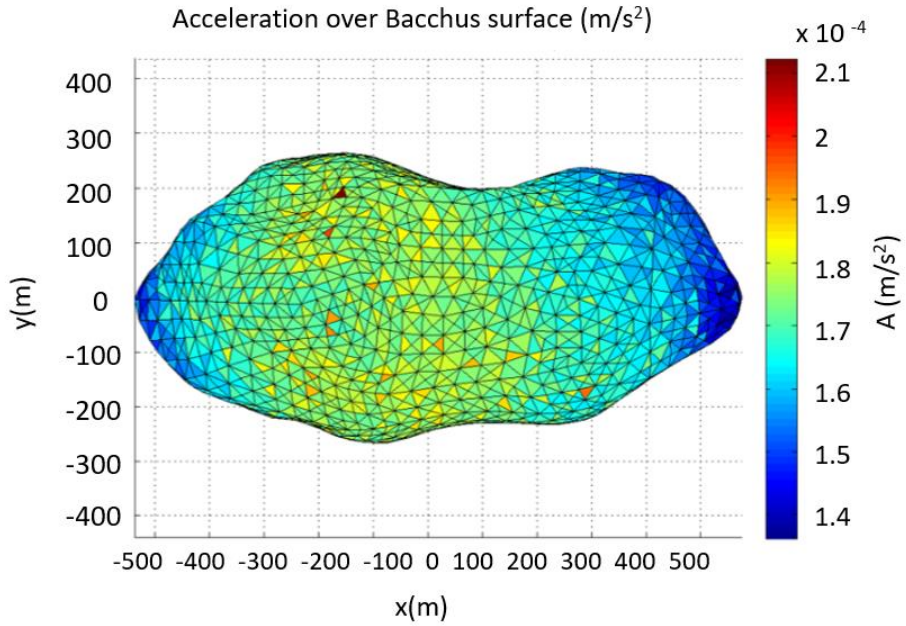

Source: Author.

Figure 3.12 - Bacchus acceleration over the surface-XZ view.

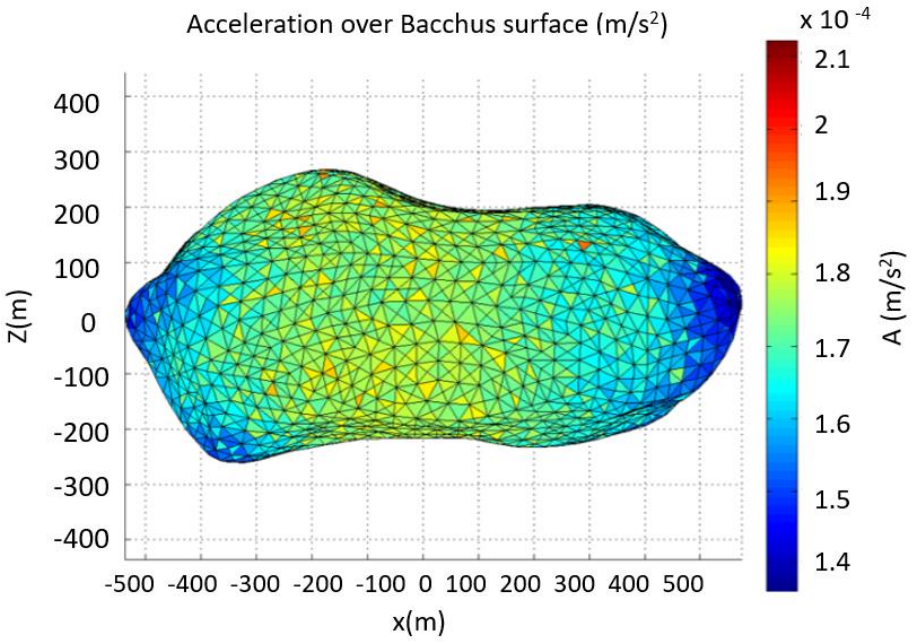

Source: Author.

Figure 3.13 - Bacchus acceleration over the surface-XZ view.

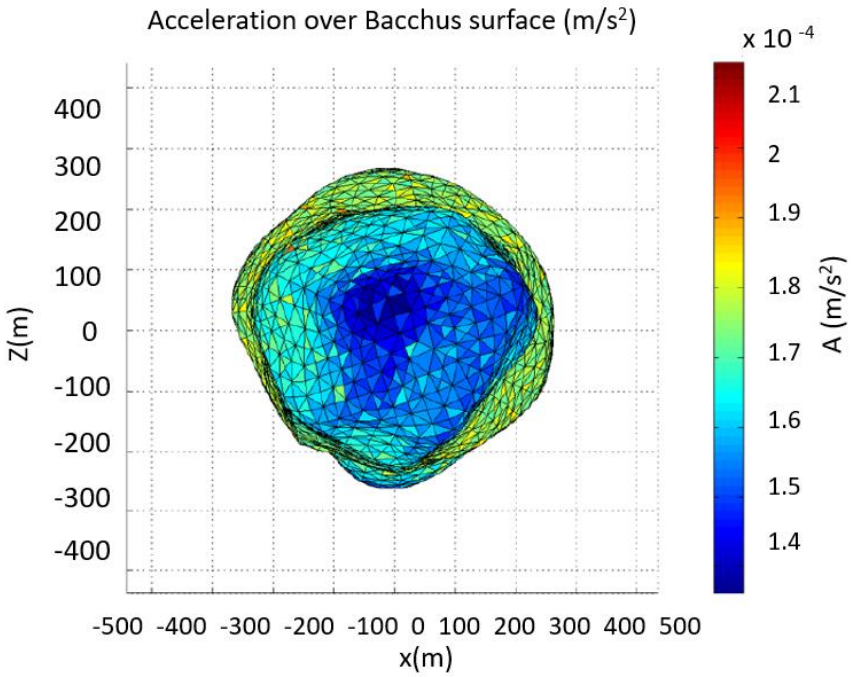

Source: Author.

Before jumping to the validation, we present some comments regarding Figure 3.6 to Figure 3.13. Bacchus shows some evidence of being a binary asteroid (BENNER, 1999). From the figures we can see that where the lobes connect, we have a higher value for both the potential and gravity acceleration, as the point gravity unites the two parts. The external lateral points of the body are the places that show the weakest potential value. The acceleration is more homogeneous over the surface, also it is possible to say that the values are lower as is the intensity.

After presenting the values for the acceleration and the potential now the most important thing is done, the validation. Figure 3.14 shows the deviation of the potential values between the Polyhedron and the FEMR.

As we can see the maximum magnitude of the difference between both methods is of 10^{-4} over the surface of the body, showing once again that the FEMR is accurate. Another result delivered from the comparison with the polyhedron is that as the polyhedron does not diverge on the surface's potential computation neither does the FEMR as their results are close to each other.

Figure 3.14 - Bacchus potential deviation over the surface.

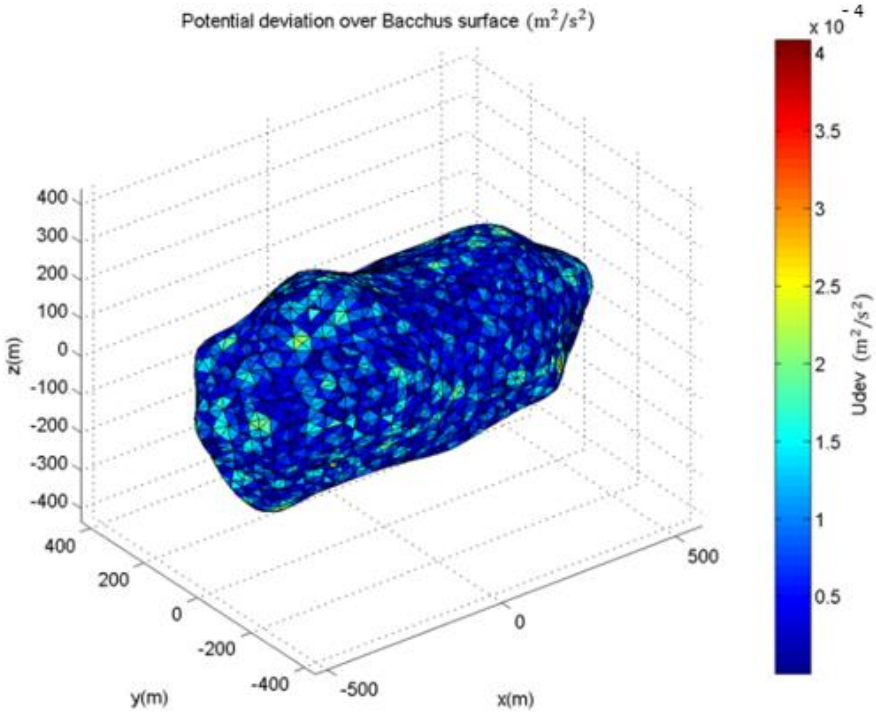

Source: Author.

3.3 Bacchus gravity coefficients

The last validation is performed comparing the gravity coefficients computed using the classic theory from Session 2.3 with the results obtained using the FEMR approach. This comparison is made with the coefficient values and with the use of another tool, the Root Mean Square (RMS). The RMS is useful to summarize gravity coefficient results and make them easier to compare (SCHEERES et al., 2020). The RMS is computed using Equation 3.15 (SCHEERES et al., 2020).

$$RMS = \sqrt{\frac{1}{2n+1}\sum_{m=0}^{n}(C_{nm}^2 + S_{nm}^2)} \tag{3.15}$$

The difference between two different gravity fields can also be computed simply considering the difference between each term, and the reference radius was set as 318 meters, the same value used for the comparative values (SCHEERES et al., 2020). The RMS and Coefficients are presented from degree 2, as for degree 1 they are zero, until degree 6 (SCHEERES et al., 2020). We choose to to compute the gravity coefficients until degree and order 6, since these are the results found in the references for comparison.

To begin with we first analyze Table 3.2, when we compare the FEMR results with the series expansion. We can see that the FEMR can reach accurate results for the coefficients as the difference when comparing it with the spherical harmonics appears on the 5th decimal place. The FEMR advantage is that it can bring a simpler way to compute the gravity coefficients as we are able to compute the coefficients with a summation (Equation 2.27 and Equation 2.28), however for more accurate results it is necessary to have more elements.

Figure 3.15 presents the RMS plot for the FEMR and the series expansion (MOTA, 2017), and from it is possible to see that the lines overlap, meaning again that the FEMR can also achieve accurate results for the gravity coefficients, being one more successful step for the validation. However, more comparisons with other asteroids must still be done.

Table 3.2 - Bacchus gravity coefficients.

	FEMR	Expansion		FEMR	Expansion
C20	1.1867E-01	1.1867E-01	S51	3.0964E-03	3.0482E-03
C21	0.00	0.00	C52	4.0542E-03	4.0886E-03
S21	0.00	0.00	S52	-4.0690E-03	-4.0868E-03
C22	1.9996E-01	1.9998 E-01	C53	-3.0772E-03	-3.0695E-03
S22	0.00	0.00	S53	-8.8157E-03	-8.7530E-03
C30	2.6212E-03	2.6487E-03	C54	-1.1289E-02	-1.1354E-02
C31	-2.4897E-02	-2.4798E-02	S54	3.8830E-03	3.9693E-02
S31	-3.4471E-03	-3.4252E-03	C55	2.8187E-02	2.81108E-02
C32	-7.822E-03	-7.8763E-03	S55	1.5996E-02	1.6103E-02
S32	5.4588E-03	5.4928E-03	C60	-5.1247E-02	-5.1222E-02
C33	2.5779E-02	5.4928E-03	C61	-2.0843E-03	-2.0818E-03
S33	1.1912E-02	1.1975E-02	S61	3.9474E-04	4.1679E-04
C40	6.01598E-02	6.0154E-02	C62	7.2266E-02	7.2218E-02
C41	-3.6945E-03	-3.6693E-03	S62	7.9858e-03	7.9756E-03
S41	-1.51360E-04	-1.6037E-04	C63	8.7194E-04	8.9406E-04
C42	-8.8217E-02	-8.8195E-02	S63	-2.4390E-03	-2.4720E-03
S42	-5.7887E-03	-5.7998E-03	C64	-7.4774E-02	-7.4726E-02
C43	2.7623E-03	2.7369E-03	S64	-1.5465E-02	-1.5568E-02
S43	2.4747E-03	2.4478-03	C65	2.1392E0-03	2.0995E-03
C44	1.1830E-01	1.1832E-01	S65	5.4919E-03	5.4081E-03
S44	1.5005E-02	1.5059E-02	C66	1.0738E-01	1.0741E-01
C50	-1.7227E-04	-1.8310E-04	S66	2.8330E-02	2.84407E-02
C51	2.9984E-02	2.9852E-02			

Source: Author.

Figure 3.15 - Bacchus RMS comparison.

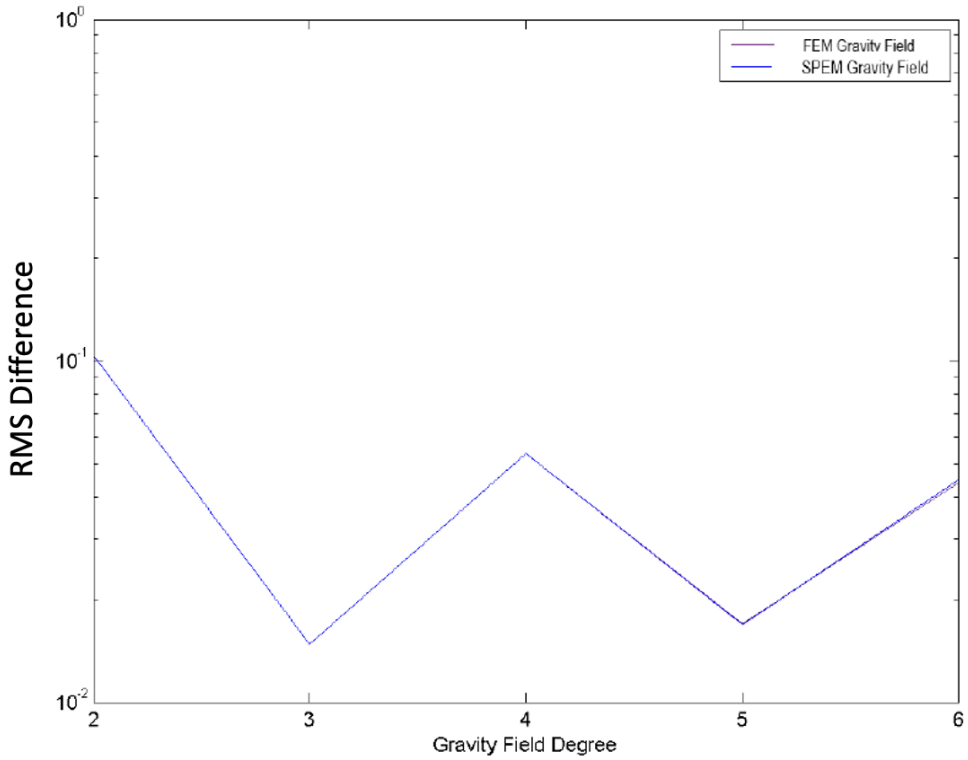

Source: Author.

3.4 Variation of Bacchus elements number

As is possible to change the number of finite elements of a model, this is done with Bacchus in order to check what happens with the accuracy when the body is exposed to such variation. This analysis is done for the comparison with the polyhedron and the comparison using the STRS. The experiment is performed varying the number of elements of the original model, with 3593 elements, setting the elements to 7255, 27811 and 54268 elements. Figure 3.16 to Figure 3.21 presents the FEMR meshes and their respective cross sections.

Figure 3.16 - Bacchus 7255 elements Mesh.

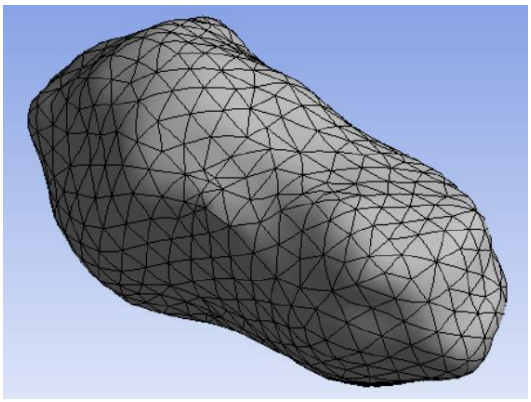

Source: Author.

Figure 3.17 - Bacchus 7255 elements Mesh Cross Section.

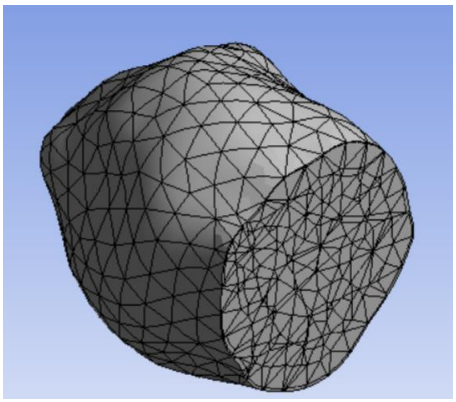

Source: Author.

Figure 3.18 - Bacchus 27811 elements Mesh.

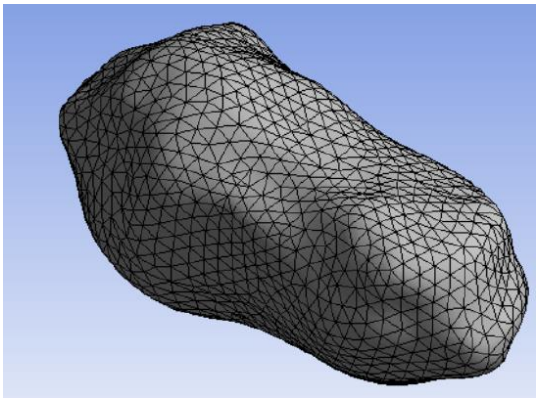

Source: Author.

Figure 3.19 - Bacchus 27811 elements Mesh Cross Section.

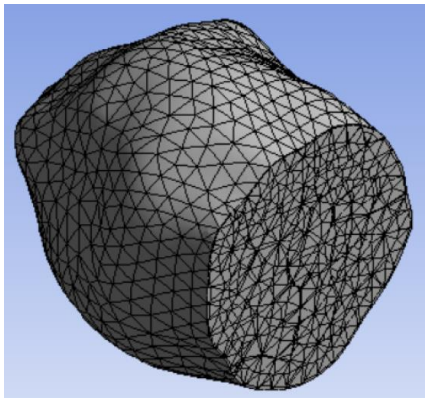

Source: Author.

Figure 3.20 - Bacchus 54268 elements mesh.

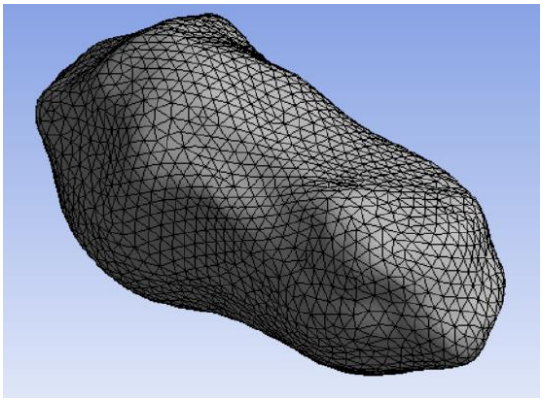

Source: Author.

Figure 3.21 - Bacchus 54268 elements mesh Cross Section.

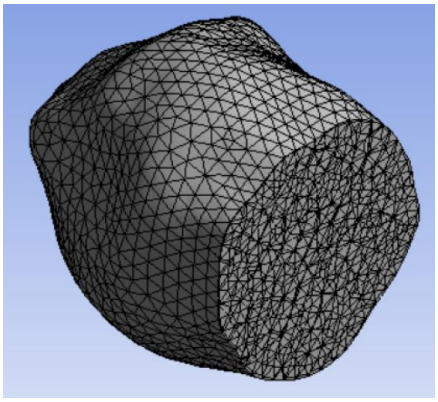

Source: Author.

We start the analysis contrasting the FEMR and the polyhedron model, comparing Figure 3.14 with Figure 3.22 to Figure 3.24 that shows the deviation of the potential over the surface is noticeable, that considering 1306 elements the model is not accurate, and the difference between the methods is considerable, with a magnitude of 10^{-2}.

Nevertheless, when we consider 3593 elements or more the model is accurate, and when compared with the polyhedron approach the maximum magnitude of the difference between methods is 10^{-5}, and as the number of elements increases the difference between methods gets lower. In summary, it is a fact that when the number of elements increases, the accuracy of the FEMR approach also increases.

At this point is necessary to make an observation regarding computer performance. To increase the number of elements we don't spend more than some minutes, the majority of processing time is when the shape model is built, a step that doesn't take more than a couple hours when the asteroid is big. Also, the computation of the potential is still very fast, increasing just a few minutes with more elements.

However, for the polyhedron method when we increase the number of facets as the equations, already presented, are more complexes than the ones used by the FEM, it can take several hours to compute the potential using the polyhedron approach with more facets.

The MEPS has a similar behavior as the polyhedron method. Computing the potential with the MEPS when the number of facets is increased takes a much longer time. Increasing the number of facets of the shape model would have as result in a much greater to obtain the analytical expression for each different shape model.

With this in mind we can see that this is a great advantage for the revisited finite element methodology. So, if you have a model with many facets the FEM can be a more suitable approach.

Figure 3.22 - Bacchus potential deviation over the surface - 7255 elements.

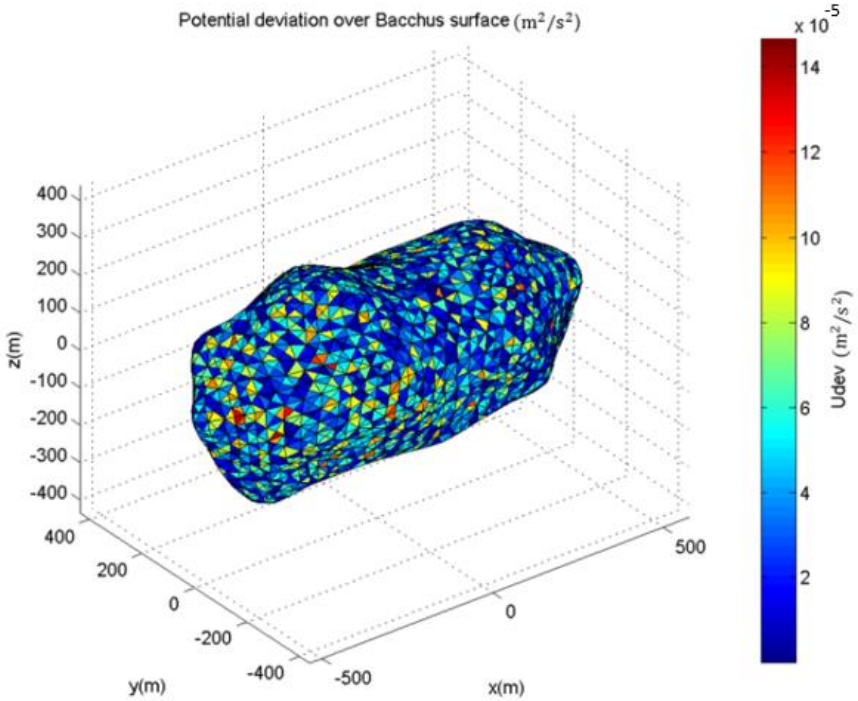

Source: Author.

Figure 3.23 - Bacchus potential deviation over the surface - 27811 elements.

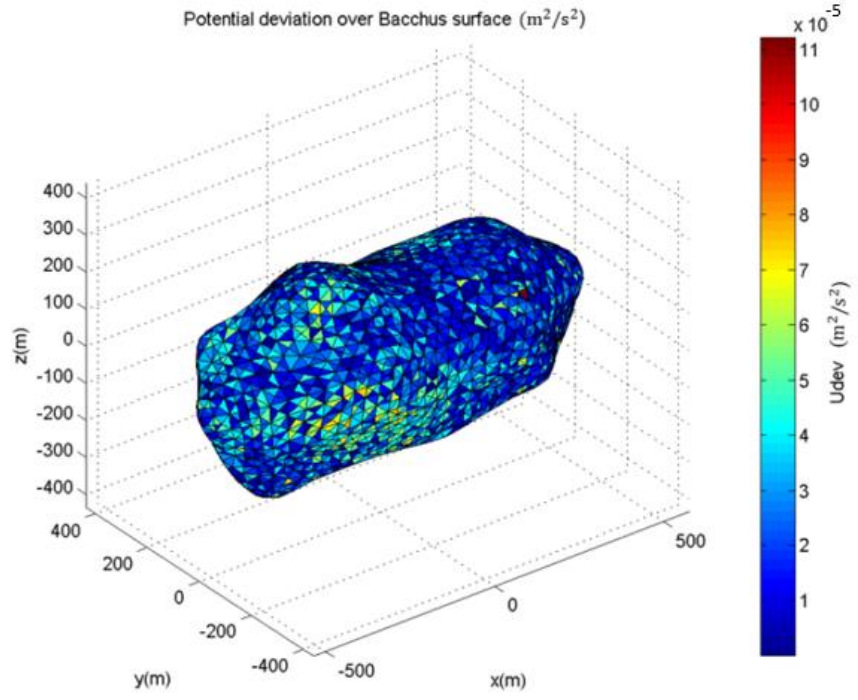

Source: Author.

Figure 3.24 - Bacchus potential deviation over the surface - 54268 elements.

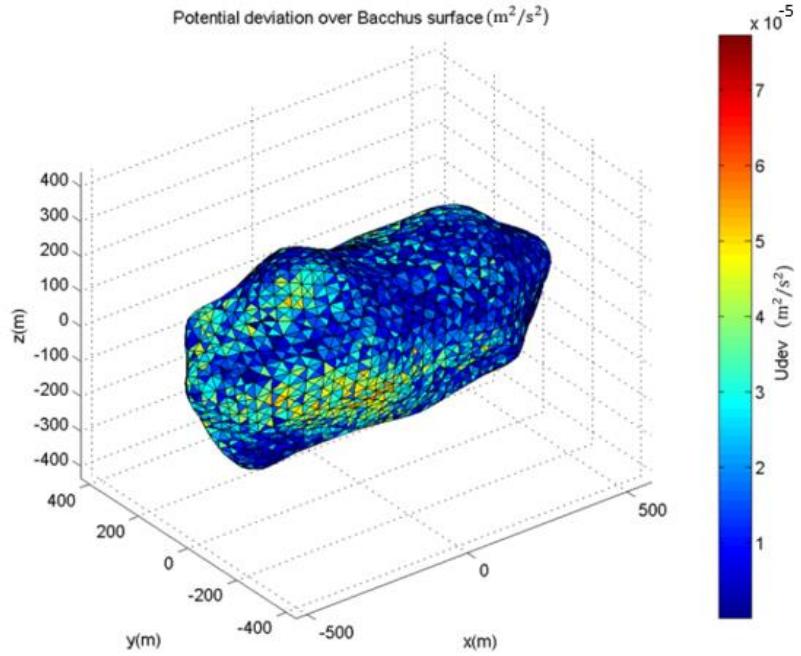

Source: Author.

After the comparison with the polyhedron, we can perform some simulations using the STRS, to perform the same comparison using the MEPS. Considering the number of elements variation from Figure 3.25 to Figure 3.30 present the results of the absolute difference comparison between methods and the difference of the velocity increment.

Let's go step by step through this analysis as we can find some answers here. Checking Figure 3.5 and Figure 3.25 we see that as the number of elements increase the differences between the FEM and the MEPS decrease. However, comparing Figure 3.25, Figure 3.26 and Figure 3.27 as we increase the number of elements the differences start to slightly increase. From previous analyses we saw that as we increase the number of elements of a FEM mesh we have more accurate results. So, a conclusion we can get here is that the FEM not only is equivalent to the MEPS but with the right number of elements it can start to perform even better than the MEPS.

However, it is important to say that there is no best model: the "best" model is the one that fits the desired application. For example, the polyhedron can have a

better performance when compared to the FEMR if we increase the number of facets, and the FEMR itself can also perform better if we have a higher number of elements. So, when picking up a model, a careful analysis of the requirements should be done.

Figure 3.25 - Spacecraft absolute velocity Increment comparison - Bacchus 7255 elements.

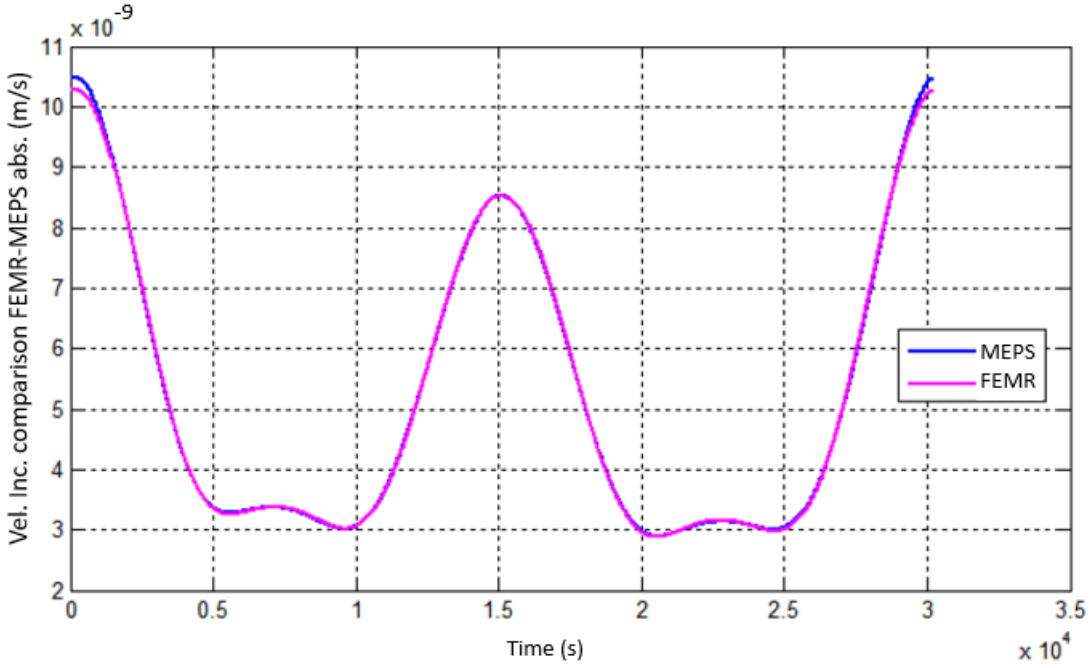

Source: Author.

Figure 3.26 - Spacecraft velocity Increment difference between FEMR and Expansion - Bacchus 7255 elements.

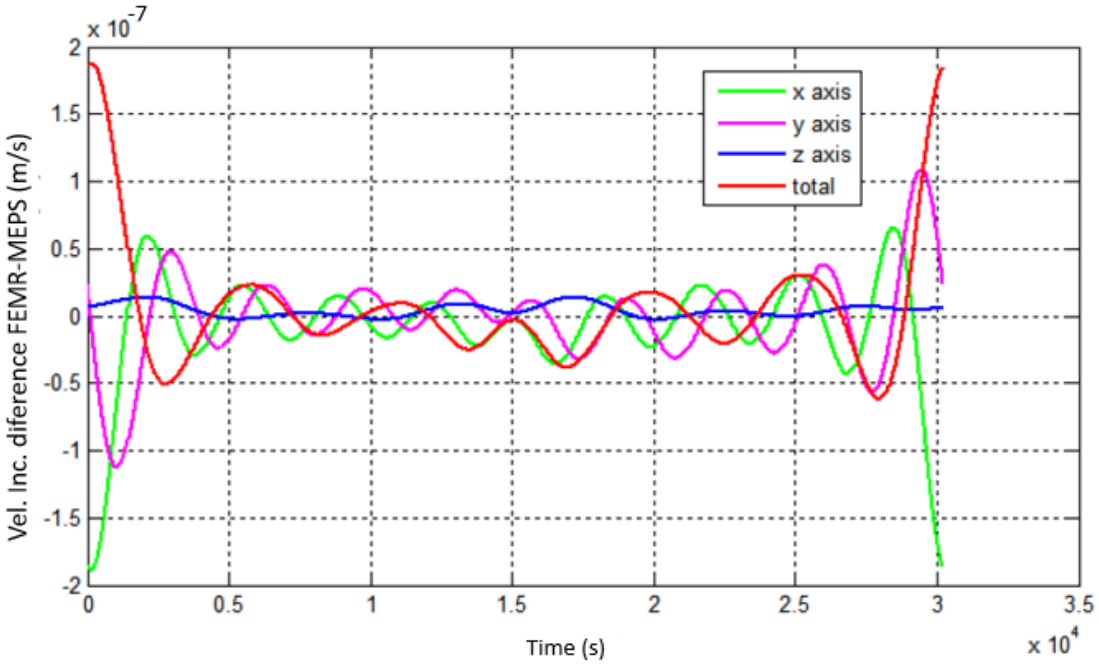

Source: Author.

Figure 3.27 - Spacecraft absolute velocity Increment comparison - Bacchus 27811 elements.

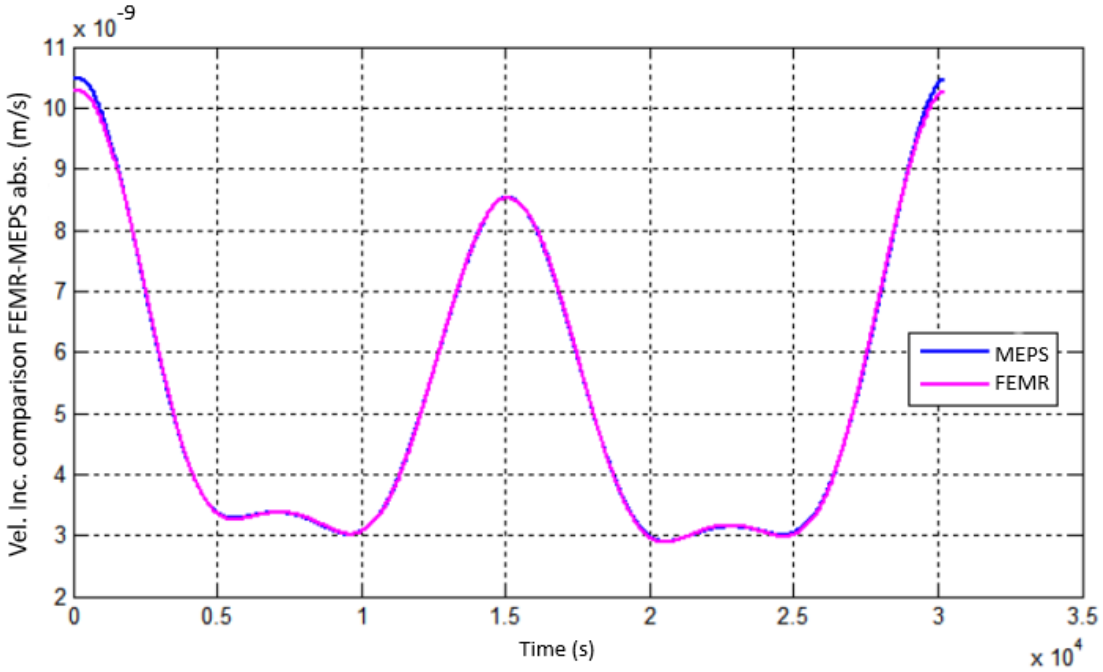

Source: Author.

Figure 3.28 - Spacecraft velocity Increment difference between FEMR and MEPS - Bacchus 27811 elements.

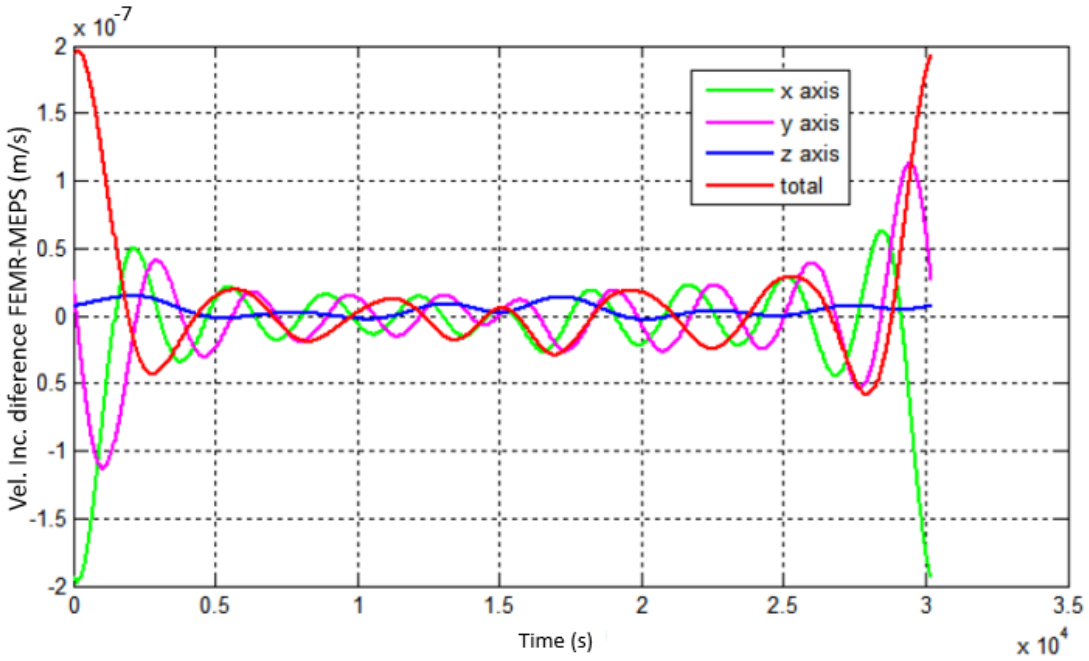

Source: Author.

Figure 3.29 - Spacecraft absolute velocity Increment comparison - Bacchus 54268 elements.

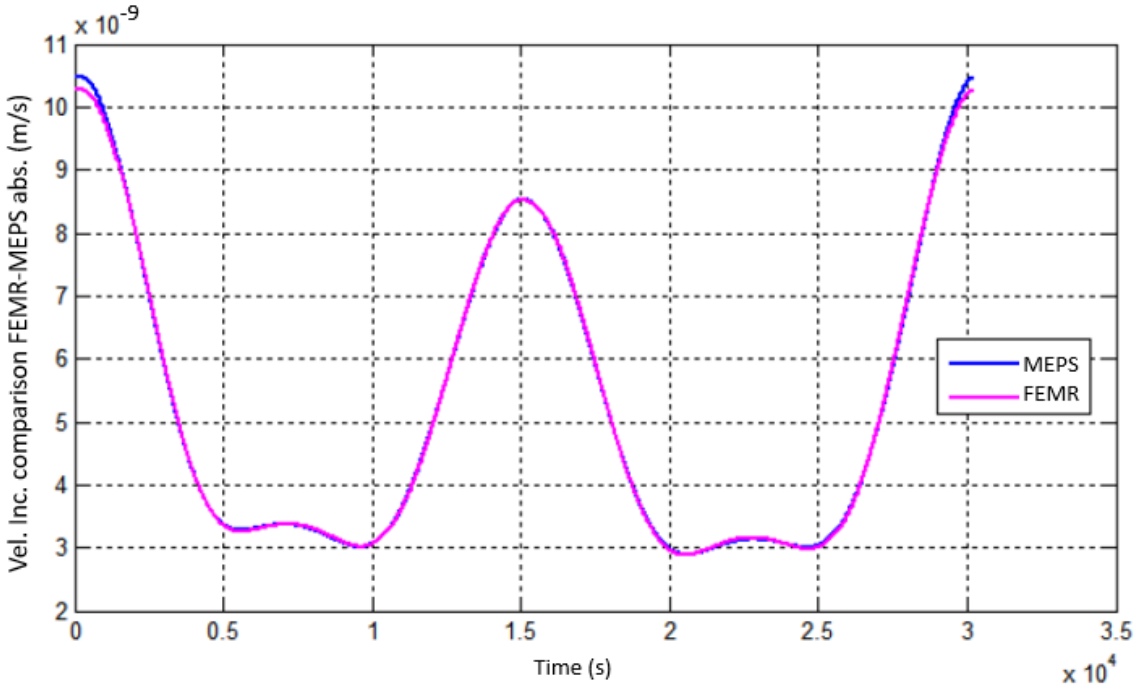

Source: Author.

Figure 3.30 - Spacecraft absolute velocity Increment comparison - Bacchus 54268 elements.

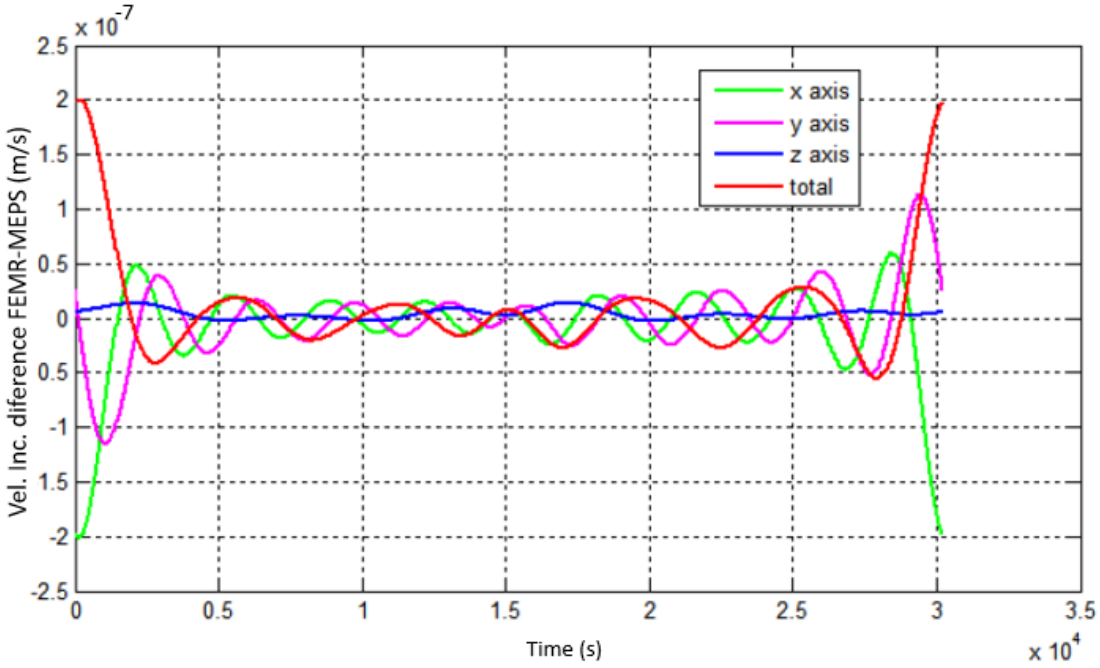

Source: Author.

4 ASTEROID 25143 ITOKAWA

The rubble-pile 25143 Itokawa, Figure 4.1, was the target of the mission Hayabusa, which had the main purpose to collect a sample of the asteroid and return it to Earth. Its dimensions are 535 x 294 x 209 meters, its density is equal to 2.5 g/cm^3, volume of 0.0241 km^3 and it is classified as an S-type asteroid. Itokawa's 3D model can be checked on Figure 4.2.

Figure 4.1 - Itokawa image as observed from Hayabusa.

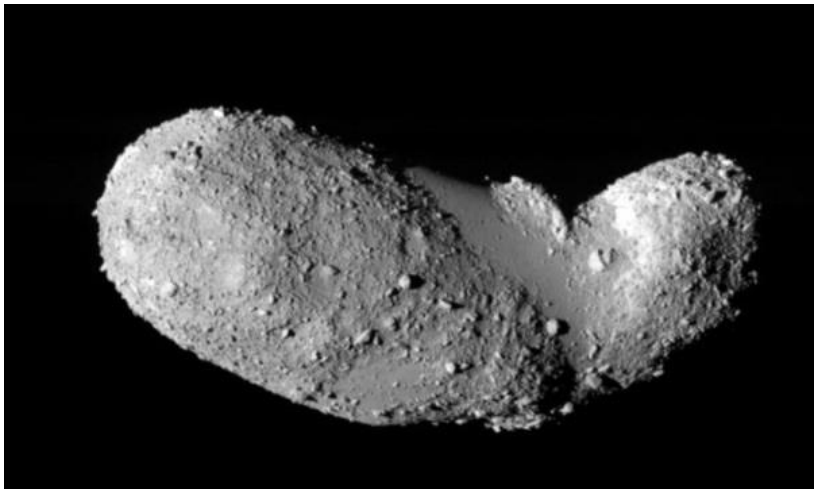

Source: Wikipedia (2021)[1].

[1] Available on https://pt.wikipedia.org/wiki/25143_Itokawa.

Figure 4.2 - Itokawa 3D model Representation.

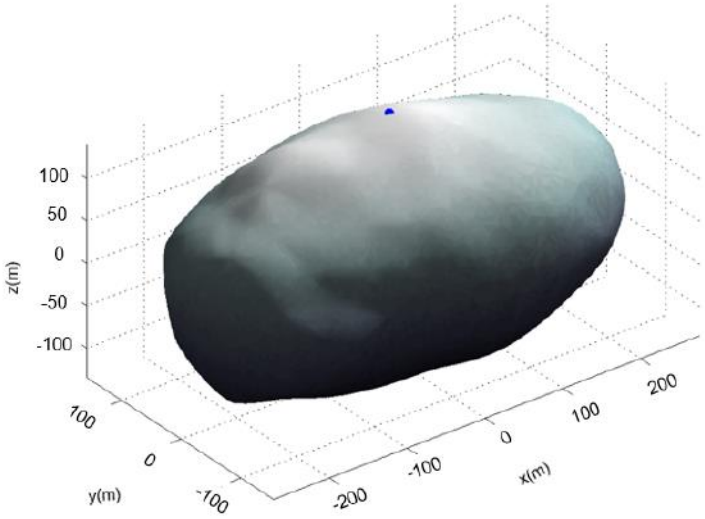

Source: Author.

The model we use for the simulations comes from radar data information; this knowledge is previous from Hayabusa. The density we consider is equal to 2.5 g/cm^3. As already mentioned, the finite element model has 3291 elements represented on Figure 4.3, and Figure 4.4 shows the cross section.

Figure 4.3 - Itokawa 3291 elements Mesh.

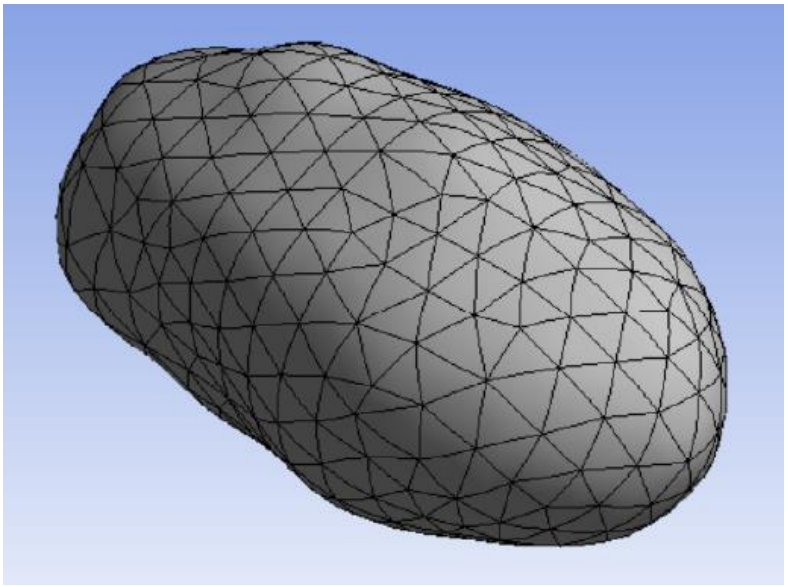

Source: Author.

Figure 4.4 - Itokawa 3291 elements Mesh Cross Section.

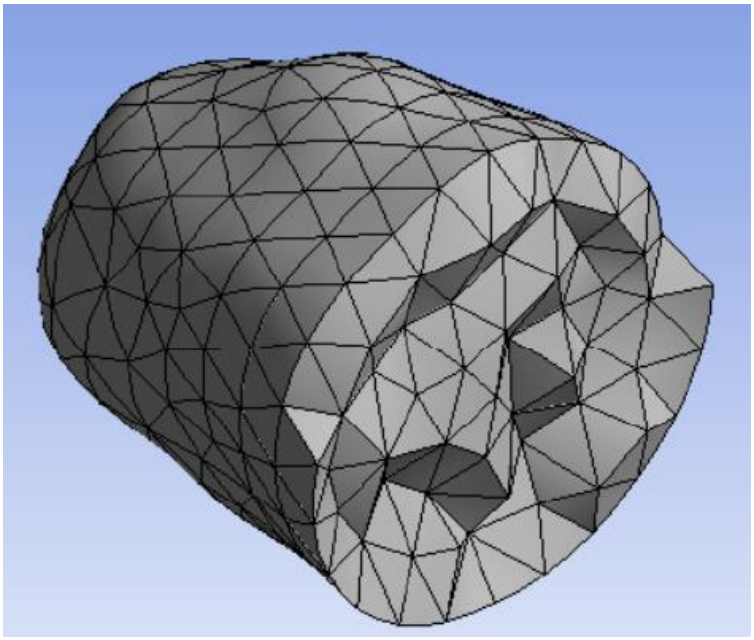

Source: Author.

4.1 Itokawa STRS comparison and validation

Once again, we consider the spacecraft scenario, now in orbit around Itokawa, which the parameters are specified in Table 4.1. The centroid coordinates and Inertia tensor are given below to check the centroid again as done for Bacchus.

$$x_c = -0.0162m$$

$$y_c = -0.0126m$$

$$z_c = -0.0049m$$

$$I = 1.0E + 016 \begin{pmatrix} 0.4896 & -0.0004 & -0.0001 \\ -0.0004 & 1.1563 & 0.0001 \\ -0.0001 & 0.0001 & 1.2170 \end{pmatrix} gm^2$$

Table 4.1- Spacecraft's orbit elements – Itokawa.

Semi-major axis(m)	400
Eccentricity	0
Inclination (degrees)	0
Right ascension of the ascending node (degrees)	0
Argument of periapsis (degrees)	0
Mean anomaly (degrees)	0

Source: Author.

When we analyze the evolution through time of the spacecraft's absolute velocity increment for each method on Figure 4.5 it is possible to observe that the FEMR is going to present accurate results again.

Figure 4.5 - Spacecraft's absolute velocity increment comparison - Itokawa 3291 elements.

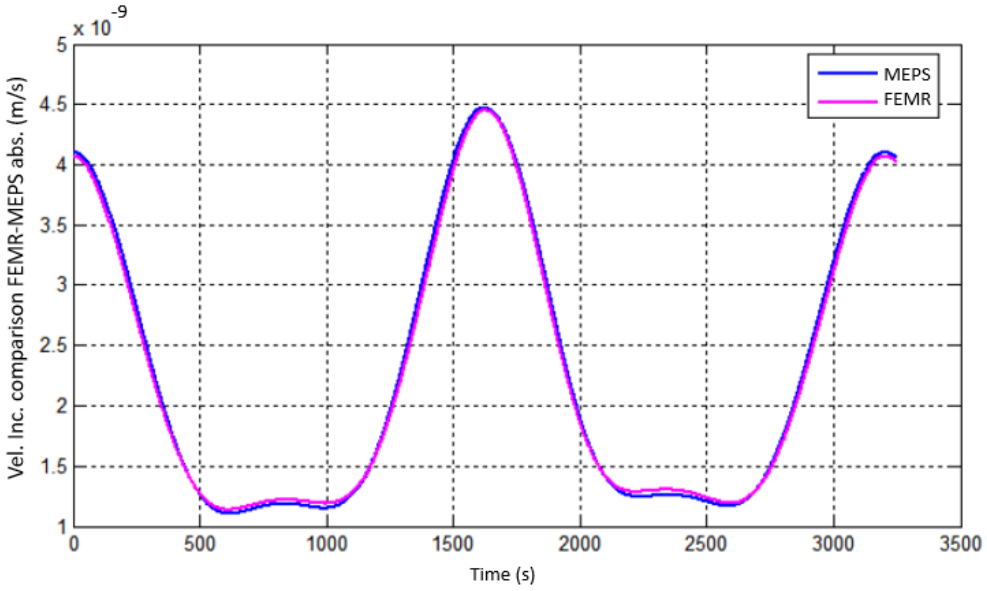

Source: Author.

Figure 4.6 presents the difference of the velocity increment between both models (FEMR and series expansion) over time for x, y, and z axes. The magnitude of the difference is low, like happened with Bacchus, having a magnitude of 10^{-8}. With this evidence we can see once again the validation of the model, and the possibility to apply the FEMR to trajectories simulations.

Figure 4.6 - Spacecraft's velocity increment difference - Itokawa 3291 elements.

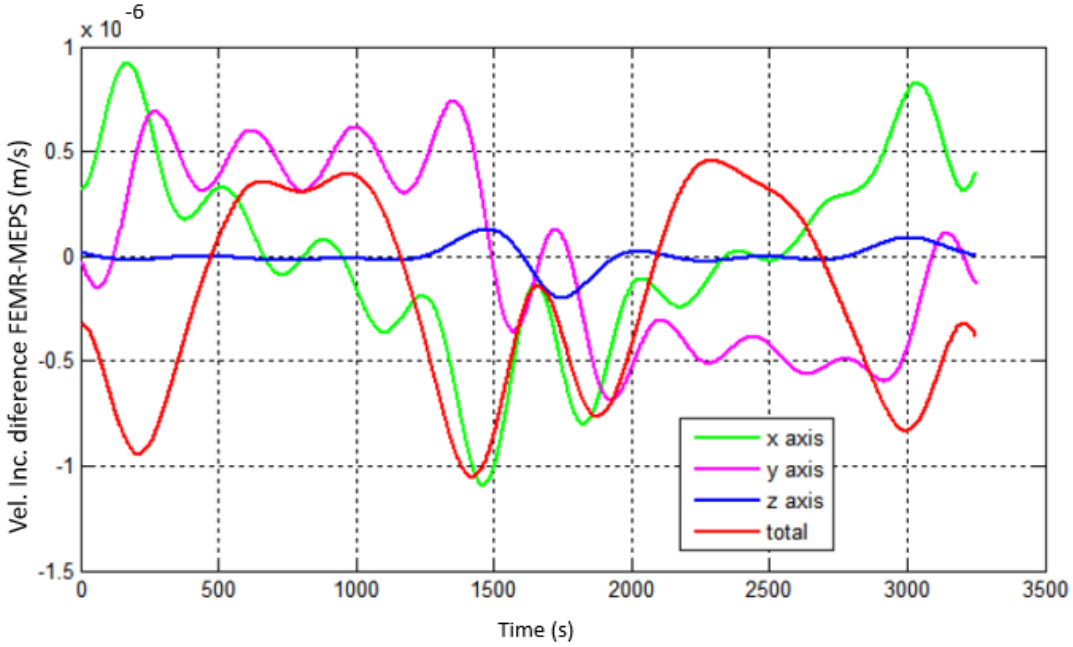

Source: Author.

4.2 Itokawa validation with the polyhedron method

Again, we plot the potential over the surface of Itokawa, Figure 4.7, the same was done with the acceleration, Figure 4.8. The different views of the figures are shown from Figure 4.9 to Figure 4.11 for the potential and from Figure 4.12 to Figure 4.14 for the acceleration.

Observing the potential variation is interesting to note that, as Bacchus, Itokawa has a more intense potential in the center of the body, becoming weaker as it propagates to its extremes.

The reason why this is interesting is that, as Bacchus, Itokawa shows some evidence that the asteroid can be a contact binary, consisting of two different bodies that gravitate each other until they touch, usually becoming a body with two different lobes.

For the acceleration the values are again more moderate, however, there are some points in the center midsection of the body where the acceleration is more intense.

Figure 4.7 - Itokawa Potential over the surface.

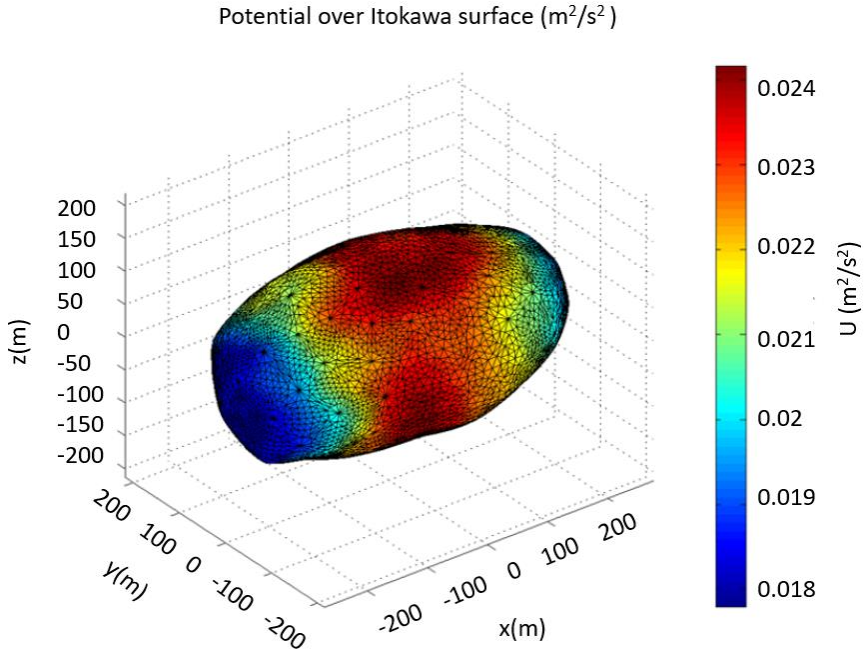

Source: Author.

Figure 4.8 - Itokawa Acceleration over the surface.

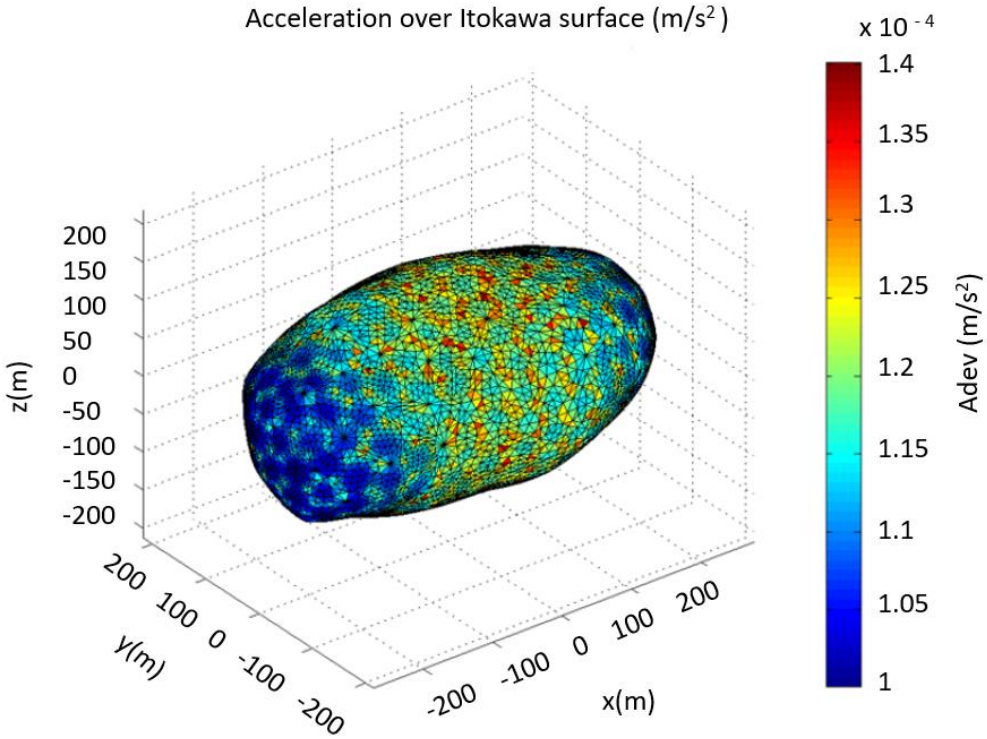

Source: Author.

Figure 4.9 - Itokawa Potential over the surface-XY view.

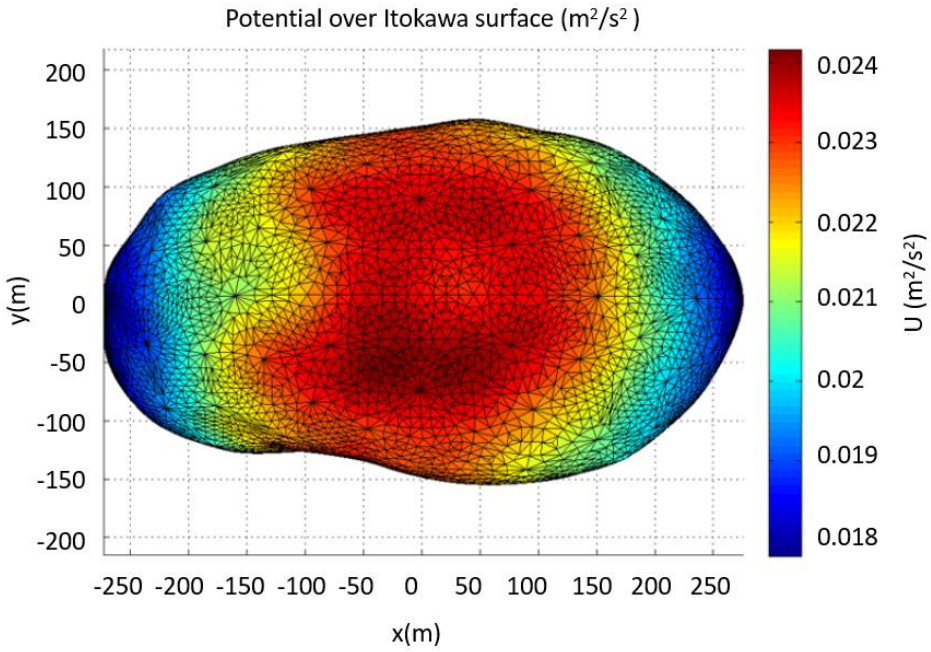

Source: Author.

Figure 4.10 - Itokawa Potential over the surface-XZ view.

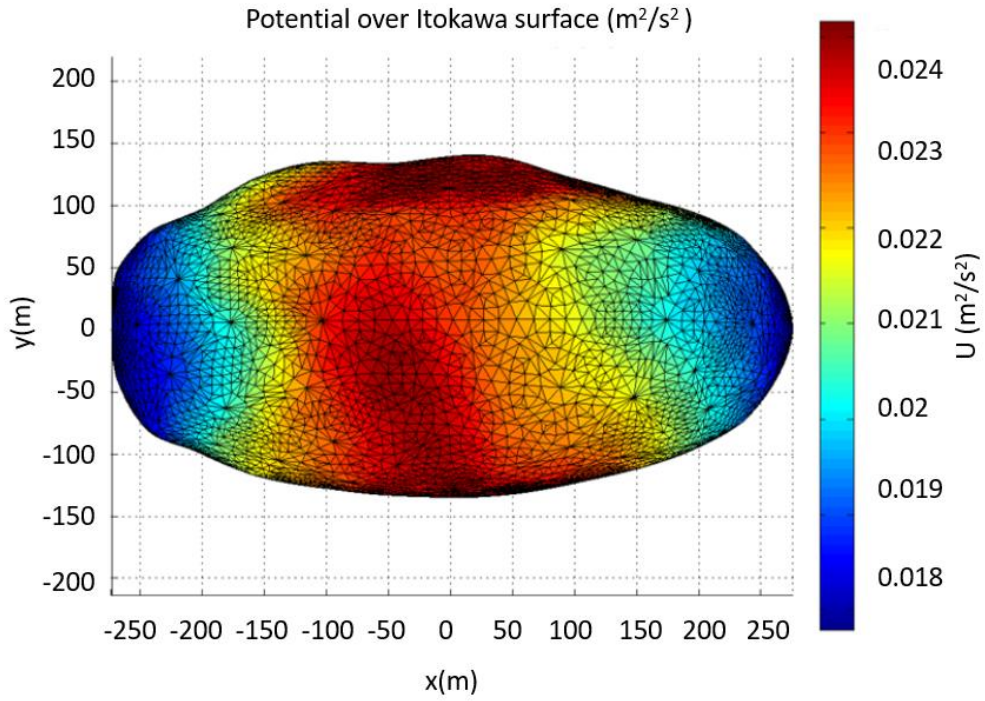

Source: Author.

Figure 4.11 - Itokawa potential over the surface-YZ view.

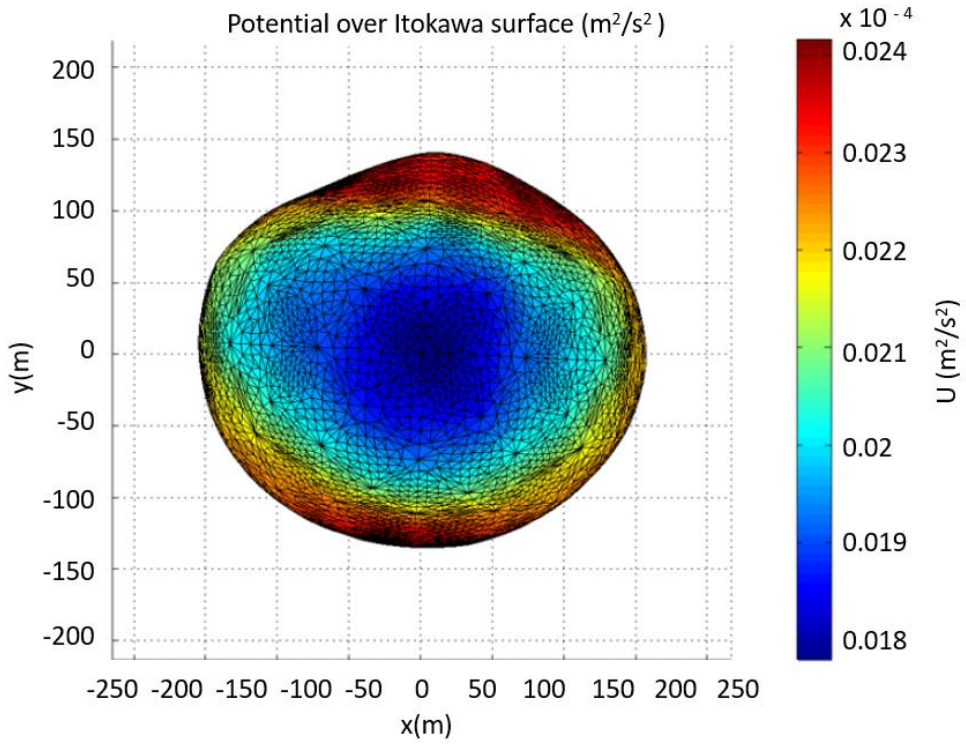

Source: Author.

Figure 4.12 - Itokawa acceleration over the surface-XY view.

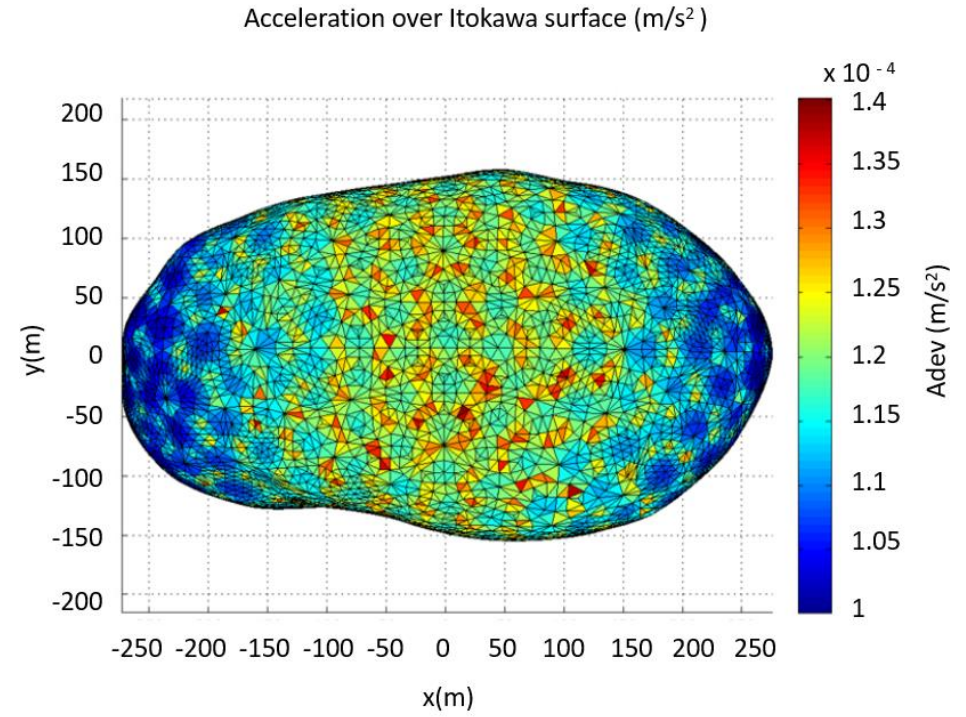

Source: Author.

Figure 4.13 - Itokawa acceleration over the surface-XZ view.

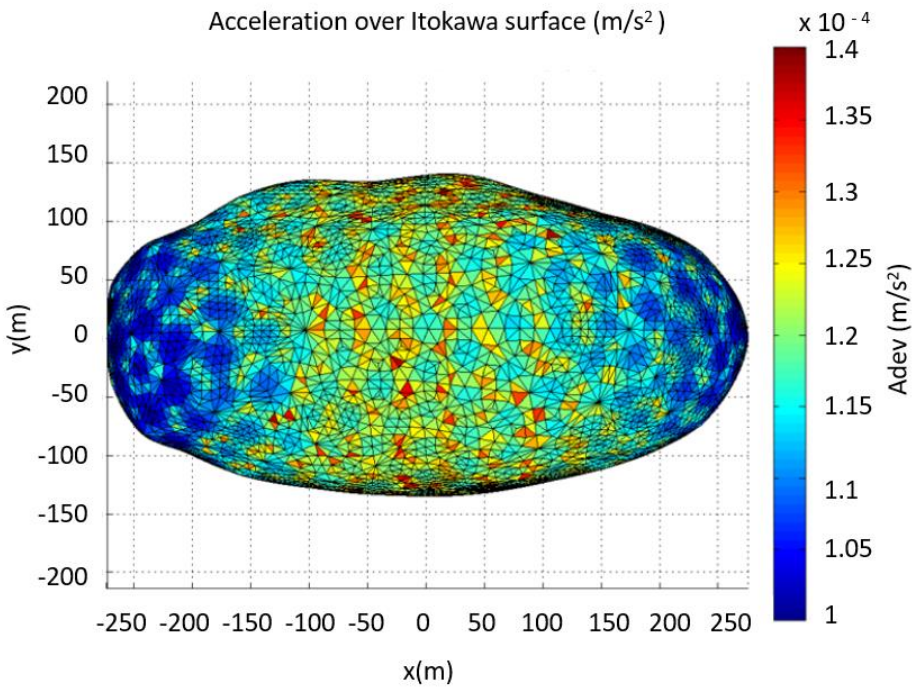

Source: Author.

Figure 4.14 - Itokawa acceleration over the surface-YZ view.

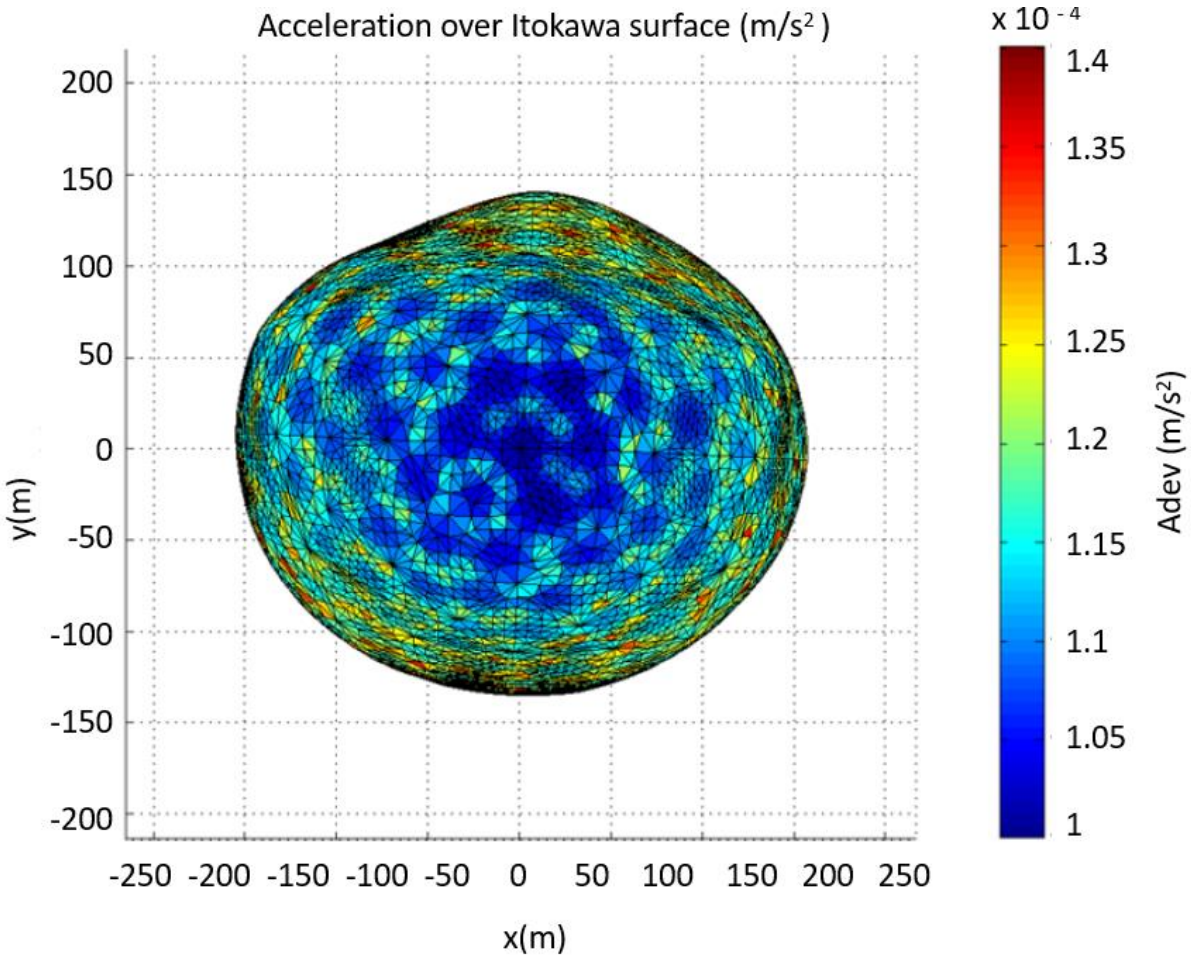

Source: Author.

Figure 4.15 shows the result for the deviation of the potential regarding the FEMR and the polyhedron method. From which it can be stated again that the differences between the two methods are small, having a magnitude of 10^{-4}.

Figure 4.15 - Itokawa potential deviation over the surface.

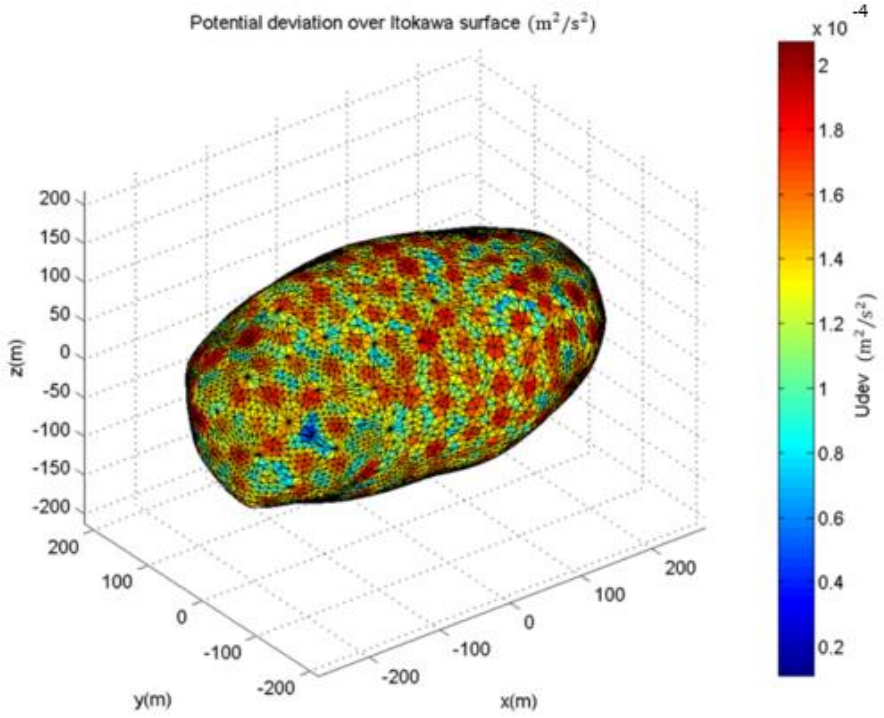

Source: Author.

4.3 Itokawa gravity coefficients

For Itokawa we perform the gravity coefficient comparison with the FEMR not only using the MEPS (MOTA, 2017), but also the classical Spherical Harmonics (SCHEERES et al., 2004). For the last one the computations are in section 2.3.

Figure 4.16 shows the plots of the RMS for the FEMR, the classic spherical harmonics, and the series expansion, and Table 4.2 the gravity coefficients. We use a reference radius of 179.1 meters. From these results we can tell that the FEMR can again deliver accurate results for the gravity coefficients, however, the higher the degree the higher the difference. Regarding specifically the gravity coefficients the difference between the FEMR and other methods start to appear in the 4th decimal place.

Figure 4.16 - Itokawa RMS comparison.

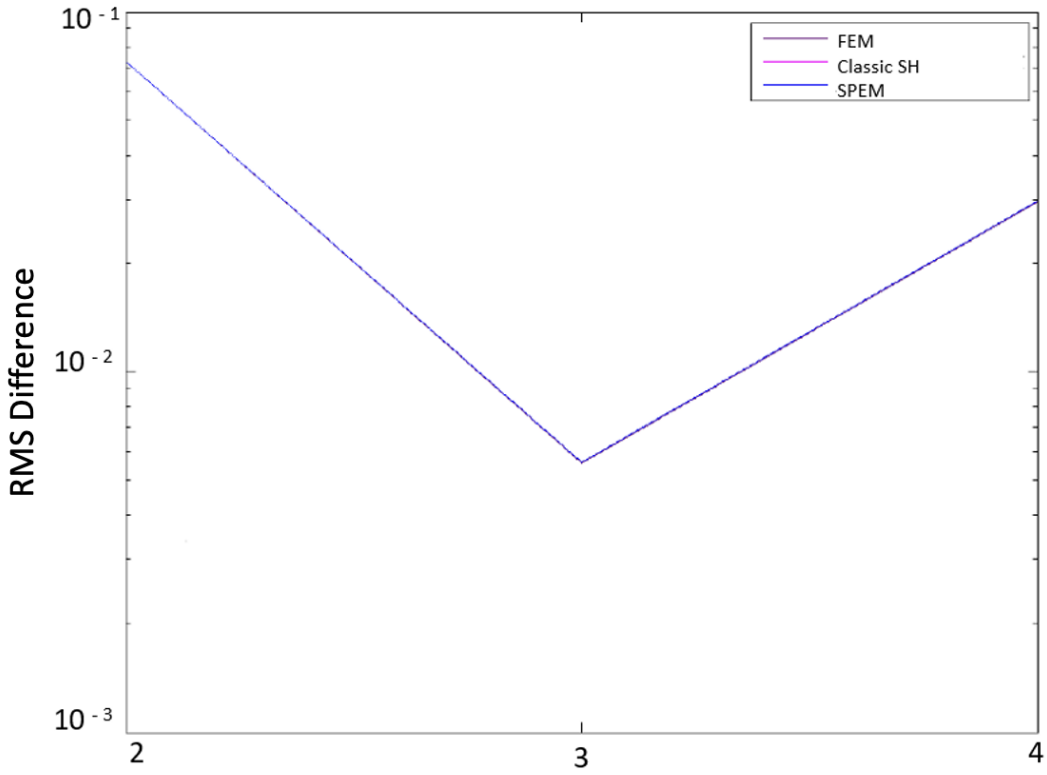

Source: Author.

Table 4.2 - Itokawa gravity coefficients comparison.

	FEMR	Classic SH	MEPS
C20	-9.1788E-02	-9.2222E-02	-9.2215E-02
C21	0.0	0.0	0.0
S21	0.0	0.0	0.0
C22	1.3449E-01	1.3511E-01	1.3511E-01

(continue)

Table 4.2 – Conclusion.

S22	0.0	0.0	0.0
C30	-2.0846E-04	-1.768E-04	-1.7681E-04
C31	3.4988E-04	2.468E-04	2.468E-04
S31	1.8901E-03	1.9196E-03	1.9196E-04
C32	-1.8476E-03	-1.9275E-03	-1.9275E-03
S32	-4.77662E-03	-4.7926E-03	-4.7926E-03
C33	-1.2169E-02	-1.2229E-02	-1.2229E-02
S33	-6.2373E-03	-6.2563E-03	-6.2563E-02
C40	3.9351E-02	3.97246E-02	3.9724E-02
C41	-1.9341E-03	-1.8445E-03	-1.8445E-03
S41	1.6656E-04	-1.744E-03	-1.7444E-03
C42	-5.3893E-02	-5.4399E-02	-5.4399E-02
S42	-2.38340E-03	-2.3396E-03	-2.3396E-03
C43	7.5196e-04	6.763E-04	6.6763E-04
S43	-1.3173E-03	1.3784E-03	1.3784E-03
C44	5.8363E-02	5.8924E-02	5.8924E-02
S44	5.9286E-03	5.8470E-03	5.8469E-03

Source: Author.

4.4 Varying the number of elements - Itokawa

To verify again what happens when we change the number of elements, we perform an analysis to check the behavior of the FEMR when adjusting the number of elements. We build a mesh for 1254 and 7912 elements as is possible to see from Figure 4.17 to Figure 4.20.

Figure 4.17 - Itokawa 1254 elements Mesh.

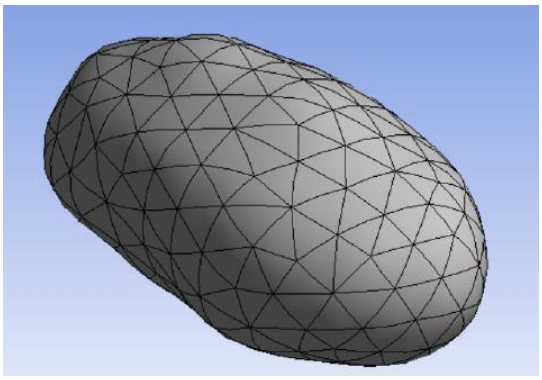

Source: Author.

Figure 4.18 - Itokawa 1254 elements Mesh Cross Section.

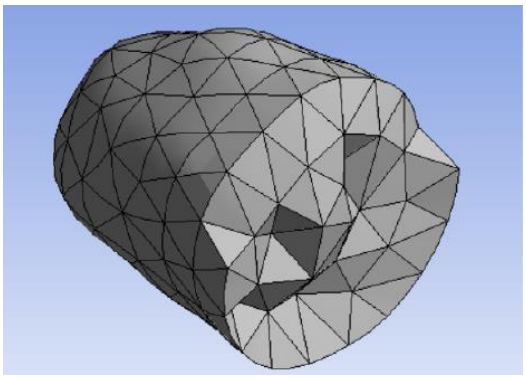

Source: Author.

Figure 4.19 - Itokawa 7912 elements Mesh.

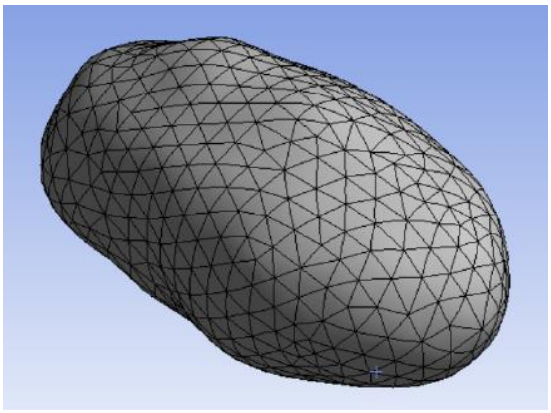

Source: Author.

Figure 4.20 - Itokawa 7912 elements Mesh Cross Section.

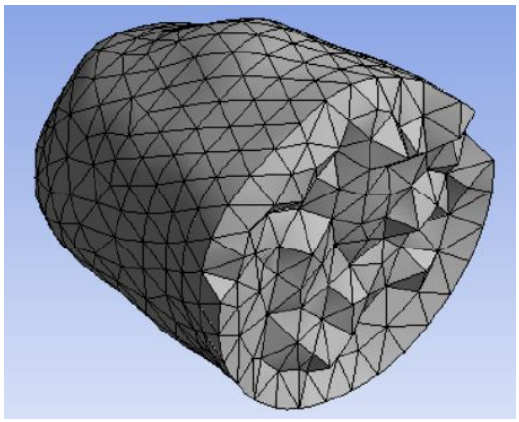

Source: Author.

We start with the comparison with the polyhedron, Figure 4.21 and Figure 4.22, as expected with the number of elements increasing it is possible to reach more accurate outputs. Again, the difference between models gets lower as more elements are inserted.

Figure 4.21 - Itokawa potential deviation over the surface - 1254 elements.

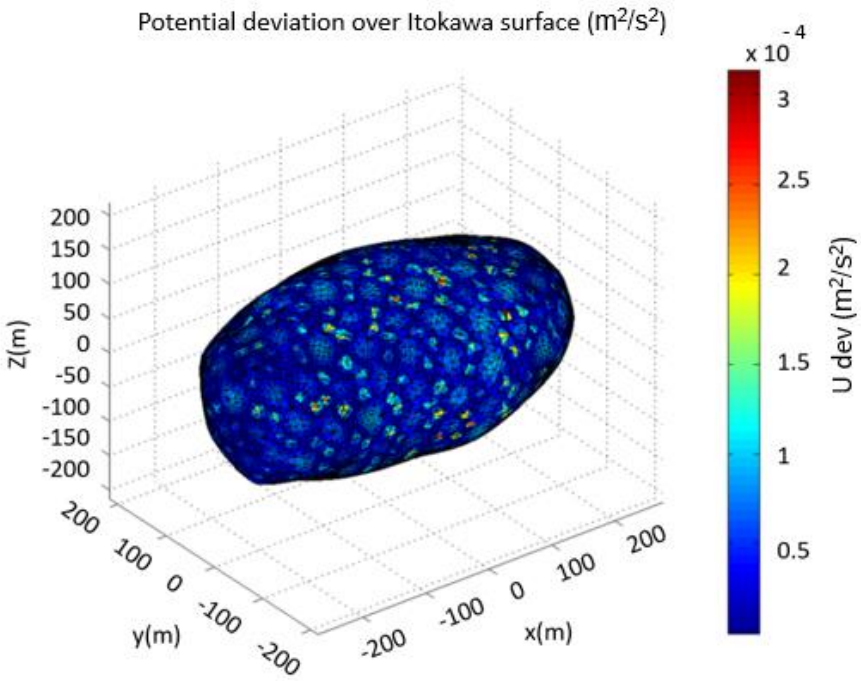

Source: Author.

Figure 4.22 - Itokawa potential deviation over the surface - 7912 elements.

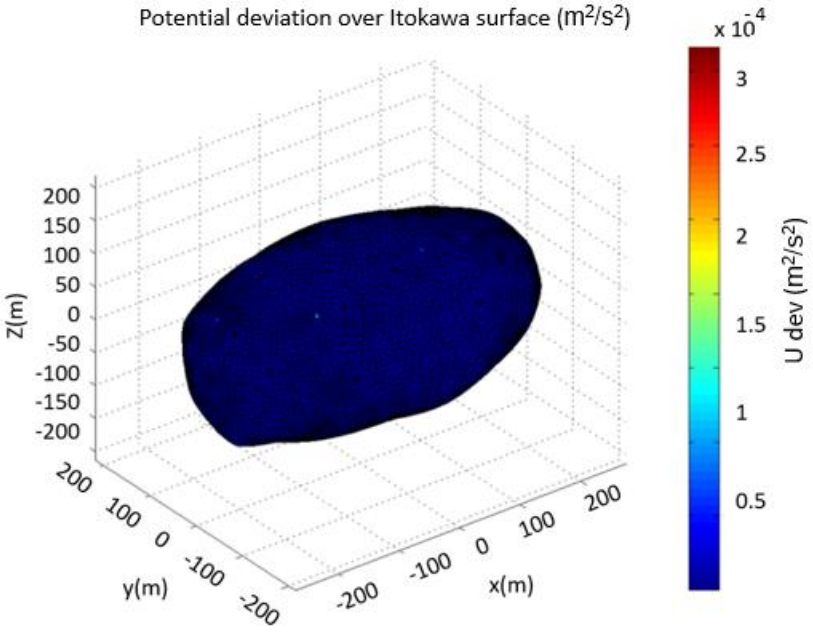

Source: Author.

Observing Figure 4.21 and Figure 4.22 for Itokawa 1254 elements produce accurate results. Paying attention to Figure 4.7, that was previously presented, it is possible to visualize that with more elements there is a slight decrease in the difference.

The interesting scenarios, again, show themselves on the plots considering the discretization with 7912 elements: the difference between the MEPS and the FEM that was decreasing starts to increase. The FEMR does not degenerate with a greater number of elements as we have seen, similarly to what happened to Bacchus, for Itokawa the FEM overpasses the series expansion method, showing that the FEMR is capable of being even more accurate.

Figure 4.23 - Spacecraft's absolute velocity increment comparison - Itokawa 1254 elements.

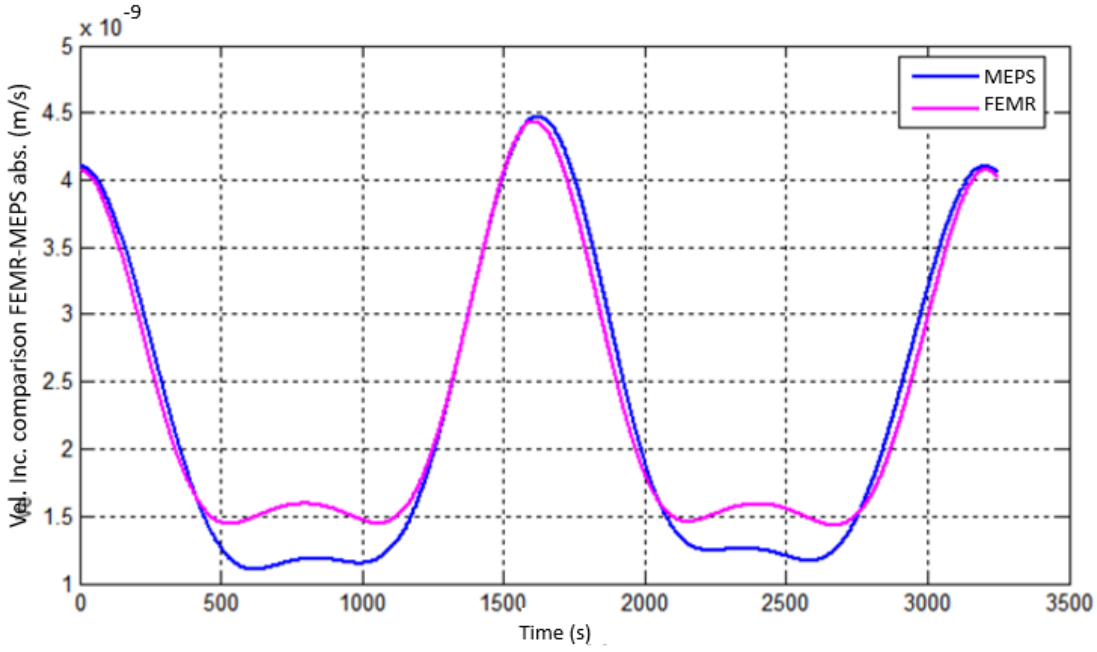

Source: Author.

Figure 4.24 - Spacecraft's velocity increment difference - Itokawa 1254 elements.

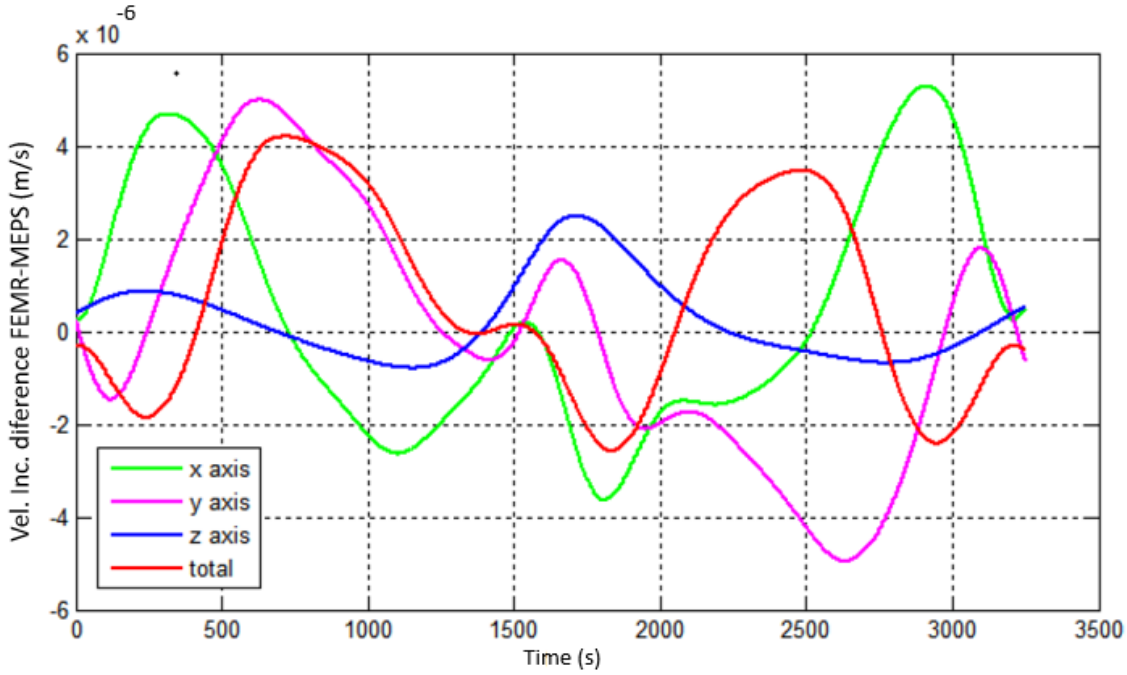

Source: Author.

Figure 4.25 - Spacecraft's absolute velocity increment comparison - Itokawa 7912 elements.

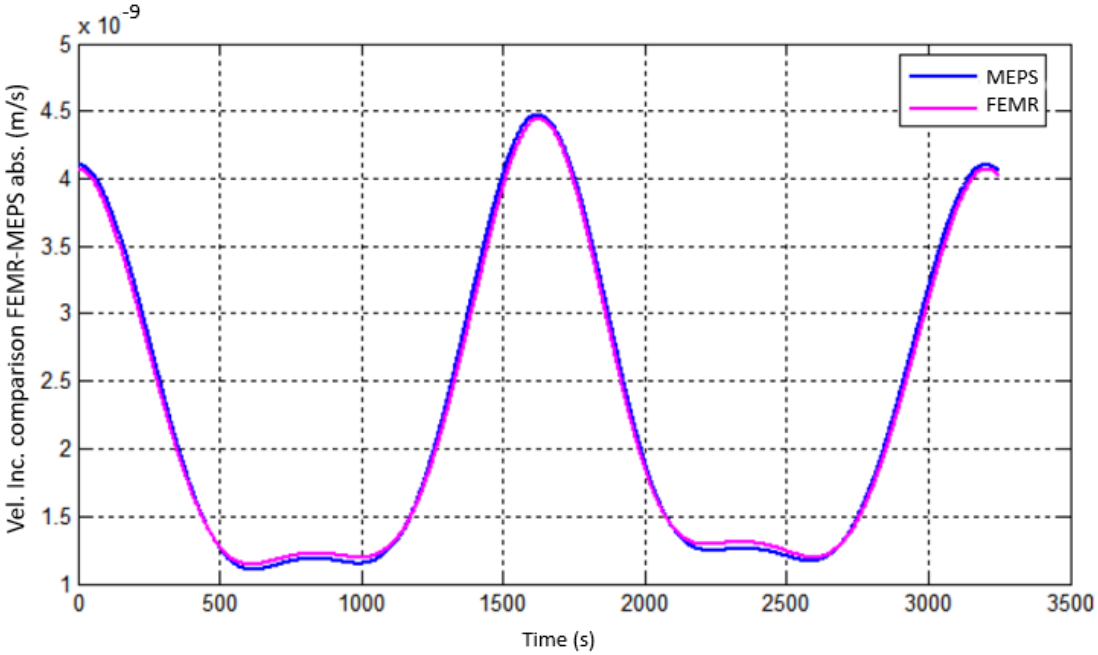

Source: Author.

Figure 4.26 - Spacecraft's velocity increment difference - Itokawa 7912 elements.

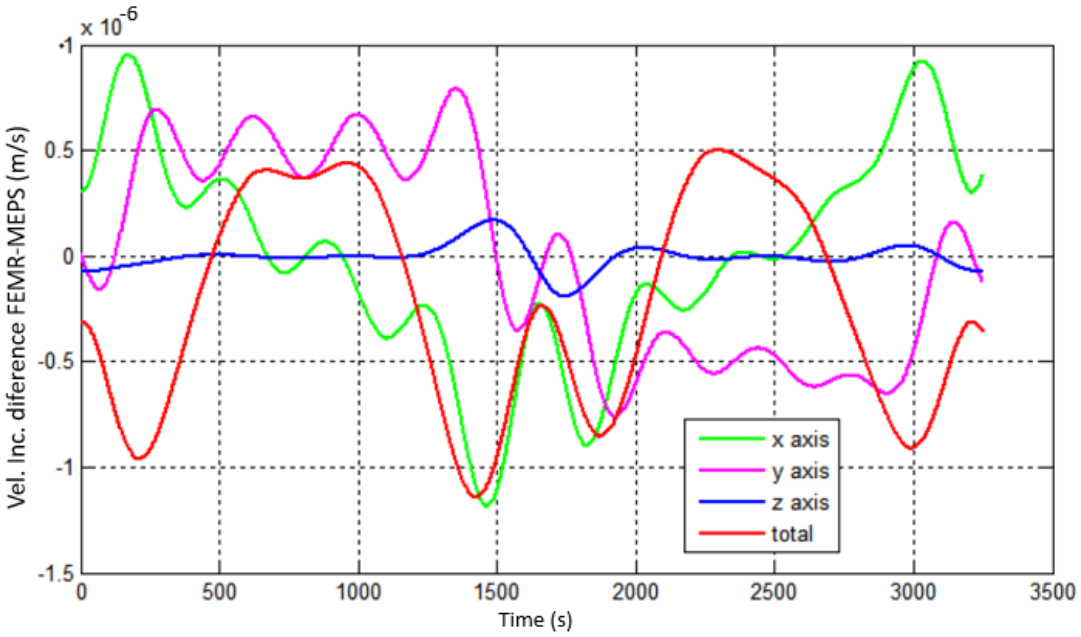

Source: Author.

5 ASTEROID 101955 BENNU

Bennu is an NEA, Figure 5.1, and has approximately 500 m of diameter, Figure 5.2. Bennu has one of the most precise orbits among the NEAs we know (CHELSEY et al., 2014). Bennu is a low albedo B-type asteroid, a subgroup of the carbonaceous C-group, and one of the darkest objects in our solar system with a very rough surface, as we can say from data collected by OSIRIS-Rex (LAURETTA et al., 2019). Another thing that is important to mention, Bennu was the target of the OSIRIS-Rex mission. OSIRIS-Rex images also suggest that (101955) Bennu is a rubble pile asteroid, with considerable porosity and surface boulders (BARNOUIN et al., 2019).

Figure 5.1 - Asteroid Bennu.

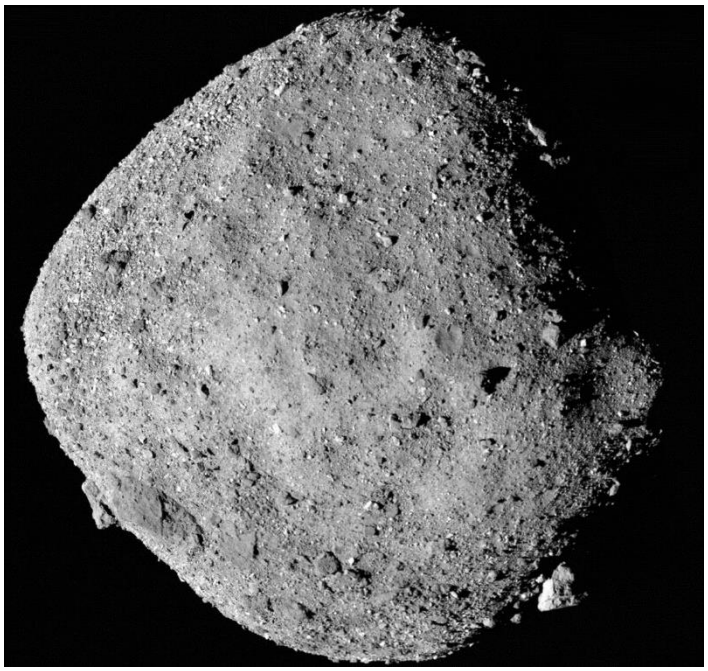

Source: Wikipedia (2021)[2].

From some data collected on the mission, pieces of evidence show a density heterogeneity within Bennu (SCHEERES et al., 2019). These images and results show the importance of studying and creating models to explore different

[2] Available on: https://pt.wikipedia.org/wiki/101955_Bennu

densities within an asteroid. So, for Bennu we not only perform the validation, but we also present the application that is the most important contribution of this work, the study of the internal density variation. This specific study was the core of the internship carried out at the University of Colorado Boulder supervised by Daniel J. Scheeres.

Figure 5.2 - Bennu 3D model representation.

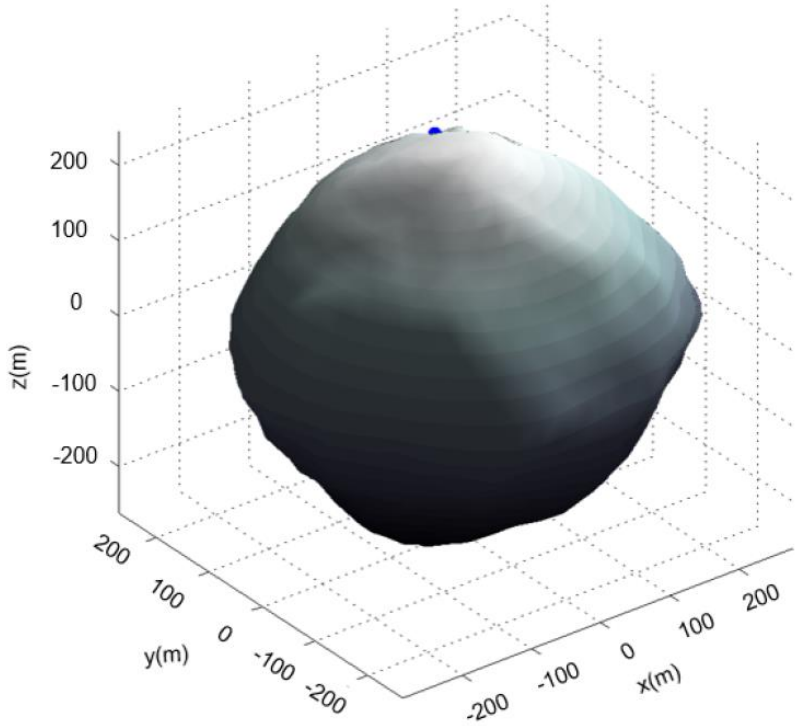

Source: Author.

Bennu's bulk density was considered as 1.26 g/cm^3, its volume is equal to 0.0623 km^3 and the FEMR mesh was created with 20294 elements, Figure 5.3 and Figure 5.4.

Figure 5.3 - Bennu 20294 elements Mesh.

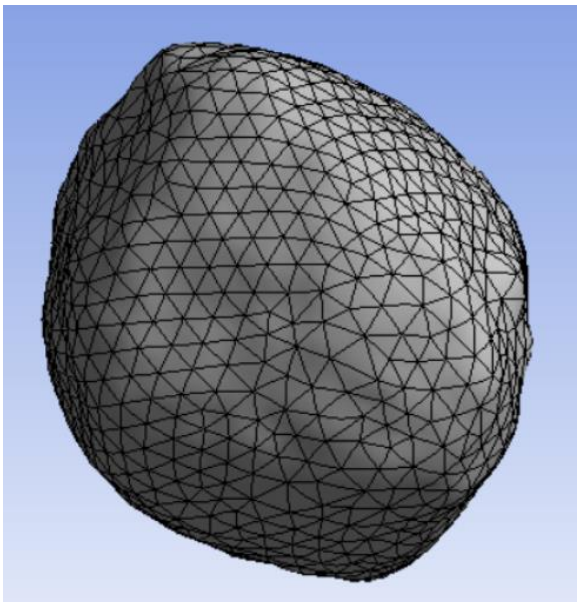

Source: Author.

Figure 5.4 - Bennu 20294 elements cross section.

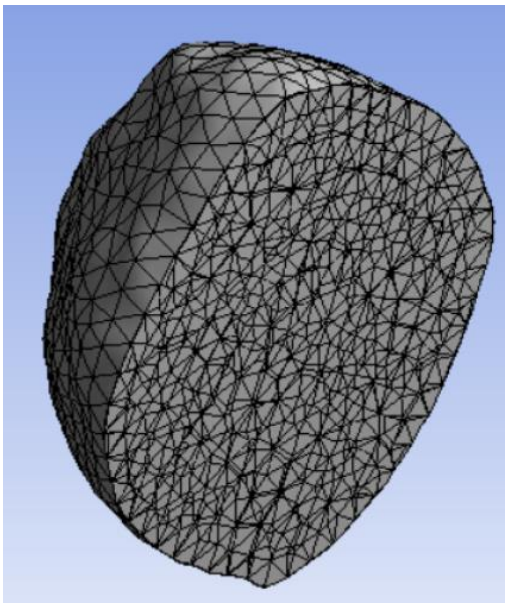

Source: Author.

5.1 Bennu STRS comparison and validation

Now we start Bennu validation, once again the centroids are checked below.

$$x_c = 0.0238m$$

$$y_c = 0.01042m$$

$$z_c = -0.0656m$$

$$I = 1.0E + 016\begin{pmatrix} 5.0384 & 0.0297 & -0.0115 \\ 0.0297 & 5.9642 & -0.0386 \\ -0.0115 & -0.0386 & 5.3289 \end{pmatrix} gm^2$$

The spacecraft orbital elements used for the STRS validation are presented on Table 5.1. Looking at Figure 5.5 and Figure 5.6 we can see that the maximum difference between both methods is around $3.5x10^{-6}$ showing again that the FEMR is accurate.

Table 5.1 - Spacecraft's orbital elements – Bennu.

Semi-major axis (m)	300
Eccentricity	0
Inclination (degrees)	0
Right ascension of the ascending node (degrees)	0
Argument of periapsis (degrees)	0
Mean anomaly (degrees)	0

Source: Author.

Figure 5.5 - Spacecraft absolute velocity Increment comparison – Bennu.

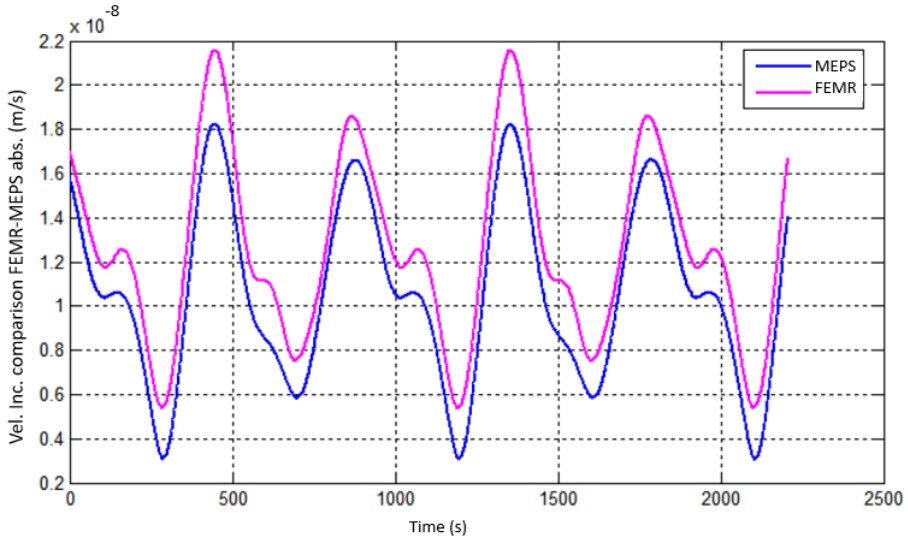

Source: Author.

Figure 5.6 - Spacecraft velocity Increment difference – Bennu.

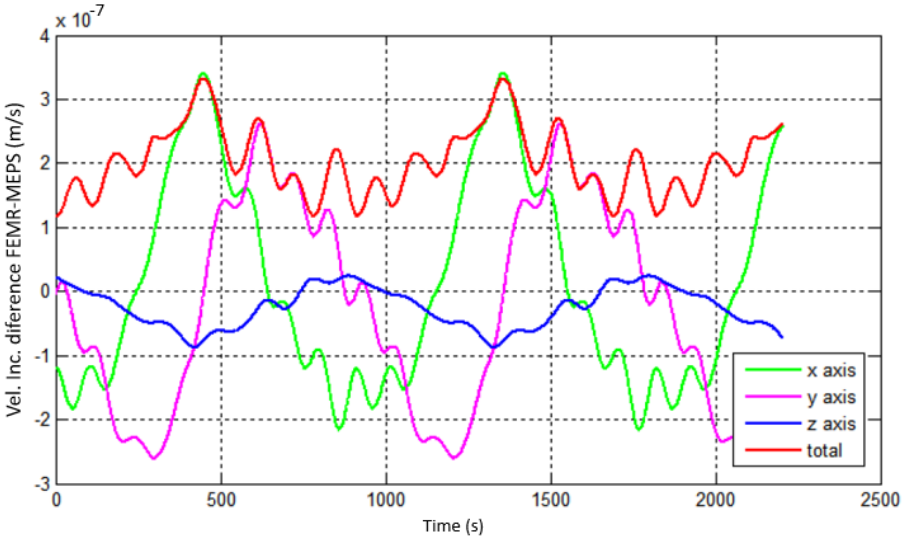

Source: Author.

5.2 Bennu FEM x polyhedron comparison

For Bennu, the bulk density was considered as 1.26g/cm^3, the potential over the surface can be seen on Figure 5.7, and the acceleration on Figure 5.8 the detailed views can also be seen from Figure 5.9 to Figure 5.14.

Bennu shows a different distribution if compared with the two previous asteroids, which was expected as it is not a contact binary. It seems that at the "higher" points of Bennu and at one of the poles the gravity is lower, for the rest of the body it varies significantly through the surface.

Figure 5.7 - Bennu Potential over the surface.

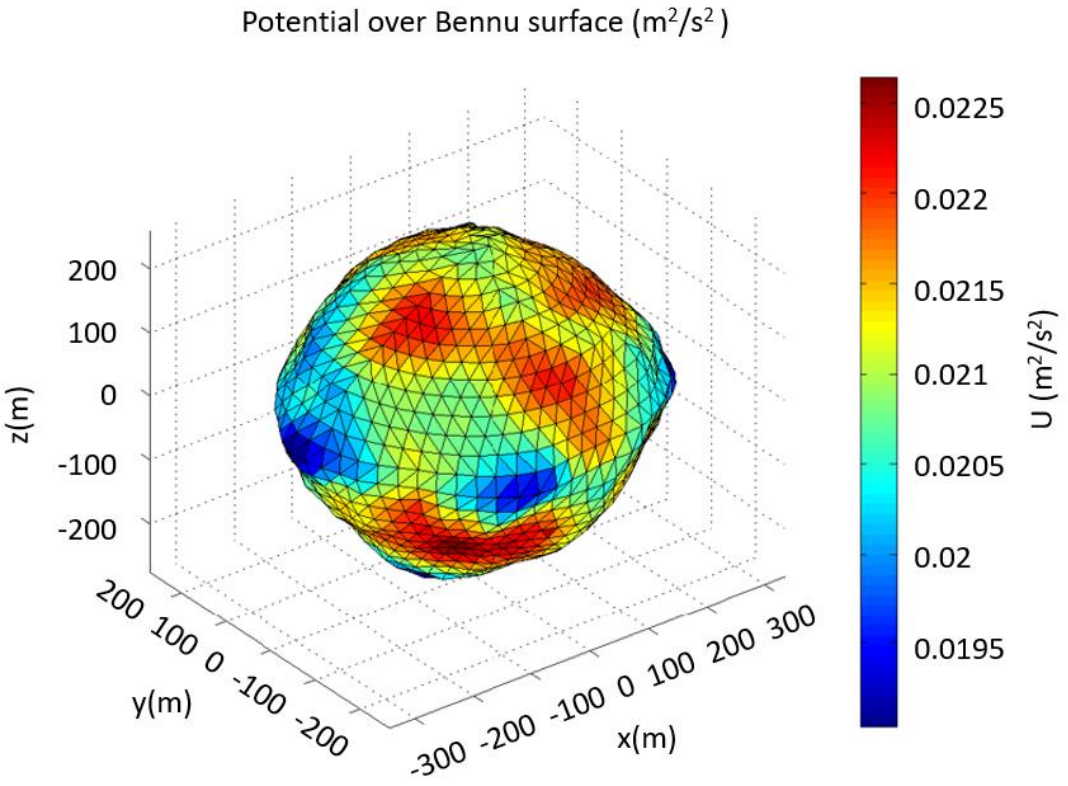

Source: Author.

Figure 5.8 - Bennu Potential over the surface-XY view.

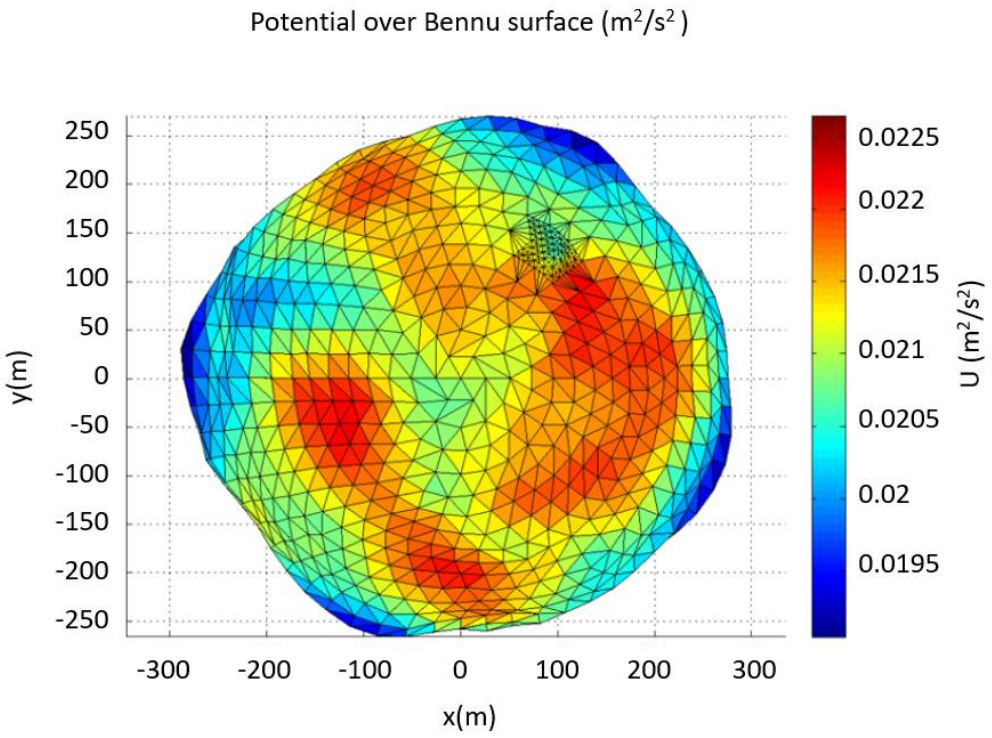

Source: Author.

Figure 5.9 - Bennu Potential over the surface-XZ view.

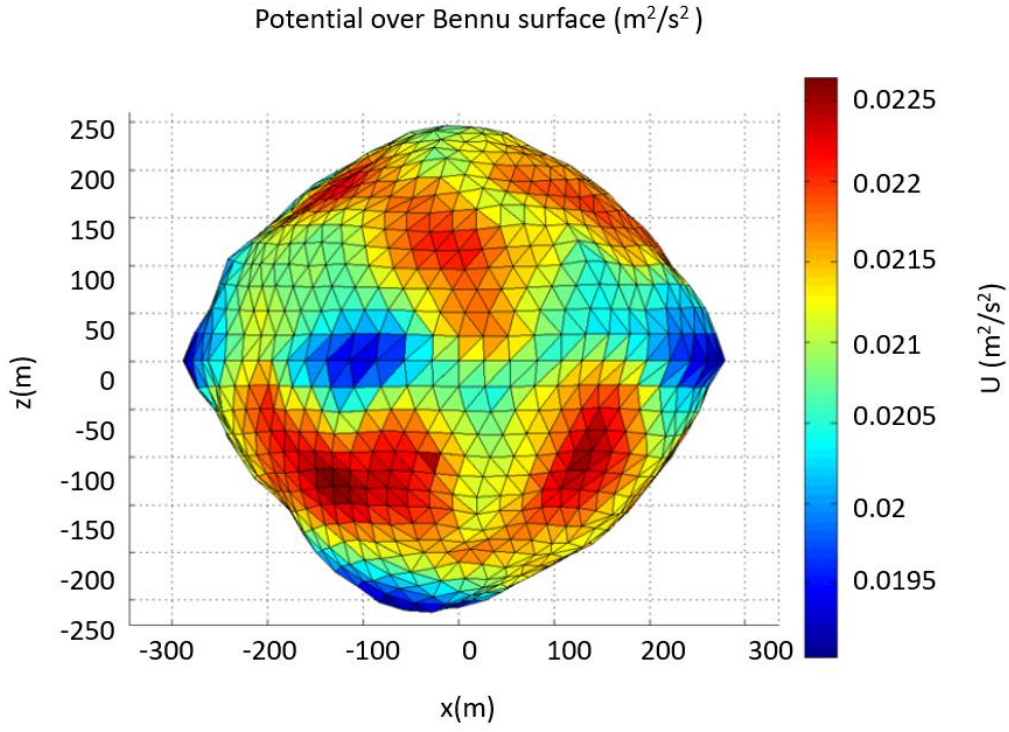

Source: Author.

Figure 5.10 - Bennu potential over the surface-YZ view.

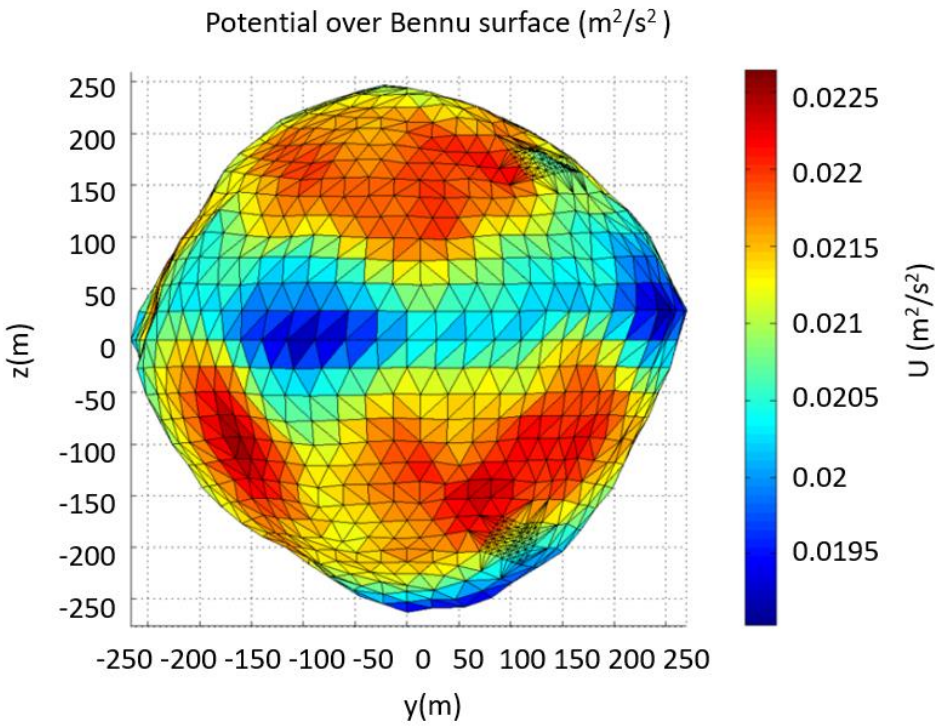

Source: Author.

Figure 5.11 - Bennu acceleration over the surface-XY view.

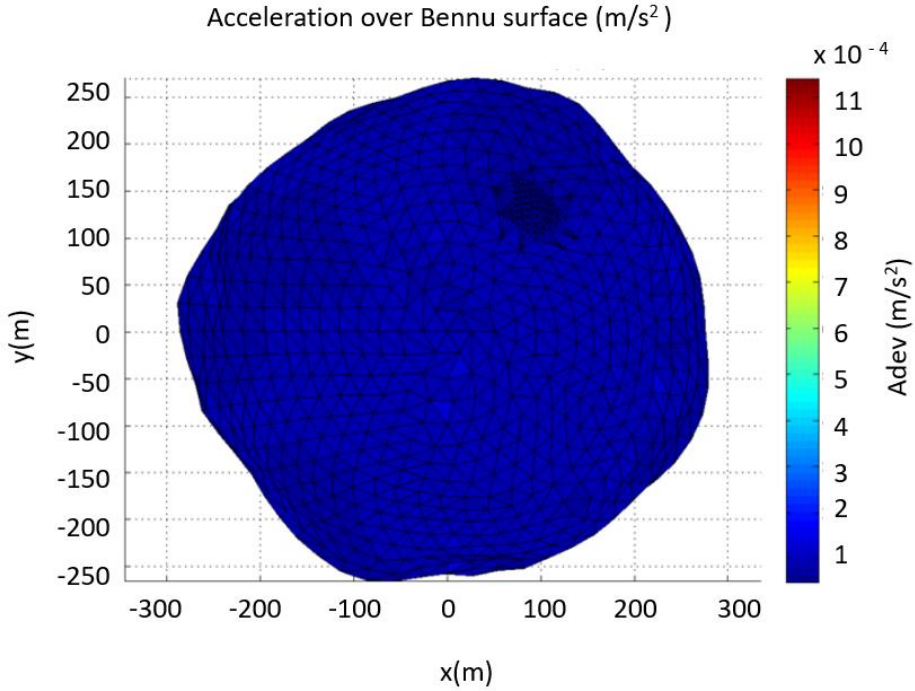

Source: Author.

Figure 5.12 - Bennu acceleration over the surface-XZ view.

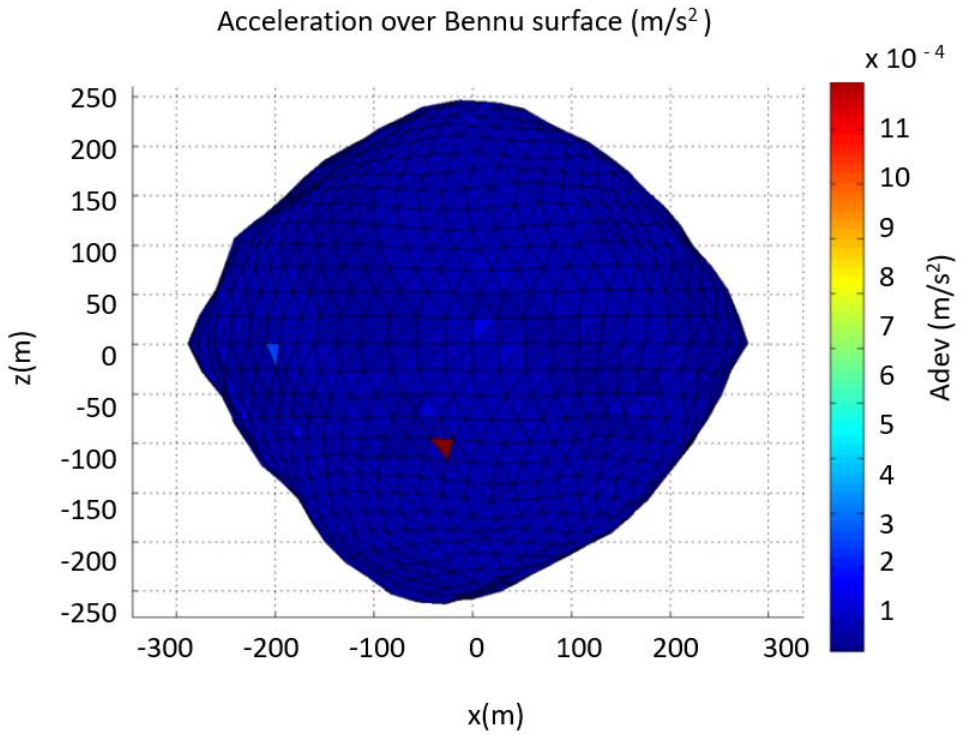

Source: Author.

Figure 5.13 - Bennu acceleration over the surface-YZ view.

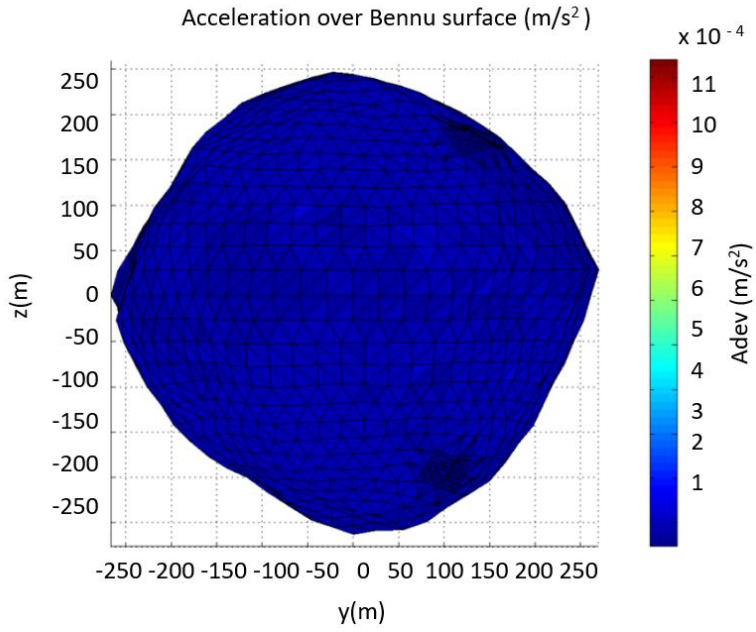

Source: Author.

Figure 5.15 carries the results of the deviation of the potential between the FEMR and the polyhedron. The deviation has a magnitude of 10^{-4}, this result leaves no doubt that the FEMR works.

Figure 5.14 - Bennu potential deviation over the surface.

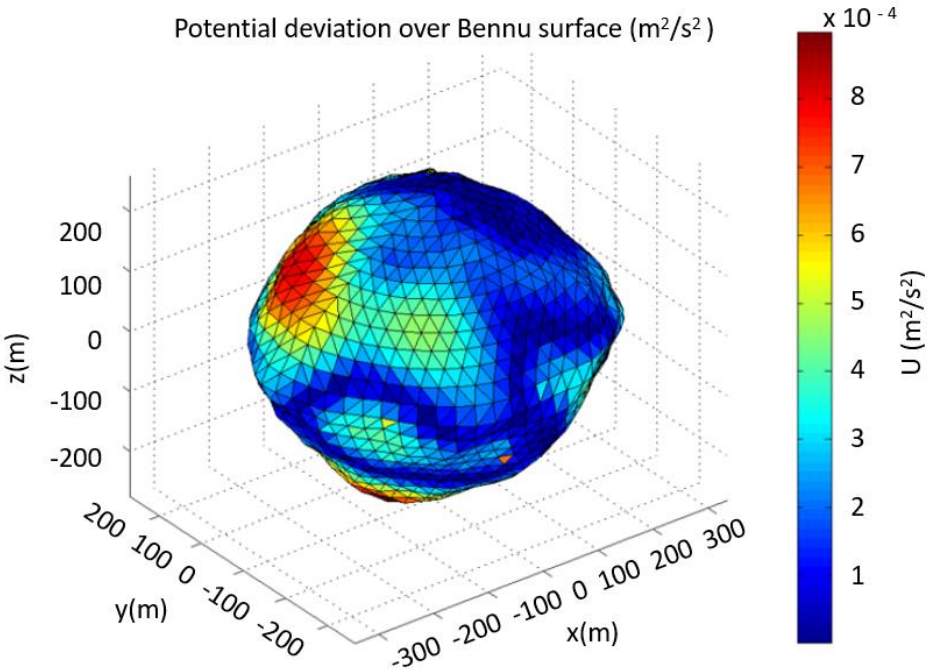

Source: Author.

5.3 Bennu gravity coefficients

For Bennu we do the comparison using data and computations performed at the Celestial and Spaceflight Mechanics Laboratory at the University of Colorado Boulder. This means that we only compare the FEMR with the classical spherical harmonics for Bennu.

Figure 5.16 shows the RMS for the spherical harmonics and the FEMR until degree 8. This plot shows accurate results; however, it is noticed that for higher degrees the difference between them increases. Even though the results are still highly coherent and can be again validated.

Figure 5.15 - Bennu RMS Comparison.

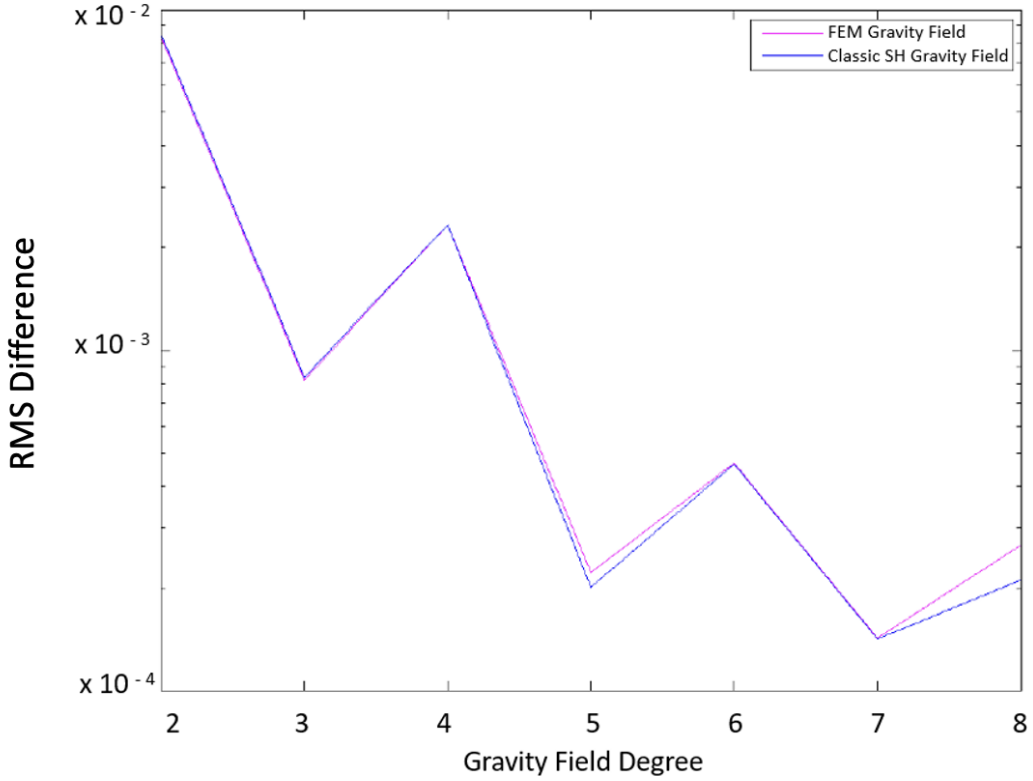

Source: Author.

5.4 Varying the number of elements - Bennu

From the previous sections the effects of the changes on the number of elements were explored. Something that was possible to notice was that the variation regarding the number of elements is very specific for each asteroid. The differences increase as the number of elements gets lower, however, increasing the number of elements can bring us surprises: it can just give an output with a lower difference or can make the FEMR to be able to overpass the other models.

For Bennu one more case is presented, built up with 69308 elements. Figure 5.17 shows the mesh and Figure 5.18 its cross section.

Figure 5.16 - Bennu 69308 elements Mesh.

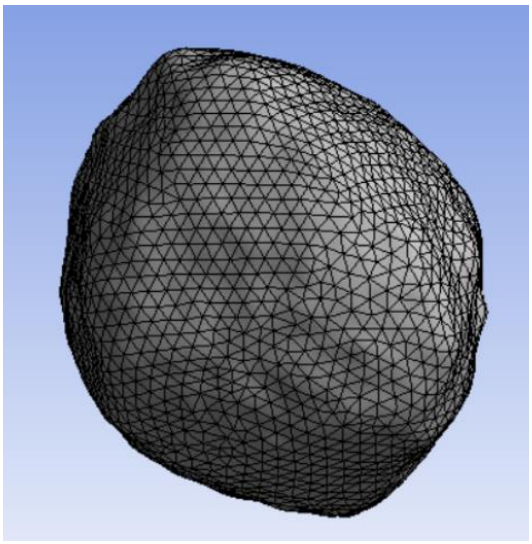

Source: Author.

Figure 5.17 - Bennu 69308 elements Mesh Cross Section.

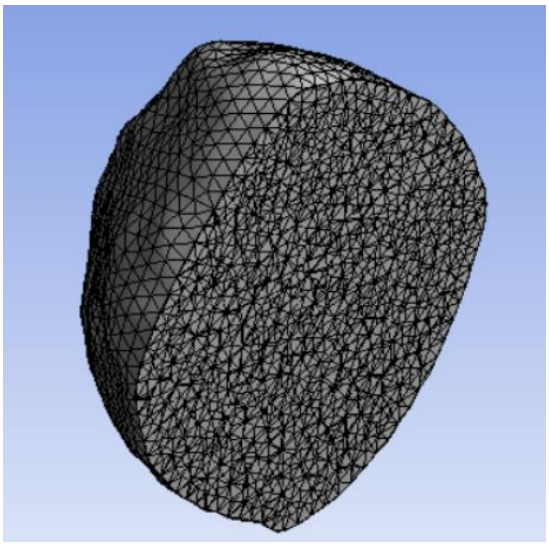

Source: Author.

Again, in this analysis, as it was possible to see from the previous ones, Figure 5.19 to Figure 5.21, show that when the number of elements is increased the precision of the finite element method also increases. Being the FEMR not only able to be equal but also to overpass the results obtained with the other methods.

Figure 5.18 - Bennu potential deviation over the surface - 69308 elements.

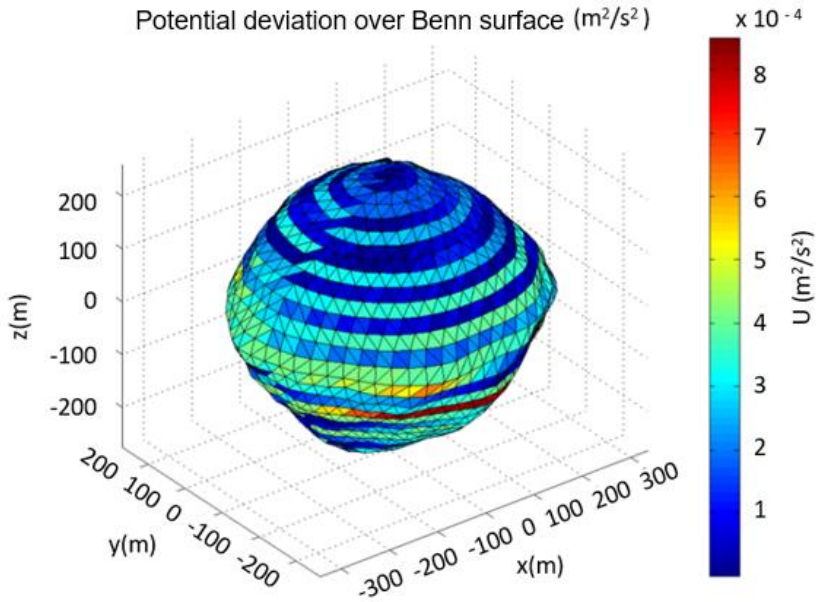

Source: Author.

Figure 5.19 - Spacecraft absolute velocity Increment comparison - Bennu 69308 elements.

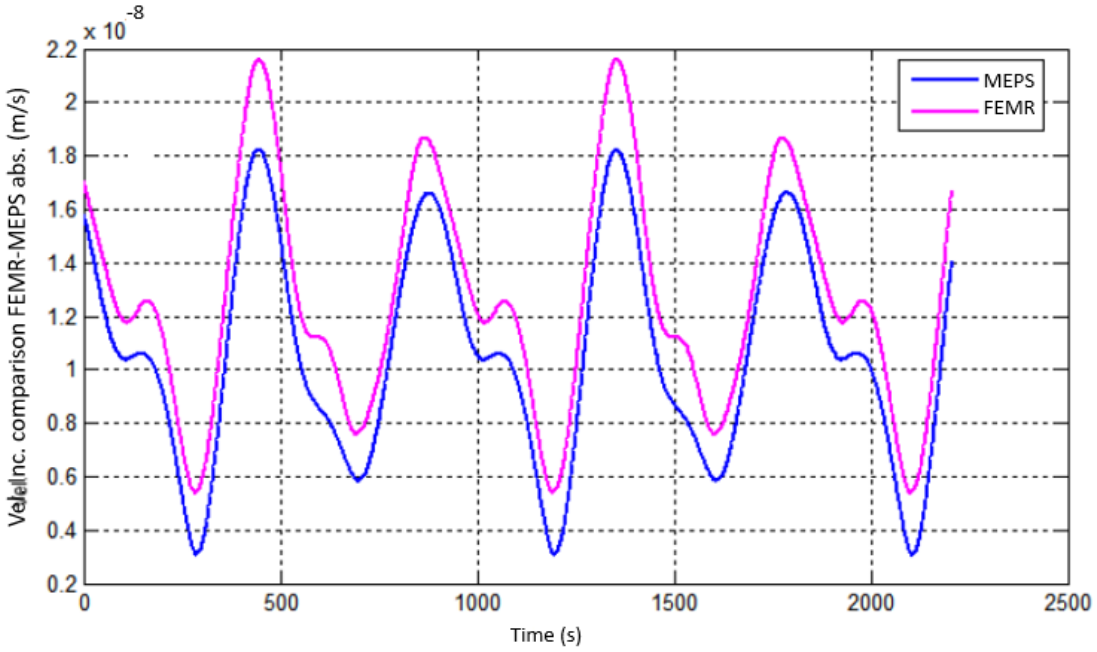

Source: Author.

Figure 5.20 - Spacecraft velocity Increment difference between FEMR and MEPS - Bennu 69308 elements.

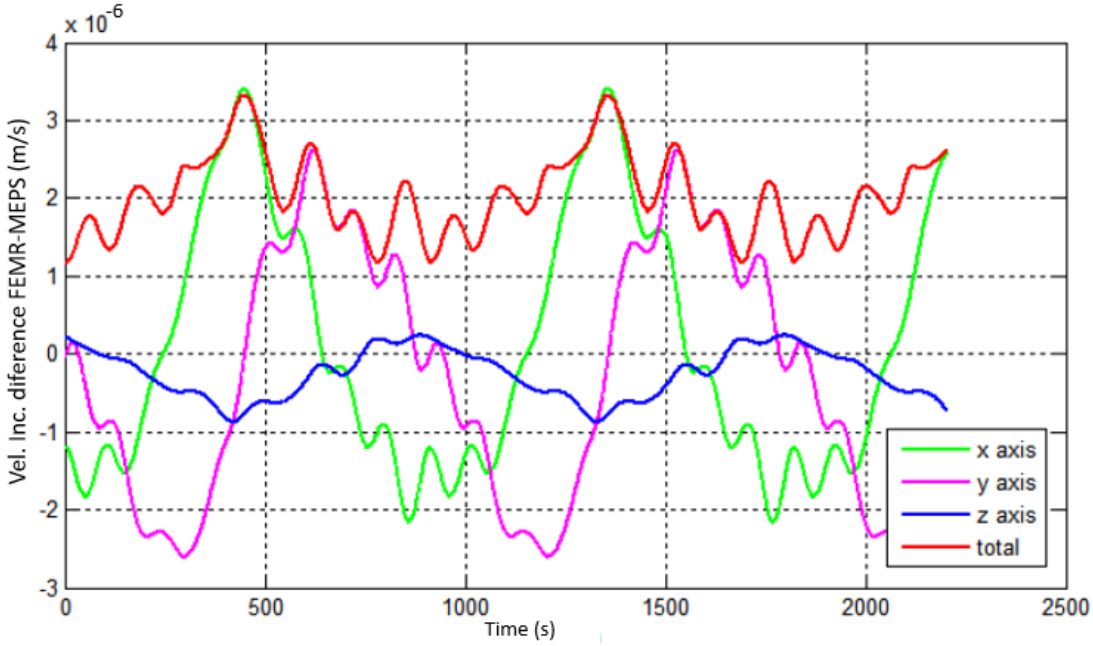

Source: Author.

6 SIMULATING TRAJECTORIES OF A SPACECRAFT

After the model validation using different techniques with three distinct asteroids, Bacchus, Bennu and Itokawa, we could show that the FEMR works, and it is accurate. Now, it is time for us to explore some possible applications of the FEMR. The first application aims to investigate the trajectory of a spacecraft.

This section presents some results of simulations of a spacecraft in orbit around the same three asteroids. It is important to mention that this is just a sample to show the power of the FEMR. The main goal of the method is not to analyze trajectory simulations, but to explore the power of the FEMR combined with other tools such as the STRS (ROCCO, 2008a; ROCCO, 2008b; ROCCO, 2013). The finite element approach was integrated in the STRS only for the three mentioned asteroids to perform part of the validation and get a sense of the spacecraft trajectories.

6.1 Bacchus trajectory simulation

The model used to perform the simulations for Bacchus will be the one with 27811 elements. The fixed orbital elements of the first simulation can be seen on Table 6.1 and we alternate the semi-major as 500, 600 and 700 meters. We vary the semi-major axis as an experiment to approach and go within the circumscribing sphere and check the evolution of the disturbance due to the gravity field. We show the example of the spacecraft's orbit around Bacchus on Figure 6.1.

Table 6.1 - Bacchus Spacecraft data.

Eccentricity	0
Inclination (degrees)	90
Right ascension of the ascending node (degrees)	90
Argument of periapsis (degrees)	0
Mean anomaly (degrees)	0

Source: Author.

Figure 6.1 - Spacecraft's orbit around Bacchus.

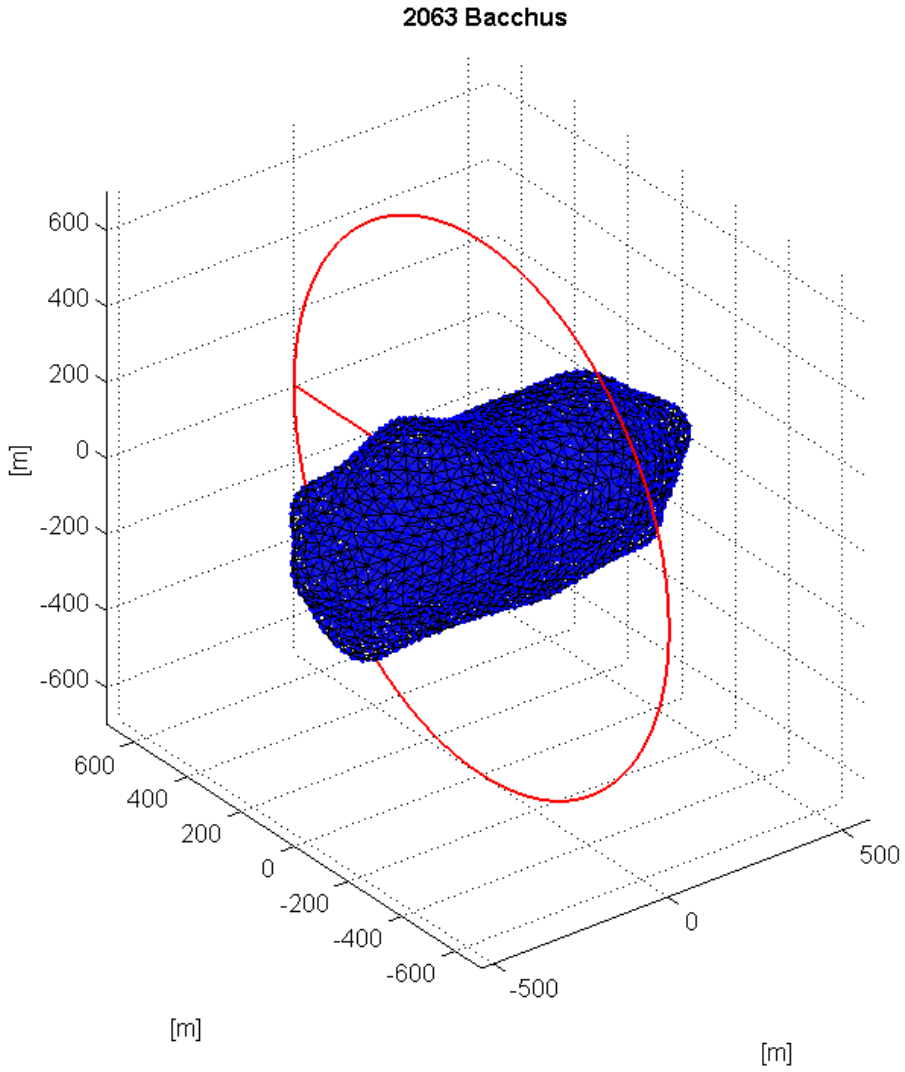

Source: Author.

Figure 6.2 to Figure 6.7 show the spacecraft's absolute velocity increment due to the gravity field disturbance and the velocity difference between the FEMR and the series expansion approach. It is known that when the gravity field is computed using the spherical harmonics the model diverges inside the circumscribing sphere (SCHEERES, 2012).

From Figure 6.2 to Figure 6.7 we can notice that the FEMR shows coherent results again, even with the change on the semi-major axis. However, we can see that as the spacecraft approaches the body, regarding the lower orbits, the differences start to slightly increase. Also, from the results comparing the FEMR

with the polyhedron neither of them diverges on the surface, so the FEMR results are accurate and preferable in such cases when the spacecraft starts to get closer to the surface of the body.

Figure 6.2 - Spacecraft absolute velocity increment comparison Bacchus a=700 meters.

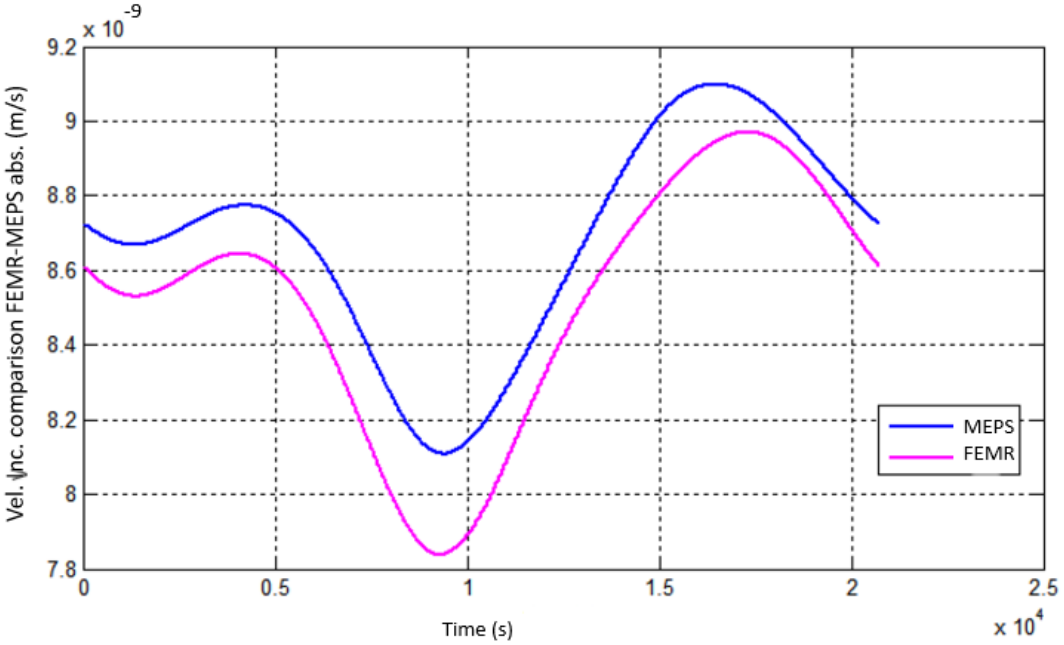

Source: Author.

Figure 6.3 - Spacecraft's velocity increment difference Bacchus a= 700 meters.

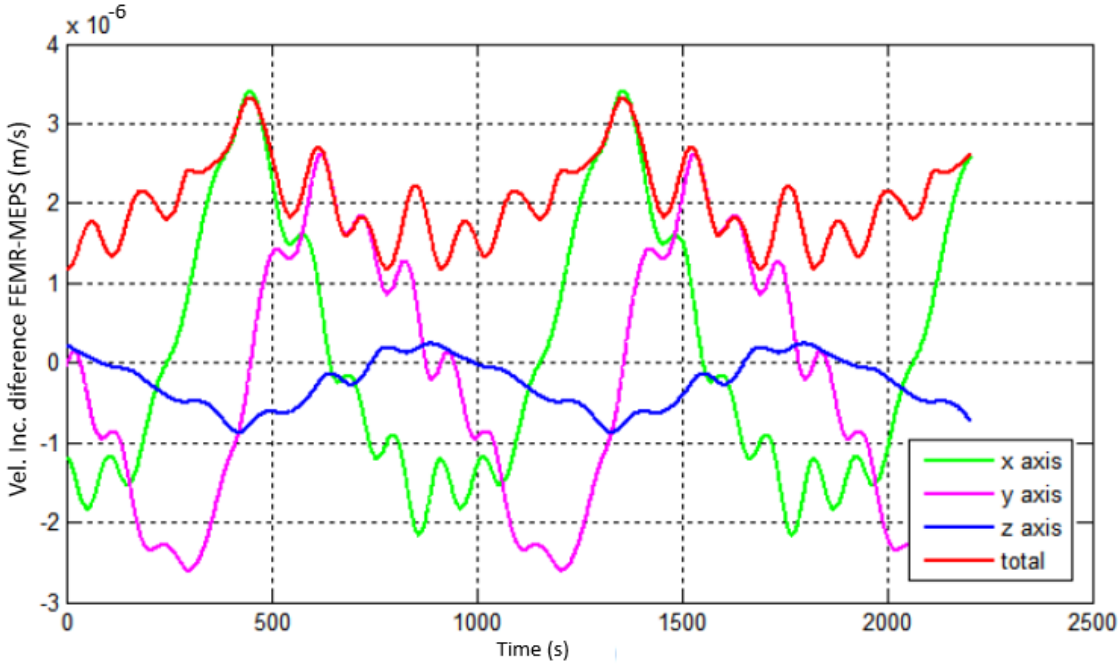

Source: Author.

Figure 6.4 - Spacecraft absolute velocity increment comparison Bacchus a=600 meters.

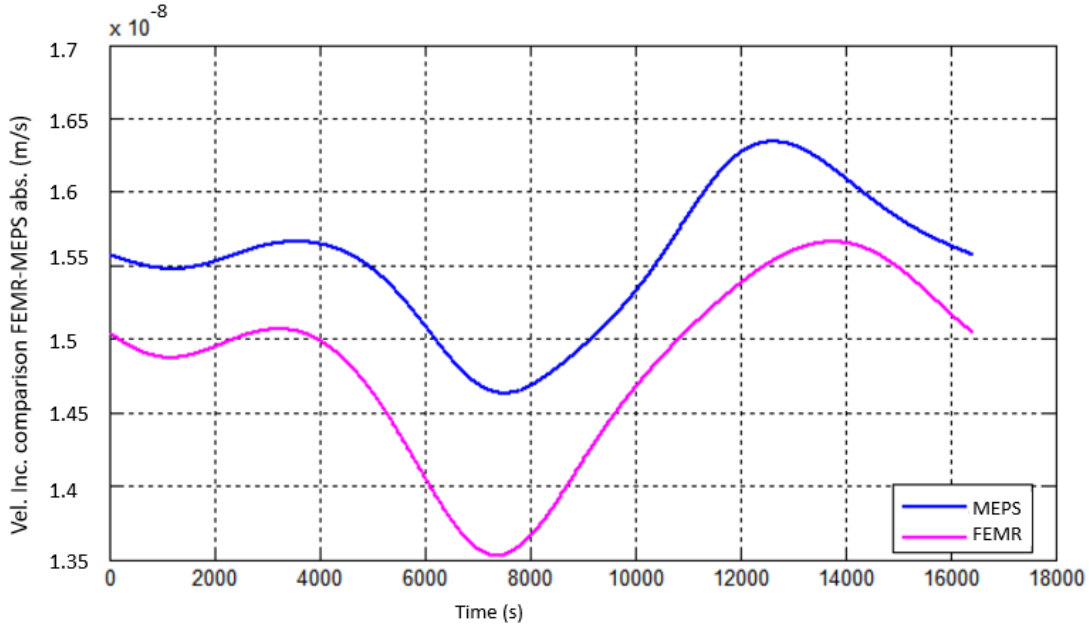

Source: Author.

Figure 6.5 - Spacecraft's velocity increment difference Bacchus a=600 meters.

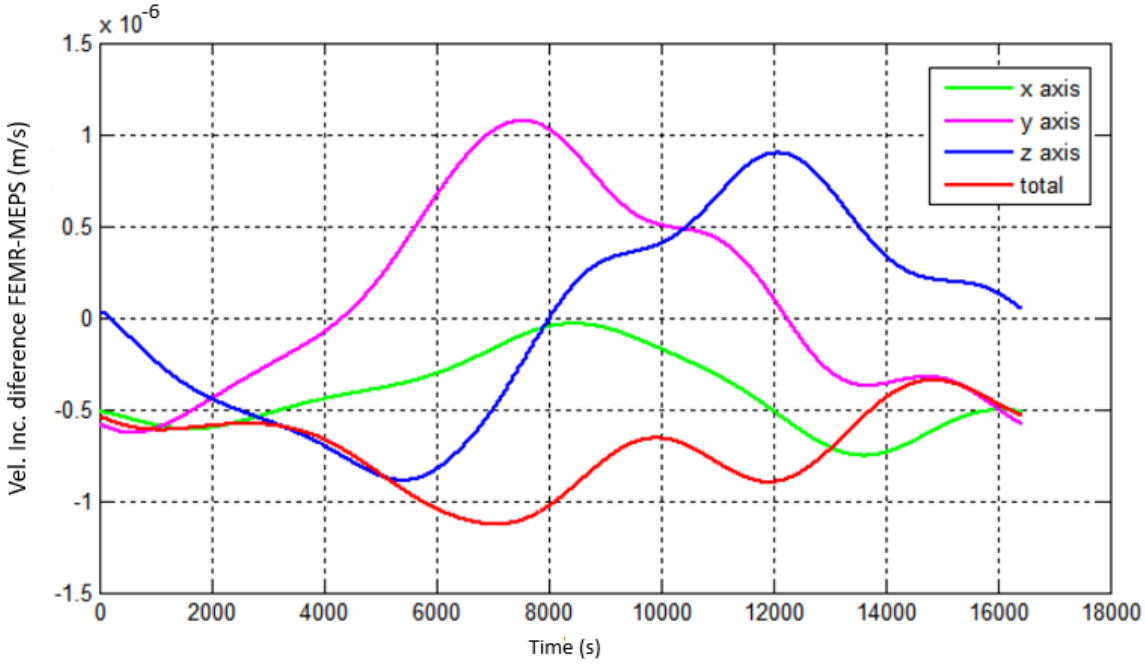

Source: Author.

Figure 6.6 - Spacecraft absolute velocity increment comparison Bacchus a=500 meters.

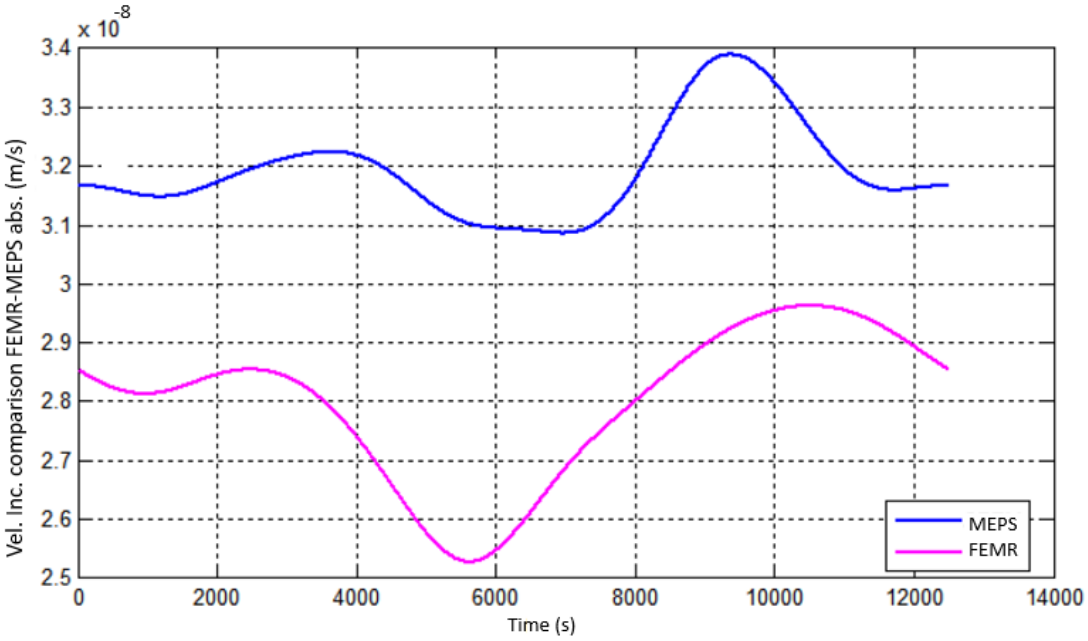

Source: Author.

Figure 6.7 - Spacecraft's velocity increment difference Bacchus a=500 meters.

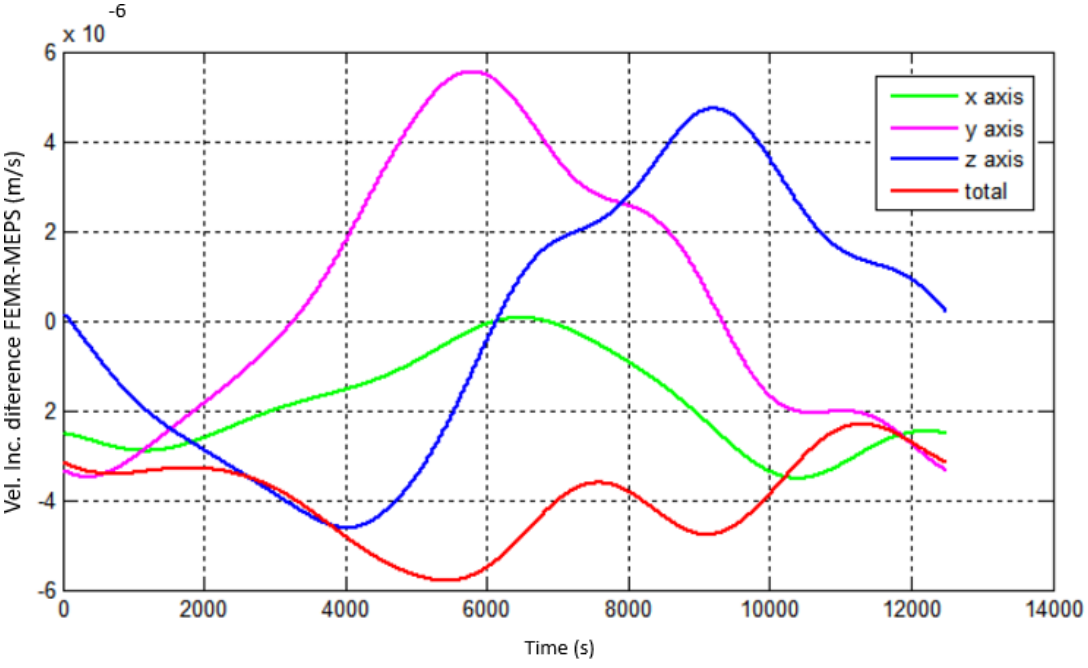

Source: Author.

Before presenting the last simulations for Bacchus, we present some extra simulations in order to investigate if these results make sense for more orbits

variations; for this we vary the inclination values. The orbital elements are shown on Figure 6.2, except for the semi-major axis that is set to 700 meters for all simulations. The inclination is varied and is set as 0, 45 and 90 degrees.

Table 6.2 - Bacchus Spacecraft data - inclination variation.

Semi-major axis(m)	700
Eccentricity	0
Right ascension of the ascending node (degrees)	0
Argument of periapsis (degrees)	0
Mean anomaly (degrees)	0

Source: Author.

From Figure 6.8 to Figure 6.13 show again the absolute velocity increment and the velocity difference between methods regarding the inclination variation. As we can see the FEMR shows again that it is accurate, and the difference between the methods remains low.

Figure 6.8 - Spacecraft absolute velocity increment comparison Bacchus i=0 degrees.

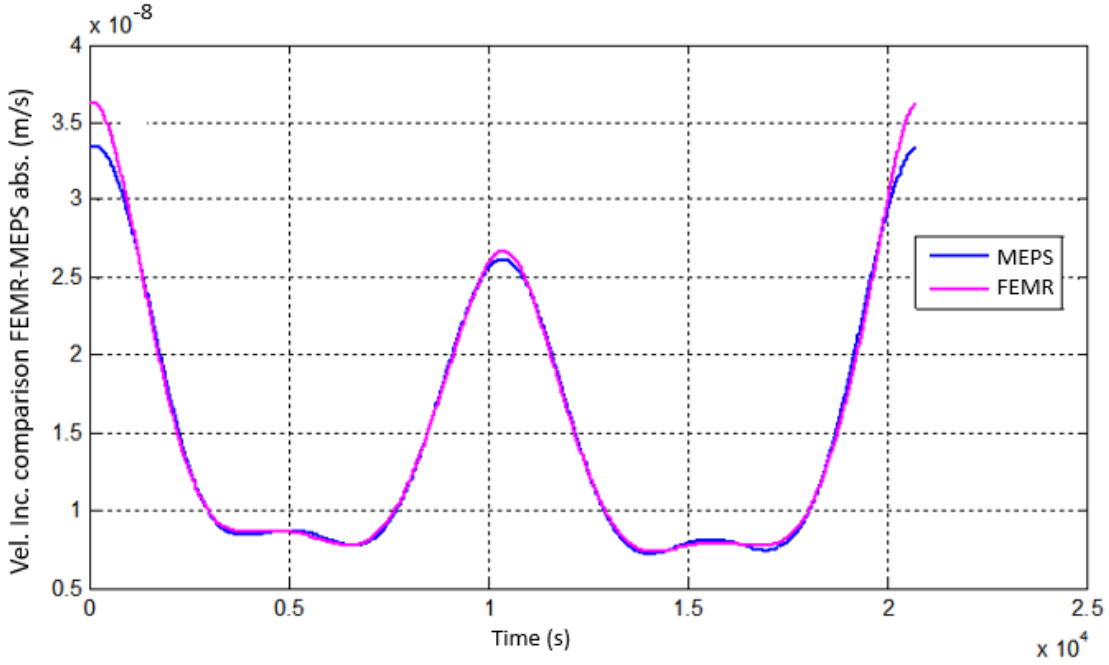

Source: Author.

Figure 6.9 - Spacecraft's velocity increment difference Bacchus i=0 degrees.

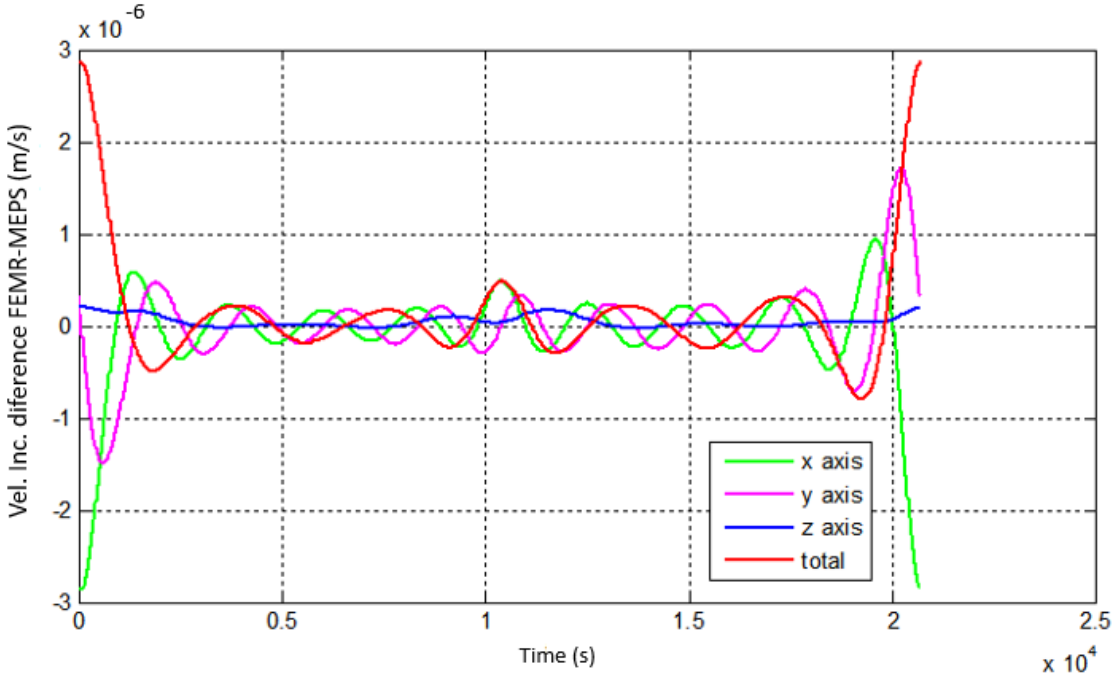

Source: Author.

Figure 6.10 - Spacecraft absolute velocity increment comparison Bacchus i=45 degrees.

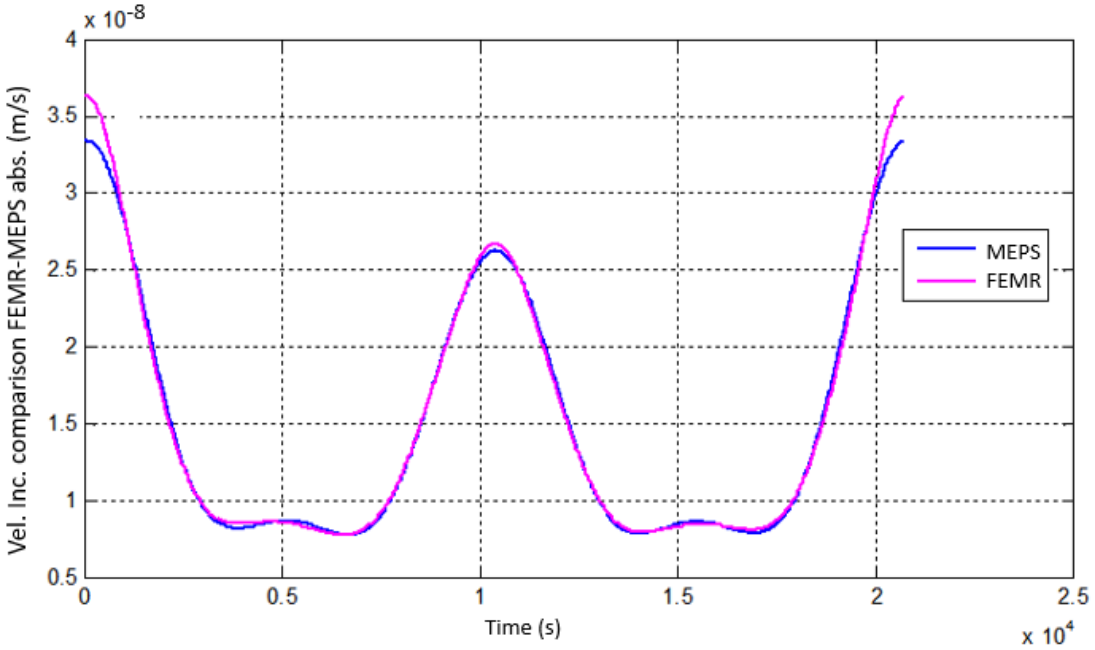

Source: Author

Figure 6.11 - Spacecraft's velocity increment difference Bacchus i=45 degrees.

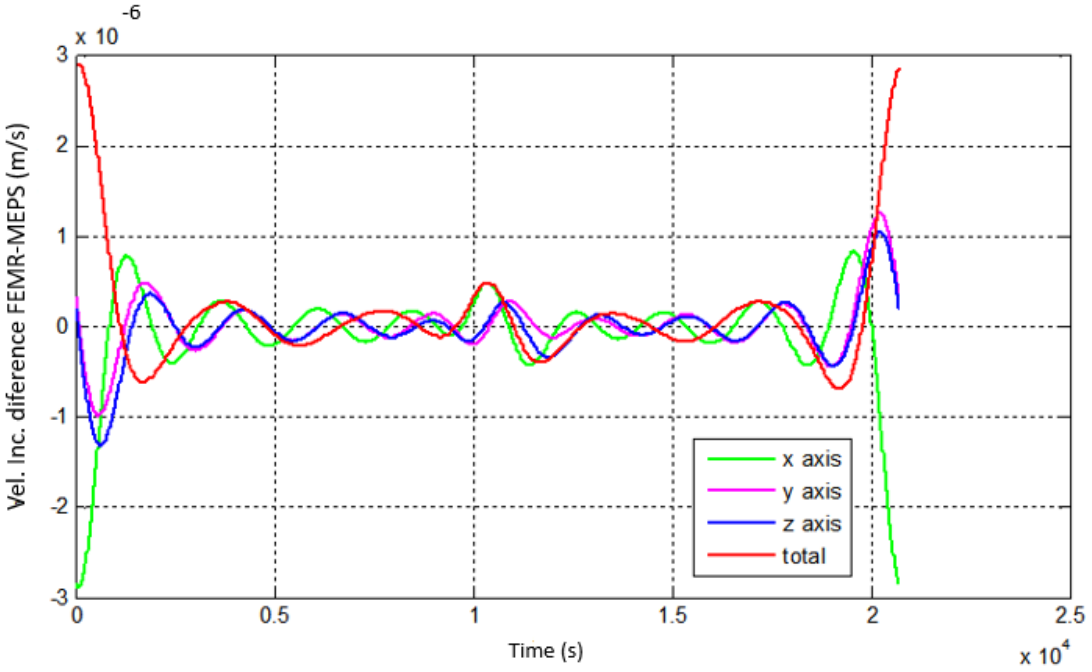

Source: Author.

Figure 6.12 - Spacecraft absolute velocity increment comparison Bacchus i=90 degrees.

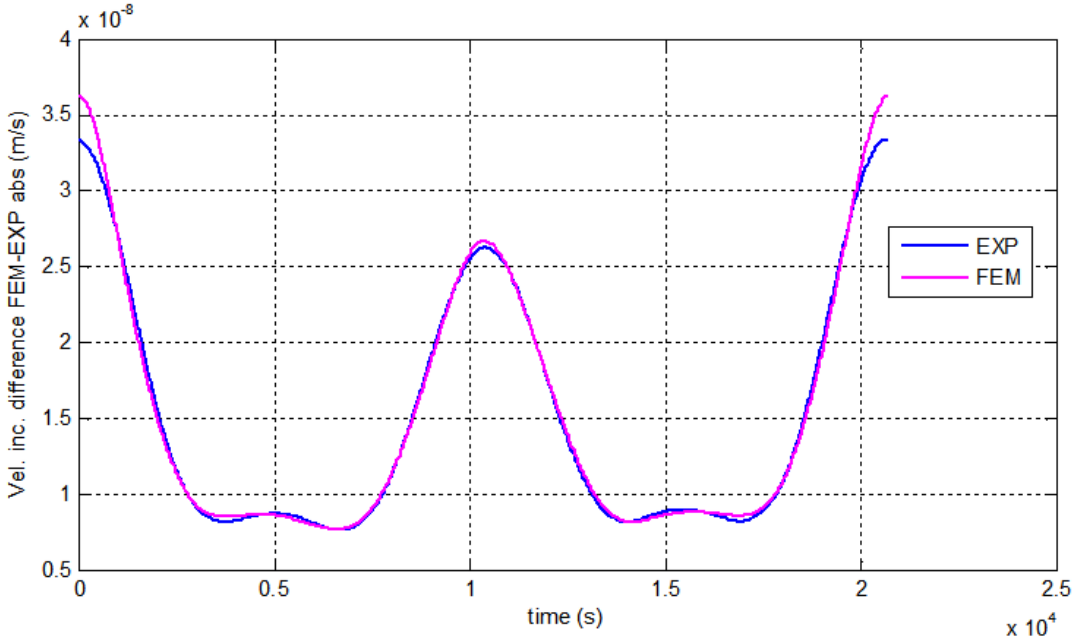

Source: Author.

Figure 6.13 - Spacecraft's velocity increment difference Bacchus i=90 degrees.

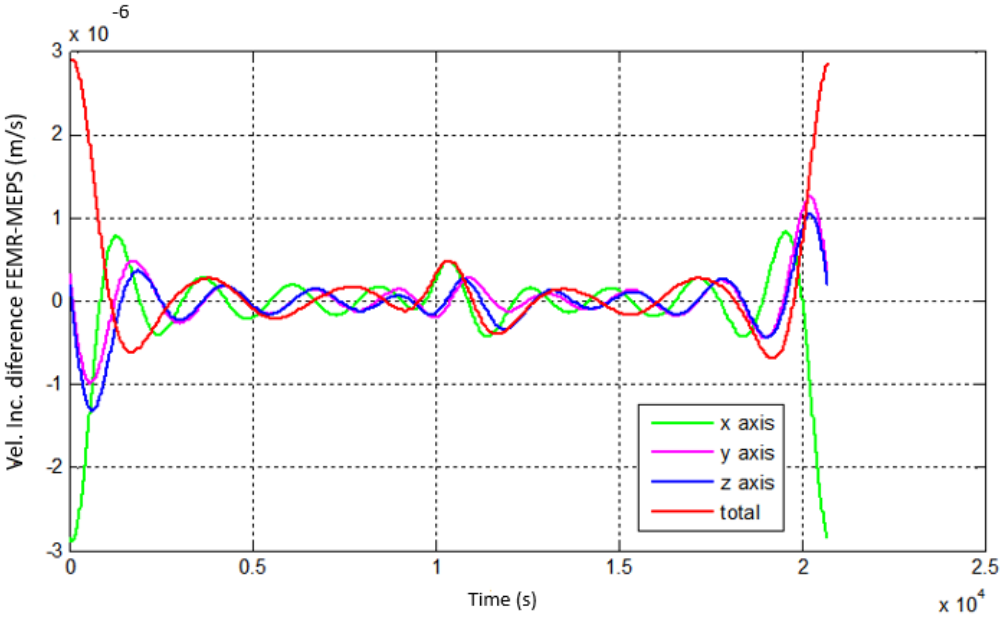

Source: Author.

As we obtained accurate results, when comparing the MEPS, we can say that both methods are equivalent. With this equivalency, if the reader wants to go deeper into trajectories simulations, we recommend looking at the work related to the MEPS (MOTA, 2017).

We perform some extra simulations completing 50 orbits to check how the orbital elements evolve. The absolute velocity increment due to the gravity field, the velocity difference between the FEMR and the MEPS presents itself again. We also show graphs to check how the semi-major axis, the inclination, and the eccentricity vary through time thanks to the gravity field perturbation. Regarding the figures that show the absolute velocity increment (Figure 6.14, Figure 6.15, Figure 6.16), we can see that as the semi-major axis decreases the absolute velocity increment due to the perturbation of the asteroid's gravity field increases. This means that the perturbation gets more intense as the semi-major axis decreases.

Figure 6.14 - Spacecraft absolute velocity increment Comparison - Bacchus a=700 meters/ 50 orbits.

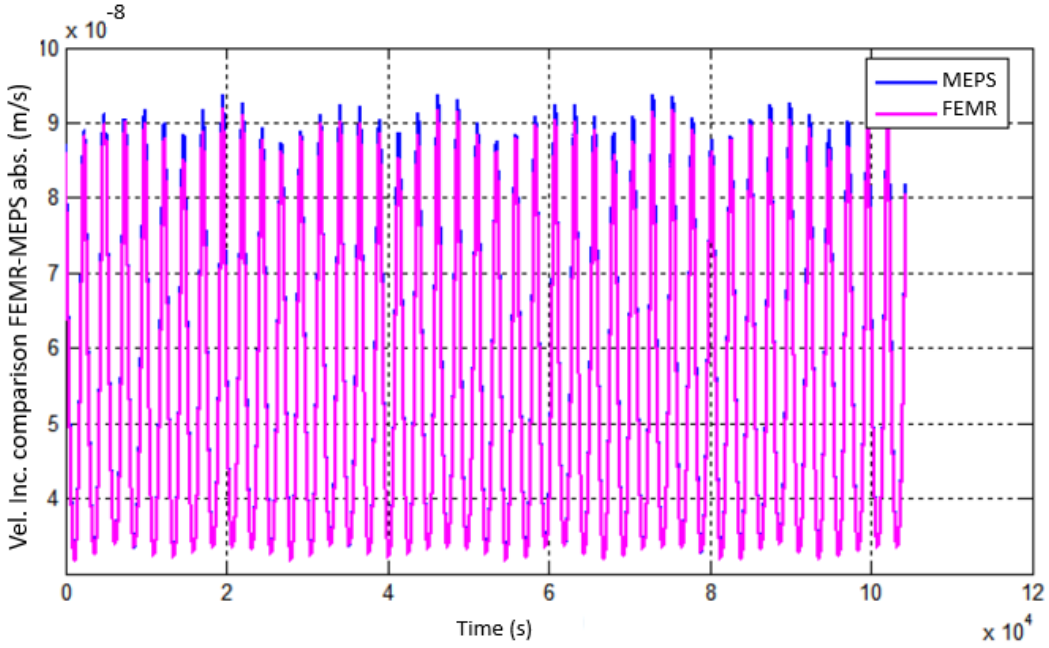

Source: Author.

Figure 6.15 - Spacecraft absolute velocity increment Comparison - Bacchus a=600 meters/ 50 orbits.

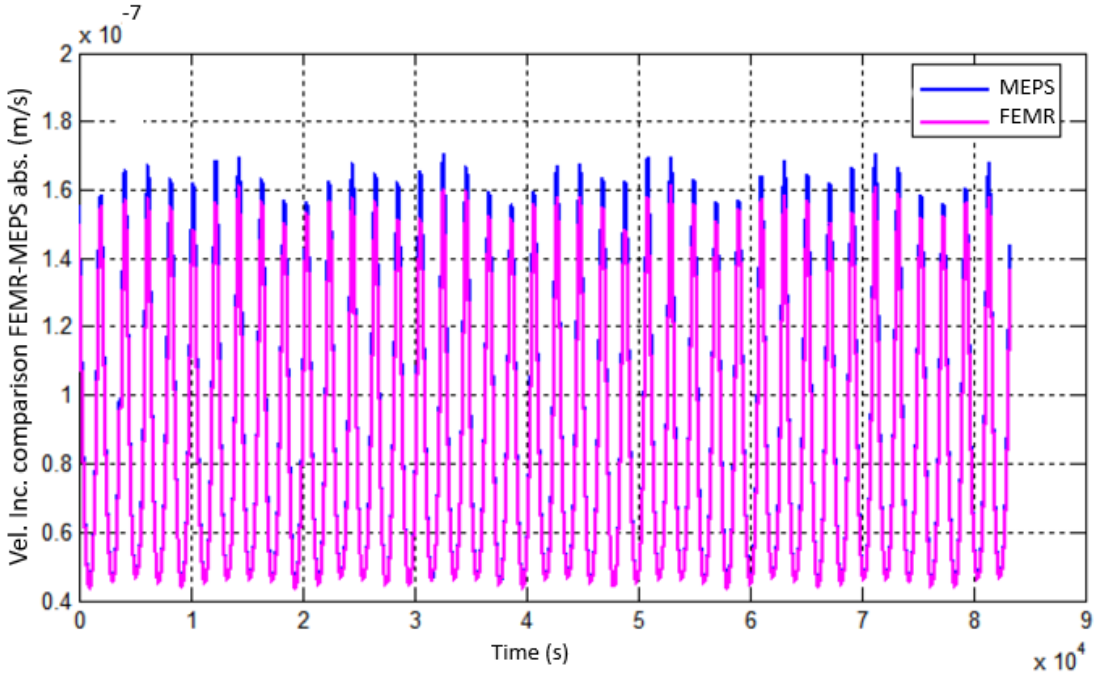

Source: Author.

Figure 6.16 - Spacecraft absolute velocity increment Comparison - Bacchus a=500 meters/ 50 orbits.

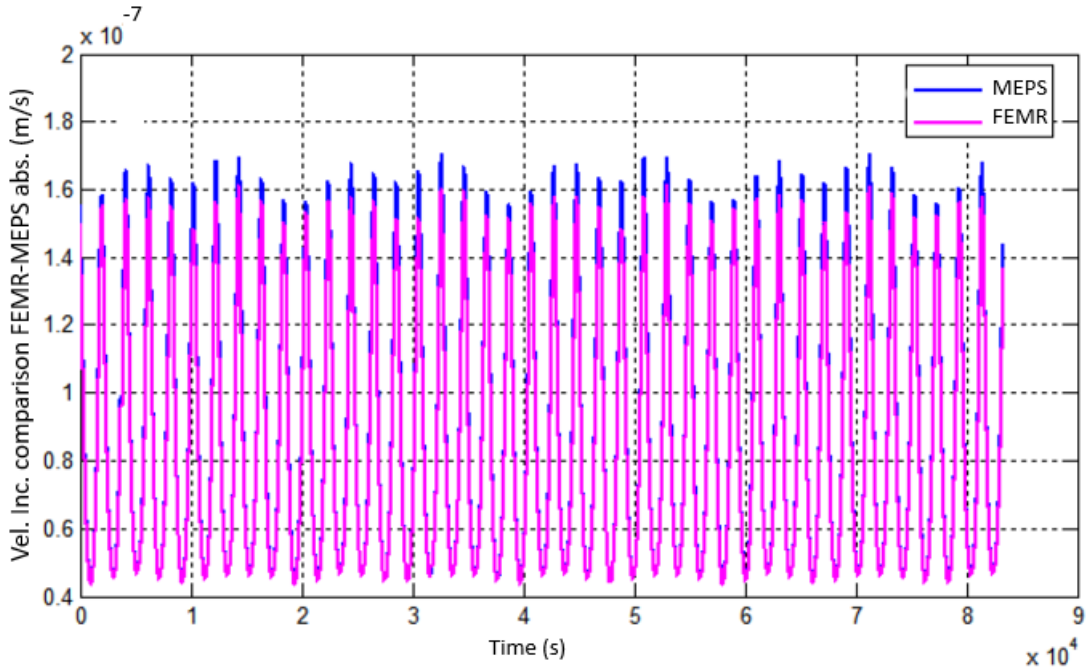

Source: Author.

Regarding the disturbing velocity difference between both methods, Figure 6.14 to Figure 6.19, as the semi-major axis increases the difference between methods also decreases. This can be a clue to the hypothesis that the FEMR is a better option for trajectory simulations that require proximity to the body.

From Figure 6.20 to Figure 6.22 we can see the deviation of one specific orbital element of interest, the semi-major axis. The figures show us that for the chosen values of the semi-major axis of the spacecraft, the variation of this orbital element is not high, keeping the orbit on track with small punctual variations.

Figure 6.17 - Velocity increment difference between FEMR and MEPS - Bacchus a=700 meters/ 50 orbits.

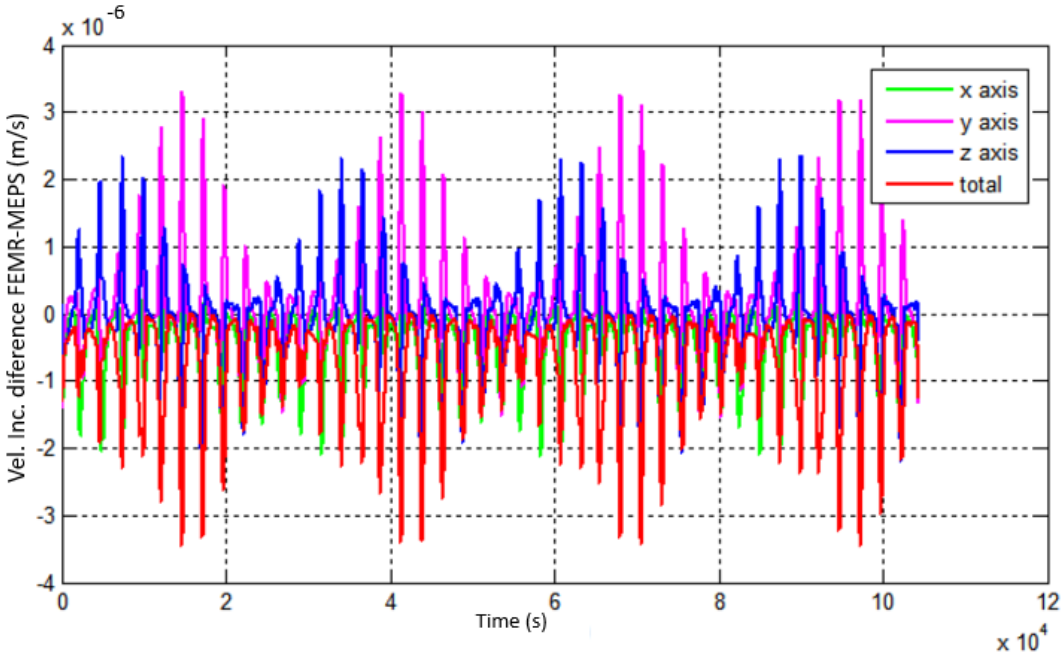

Source: Author.

Figure 6.18 - Velocity increment difference between FEMR and MEPS - Bacchus a=600 meters/ 50 orbits.

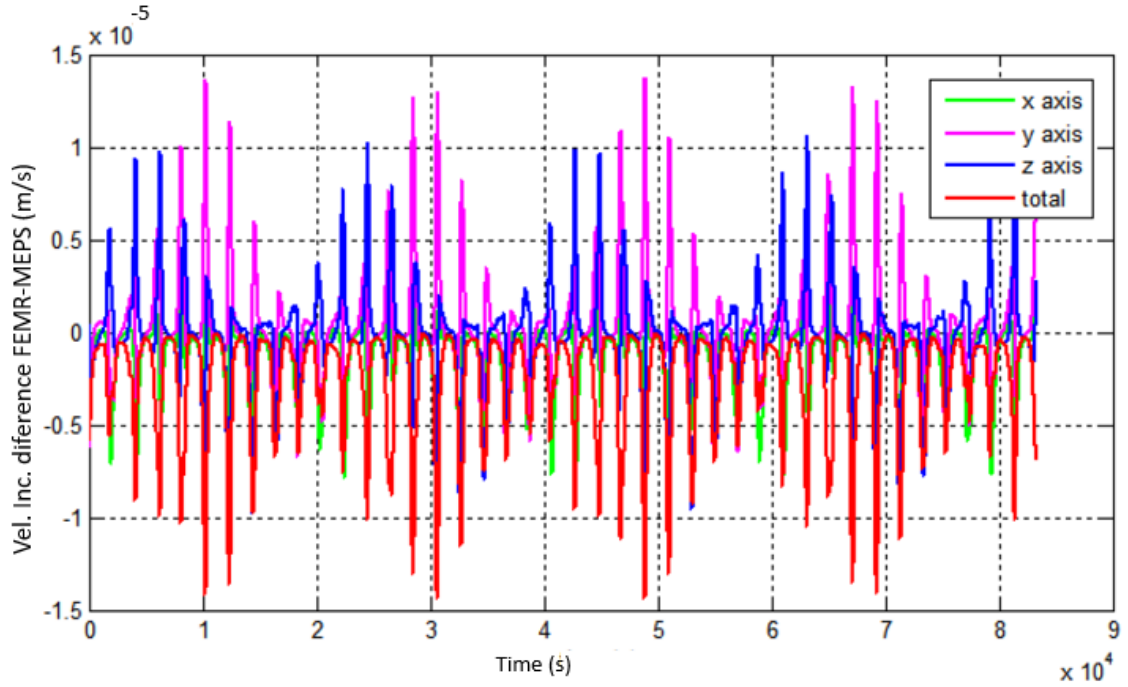

Source: Author.

Figure 6.19 - Velocity increment difference between FEMR and MEPS - Bacchus a=500 meters/ 50 orbits.

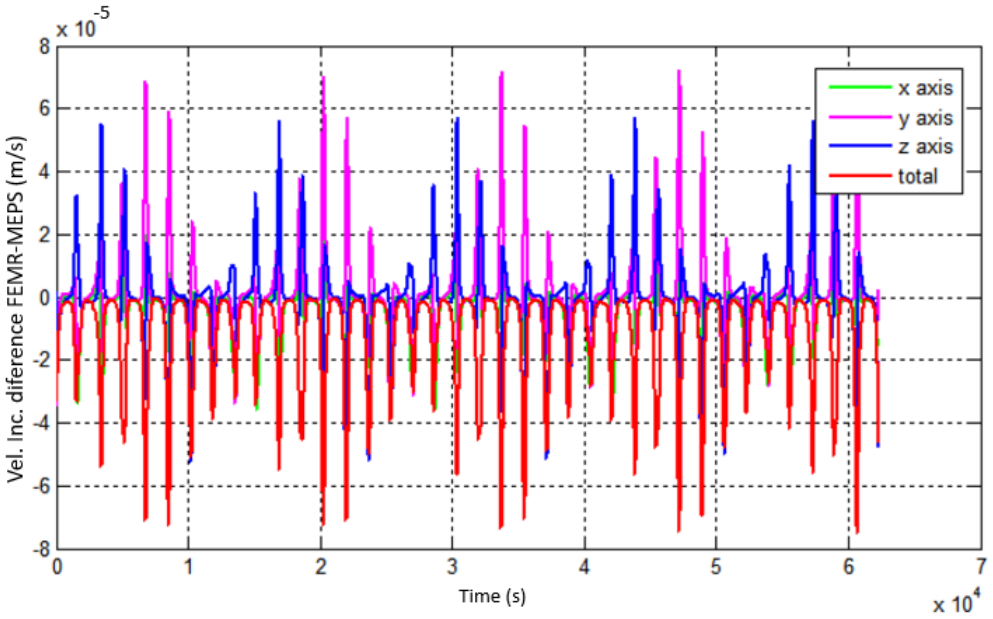

Source: Author.

Figure 6.20 - Semi-major axis variation - Bacchus a=700 meters/ 50 orbits.

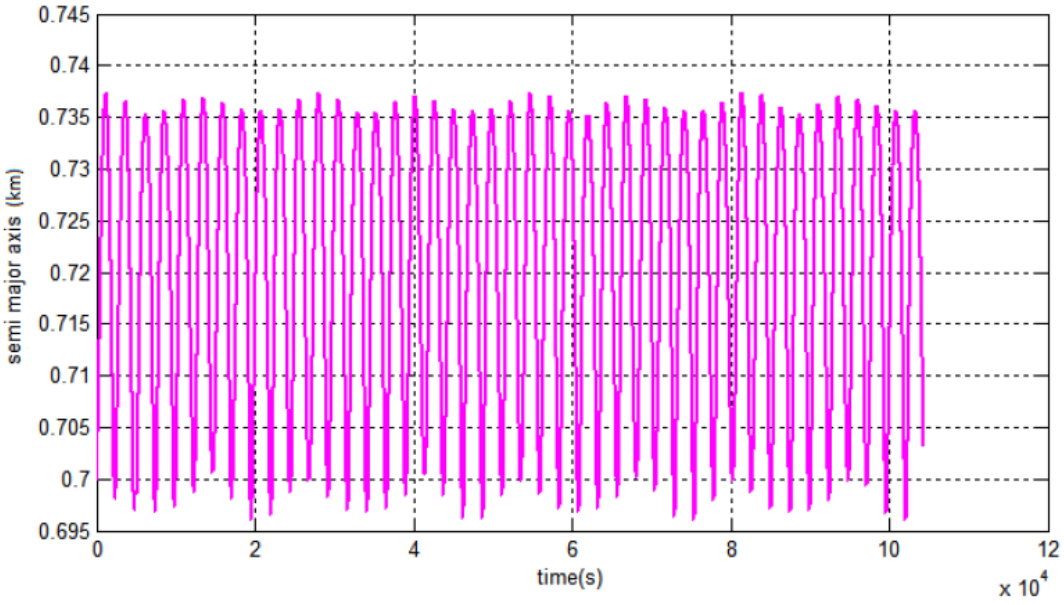

Source: Author.

Figure 6.21 - Semi-major axis variation - Bacchus a=600 meters 50 orbits.

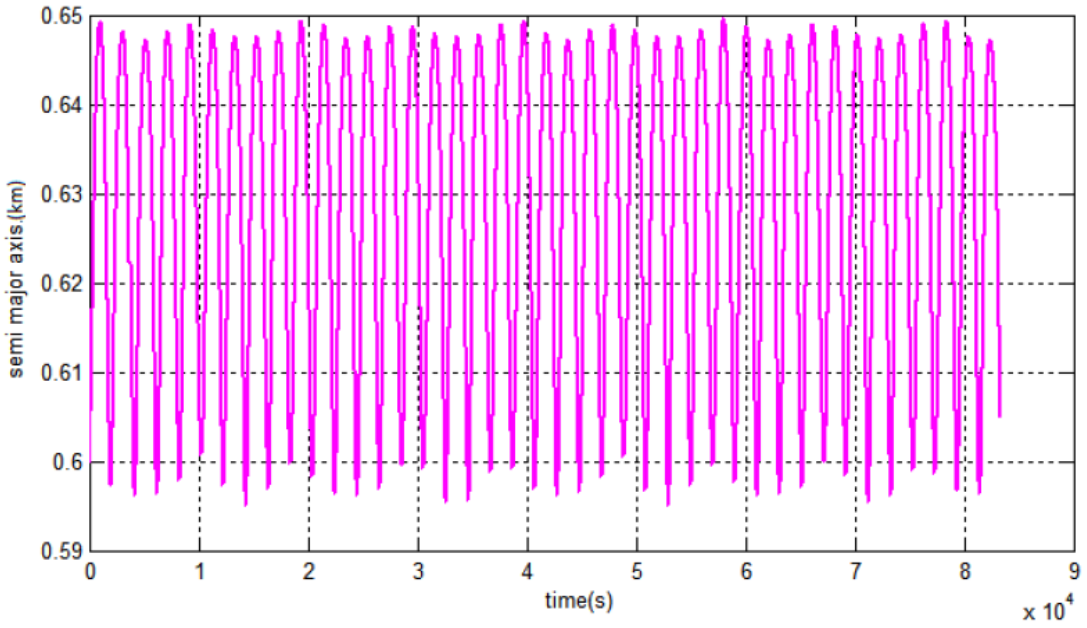

Source: Author.

Figure 6.22 - Semi-major axis variation - Bacchus a=500 meters/ 50 orbits.

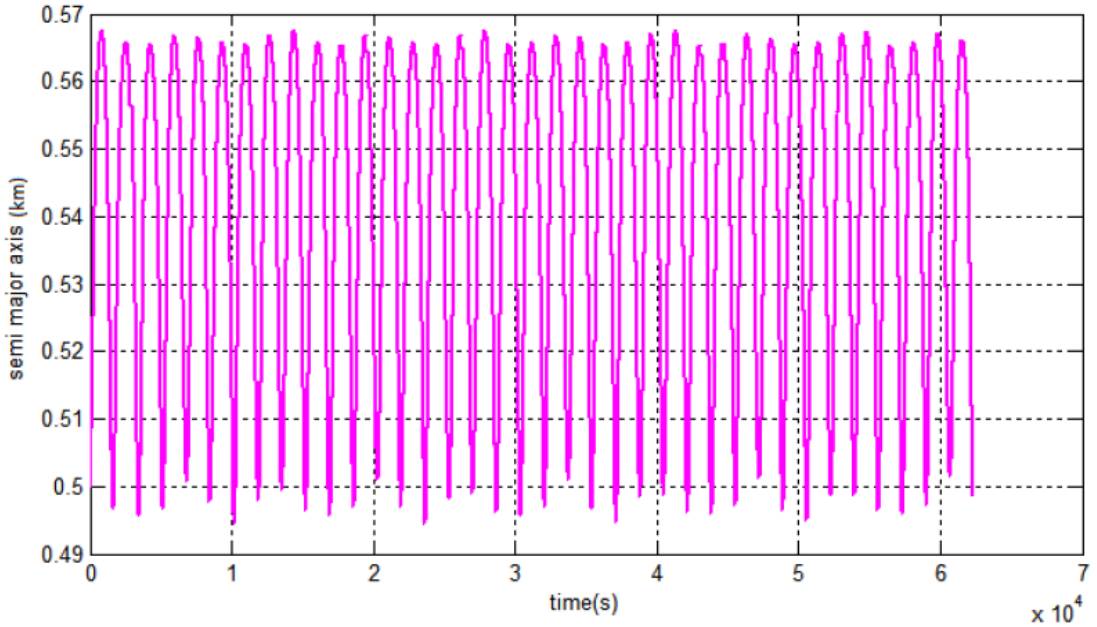

Source: Author.

6.2 Itokawa trajectory simulation

The analysis for Itokawa is analogous to the one made for Bacchus. Table 6.3 shows the fixed orbital parameters. Figure 6.23 shows an example of the spacecraft's orbital path. The finite element model we use for the simulations has 3291 elements, and we set the semi-major axis to 200, 250 and 300 meters.

Table 6.3 - Itokawa spacecraft data.

Eccentricity	0
Inclination (degrees)	0
Right ascension of the ascending node (degrees)	0
Argument of periapsis (degrees)	0
Mean anomaly (degrees)	0

Source: Author.

Figure 6.23 - Spacecraft's orbit around Itokawa.

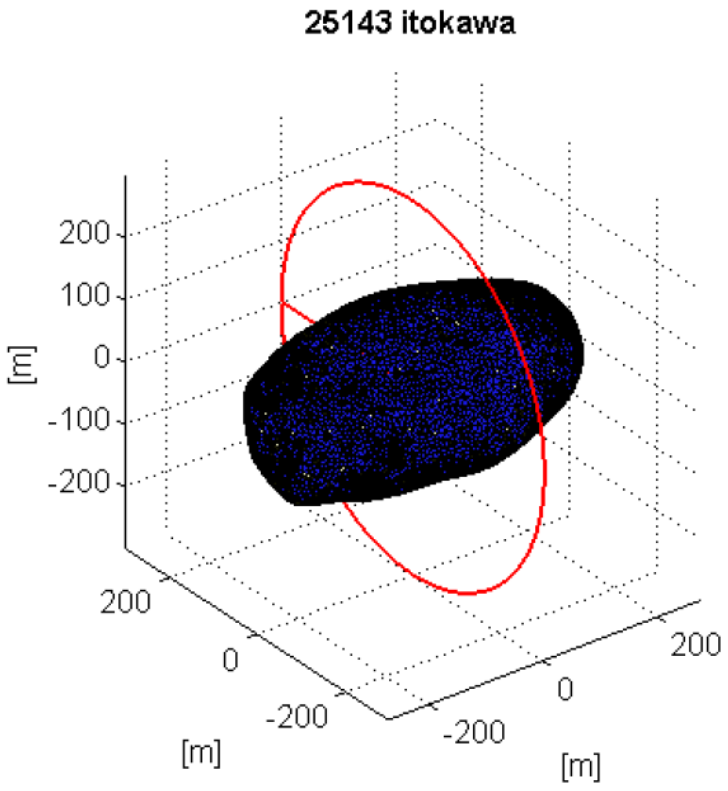

Source: Author.

We, again, analyze the simulation results by comparing the FEMR and the series expansion. From Figure 6.24 to Figure 6.29 we notice that with the decrement of the semi-major axis the difference between both methods increases. As the semi-major axis decreases the spacecraft starts to get closer to the circumscribing sphere. We know from the previous sections from the comparisons with the polyhedron that the FEMR does not diverge on the surface of the asteroid, this fact can be a hint that the FEMR can be a better option for scenarios of greater proximity to the surface of small bodies.

Figure 6.24 - Spacecraft absolute velocity increment comparison - Itokawa 300 meters.

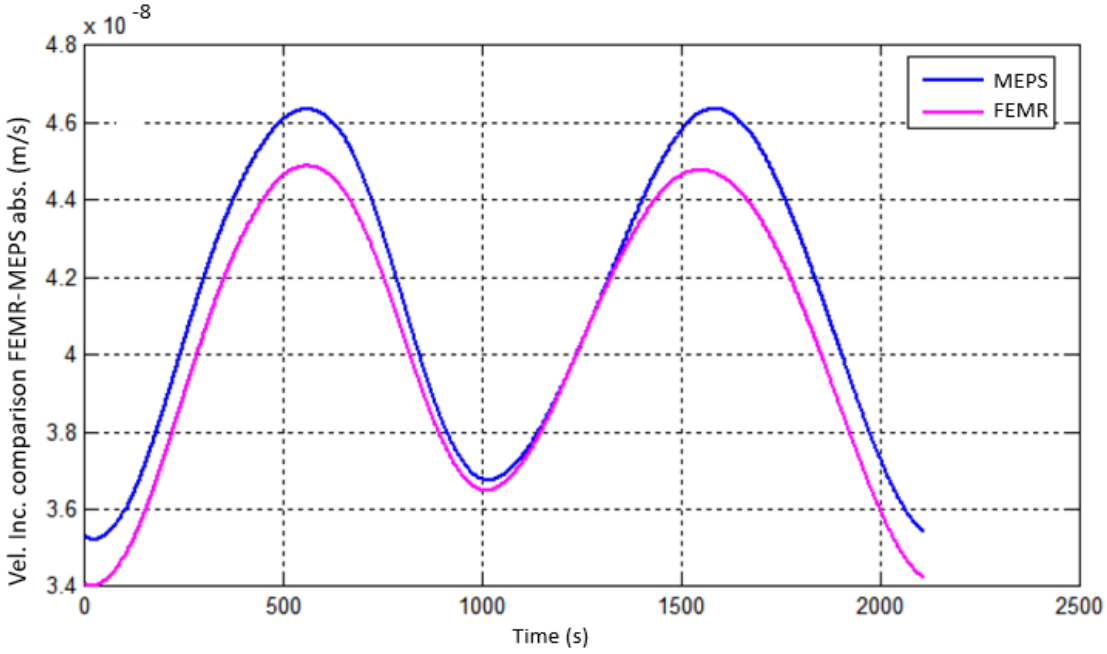

Source: Author.

Figure 6.25 - Spacecraft's velocity increment difference - Itokawa 300 meters.

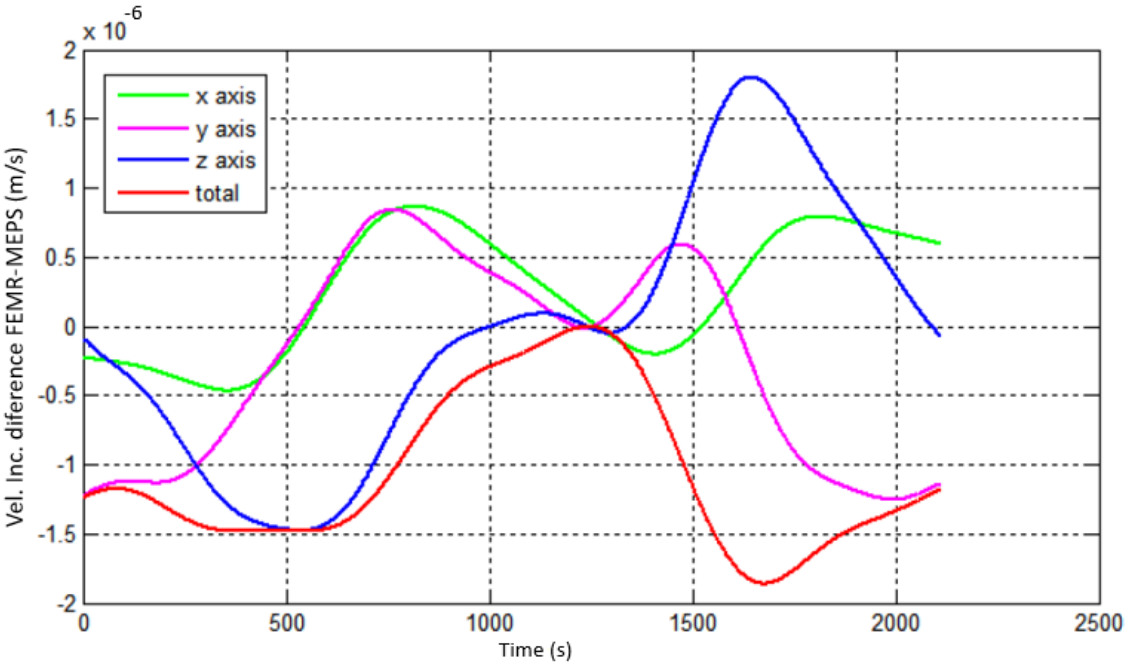

Source: Author.

Figure 6.26 - Spacecraft absolute velocity increment comparison - Itokawa 250 meters.

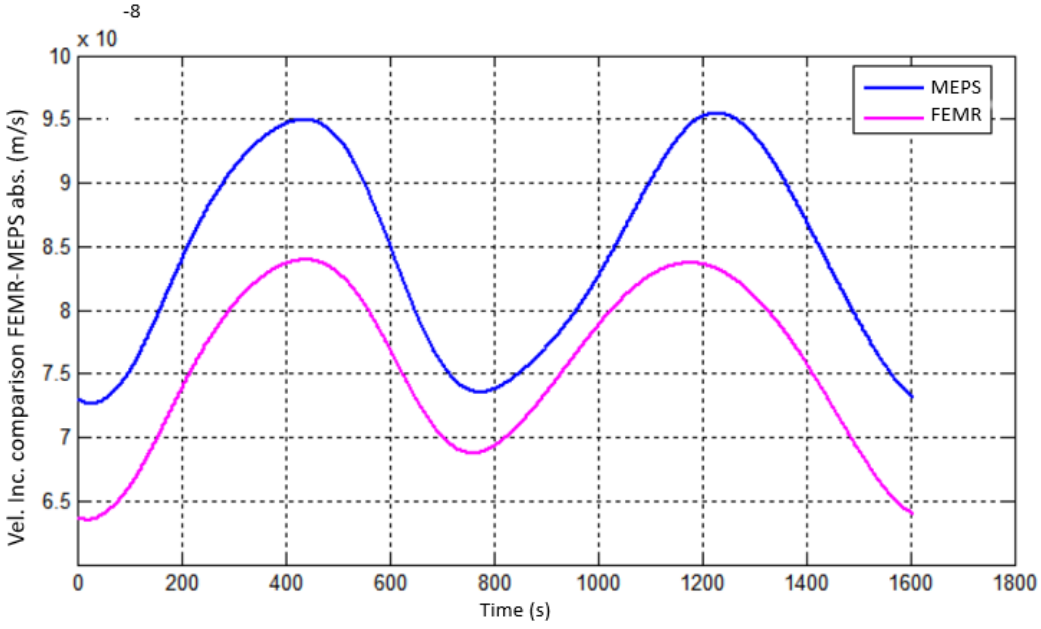

Source: Author.

Figure 6.27 - Spacecraft's velocity increment difference - Itokawa 250 meters.

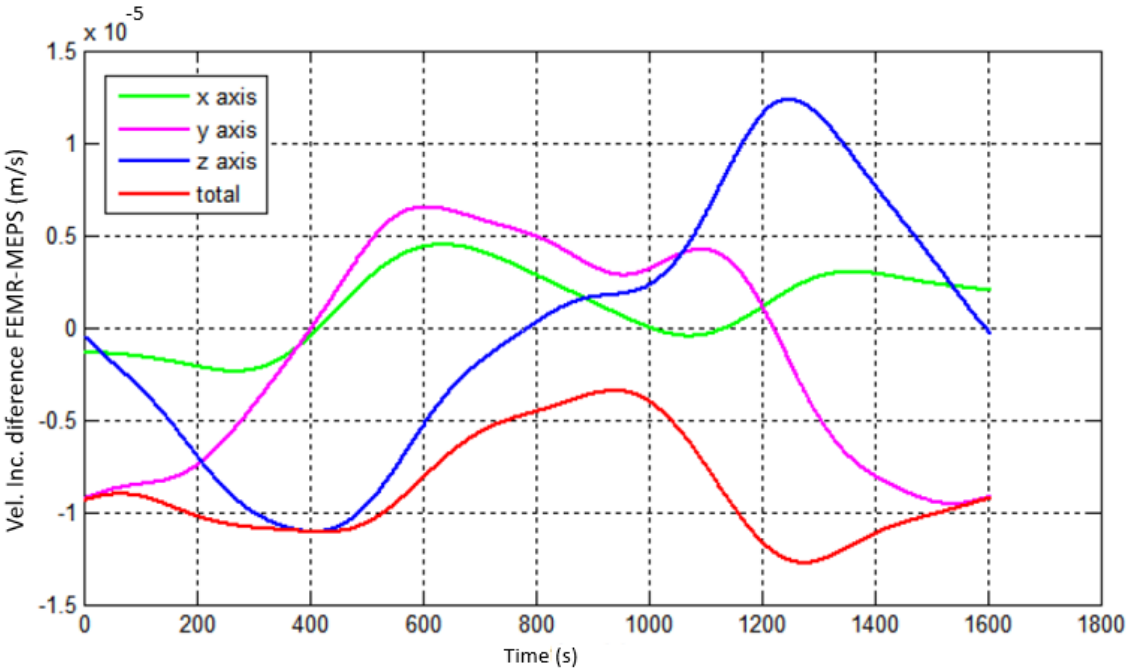

Source: Author.

Figure 6.28 - Spacecraft absolute velocity increment comparison - Itokawa 200 meters.

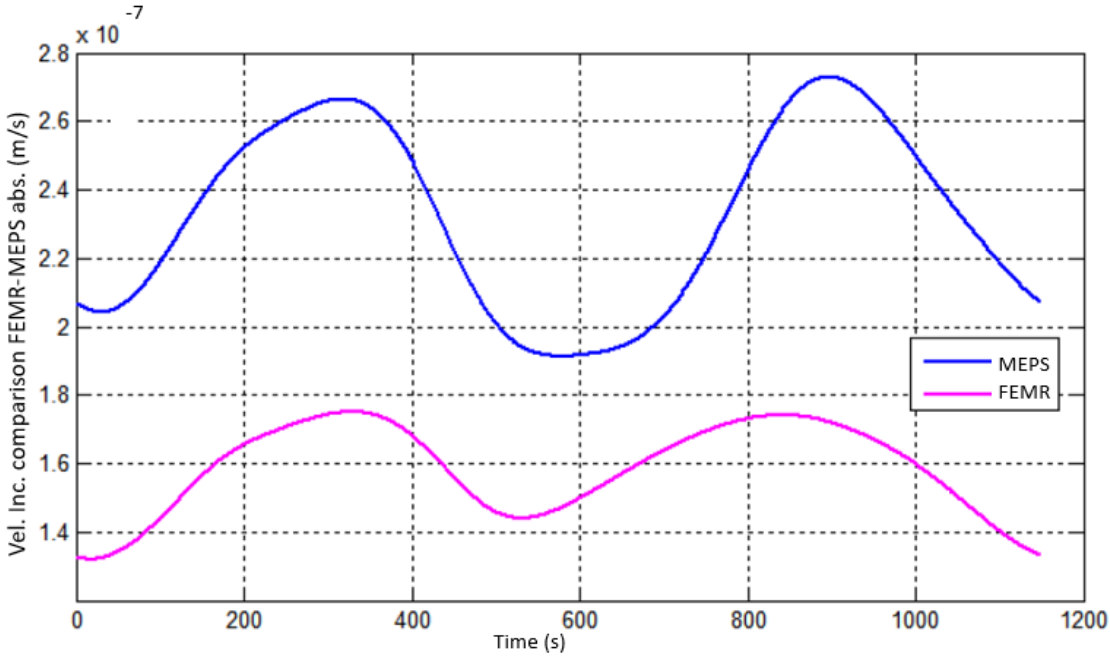

Source: Author.

Figure 6.29 - Spacecraft's velocity increment difference - Itokawa 200 meters.

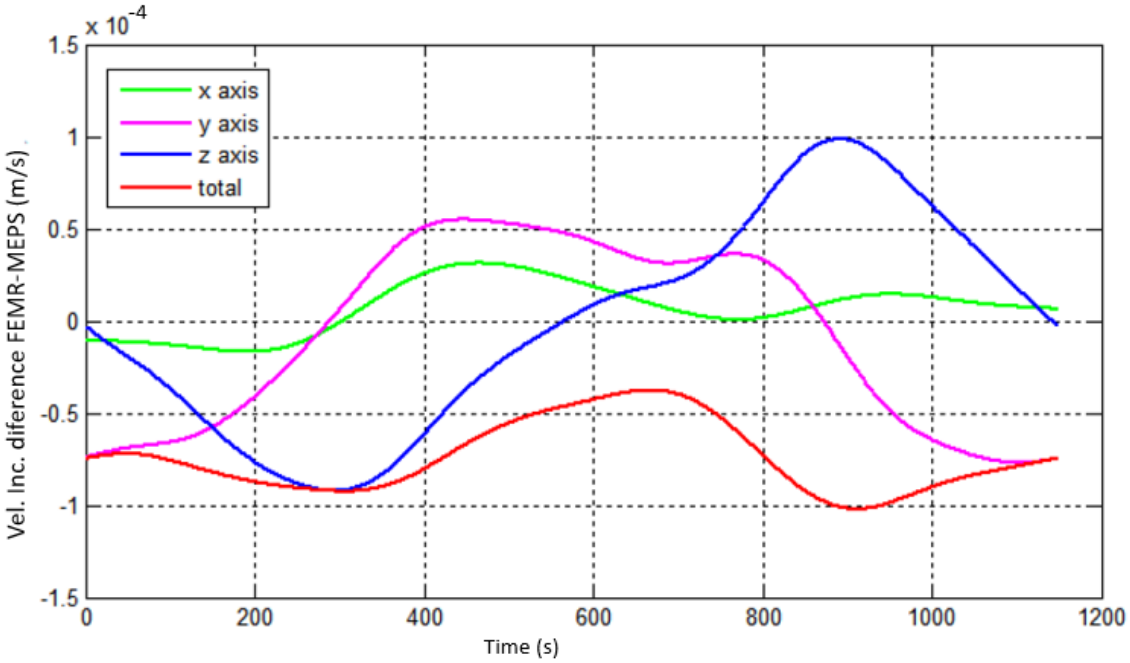

Source: Author.

After this preliminary analysis, we perform more simulations to check the behavior of the spacecraft trajectory when we consider the velocity increment due to the asteroid`s perturbation in the dynamics. We perform a simulation of 50 orbits to show the evolution of the orbit as the spacecraft approaches Itokawa. For this asteroid, the results were more interesting and the differences more intense.

Figure 6.30 to Figure 6.35 presents the comparisons of the increment velocity due to the gravity field for the approaches of interest considering a semi-major axis of 300, 250 and 200 meters.

In Figure 6.30, Figure 6.31 and Figure 6.32, we can see that the magnitude of the velocity increment due to the gravity field perturbation increases as the semi-major axis decreases. Looking at each figure individually, we see the same comportment: the velocity increment increases until 0.5 seconds and then it starts to get lower until it gets closer to zero in the final moments of the simulation. This is a clue that the spacecraft gets close to the asteroid, and then the gravity field of Itokawa starts to degenerate the orbit to a point that the spacecraft moves away from the body.

From Figure 6.33 to Figure 6.35 we see that the magnitude of the difference between methods increases with the decrement of the semi-major axis per simulation.

Finally, Figure 6.36 to Figure 6.38 show the evolution of the semi-major axis for Itokawa's simulations. For the simulation considering an initial semi-major axis of 300 meters the evolution of the semi-major axis evolves more smoothly, and the value of the semi-major axis increases considerably. For the other initial semi-major axis, we see that the semi-major evolves in a more abrupt way, and as the initial semi-major axis decreases the final value of the spacecraft's semi-major axis increases, reaching a maximum of 2.5 km for the last simulation.

Figure 6.30 - Spacecraft absolute velocity increment comparison - Itokawa 300 meters/ 50 orbits.

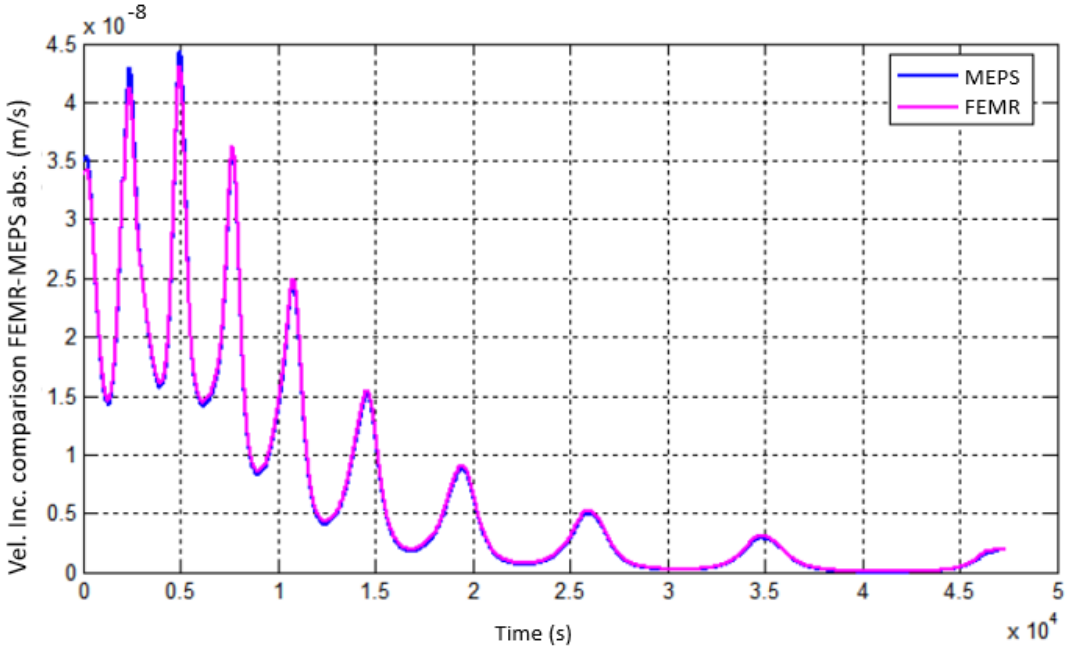

Source: Author.

Figure 6.31 - Spacecraft absolute velocity increment comparison - Itokawa 250 meters/ 50 orbits.

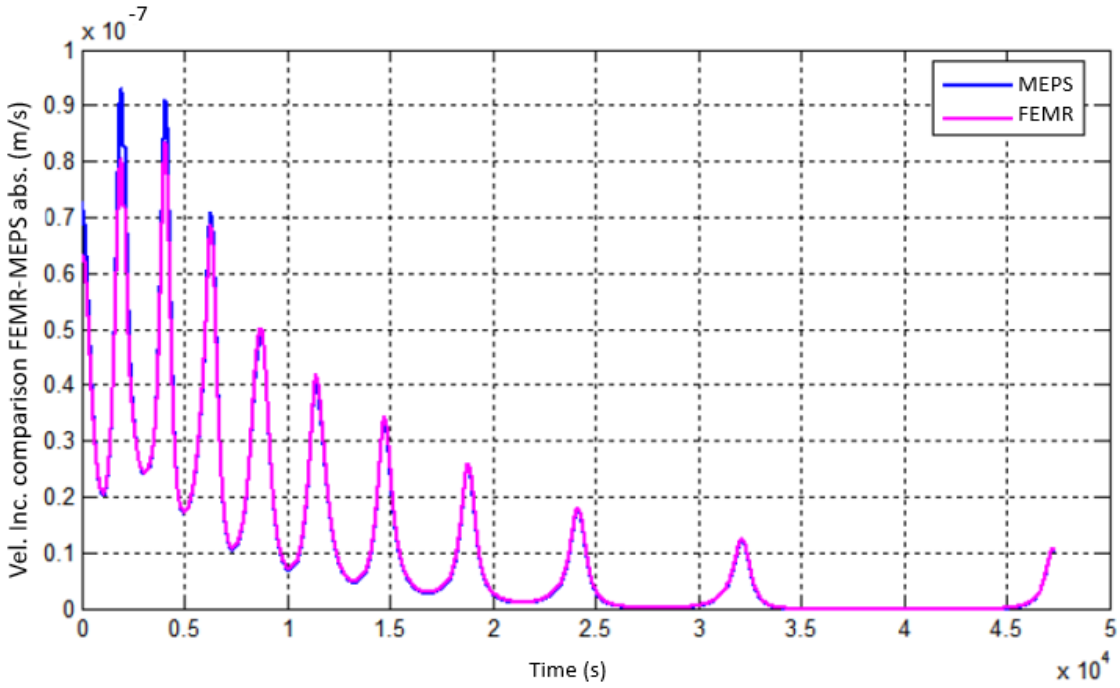

Source: Author.

Figure 6.32 - Spacecraft absolute velocity increment comparison - Itokawa 200 meters/ 50 orbits.

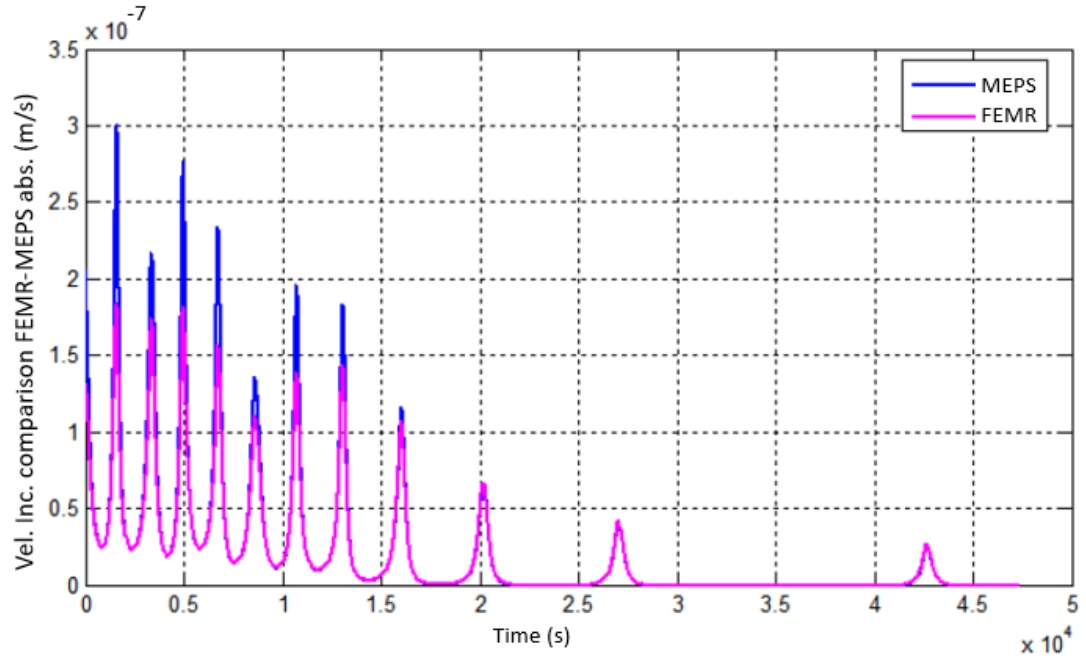

Source: Author.

Figure 6.33 - Velocity increment difference between FEMR and MEPS - Itokawa a=300 meters/ 50 orbits.

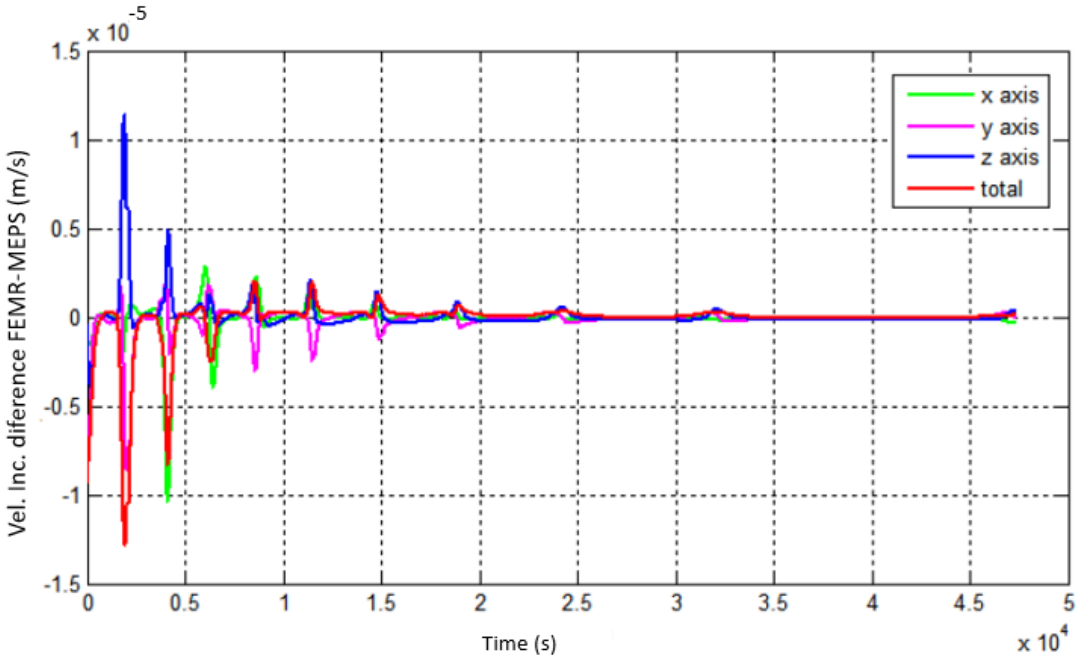

Source: Author.

Figure 6.34 - Velocity increment difference between FEMR and MEPS - Itokawa a=250 meters/ 50 orbits.

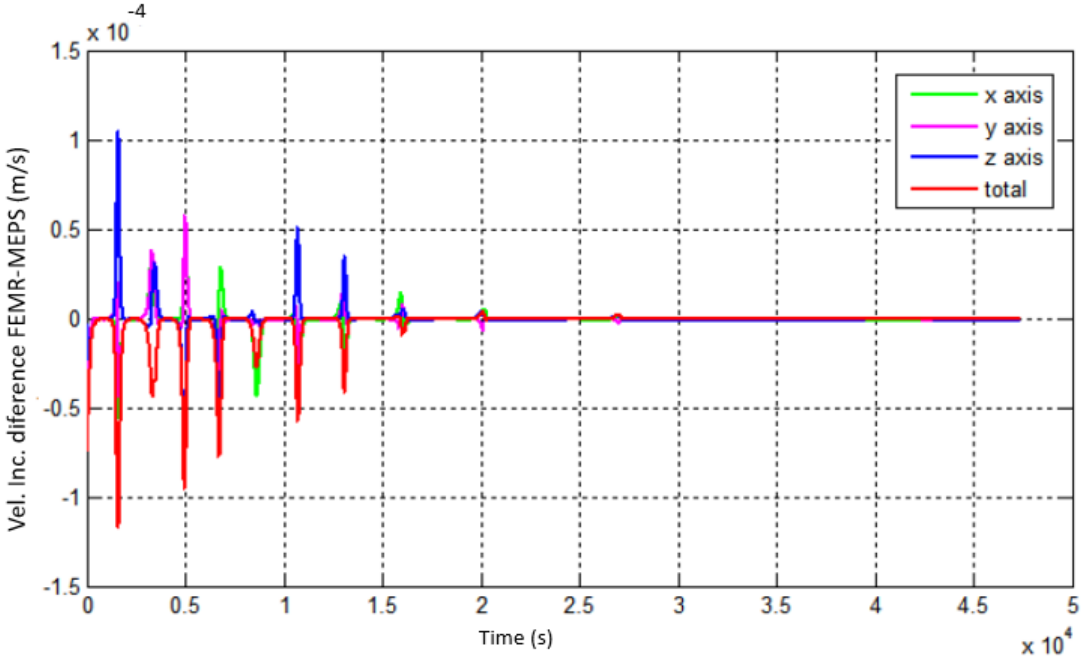

Source: Author.

Figure 6.35 - Velocity increment difference between FEMR and MEPS - Itokawa a=200 meters/ 50 orbits.

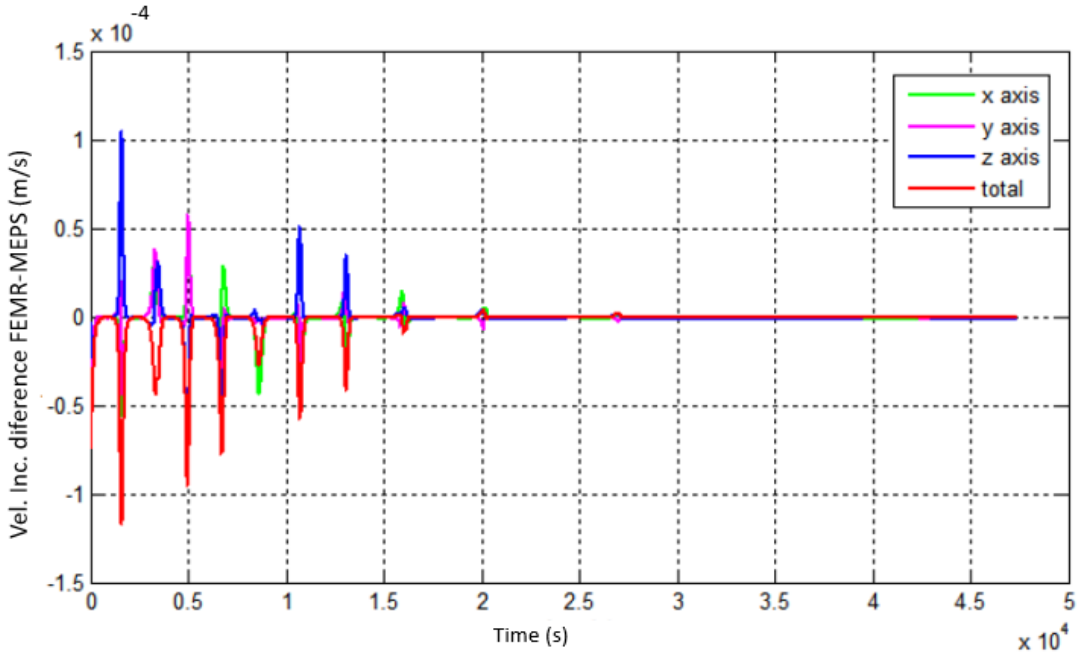

Source: Author.

Figure 6.36 - Semi-major axis variation - Itokawa a=300 meters/ 50 orbits.

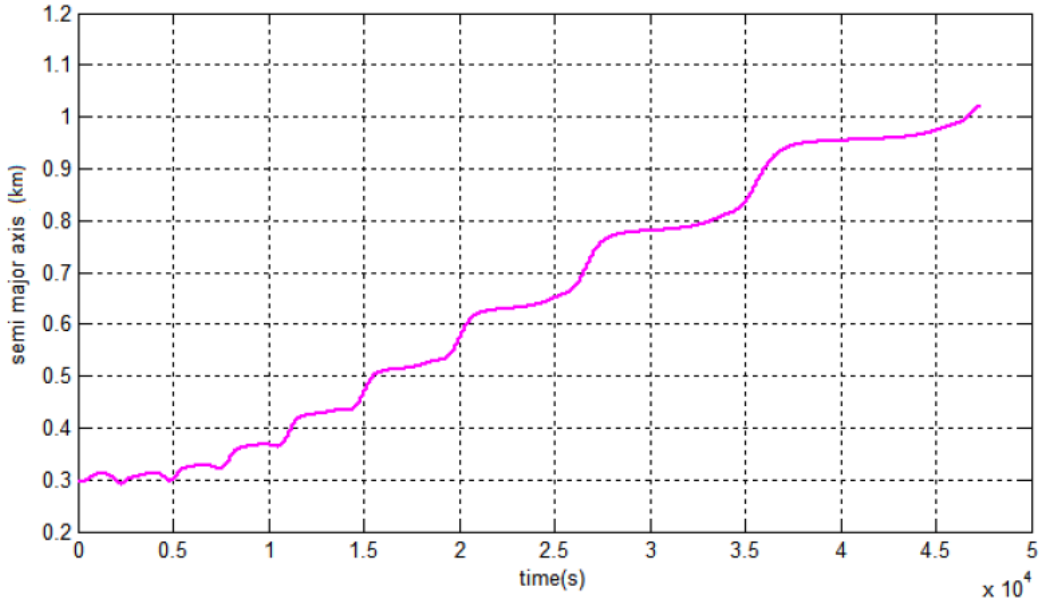

Source: Author.

Figure 6.37 - Semi-major axis variation - Itokawa a=250 meters 50 orbits.

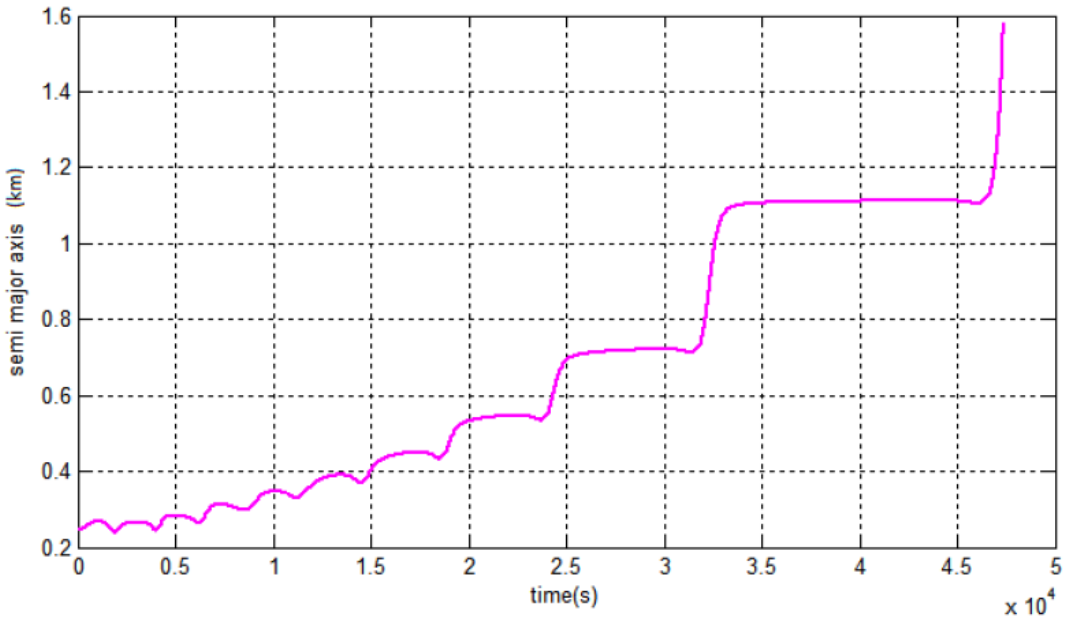

Source: Author.

Figure 6.38 - Semi-major axis variation - Itokawa a=250 meters 50 orbits.

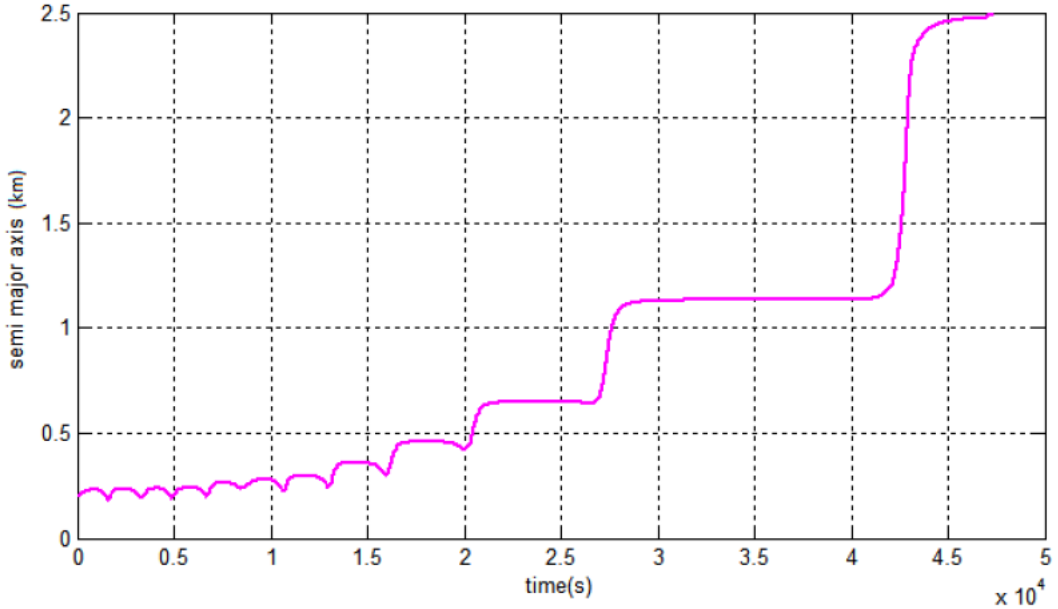

Source: Author.

6.3 Bennu trajectory simulation

For the final trajectory simulations, the asteroid chosen was Bennu. The FEMR model has 20393 elements, and the fixed orbital parameters are presented on Table 6.4. We vary the semi-major axis again, the values are 350 and 450 meters. Figure 6.39 shows the vehicle orbit around the spacecraft.

Table 6.4 - Bennu spacecraft data.

Eccentricity	0
Inclination (degrees)	0
Right ascension of the ascending node (degrees)	0
Argument of periapsis (degrees)	0
Mean anomaly (degrees)	0

Source: Author.

Figure 6.39 - Spacecraft's orbit trajectory around Bennu.

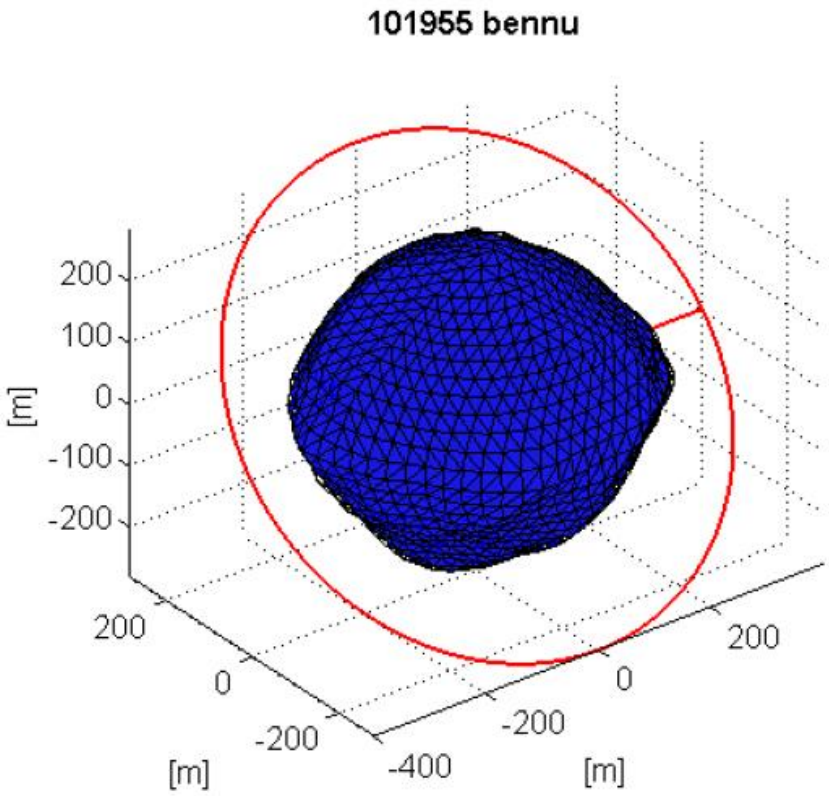

Source: Author.

Figure 6.40, Figure 6.42 and Figure 6.44 presents the absolute velocity increment due to the gravity field perturbation for the FEMR and the series expansion. The velocity increment gets lower as the semi-major axis increases in the different simulations.

For the velocity increment difference between the compared methods (Figure 6.41, Figure 6.43 and Figure 6.45) the magnitude of the difference is still low. However, like for the other asteroids the difference increases as the semi-major axis decreases.

Figure 6.40 - Spacecraft absolute velocity increment comparison - Bennu a=450 meters.

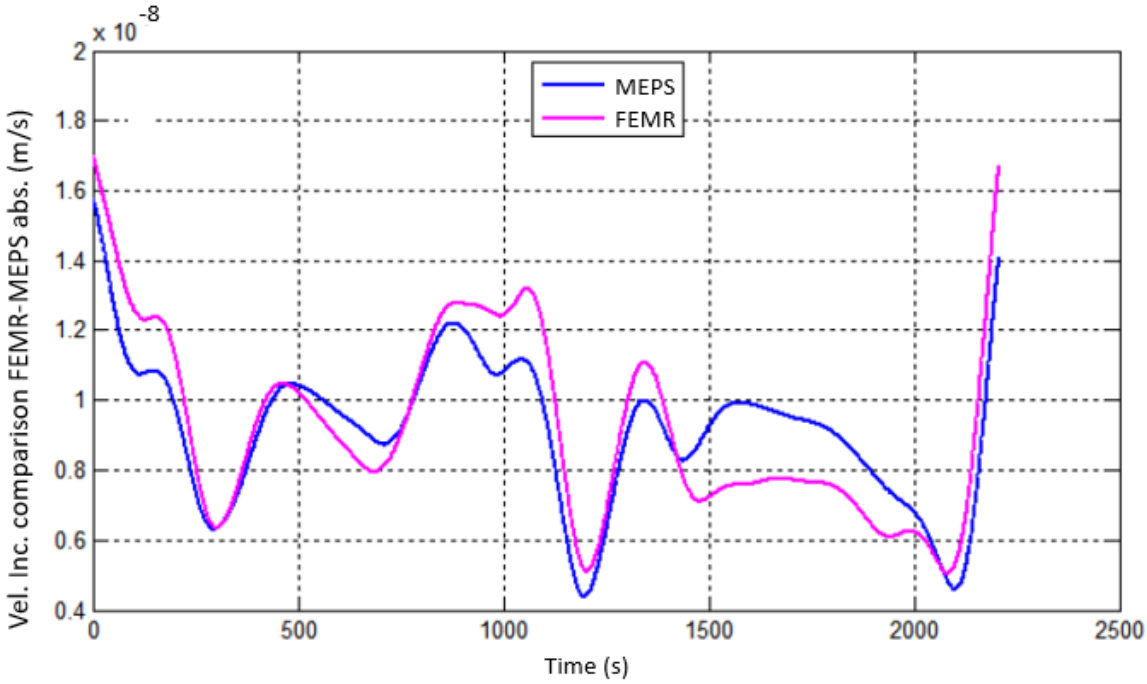

Source: Author.

Figure 6.41 - Spacecraft's velocity increment difference - Bennu a=450 meters.

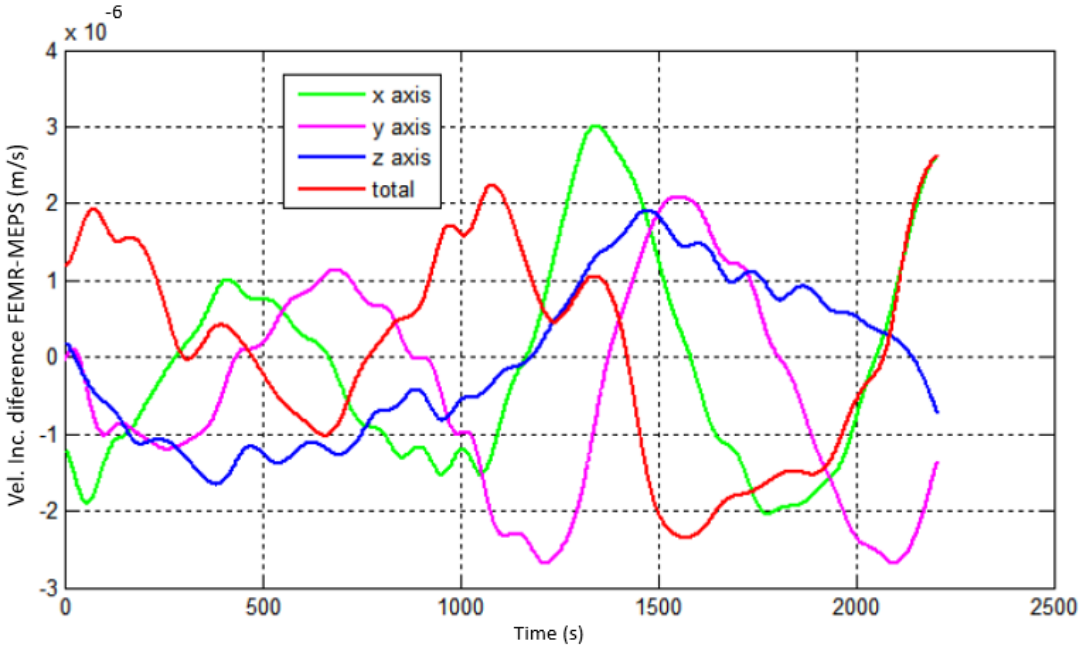

Source: Author.

Figure 6.42 - Spacecraft absolute velocity increment comparison - Bennu a=350 meters.

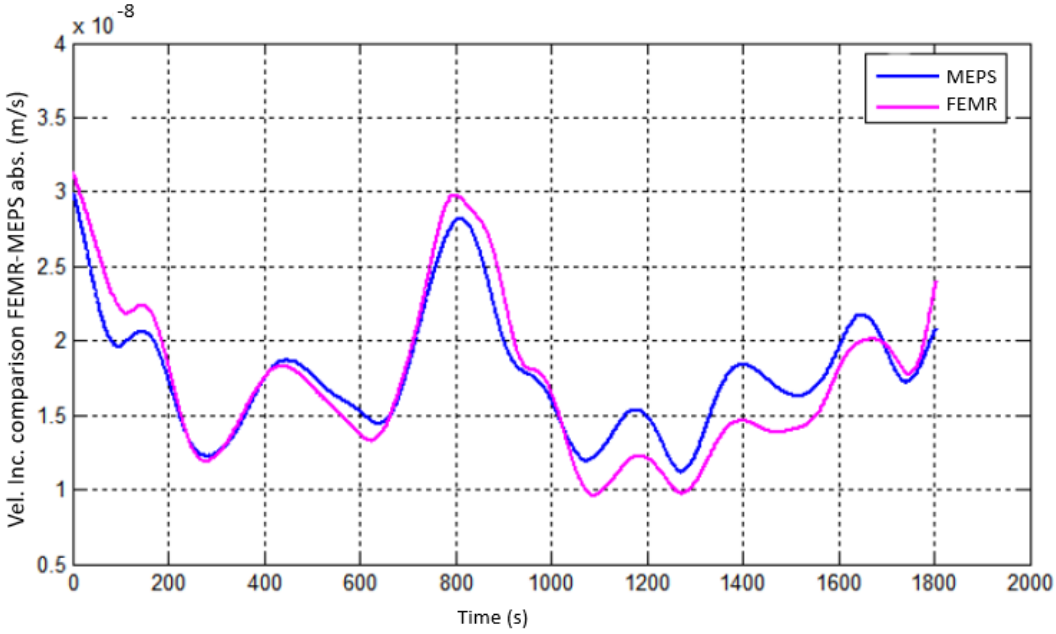

Source: Author.

Figure 6.43 - Spacecraft's velocity increment difference - Bennu a=350 meters.

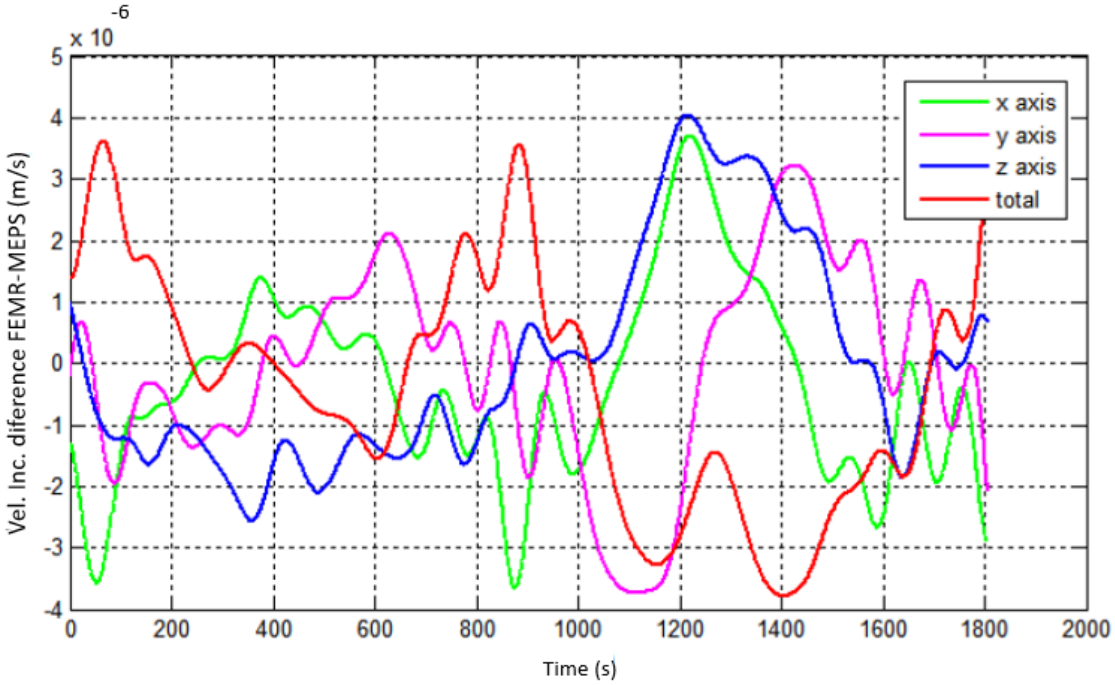

Source: Author.

Figure 6.44 - Spacecraft absolute velocity increment comparison - Bennu a=300 meters.

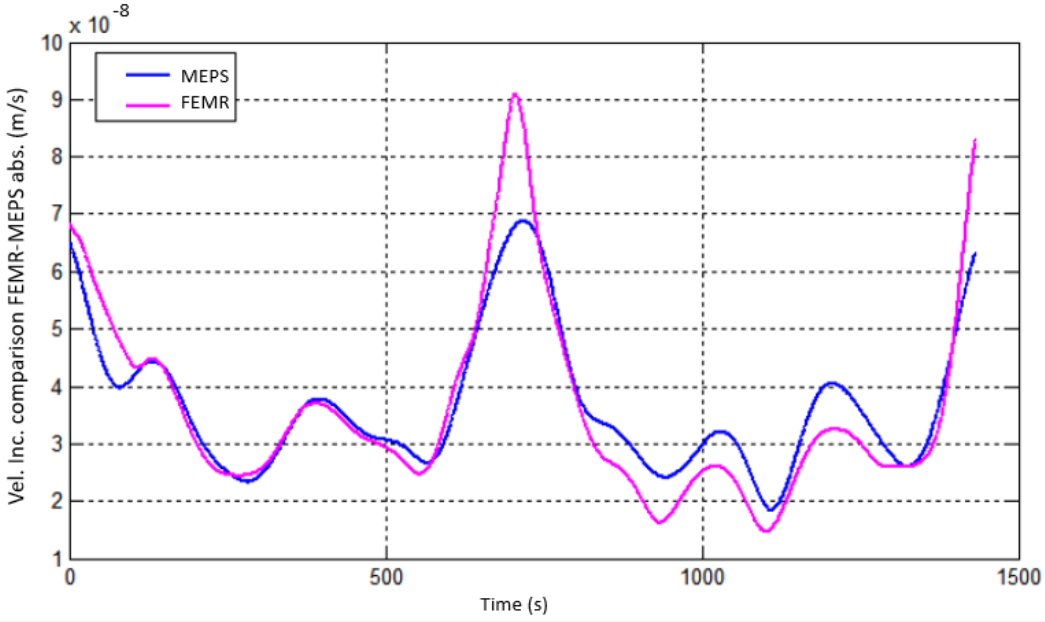

Source: Author.

Figure 6.45 - Spacecraft's velocity increment difference - Bennu a=300 meters.

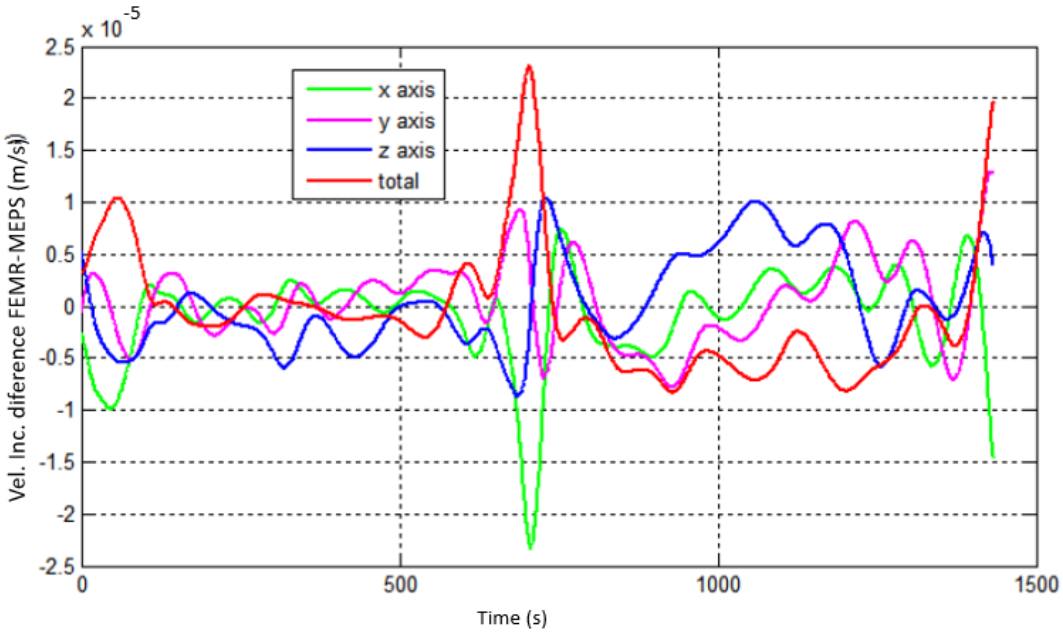

Source: Author.

For Bennu's last simulations when we consider the velocity increment due to the gravity field disturbance inserted in the dynamics of the spacecraft to analyze the orbital trajectory evolution, we have a particular case. When we consider the semi-major axis of 350 meters the spacecraft crashes on Bennu's surface. For this reason, the only simulation we show here is the one considering a semi-major axis of 400 meters.

For the first and only simulation considering the semi-major axis of 400 meters, the absolute velocity increment keeps a magnitude of 10^{-8}, Figure 6.46. The difference between both methods remains low, the magnitude is 10^{-6} as we can see from Figure 6.47. Still, for this simulation Figure 6.48 shows the variation of the semi-major axis that increases smoothly at a constant rate.

Figure 6.46 - Spacecraft absolute velocity increment comparison - Bennu a=450 meters/ 50 orbits.

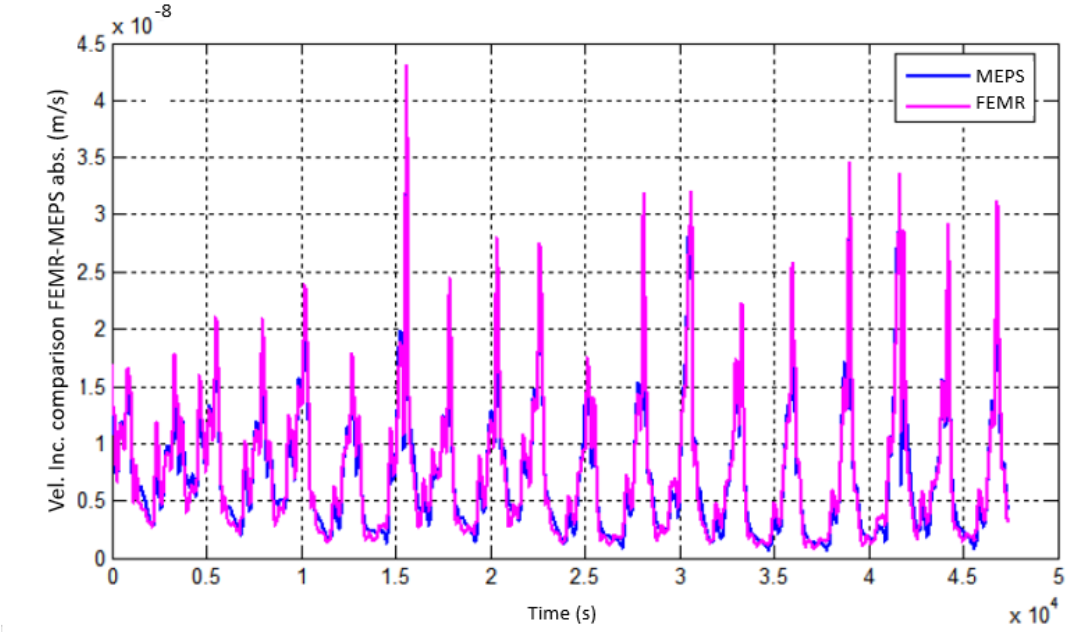

Source: Author.

Figure 6.47 - Velocity increment difference between FEMR and MEPS - Bennu a=450 meters/ 50 orbits.

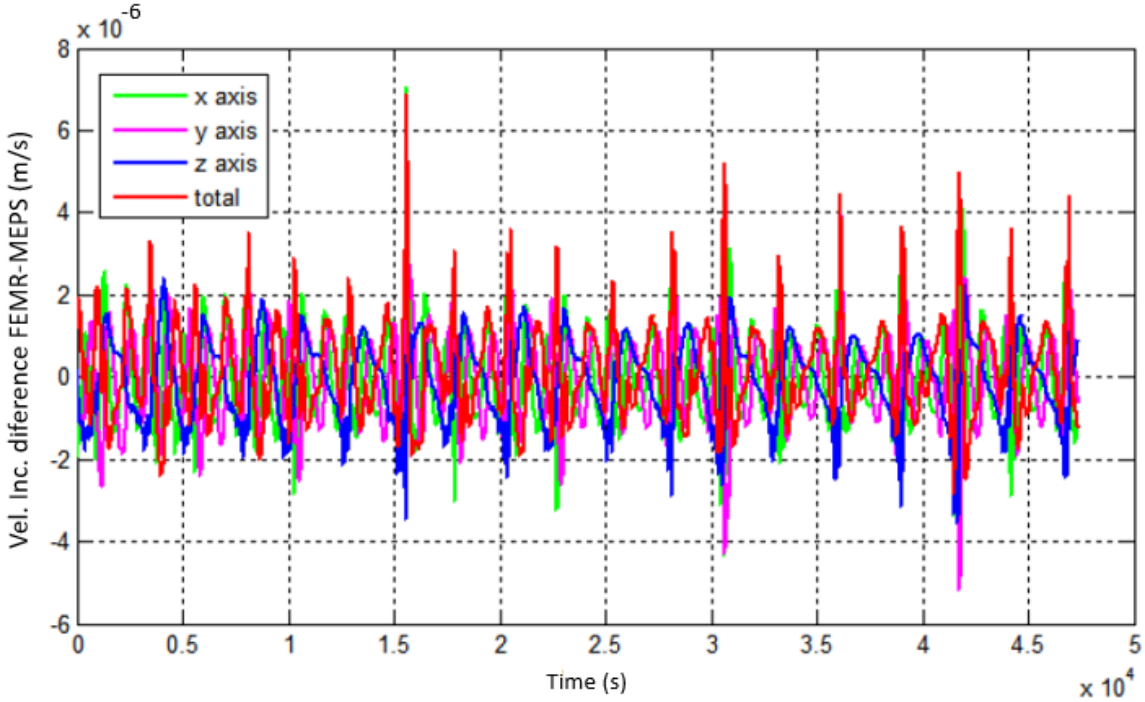

Source: Author.

Figure 6.48 - Semi-major axis variation - Bennu a=400 meters/ 50 orbits.

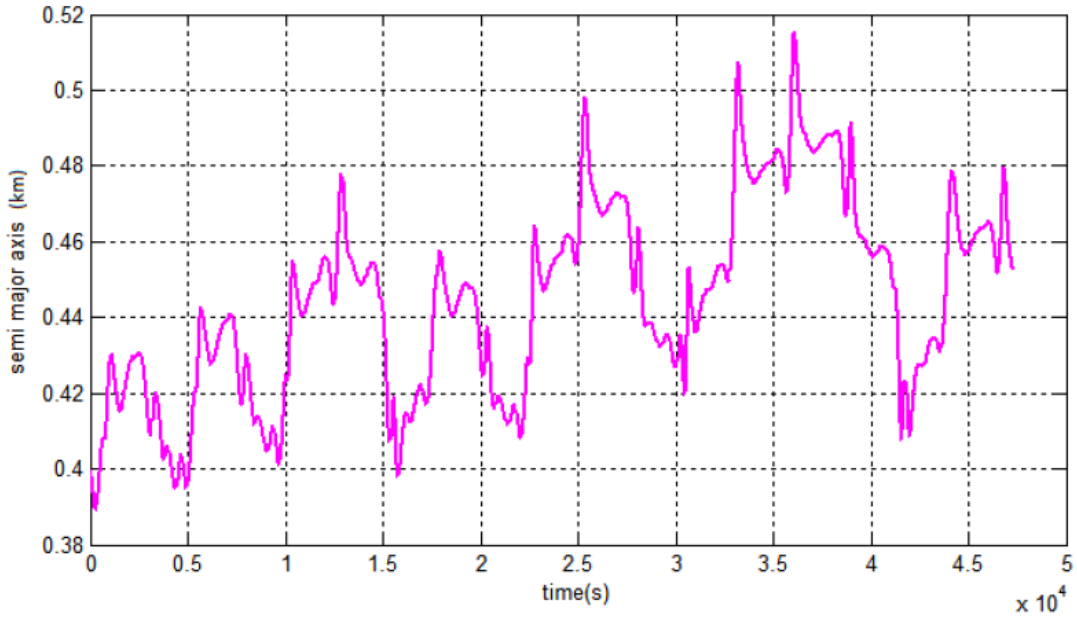

Source: Author.

7 CONSIDERING HETEROGENEITIES WITHIN BENNU

Now that we validated the FEMR and showed that it presents accurate results, it is possible to show another application for this approach. As this approach brings with it a sophisticated model that is capable of refining with mastery even the interior of the body. It is a good option to study how different densities within the body can affect the gravity field. The model also enables a lot of freedom to think about the different possibilities and scenarios when thinking about the heterogeneous density case.

We believe that asteroids are like sandy beaches with some boulders spread throughout the surface. Translating to asteroids, we can say that the background of the body would have a lighter density and some boulders with a higher density. OSIRIS-REx data also confirmed the hypothesis that asteroids also have voids, that is empty spaces with no density at all.

In this section we perform three different types of analysis. The first analysis is a first experiment to check the behavior of the asteroid's potential when different densities are considered The second brings a first experiment showing what happens when we insert rocks into the asteroid, the second contemplates a hybrid model in which we use the polyhedron to obtain the gravity field of the background and the FEMR to obtain the gravity field of the boulders and voids (when we consider this type of element). After these computations both results are combined to obtain the final result. For this study, the constraint is the mass of the asteroid, that is always constant. We model the background with a density ρ_p and the boulders with a density ρ_b, Equation 7.1.

$$\rho_{bulk} V_{polyhedron} = \rho_{background} \left(V_{background} + f \sum_{b=1}^{B} V_{boulder} \right) \qquad (7.1)$$

Where ρ_{bulk} is equal to 1260 kg/m^3 is the bulk density (CHESLEY, 2014), $V_{polyhedron}$is the polyhedron shape model volume, $V_{boulder}$ the volume of a boulder element, B is the number of boulders, and f is a factor, adopted as 2. When we built the equation the factor f was thought as a weight to adjust the density of the boulders, meaning that the boulders have twice the density of the

surrounding material. For the cases that voids are considered a similar computation is done, Equation 7.2.

$$\rho_{bulk} V_{polyhedron} = \rho_{background} \left(V_{background} + f \sum_{b=1}^{B} V_{boulder} - \sum_{v=1}^{V} V_{void} \right) \qquad (7.2)$$

Where V_{void} is the volume of a void element and V the number of voids. In the next sections, scenarios are introduced to explore and evaluate the application of the hybrid model.

Our third analysis considers only the FEMR method to compute the gravity field of the body, and then we compare it with results computed using the classic methodology, like we did in the previous sections.

We must also point that the tool we use for this analysis is a tridimensional grid. We build this grid and insert it into the asteroid so we can choose where to allocate boulders and voids. Each line of the grid is separated by a distance d, and at each point where the grid lines meet a virtual sphere of diameter D is placed. The elements with centroid inside the spherical range D are considered as boulders, Figure 7.1. As we create the sphere, we place the elements with centroid's coordinates that are inside the range D are activated and considered to build the boulder regions.

Figure 7.1 - Grid representation.

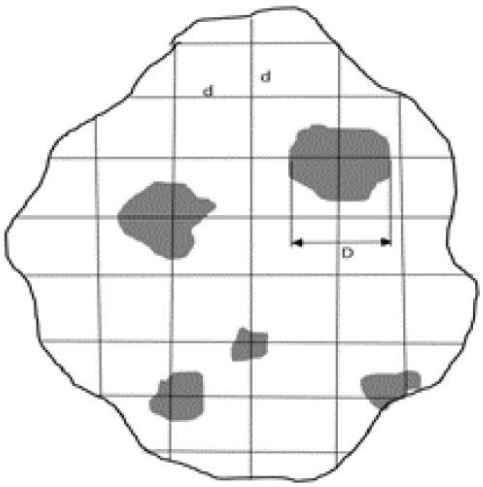

Source: Author.

7.1 A first experiment regarding different densities

As a first exercise we perform an analysis that aims to check the behavior of the asteroid's gravity potential when we consider different densities within the body. For that we consider three different cases. The first study considers an agglomerate of boulders close to the surface, Figure 7.2.

For the second and third cases these agglomerates are moved towards the direction of the asteroid centroid, Figure 7.3 and Figure 7.4.

Figure 7.2 – Experiment 1 distribution.

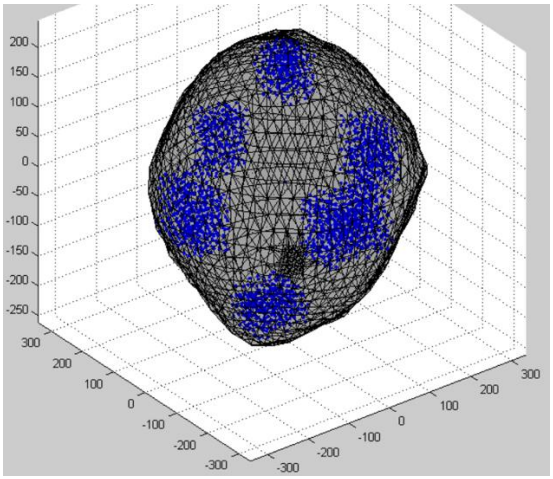

Source: Author.

Figure 7.3 – Experiment 2 distribution.

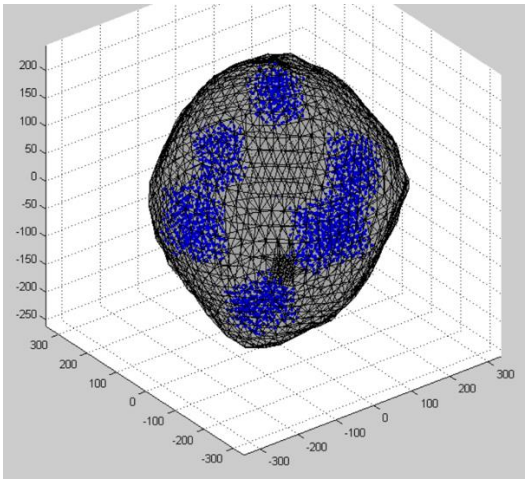

Source: Author.

Figure 7.4 - Experiment 3 distribution.

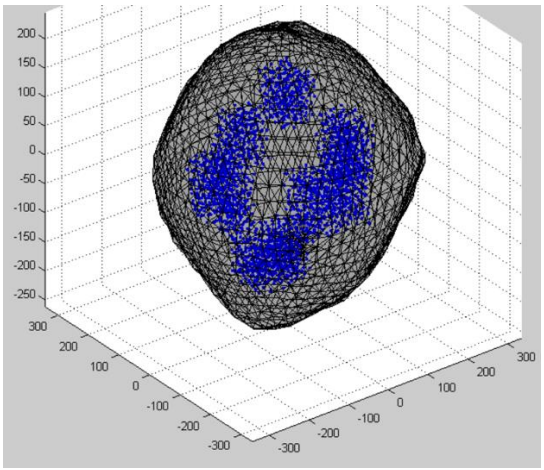

Source: Author.

Figure 7.5 - Experiment 1 potential.

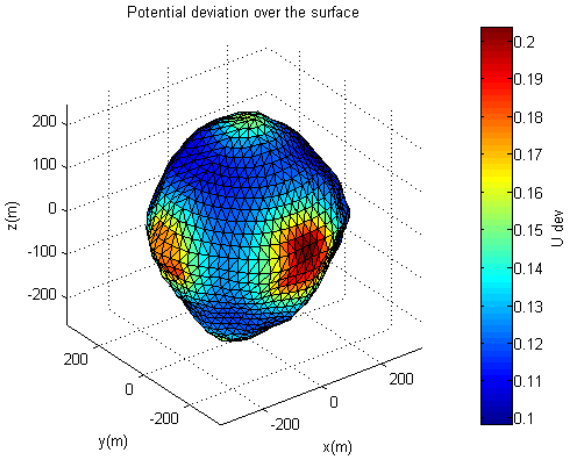

Source: Author.

From Figure 7.5 to Figure 7.7 we can see the difference between the potential considering constant densities and the gravity potential that results of the previous boulders distributions. These figures shows us that for the first case the differences are higher because we are computing the potential over the surface where the boulders are placed. And as they move inwards the difference decrease, however, is still significant.

From these first results we can say that the potential presents relevant differences when a heterogeneous body is considered. With this we proceed to the next analysis.

Figure 7.6 - Experiment 2 potential.

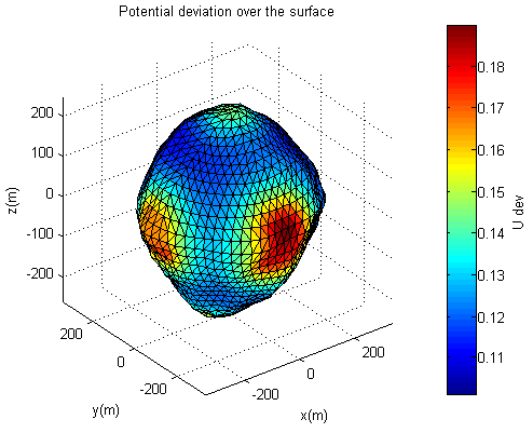

Source: Author.

Figure 7.7 - Experiment 3 potential.

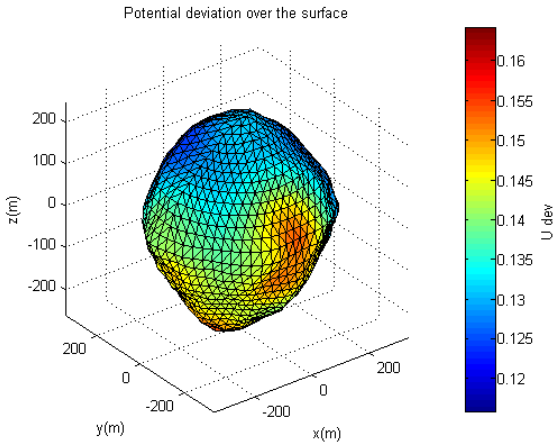

Source: Author.

7.2 An Introduction to Heterogeneities, the hybrid model

In this section we aim to present some distinct analysis considering different densities. We contemplate different scenarios: first only boulders, then, boulders and voids, and finally scenarios with a random distribution of densities. With this we aim to verify how the potential evolves and if it is affected in a relevant way when considering these different elements. All these scenarios make use of the hybrid model, and we present them in the next subsections.

7.2.1 Boulders grid

The first analysis considering different densities, we start examining the asteroid with a lighter background and denser boulders spread through the body, this is the first approximation to check how the body's potential reacts.

To build this model, Figure 7.1, the grid is inserted within Bennu. We obtain the different densities using Equation 7.1. We perform simulations considering different values for the grid distance, d, starting with 50 meters increasing by steps of 5 meters being the last d considered as 100 meters. The values for the sphere diameter range vary from 5 to 30 meters, increasing with the same step as the grid distance does.

With different grid considerations, we obtain distinct density values as the mass is constrained. With this in mind we can verify the evolution of the different values of densities for different grids with Figure 7.8 and Figure 7.9.

As the grid lines get closer and the sphere range increases its value, the value of both densities decreases. This happens because of the higher volume of boulders, as it increases to keep the mass constraint the density will naturally decrease. Both densities behave the same way because they are closely related.

The variation of the potential and gravity acceleration are the most important result of this analysis because it is going to show if their values change and how they do it considering different configurations for the body regarding the boulder insertion. To do so, we present in Figure 7.10 and Figure 7.11 the evolution of the potential and acceleration with a simple average, Equation 7.3.

$$\Delta u = \frac{\left|U_{comb} - U_{poly}\right|}{U_{poly}} \tag{7.3}$$

Where U_{comb} is the potential combining boulders and voids and U_{poly} the potential of the polyhedron.

We analyze three plots to get some conclusions: Figure 7.10 and Figure 7.11 show the potential and acceleration average deviation, and Figure 7.12 the percentage of the asteroid made of boulders for each case. Observing these graphics, we notice that the closer the grid and the higher the value of the range

sphere's diameter, the higher the difference of the potential and acceleration, both have the same variation. As the differences increase, the mass of the asteroid made of boulders also increases, being this the reason for the change of the potential and acceleration values. These plots also mean that with the insertion of other elements, such as boulders, the potential and acceleration change. This is the important question answered by these results.

Figure 7.8 - Background density variation.

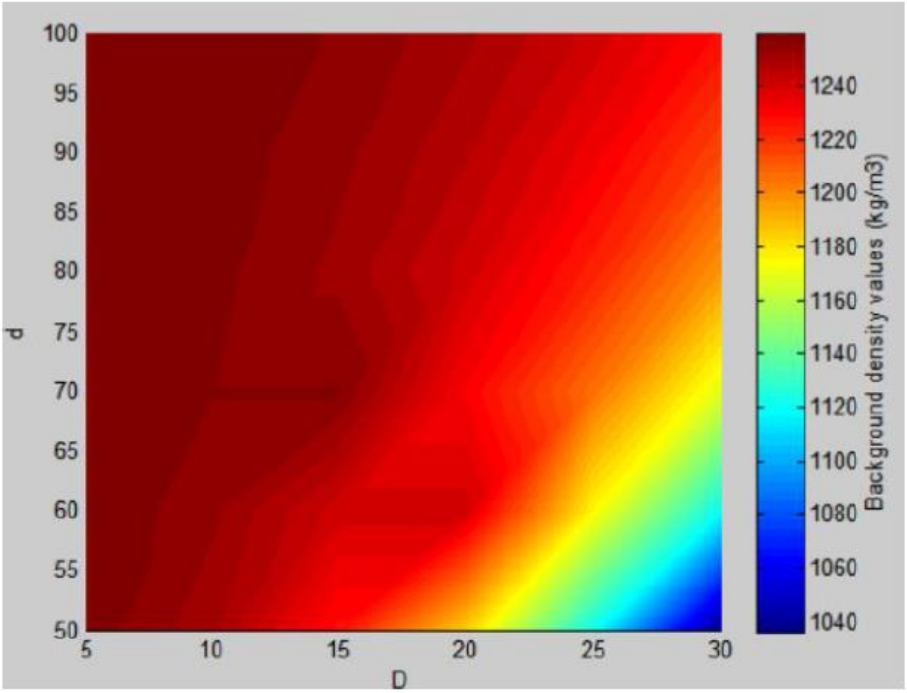

Source: Author.

Figure 7.9 - Boulders density variation.

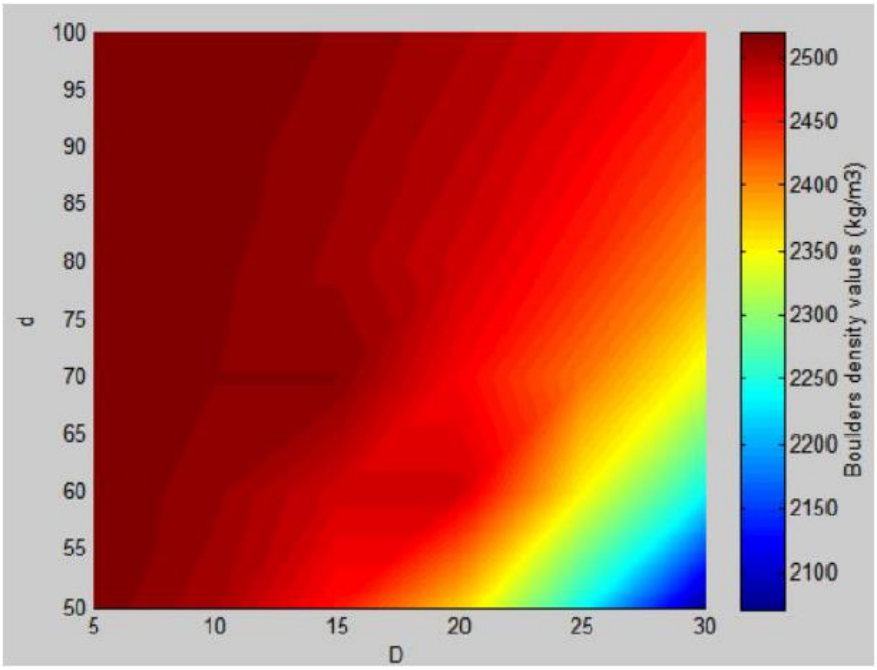

Source: Author.

Figure 7.10 - Potential average deviation.

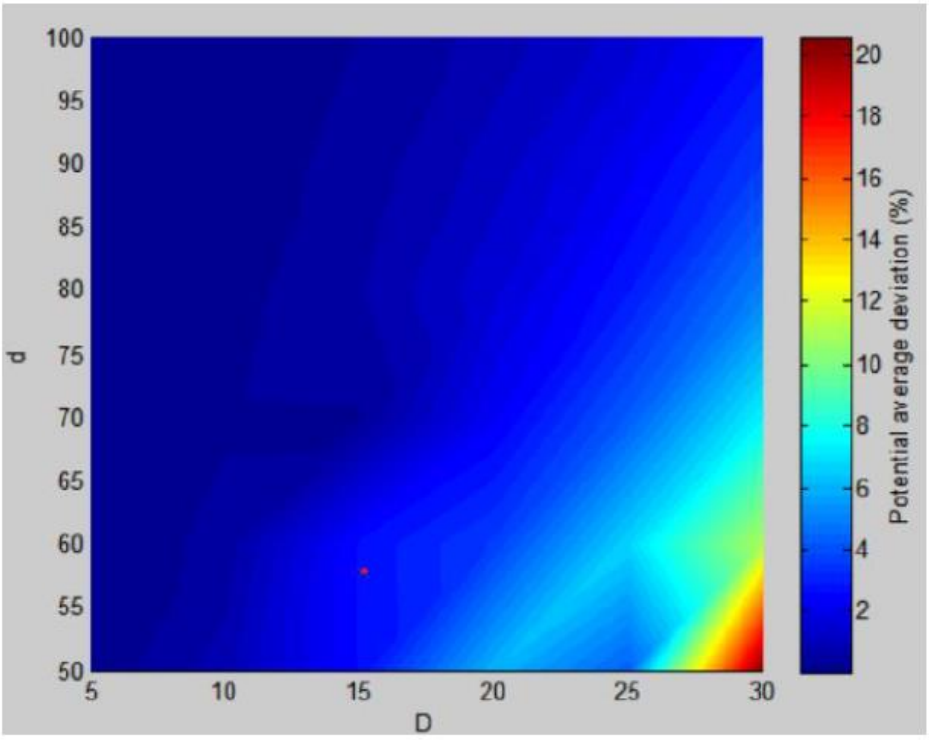

Source: Author.

Figure 7.11 - Acceleration average deviation.

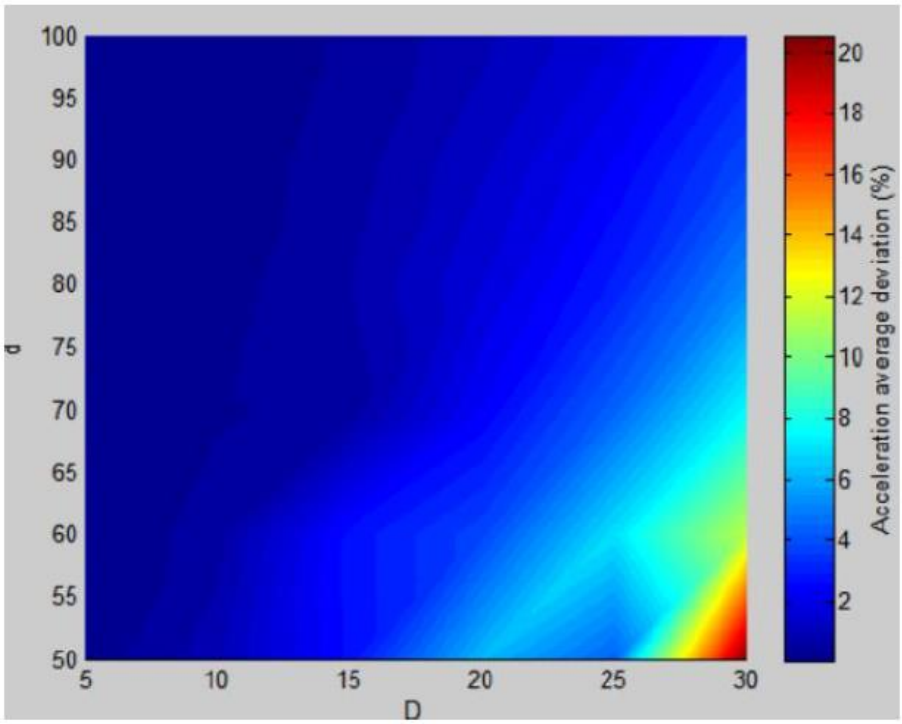

Source: Author.

Figure 7.12 - Percentage of the body constituted of boulders.

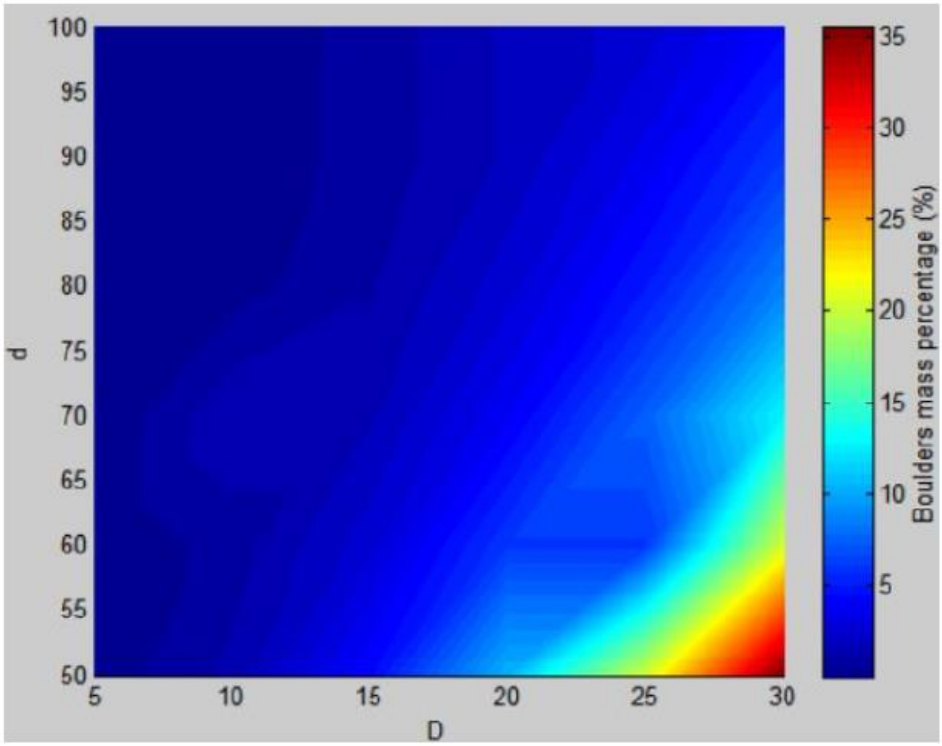

Source: Author.

7.2.2 Random grid

We easily note that a scenario considering only boulders spread throughout the body in a very systematic way is not realistic. To deliver a more plausible framework, boulders and voids were randomly inserted within the body, as nature does not follow a human-made simplistic pattern. To achieve this, the grid distance changes exactly like the last case presented in the last subsection. However, a random algorithm was created to select the diameter values of the sphere.

We select *D* values from 5 to 30 meters. To begin with, we only consider boulders. Figure 7.13 and Figure 7.14 presents the potential and acceleration average deviation between the case considering a constant density and the heterogeneous cases that consider the presence of boulders. These values are presented as percentages on the y-axes; the x-axes show the values of the grid distance. As the grid distance, d, gets smaller the potential average difference increases. Figure 7.15 shows the percentage of the asteroid's mass that consists of boulders and again, this is shown on the y-axis.

These three plots have remarkably similar patterns, the acceleration and potential figures show the same values with a small difference between them for both, the differences between the homogeneous and heterogeneous cases increase as the grid distance decreases. Figure 7.15 presents the same pattern again and as the grid distance diminishes the asteroid's percentage of mass consisting of boulders increases, which means that there are more boulders.

From all these facts it is possible to say that when the number of boulders starts to increase, the asteroids become less homogeneous which means that the deviations, when compared to a constant density case, will also increase. For this case, the maximum percentage of boulders is close to 60%, which represents a highly non-homogeneous body. It is also important to notice that the pikes when we have $d = 95m$, Figure 7.13 to Figure 7.15, happen because there's an unexpected increase in the percentage of boulders for this specific value, and as these simulations used random values for D, this was not controlled or expected to happen.

Figure 7.13 - Potential deviation - Random boulders.

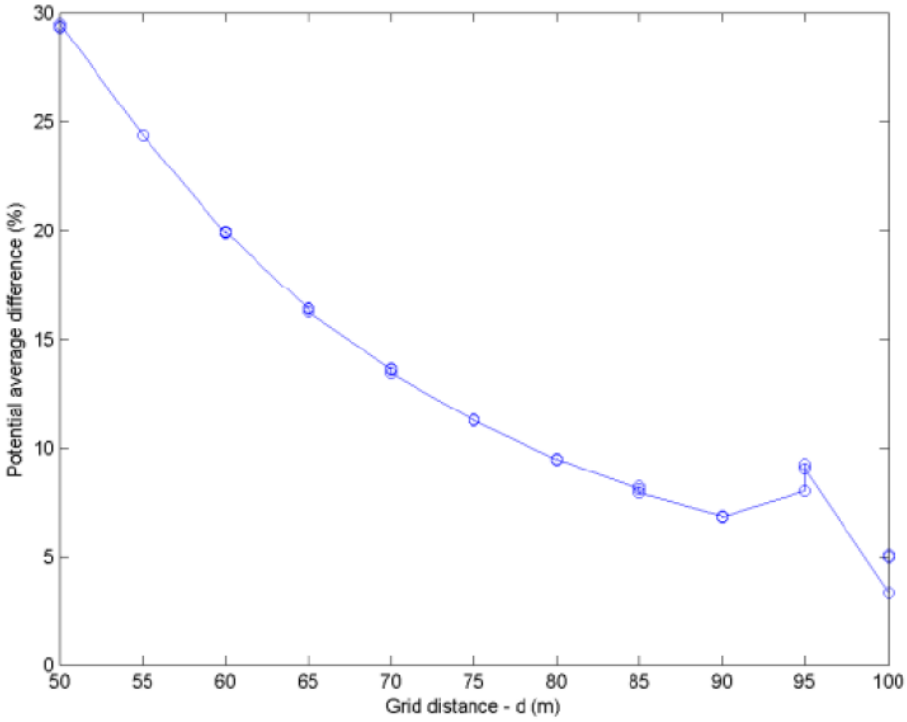

Source: Author.

Figure 7.14 - Acceleration deviation - Random boulders.

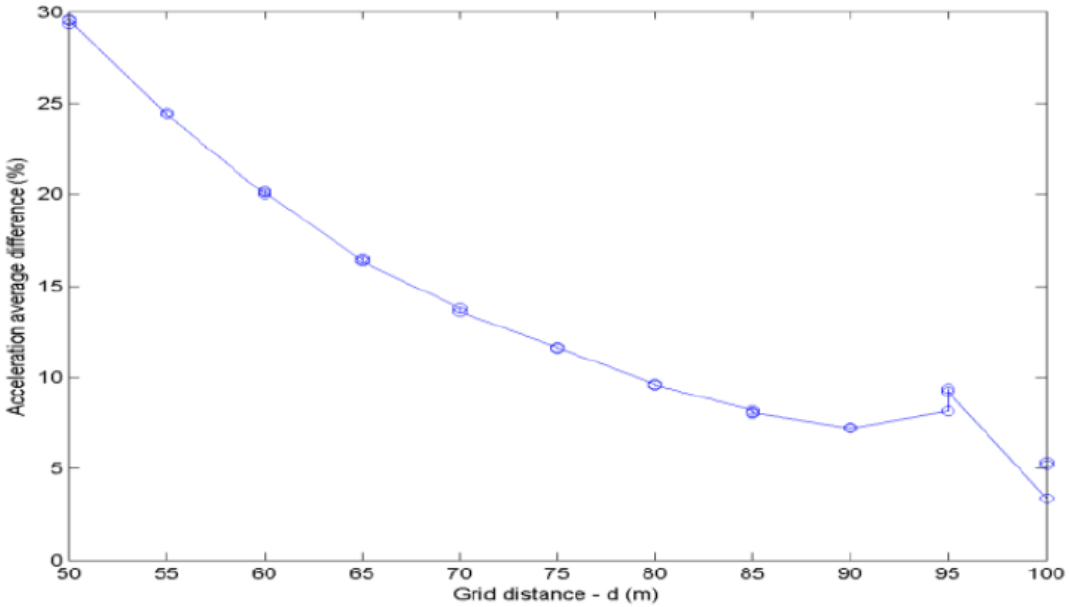

Source: Author.

Figure 7.15 - Percentage of the body constituted of boulders - Random boulders.

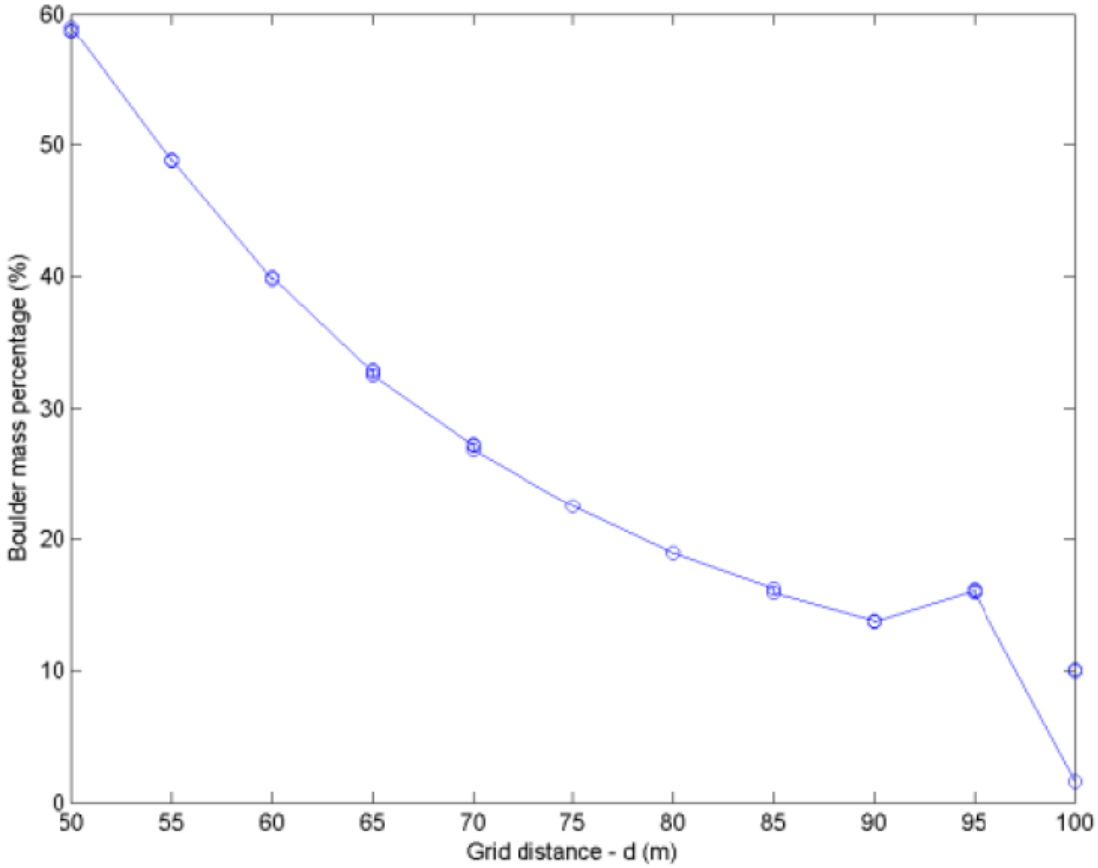

Source: Author.

7.2.3 Random grid considering voids

To deliver an even more realistic scenario, this case will consider not only boulders. Asteroids are more complex than people can think, having different constitutions, empty spaces, porosity, and so on. Regarding this, the current subsection carries a case that also considers voids within the body. For this, a grid with a fixed d value is created and another algorithm selects if the element inside the range (that is again randomly selected exactly like the case considered in the last subsection) is going to be a boulder or a void. We perform two sets of 10 cases, two values were set for the grid distance for the first set 50 meters, and the second 75 meters.

Table 7.1 shows the percentage of boulders and voids for each value of d considered, Figure 7.16 and Figure 7.17 show the average of the potential

deviation for the 10 simulations and both grids' distances considered. For the case of d equal to 75 meters, that represent a larger distance for the grid, the number of boulders and voids are reduced, so checking Figure 7.16 the deviation of the potential presents much lower values, as the boulder and voids distribution is closer to that of a constant density case due to the reduced number of elements.

For the closer grid, combining the data from Table 7.1 and Figure 7.16, the deviation of the values of the potential through the surface of the asteroid are much higher for this case, however, there is a massive number of boulders and a relevant number of voids, representing a body that has a high degree of in-homogeneity. These results once again say that different densities affect the potential of the asteroid.

Table 7.1 - Percentages of voids and boulders, 50 and 75 meters grid distance.

Case	Boulders distribution *d* = 50m (%)	Voids distribution *d* = 50m (%)	Boulders distribution *d* = 75m (%)	Voids distribution *d* = 75m (%)
1	41.58	21.23	12.85	6.44
2	41.98	20.70	12.69	6.44
3	41.70	20.81	12.98	6.29
4	41.59	20.88	12.86	6.33
5	41.84	20.73	12.57	6.41
6	41.58	20.73	12.57	6.41
7	41.98	20.70	12.84	6.42
8	41.58	21.23	12.85	6.44
9	41.58	21.23	12.69	6.44
10	41.98	20.70	12.85	6.44

Source: Author.

Figure 7.16 - Potential deviation – boulders and voids grid *d = 50m.*

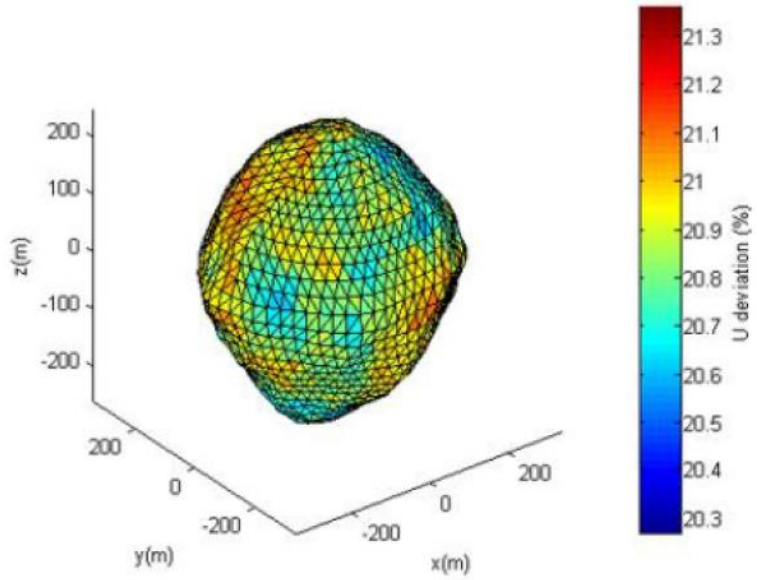

Source: Author.

Figure 7.17 - Potential deviation – boulders and voids grid *d = 75.*

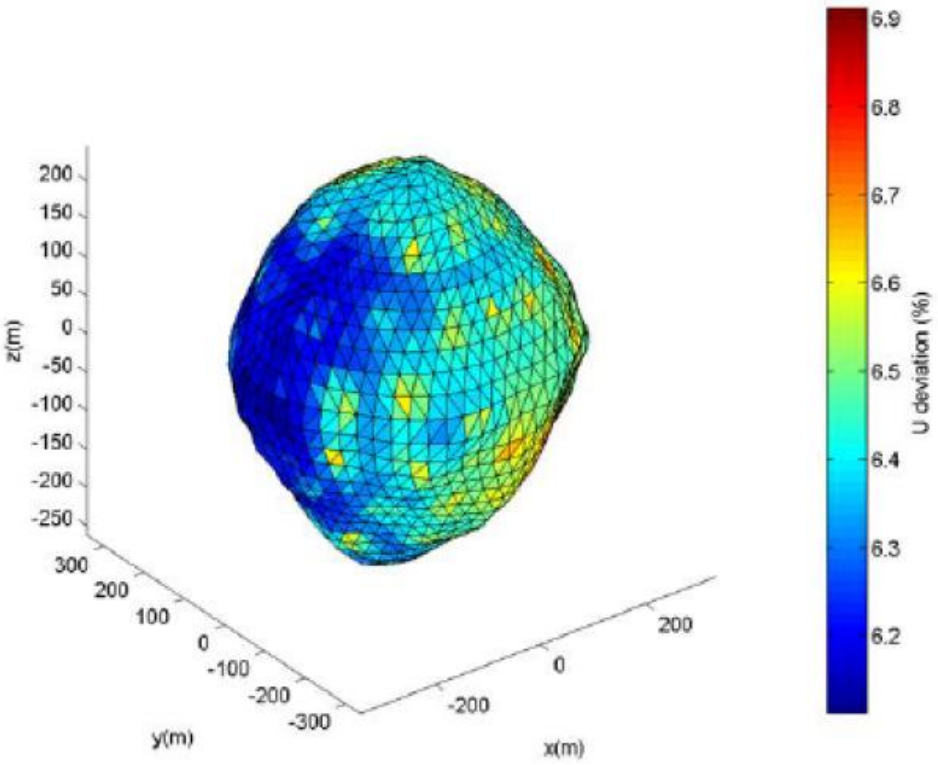

Source: Author.

7.3 An introduction to heterogeneity, gravity coefficients

In this section, we built 18 different distributions using the grid tool, d goes from 50 to 100 meters, increasing by 10, and D was considered as 15, 30, and 50 meters for each different value of d.

From Figure 7.18 to Figure 7.20, we can see the gravity RMS difference between the case considering a constant density and the case considering heterogeneities. For D values equal to 15 m, 30 m, and 50 m, respectively, the x-axis shows the degree from 1 to 4. As the values of D increase, we see from these figures that the RMS values increase. An answer for this is that with a value of D equals 15 meters, it is possible to achieve a more homogeneous body with a high number of boulders, however, still more homogeneous. As this value goes up, the differences increase because the body presents more heterogeneities within it, which give us greater differences.

Regarding the different degrees of the coefficients, there is no pattern when we analyze the D values together. Although we can say that when changing these values, the mass distribution also changes, and so there are different patterns for each one of the simulations as the coefficients are very sensitive to the changing of the mass distribution.

After this set of analysis, we do a second set inserting voids. For these cases the grid is fixed for voids (d = 70 m) and boulders (d = 50 m). Different values of D are considered, Figure 7.21. First of all, from what we learnt with the previous analysis, from the void values that have a range of D equal to 30 or 50 meters, the model has more heterogeneities as more voids are inserted. For the other values we have lower values meaning the presence of a more homogeneous body.

Figure 7.18 - Gravity coefficients RMS D = 15m.

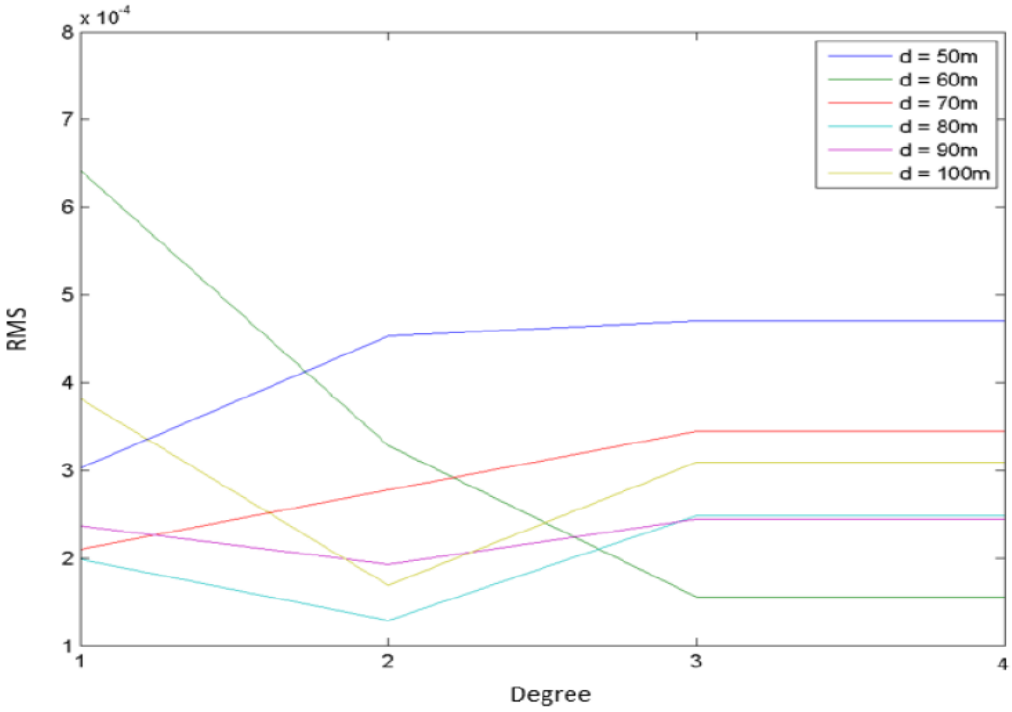

Source: Author.

Figure 7.19 - Gravity coefficients RMS D = 30m.

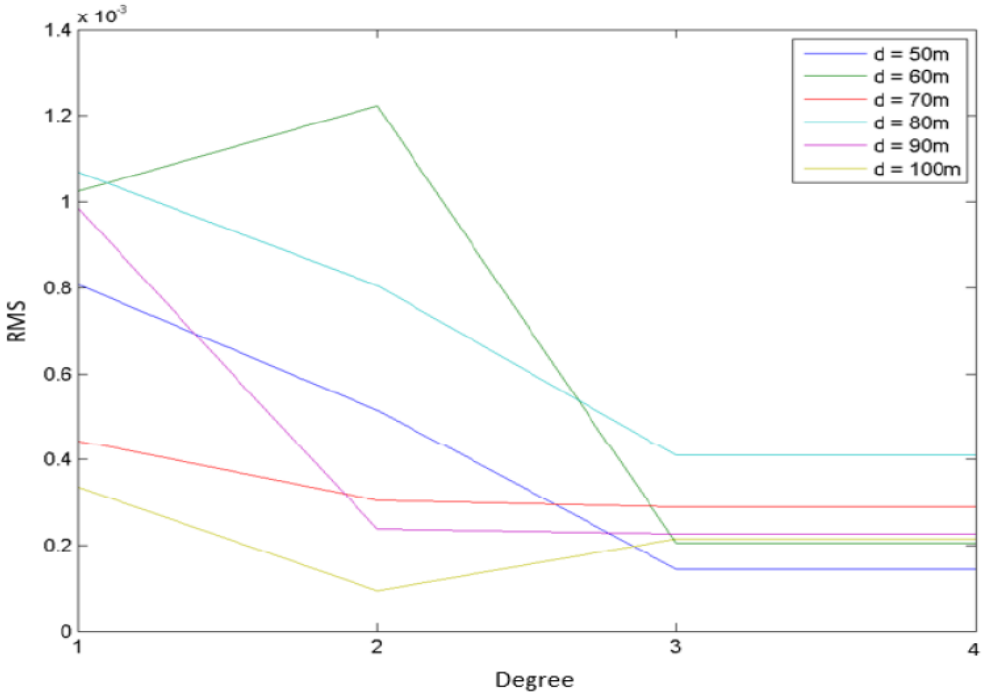

Source: Author.

Figure 7.20 - Gravity coefficients RMS D = 50m.

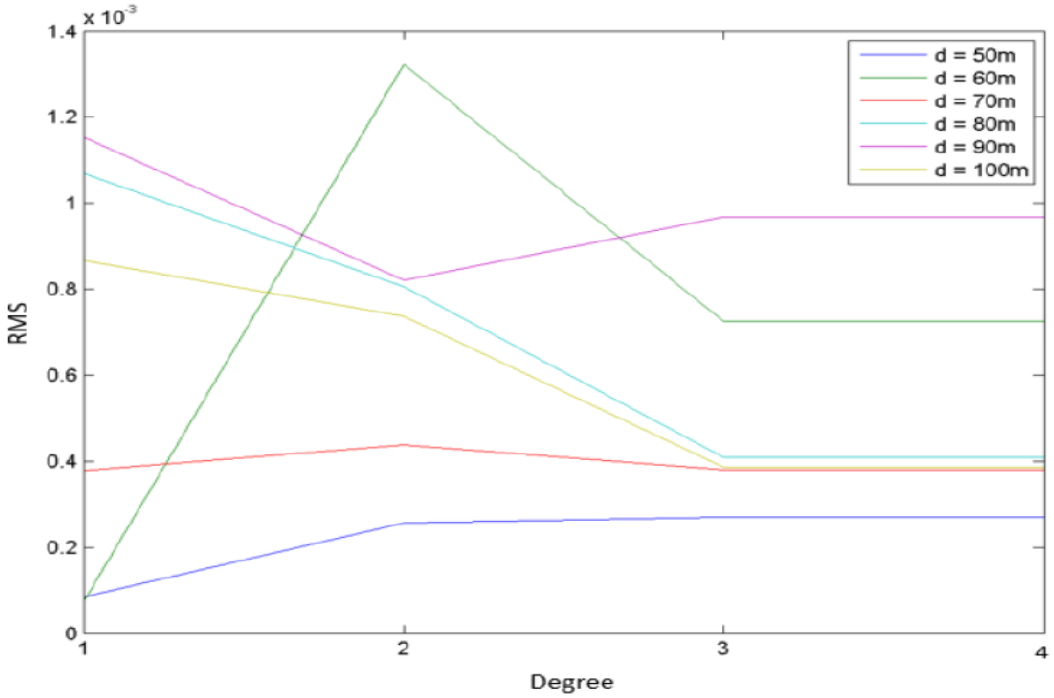

Source: Author.

Figure 7.21 - Gravity coefficients RMS boulders and voids.

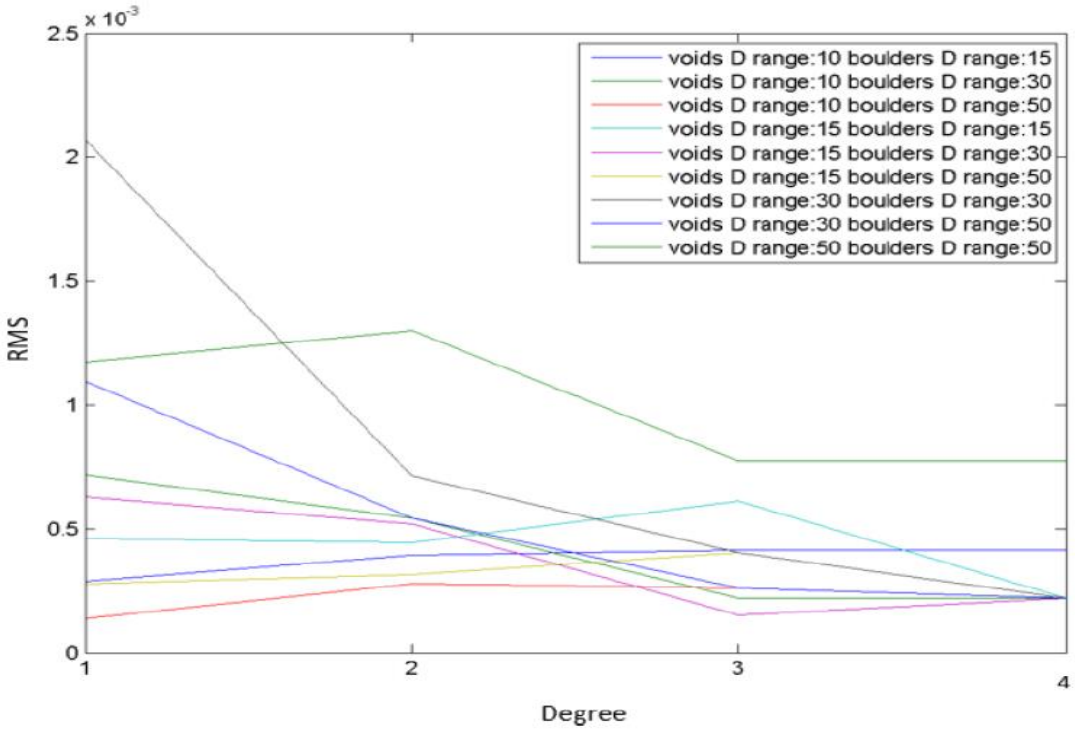

Source: Author.

Exploring feasible scenarios

Before reaching the conclusion of both this study and the thesis, we present here the most precious application of the methodology. Due to the nature of the FEM mesh discretization, we are capable of explore the feasibility of various mass distributions, comparing it with mission data.

To do so we compare results considering different densities distribution layouts with data obtained from the OSIRIS-Rex mission shared at the time in the University of Colorado Boulder. These data consist on gravity coefficients estimated from the tracking of particles ejected from Bennu. With the coefficients we are capable of compare these values with the ones we obtain with our methodology to check the feasibility of our scenarios and bring they closer to reality.

Figure 7.22 presents the RMS considering multiple boulder/voids distributions, the RMS computed when a constant density gravity field is considered and the particle uncertainties are the uncertainty related with the tracking of the particles performed by the OSIRIS-Rex mission. We can see that all the cases are statistically significant until degree 8, and as the mass distribution changes the RMS result is altered.

Figure 2.1 presents the RMS differences between the homogeneous case and the ones computed considering different densities, the red line gives the uncertainties, and the magenta line the difference between the RMS computed with the constant density approach and the estimated RMS from the particles tracking. This plots indicates that the closer the case is from the magenta plot the closer to reality the case is bringing light to the search for feasible scenarios that can get closer to reality and brings some important answers and clues to science.

Figure 7.22 - RMS for feasibility analysis.

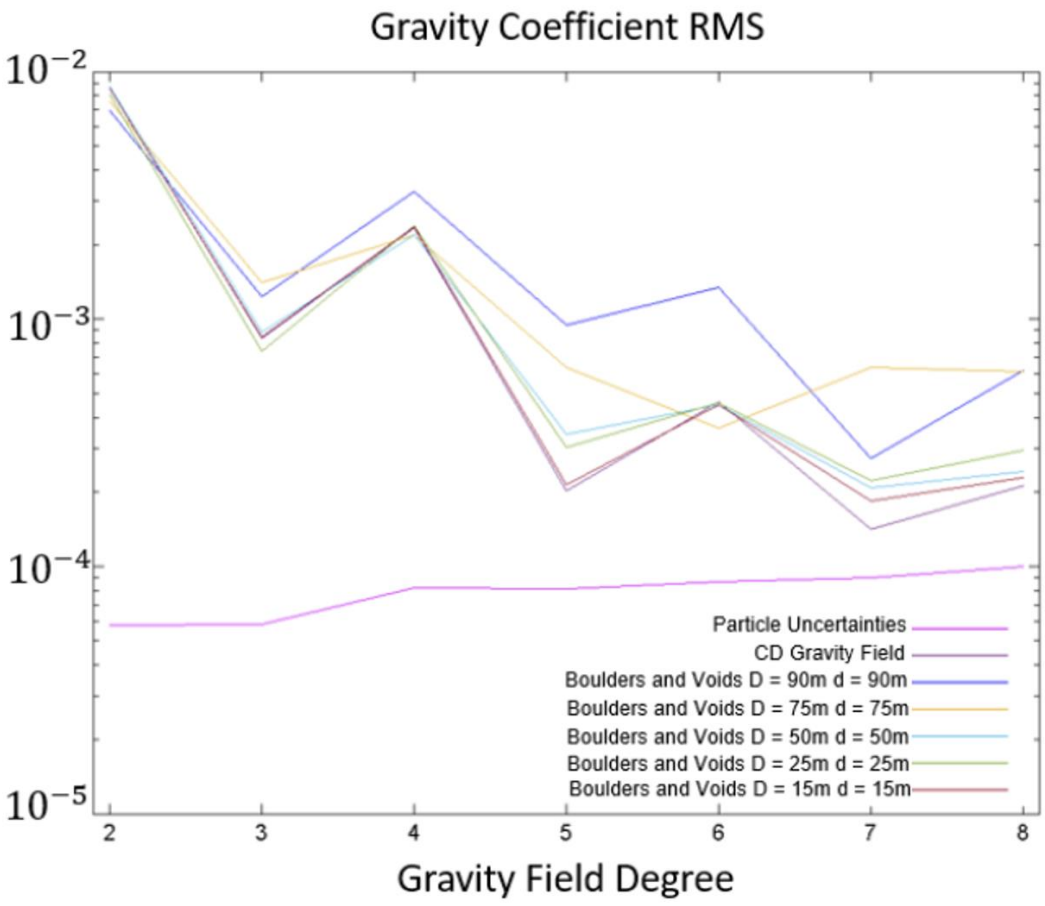

Source: Author.

Figure 7.23 - RMS difference for feasibility analysis.

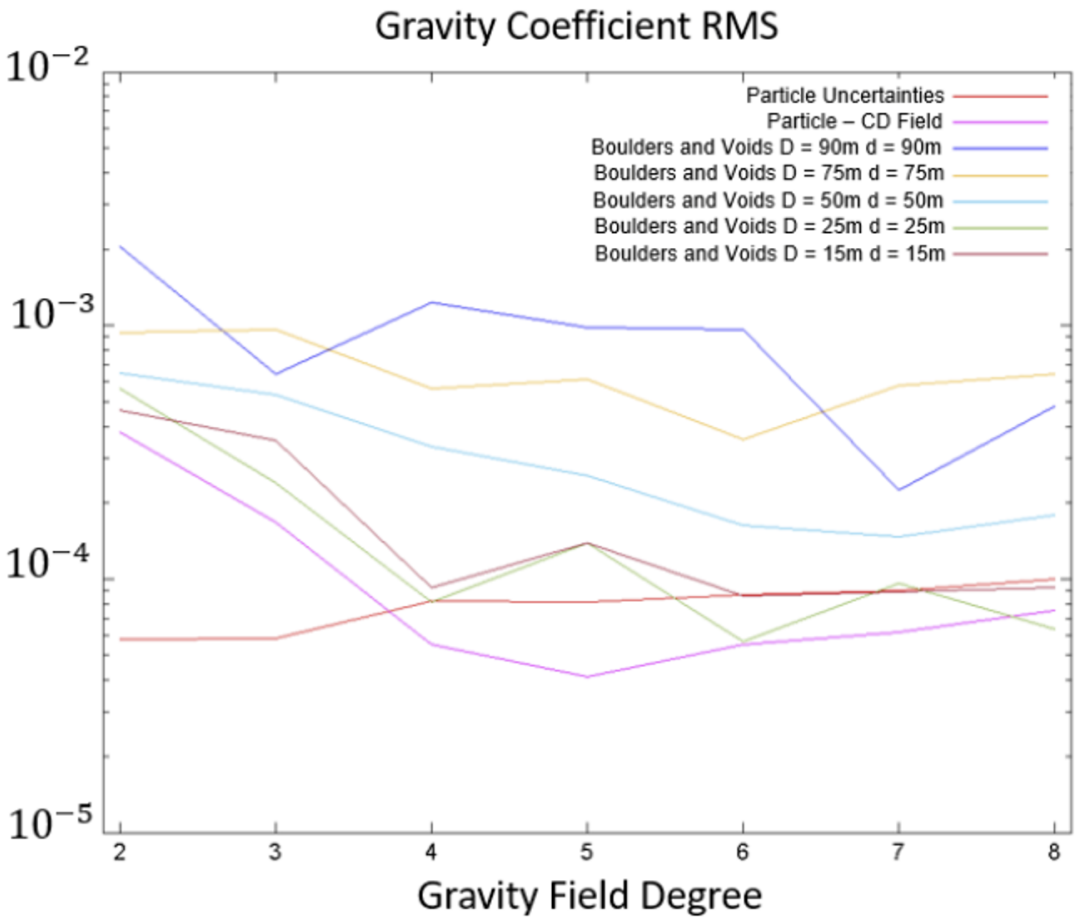

Source: author.

8 CONCLUSIONS

Our main goal in this thesis was to validate the hypothesis of obtaining the gravitational potential of a small body, using some tools and definitions from the Finite Element Method and the mass concentration theory. We have done so to show that the model is trustworthy, that it works, and that it can be used to compute accurately the gravity field.

To start, we created a finite element model using a tetrahedral mesh from polyhedral shape models obtained from radar observations or space mission's data. With the model on hand, we associated the Method of Mass Concentrations with our discretization approach of Finite Elements to obtain the gravity field of the asteroid. Then, we created this model considering an intricate discretization for the body in which not only the surface was considered, but also the interior of the body. This means that for the model introduced in this work a 3D mesh was built giving a lot of freedom to perform various analyses.

We have selected three asteroids for this work. The first one was the asteroid 2063 Bacchus that was chosen to perform the first exercise with the model. The second asteroid was 25143 Itokawa. We selected Itokawa because of the great amount of data from the Hayabusa mission that aimed to collect a sample of the asteroid. The third and last small body was 101955 Bennu that was selected because it was the target of the OSIRIS-REx mission.

After obtaining the finite elements models for the three asteroids we performed the validations. After careful analyses and conversations, we defined that one of the approaches to validate the model and check the results would be the polyhedron model. We opted for the polyhedron because it does not diverge on the surface of the body and this is an interesting layout, especially regarding close proximity and landing, this would be the perfect scenario to test the limits of a new model.

We performed simulations for each one of the three asteroids. The gravity potential and acceleration were obtained through the surface of the body. Then, we compared FEMR results with the polyhedron model for the first validation that

showed that the FEMR presents accurate results as the difference between both methods have a magnitude between 10^{-5} and 10^{-4}.

Another interesting thing to notice from these models is that the potential for Bacchus and Itokawa that are believed to be contact binaries is more intense where would in theory be the intersection of the two lobes of the binary.

After the successful results comparing the FEMR with the polyhedron, we accomplished another validation, this time comparing the results of the gravity coefficients obtained with finite element definitions with the ones obtained with the classical spherical harmonics methodologies.

For this approach, the RMS of the gravity coefficients were obtained. The RMS was used because the coefficients vary a lot in terms of magnitude for different orders and degrees and also because there are a big number of coefficients, and the RMS brings with it a much more elegant presentation with accuracy making the analysis simpler and more visual.

Once again, the FEMR showed accurate results when we compared it with the other methods being once again validated. We also showed that the FEMR is more than a general model because it can not only be applied for any asteroid but also shows flexibility, being used to compute not only the potential but also the spherical harmonics in a much simpler way. An important note is that for higher degrees the results start to present a higher difference, something that can be easily fixed considering more elements, we leave this point for future studies though.

The last validation we have done involved the STRS so it could not only perform a validation but also show a practical application of the FEMR. The FEMR was inserted into the STRS for the three asteroids so, the velocity increment of the spacecraft due to the potential could be compared with the one obtained by the MEPS for the last validation. With these results, we also showed that the FEMR can be used to analyze the trajectory of a spacecraft. However, it is important to say that this is done to only show a possible application, leaving a more complete analysis to future works. The reason for this choice is that this specific study does not aim to perform and focus on spacecraft trajectories, and just showing

trajectory simulations would not bring innovations, as the only innovation would be the model itself.

We completed these validations and observed that they not only legitimate the Finite Element application to gravity fields, but they also show that, with the right number of elements, it can overpass the accuracy of other methods like the polyhedron and the series expansion method. Although, an important thing to have in mind here is that there is no best model among all. The polyhedron, for example, can also show better results when we increase the number of facets. So, we conclude that the best model is the one that fits the application.

In the last study we explore an application of the model, being original not for its application but because of the way it is done and the answers it can deliver in the future. The application is also important because it shows something only the FEMR can achieve thanks to the mesh sophisticated refinement, different from the evaluation of the potential, as many methods can already deliver accurate answers.

For the investigation of heterogeneity, we chose Bennu. We evaluated some scenarios using the FEMR model, as it brings the possibility to explore how to map the heterogeneity in a very freeway being able to consider the most possible different ways to map a body. The results presented here show that not only the acceleration and the potential are affected by changing density values, but also shows that the gravity coefficients change.

With this, it is possible to conclude that the FEMR model here delivered can be used to compute gravity fields of asteroids, and not only for that but for other applications, and some of them are left to future works. The FEMR can be used to explore heterogeneities in many ways and answer important questions about them. As this approach uses the FEMR, it is possible to analyze the internal tensions within the body and failure modes, however, as the goal of this thesis is to create models to compute and analyze the potential of the body this will be done in future works as it would be out of the scope of this specific study.

REFERENCES

AGOSTINHO, A. C. **Controle por modos deslizantes aplicado ao movimento de atitude de satélites submetidos aos torques perturbadores gerados pelo movimento de um líquido.** 2019. 199 p. Tese (Doutorado em Mecânica Espacial e Controle) - Instituto Nacional de Pesquisas Espaciais (INPE), São José dos Campos, 2019. Available at: <http://urlib.net/rep/8JMKD3MGP3W34R/3T633UL>. Access on: Sept. 9, 2021.

ARAUJO, N.C. **Controle de trajetórias ao redor de Júpiter visando a aproximação das luas galileanas**. 2017. 303 p. Dissertação (Mestrado em Engenharia e Tecnologia Espaciais) — Instituto Nacional de Pesquisas Espaciais (INPE), São José dos Campos, 2017. Available at: <http://urlib.net/rep/8JMKD3MGP3W34P/3NMG9E5>. Access on: Sept. 9, 2021.

ARAUJO, N. C.; ROCCO, E.M. Mapping the Galilean moon's disturbance acting on a spacecraft's trajectory. **Journal of Physics: Conference Series**, v. 911, n. 1, e012010, 2017. Available at: <https://www.researchgate.net/publication/320633233> Access on: Sept. 9, 2021.

ARAUJO, N.C.; ROCCO, E.M. Evaluating the disturbances acting on a spacecraft on orbit around Europa. **Journal of Physics: Conference Series**, v. 1365, n. 1, e 012014, 2019. Available at: <https://www.researchgate.net/publication/337018032> Access on: Sept. 9, 2021.

BALMINO, G. Gravitational potential harmonics from the shape of an homogeneous body. **Celestial Mechanics and Dynamical Astronomy**, v. 60, n. 3, p. 331–364, 1994.

BARNOUIN, O. S. et al. Shape of (101955) Bennu indicative of a rubble pile with internal stiffness. **Nature Geoscience**, v. 12, n. 4, p. 247-252, 2019.

BATE, R.R. et al. **Fundamentals of astrodynamics**. [S.l.]: Courier Dover Publications, 2020.

BEATTY, M.F. The moment of inertia tensor. In: _____. **Principles of engineering mechanics**: mathematical concepts and methods in science and engineering. Boston, MA, EUA: Springer, 2006. p. 355-404.

BENNER, L. A. et al. Radar observations of Asteroid 2063 Bacchus. **Icarus**, v. 139, n. 2, p. 309–327, 1999. Available at: <https://www.sciencedirect.com/science/article/pii/S0019103599960943> Access on: Sept. 9, 2021.

BERN, M.; PLASSMANN, P. **Mesh generation**. [S.l.]: Pennsylvania State University, Department of Computer Science and Engineering, College of Engineering, 1997.

BOTTKE, W. F. et al. Understanding the distribution of near-earth asteroids. **Science**, v. 288, n. 5474, p. 2190–2194, 2000. Available at: <https://doi.org/10.1126/science.288.5474.2190> Access on: Sept. 9, 2021.

_____. The Yarkovsky and YORP effects: implications for asteroid dynamics. **Annual Review of Earth and Planetary Sciences**, v. 34, p. 157–191, 2006.

BOWELL, E.; CHAPMAN, C. R.; GRADIE, J. C.; MORRISON, D.; ZELLNER, B. Taxonomy of asteroids. **Icarus**, v. 35, n. 3, p. 313–335, 1978.

CHANDRUPATLA, T.R. et al. **Introduction to finite elements in engineering**. Pearson: Prentice Hall, 2002.

CHANUT, T. et al. Dynamics in the vicinity of (101955) Bennu: solar radiation pressure effects in equatorial orbits. **Monthly Notices of the Royal Astronomical Society**, v. 470, n. 3, p. 2687–2701, May 2017.

CHAPMAN, C. R. S-type asteroids, ordinary chondrites, and space weathering: the evidence from Galileo's fly-bys of Gaspra and Ida. **Meteoritics & Planetary Science**, v. 31, n. 6, p. 699–725, 1996.

CHAPMAN, C. R.; MORRISON, D.; ZELLNER, B. Surface properties of asteroids: a synthesis of polarimetry, radiometry, and spectrophotometry. **Icarus**, v. 25, n. 1, p. 104–130, 1975.

CHESLEY, S. R. et al. Orbit and bulk density of the OSIRIS-REx target asteroid (101955) Bennu. **Icarus**, v. 235, p. 5–22, 2014.

CHOBOTOV, V. A. **Orbital mechanics**. Reston, VA, EUA: American Institute of Aeronautics and Astronautics, 2002.

CLOUGH, R. W. The finite element method in plane stress analysis. In: ASCE CONFERENCE ON ELECTRONIC COMPUTATION, 2., 1960, Pittsburgh PA. **Proceedings…** 1960.

CURTIS, H. **Orbital mechanics for engineering students: revised reprint**. [S.l.]: Butterworth-Heinemann, 2020.

DECHAMBRE, D.; SCHEERES, D.J. Transformation of spherical harmonic coefficients to ellipsoidal harmonic coefficients. **Astronomy & Astrophysics**, v. 387, n. 3, p. 1114-1122, 2002.

FUJIWARA, A. et al. The rubble-pile asteroid Itokawa as observed by Hayabusa. **Science**, v. 312, n. 5778, p. 1330–1334, 2006. Available at: <https://doi.org/10.1126/science.1125841> Access on: Sept. 9, 2021.

FURFARO, R. et al. Modeling irregular small bodies gravity field via extreme learning machines and Bayesian optimization. **Advances in Space Research**, v. 67, n. 1, p. 617-638, 2021.

GEISSLER, P. et al. Erosion and ejecta reaccretion on 243 Ida and its moon. **Icarus**, v. 120, n. 1, p. 140–157, 1996. Available at: <https://doi.org/10.1006/icar.1996.0042> Access on: Sept. 9, 2021.

GEISSLER, P.; PETIT, J.-M.; GREENBERG, R. Ejecta reaccretion on rapidly rotating asteroids: implications for 243 Ida and 433 Eros. In: COMPLETING THE INVENTORY OF THE SOLAR SYSTEM, 107., 1996. **Proceedings…** Astronomical Society of the Pacific Conference, 1996. p. 57–67.

GLASSMEIER, K.-H. et al. The ROSETTA mission: flying towards the origin of the solar system. **Space Science Review**, v. 128, n. 1-4, p. 1–21, 2007.

GOMES, W.; ROCCO, E.M. Design of a fuzzy PID controller for application in satellite attitude control system. In: WORKSHOP ON SPACE ENGINEERING AND TECHNOLOGY, 2012. **Proceedings….** 2012. p. 1-8.

GONÇALVES, L. D. **Manobras orbitais de satélites artificiais lunares com aplicação de propulsão contínua.** 2013. 301 p. Dissertação (Mestrado em Mecânica Espacial e Controle) – Instituto Nacional de Pesquisas Espaciais (INPE), São José dos Campos, 2013. Available at: <http://urlib.net/rep/8JMKD3MGP7W/3DL2KKS>. Access on: Sept. 9, 2021.

GONÇALVES, L.D. **Trajetórias perturbadas por forças de origem gravitacional e não gravitacional aplicadas a um satélite artificial na vizinhança de Marte, Fobos e Deimos**. 2018. 197 p. Tese (Doutorado em Engenharia e Tecnologia Espaciais/Mecânica Espacial e Controle) — Instituto Nacional de Pesquisas Espaciais (INPE), São José dos Campos, 2018. Available at: <http://urlib.net/rep/8JMKD3MGP3W34R/3QTLK85>. Access on: Sept. 9, 2021.

GONÇALVES, L. D.; ROCCO, E. M.; MORAES, R. V. Influência da pressão da radiação solar e do Albedo lunar na órbita de um satélite artificial. In: WORKSHOP EM ENGENHARIA E TECNOLOGIA ESPACIAIS (WETE), 2014. **Anais...** São José dos Campos: INPE, 2014. Available at: <http://urlib.net/rep/8JMKD3MGP5W34M/3HEA5KS> Access on: Sept. 9, 2021.

GONÇALVES, L. D.; ROCCO, E. M.; MORAES, R. V. de. Orbital maneuvers of a lunar artificial satellite, under the action of gravitational and non-gravitational

perturbation forces. In: INTERNATIONAL SYMPOSIUM ON SPACE FLIGHT DYNAMICS, 2015. Munich, Germany. **Proceedings…** 2015. Available at: <http://urlib.net/rep/8JMKD3MGP3W34P/3KH6J52> Access on: Sept. 9, 2021.

GONÇALVES, L.D.; ROCCO, E.; MORAES, R. D. Orbital trajectories in Deimos vicinity considering perturbations of gravitational origin. **Journal of Physics. Conference Series**, v. 911, n. 1., 2017. Available at: <http://dx.doi.org/10.1088/1742-6596/911/1/012022> Access on: Sept. 9, 2021.

GRADIE, J.; TEDESCO, E. Compositional structure of the asteroid belt. **Science**, v. 216, n. 4553, p. 1405–1407, 1982. Available at: <https://doi.org/10.1126/science.216.4553.1405> Access on: Sept. 9, 2021.

HIRABAYASHI, M.; SCHEERES, D.J. Failure mode diagram of rubble pile asteroids: application to (25143) asteroid Itokawa. **Proceedings of the International Astronomical Union**, v. 10, n. S318, p. 122–127, 2015. Available at: <https://doi.org/10.1017/S1743921315007188> Access on: Sept. 9, 2021.

_____. Rotationally induced failure of irregularly shaped asteroids. **Icarus**, v. 317, p. 354–364, 2019.

HO-LE, K. Finite element mesh generation methods: a review and classification. **Computer-Aided Design**, v. 20, n. 1, p. 27–38, 1988.

JUNKINS, J. L. Investigation of finite-element representations of the geopotential. **AIAA Journal**, v. 14, n. 6, p. 803–808, 1976.

KAULA, W.M. **Theory of satellite geodesy:** applications of satellites to geodesy. Mineola, NY, EUA: [s.n.], 2013.

KEIL, K.; HAACK, H.; SCOTT, E.R.D. Catastrophic fragmentation of asteroids: evidence from meteorites. **Planetary and Space Science,** v. 42, n. 12, p. 1109-1122, 1994.

KELLOGG, O.D. **Foundations of potential theory.** [S.l.]: Courier Corporation, 1953.

KOCH, K.R.; MORRISON, F. A simple layer model of the geopotential from a combination of satellite and gravity data. **Journal of Geophysical Research**, v. 75, n. 8, p. 1483-1492, 1970.

LAURETTA, D.S. OSIRIS-REx Asteroid Sample-Return Mission. In: PELTON, J.; ALLAHDADI, F. (Ed.). **Handbook of cosmic hazards and planetary defense.** [S.l.]: Springer, 2015. p. 543–567.

LAURETTA, D.S. et al. The unexpected surface of asteroid (101955) Bennu. **Nature**, v. 568, n. 7750, p. 55–60, 2019.

MACMILLAN, W.D. **The theory of the potential**. Dover : [s.n.], 1958.

MAGRI, C. et al. Radar observations and a physical model of Asteroid 1580 Betulia. **Icarus**, v. 186, n. 1, p. 152-177, 2007.

MARGOT, J.L. Binary asteroids in the near-Earth object population. **Science**, v. 296, n. 5572, p. 1445-1448. 2002.

MARZARI, F.; WEIDENSCHILLING, S.J. Eccentric extrasolar planets: the jumping Jupiter model. **Icarus**, v. 156, n. 2, p. 570-579, 2002.

MILLER, J.K. et al. Determination of shape, gravity, and rotational state of asteroid 433 Eros. **Icarus**, v. 155, n. 1, p. 3-17, 2002.

MONTENBRUCK, O.; GILL, E.; LUTZE, F. Satellite orbits: models, methods, and applications. **Applied Mechanics Review,** v. 55, n. 2, p. B27–B28, 2002.

MORAES, R.V.; GONÇALVES, L.D.; ROCCO, E.M. Trajectories in the neighborhood of Phobos and Deimos aiming coverage and approaching.In:COSPAR SCIENTIFIC ASSEMBLY, 42., 2018, Pasadena, California. **Proceedings…** 2018. Available at: <http://urlib.net/rep/8JMKD3MGP3W34R/3RFK9D8> Access on: Sept. 9, 2021.

MOTA, M. L. **Modelo do campo gravitacional de um corpo com distribuição de massa irregular utilizando o método da expansão do potencial em série e determinação de seus coeficientes dos harmônicos**

esféricos. 2017. 246 p. Tese (Doutorado em Engenharia e Tecnologia Espaciais/Mecânica Espacial e Controle) - Instituto Nacional de Pesquisas Espaciais (INPE), São José dos Campos, 2017. Available at: <http://urlib.net/8JMKD3MGP3W34P/3PQ2FAB> Access on: Sept. 9, 2021.

MOTA, M. L.; ROCCO, E. M. Equilibrium points stability analysis for the asteroid 21 Lutetia. **Journal of Physics: Conference Series,** v. 1365, n. 1, e 012007, 2019.

NAGGY, D. The prism method for terrain corrections using digital computers. **Pure and Applied Geophysics,** n. 63, p. 31-39, Dec. 1966.

OWEN, S.J. A survey of unstructured mesh generation technology. **IMR**, v. 239, p. 267, 1998.

PARK, R.S. et al. Estimating small-body gravity field from shape model and navigation data. **Journal of Guidance, Control, and Dynamics**, v. 33, n. 1, p. 212–221, 2010.

ROCCO, E.M. Analysis of the deviations of the trajectory due to the terrestrial albedo applied to some scientific missions. In: INTERNATIONAL CONFERENCE ON MATHEMATICAL PROBLEMS IN ENGINEERING, 2008, Genova, Italy. **Proceedings…** 2008a.

_____. Perturbed orbital motion with a pid control system for the trajectory. In: COLÓQUIO BRASILEIRO DE DINÂMICA ORBITAL, 14., 2008, Águas de Lindóia, Brazil. **Anais...** 2008b.

_____. Closed loop control system applied to earth-moon transfer maneuver using continuous thrust. In: COSPAR SCIENTIFIC ASSEMBLY, 38., 2010. **Proceedings…** 2010. p. 5.

_____. Evaluation of the approaching trajectories for landing on the asteroid 216 Kleopatra. In: IBERO-LATIN-AMERICAN CONGRESS ON COMPUTATIONAL METHODS IN ENGINEERING, 40., 2019. **Proceedings…** 2019. p. 1-17.

ROCCO, E. M; GONÇALVES, L. Simulation of the trajectories described by a space vehicle around the asteroid 243 Ida and its natural satellite Dactyl. **Journal of Physics: Conference Series,** v. 911, e012019, 2017. Available at: <http://dx.doi.org/10.1088/1742-6596/911/1/012019> Access on: Sept. 9, 2021.

ROCCO, E.M. et al. Station keeping of constellations using multiobjective strategies. **Mathematical Problems in Engineering**, v. 2013, 2013.

ROMAIN, G.; BARRIOT, J.P. Ellipsoidal harmonic expansions of the gravitational potential: theory and application. **Celestial Mechanics and Dynamical Astronomy,** v. 79, v. 4, p. 235-275, 2001. Available at: <http://dx.doi.org/10.1023/A:1017555515763> Access on: Sept. 9., 2021.

RUSSELL, C.T. et al. Dawn at Vesta: testing the protoplanetary paradigm. **Science**, v. 336, n. 6082, p. 684-686, 2012.

RUSSELL, R.P.; ARORA, N. Global point mascon models for simple, accurate, and parallel geopotential computation. **Journal of Guidance, Control, and Dynamics**, v. 35, n. 5, p. 1568–1581, 2012.

SANTOS, W. G. **Discrete multiobjective optimization applied to the spacecraft actuators command problem and tested in a hardware-in-the-loop rendezvous simulator.** 2015. 160 p. Tese (Doutorado em Mecânica Espacial e Controle) — Instituto Nacional de Pesquisas Espaciais (INPE), São José dos Campos, 2015. Available at: <http://urlib.net/rep/8JMKD3MGP3W34P/3HRTNES> Access on: Sept. 9., 2021.

SCHEERES, D.J. Orbital mechanics about small bodies. **Acta Astronautica**, v. 72, p. 1-14, 2012.

SCHEERES, D.J. et al. Dynamics of orbits close to asteroid 4179 Toutatis. **Icarus**, v. 132, n. 1, p. 53-79, 1998.

_____. Evaluation of the dynamic environment of an asteroid: applications to 433 Eros. **Journal of Guidance, Control, and Dynamics**, v. 23, n. 3, p. 466-475, 2000.

_____. The dynamical environment about asteroid 25143 Itokawa, target of the Hayabusa mission. In: AIAA/AAS ASTRODYNAMICS SPECIALIST CONFERENCE AND EXHIBIT, 2004. **Proceedings…** 2004. p. 4864.

_____. The dynamic geophysical environment of (101955) Bennu based on OSIRIS-REx measurements. **Nature Astronomy**, v. 3, n. 4, p. 352-361, 2019.

_____. Janus: a NASA SIMPLEx mission to explore two NEO Binary Asteroids. In: AGU FALL MEETING, 2020. **Abstracts…** 2020. p. A252-01.

_____. Heterogeneous mass distribution of the rubble-pile asteroid (101955) Bennu. **Science Advances**, v. 6, n. 41, eabc3350, 2020.

SILVA, M.R. **Estudo de uma missão espacial aos pontos colineares lagrangianos no sistema Terra-Lua.** 2017. 249 p. Tese (Doutorado em Mecânica Espacial e Controle) — Instituto Nacional de Pesquisas Espaciais (INPE), São José dos Campos, 2017. Available at: <http://urlib.net/rep/8JMKD3MGP3W34P/3PDP29P> Access on: Sept. 9, 2021.

STANBRIDGE, D. et al. Lucy: navigating a Jupiter Trojan Tour. In: AAS/AIAA ASTRODYNAMICS SPECIALIST CONFERENCE, 2017, Stevenson, WA, EUA. **Proceedings…** 2017. Available at: <https://www.researchgate.net/publication/323228730> Access on: Sept. 9, 2021.

USUI, T. et al. The importance of Phobos sample return for understanding the Mars-Moon system. **Space Science Reviews**, v. 216, n. 4, p. 1-18, 2020.

VENDITTI, F.C.F. **Manobras orbitais ao redor de corpos irregulares.** 2013. 228 p. Tese (Doutorado em Mecânica Espacial e Controle) — Instituto Nacional de Pesquisas Espaciais (INPE), São José dos Campos, 2013. Available at: <http://urlib.net/rep/8JMKD3MGP7W/3F7Q5U2> Access on: Sept. 9, 2021.

VEVERKA, J. et al. NEAR at Eros: imaging and spectral results. **Science**, v. 289, n. 5487, p. 2088-2097, 2000.

VOKROUHLICKÝ, D. et al. The Yarkovsky and YORP effects. **arXiv preprint**. 2015. Available at: <https://arxiv.org/pdf/1502.01249.pdf> Access on: Sept. 9, 2021.

WALDVOGEL, J.M.; POULIKAKOS, D. Solidification phenomena in picoliter size solder droplet deposition on a composite substrate. **International Journal of Heat and Mass Transfer,** v. 40, n. 2, p. 295-309, 1997.

WALSH, K.J. Rubble pile asteroids. **Annual Review of Astronomy and Astrophysics**, v. 56, p. 593-624, 2018.

WALSH, K.J.; RICHARDSON, D.C.; MICHEL, P. Rotational breakup as the origin of small binary asteroids. **Nature**, v. 454, n. 7201, p. 188-191, 2008.

WANG, T.N.E.; RAUCH, R. Back to elements-tetrahedra vs. hexahedra. In: INTERNATIONAL ANSYS CONFERENCE, 2004. **Proceedings…** 2004.

WATANABE, S. et al. Hayabusa2 mission overview. **Space Science Reviews**, v. 208, n. 1, p. 3-16, 2017.

WERNER, R.A.; SCHEERES, D.J. Exterior gravitation of a polyhedron derived and compared with harmonic and mascon gravitation representations of asteroid 4769 Castalia. **Celestial Mechanics and Dynamical Astronomy,** v. 65, n. 3, p. 313–344, 1996.

WITTICK, P.T.; RUSSELL, R.P. Mascon models for small body gravity fields. In: AAS/AIAA ASTRODYNAMICS SPECIALIST CONFERENCE, 2017. **Proceedings…** 2017. p. 17-162.

YU, Y. et al. A finite element method for computational full two-body problem: I. the mutual potential and derivatives over bilinear tetrahedron elements. **Celestial Mechanics and Dynamical Astronomy,** v. 131, n. 11, p. 51, 2019.

ZHENJIANG, Z. et al. The method to determine spherical harmonic model of asteroid based on polyhedron. In: INTERNATIONAL CONFERENCE ON COMPUTER AND ELECTRICAL ENGINEERING (ICCEE 2010), 3., 2012. **Proceedings…** 2012.